

1-1-2012

Synthesis, spectroscopic, and electrochemical properties of 3d metal and ruthenium complexes with phenolate and catecholate ligands

Frank Donald Lesh
Wayne State University,

Follow this and additional works at: http://digitalcommons.wayne.edu/oa_dissertations



Part of the [Inorganic Chemistry Commons](#)

Recommended Citation

Lesh, Frank Donald, "Synthesis, spectroscopic, and electrochemical properties of 3d metal and ruthenium complexes with phenolate and catecholate ligands" (2012). *Wayne State University Dissertations*. Paper 451.

This Open Access Dissertation is brought to you for free and open access by DigitalCommons@WayneState. It has been accepted for inclusion in Wayne State University Dissertations by an authorized administrator of DigitalCommons@WayneState.

**SYNTHESIS, SPECTROSCOPIC, AND
ELECTROCHEMICAL PROPERTIES OF 3d METAL AND
RUTHENIUM COMPLEXES WITH PHENOLATE AND
CATECHOLATE LIGANDS**

by

FRANK DONALD LESH

DISSERTATION

Submitted to the Graduate School

of Wayne State University,

Detroit, Michigan

in partial fulfillment of the requirements

for the degree of

DOCTOR OF PHILOSOPHY

2012

MAJOR: CHEMISTRY (Inorganic)

Approved by:

Advisor

Date

DEDICATION

I could not even imagine being in the position I am today without the infinite support of my family all throughout my life. I am forever indebted to my parents for they have flawlessly managed to put the happiness of my sister and me first in their lives. Their endless patience, encouragement, and immeasurable assistance never faltered even through the toughest of times. Treasured most is how they have granted me the independence to pave my own path while insistently alleviating me of the many burdens stumbled upon along the way. I am grateful for their advice, willingness to listen, model work ethic, and frequent reminders to maintain a healthy balance when overly absorbed by work.

I must also dedicate this work to one of my best friends who is unfortunately no longer here. Jason Dallos acted as a big brother and mentor to me in many aspects of my life. His intriguing passion for knowledge sparked an enthusiasm in me for scientific curiosity and is what ultimately inspired me to pursue graduate studies. I valued Jason for always keeping a positive attitude, and for being so deeply thinking and creative.

I am grateful to have exceptional friends who have unfailingly supplied me with the mindless entertainment necessary to keep perspective in life. The most notable of these characters are Adam Harper, Jaafar “Guapo” Beydoun, and Ryan “The G.O.A.T” Wood. Even though they only have the slightest idea of how chemistry actually impacts the world, their devastating workouts and epic words of motivation helped keep me determined and ambitious towards this intellectual pursuit.

ACKNOWLEDGEMENTS

This dissertation is the result of the support of many remarkable individuals and countless obstacles. My journey through this program was a complicated one to say the least, but it was the thrill of the challenge that kept me pushing forward as I struggled at nearly every step of the way.

First and foremost, I owe my utmost gratitude to my advisor Prof. Cláudio Verani who made this a truly rewarding experience and has empowered me with the confidence to face all challenges that life shall bring. Rather than making complex problems more complicated, as I often do, he taught me to step back and to logically dissect difficult problems from a fundamental approach. The first time I met Dr. Verani I remember him telling me that, “you don’t have to be a genius to get your Ph.D., you just have to be willing to put in the time and effort—the Ph.D. is a stamp on your forehead: Problem solver!” This attitude, along with his value for hard work and his enthusiasm in teaching, is what initially caught my attention to become a part of his group. I will forever appreciate his patience in allowing me time to develop and grow as a scientist and a person. You cannot put a price tag on the stimulating environment that he fostered which allowed me the chance to prove myself. Dr. Verani measures ones success as General George S. Patton once expressed: “by how high one bounces when one hits bottom, not by how high one climbs.” At times when I felt defeated and hopeless, he kept my head up, steered me back on course when I lost direction, kept faith in my will to fight, and believed in me at times when I did not even believe in myself. He has seen me at my lowest of lows and he persistently went to great lengths to fight to keep me in this

program. His personable behavior, flexibility, passion for science and music, unflinching encouragement, invaluable guidance, laser focus, tenacity, and general concern for the “human element” are attributes I will always admire. I appreciate that early on he was able to provide me with funding in the form of research assistantships to optimize my time for research. At this point in my career, I hope that I have finally gained his trust and left my mark on his research group.

I must next extend my sincere appreciation to my research committee members Prof. Stephanie L. Brock, Prof. Christine S. Chow, and Prof. Gavin Lawes for their valuable time, advice, and critical suggestions over the course of this work. They are all extraordinary individuals, but two of these people have left an especially notable imprint on my graduate experience. My full respect goes out to Prof. Brock for being absolutely perfect at all times, exceedingly organized, and a true model of professionalism for others to follow. I will forever be particularly grateful for the incredible influence Prof. Chow has had on my graduate career. The additional opportunity she arranged for me to demonstrate competency and continue in this program truly speaks volumes about her character and is just one example of the overall genuine concern she holds for the achievement of students.

Marco Allard has become one of my best friends and most supportive mentors during this long road. His consistent selflessness and willingness to offer a helping hand is a rare attribute and not often properly acknowledged. I appreciate his brutally honest criticisms that forced me to become stronger and the many stimulating discussions of proposed research and life in general that provided me valuable insight. Marco’s

indispensible practical knowledge played an integral part for day-to-day stumbling blocks. He is a natural “problem solver” and he was patient enough to show me the importance of proper planning and the ropes of working intelligently. Although Marco is the perfect example of “nice guys finishing last,” there is no doubt in my mind that one day he will have a prosperous research group to call his own.

Another one of my best friends and chief mentors is Jeff Driscoll. Consider yourself lucky if you have a person like Jeff in your life. The daily lab experience for me would not have been the same without Jeff. His perpetual positive energy is contagious and his inspiring words of support gave me courage to succeed. This special individual has seen war and destruction firsthand, and we journeyed together as he took me under his wing and helped me through my little battle within this program. He constantly reminded me to consider every hurdle as “just another opportunity to kick some ass!” I appreciate having a friend like Jeff who is always just a call away for bearing the brunt of all of my frustrations.

Within the first minutes of introducing myself to Rajendra Shakya he labeled me as “just another lazy American.” Fortunately, I believe by this point I have proved him wrong! I am most thankful to have had a mentor like Rajendra who always made himself accessible to answer questions. His patience in training me synthetic techniques was particularly valuable in the early stages of my research. I admire Rajendra for his brute force work ethic and his trusted friendship.

Our crowned lab safety inspector Sarmad Hindo was not the easiest going of my labmates back when I started in the Verani group. To be honest, I was literally afraid of

Sarmad for the longest time. Soon enough I realized that Sarmad is not actually that bad after all. Sarmad has always offered me great words of advice and was second author on my first published article for performing the amphiphilic studies.

And then came along enough estrogen to infest our male-dominated lab forever! Rama “drama” Shanmugam is one of the most competitive and persistent people on the face of this planet. I witnessed the metamorphosis of a quiet and obedient little girl to a loud and defiant woman. She is tough. Rama has praised me, hated me, helped me, mentally tortured me, and defended me (sometimes all in the course of a single day). She is my older, little Indian sister I never had. I will remember Rama for introducing me to “radioactive” rice, for acting as her substitute Hanuman for the past five years, and for holding the reign of Langmuir–Blodgett Queen. She is appreciated for carrying out the surface experiments of the compounds in my second and third published articles.

Dajena Tomco, Dakshika Wanniarachchi, and Lanka Wickramasinghe have dependably brightened the lab environment with their delightful smiles. I appreciate these ladies the most for putting up with the majority of my silly antics. Their cheerful, optimistic, upbeat, and positive nature always brought hope and encouragement. Debashis Basu is valued for his vibrant passion, enthusiasm, and interest. Watching them all grow is very pleasing. I would like to wish them, along with Ryan Thomas, all the best of luck!

I would like to acknowledge all of the hard work, time, and effort of the individuals with whom I had collaborations. Prof. Mary T. Rodgers is acknowledged for the mass spectrometric data of some of our larger systems. Prof. John F. Endicott is

thanked for sharing his vast knowledge and criticisms in our group meetings, and for his expertise in emission spectroscopy. Prof. H. Bernhard Schlegel is appreciated for overseeing the DFT calculations on numerous studies. Dr. Richard L. Lord played a huge role in computationally elucidating the intricate electrochemistry of our amino-catecholate systems. The completion of these projects relied heavily on his competence and insightful comments. His friendship, positive attitude, critical suggestions, and model conduct are gratefully acknowledged.

Dr. Mary Jane Heeg is greatly appreciated for solving the X-ray crystallographic structures. Her meticulousness and punctuality was always a great help. Dr. Lew M. Hryhorczuk is acknowledged for performing the mass spectrometric analyses in a consistently prompt fashion. Most of the time, he was the determining factor of whether I was going to have a “good” or “bad” day! Lew and I have shared many great laughs and his company and wise words of advice will definitely be missed. I also want to thank Dr. Brian Shay for mass spectra analyses and Dr. Bashar Ksebati for NMR training.

My heartfelt appreciation goes to Sharon Kelly for her kind words of advice, patience, and faith in times of desperate need. She is a grandmother to this department and has gone to great lengths for myself and many other people. Her true compassion for the success of students is an amazing trait. I must also acknowledge Melissa Barton for her superior organizational skills and assistance during the completion of this work.

I would like to thank the office support and administrative staff in the chemistry department, including Erin Bachert, Marty Krol, Nestor Ocampo, Lora Dakhi, Beverly

Jacobs, Diane Klimas, Linda Jackson, Diana Kudla, Berny Miesik, Debbie McCreless, Francine Owczarek, Mary Wood, and others for their assistance.

I express my gratitude to Prof. Maryfrances Barber, Prof. Alexander Benderskii, Prof. Richard Lindvedt, Prof. Michael Maguire, Prof. David Coleman, and Prof. Patsy Coleman for their guidance when I was a teaching assistant.

Financial support was provided by the Institute for Manufacturing Research (IMR) grant, National Science Foundation (NSF), Department of Energy (DOE), and the American Chemical Society's Petroleum Research Fund (ACS-PRF).

TABLE OF CONTENTS

Dedication.....	ii
Acknowledgements.....	iii
List of Figures.....	xi
List of Tables.....	xv
List of Schemes.....	xvi
Chapter 1 – Introduction.....	1
Chapter 2 – Experimental and Characterization Techniques.....	7
Chapter 3 – On the Effect of Coordination and Protonation Preferences in the Amphiphilic Behavior of Metallosurfactants with Asymmetric Headgroups.....	22
Chapter 4 – A Modular Approach to Redox-Active Multimetallic Hydrophobes of Discoid Topology.....	68
Chapter 5 – Investigation of the Electronic, Photosubstitution, Redox, and Surface Properties of New Ruthenium(II)-containing Amphiphiles.....	86
Chapter 6 – Unexpected Formation of a Cobalt(III) Phenoxazinylate Electron Reservoir.....	120
Chapter 7 – The Rich Electron Transfer Behavior of Iron(III) and Gallium(III) Complexes with a Redox-Active Bis(phenolate) Phenylenediamine Ligand.....	135
Chapter 8 – Conclusions and Perspectives.....	159
Appendix A – Supplementary Material for Chapter 3.....	165
Appendix B – Supplementary Material for Chapter 4.....	169
Appendix C – Supplementary Material for Chapter 5.....	182
Appendix D – Supplementary Material for Chapter 6.....	197
Appendix E – Supplementary Material for Chapter 7.....	220

Appendix F – Permission/License Agreements for Copyrighted Material.....	223
Abstract.....	245
Autobiographical Statement.....	247

LIST OF FIGURES

Figure 2.1 Generic shape of a cyclic voltammogram.....	13
Figure 2.2 Electron spin and singlet/triplet excited states.....	15
Figure 2.3 Potential-energy curve for phosphorescence.....	16
Figure 3.1 ESI(pos) peak clusters with experimental (bars) and simulated (continuum) isotopic distributions for 1–4 . The relative abundance axis of each complex is omitted for clarity.....	27
Figure 3.2 ORTEP diagram at 50% probability for $[\text{Ni}^{\text{II}}(\text{L}^{\text{tBu}^{\text{A}}})(\text{OAc})]\cdot\text{CH}_3\text{OH}$ (5). Solvent and hydrogen atoms are excluded for clarity.....	30
Figure 3.3 ORTEP diagram at 50% probability for $[\text{Ni}^{\text{II}}(\text{L}^{\text{A}})_2]\cdot\text{CH}_3\text{OH}\cdot\text{H}_2\text{O}$ (6). Solvents and hydrogen atoms are excluded for clarity.....	31
Figure 3.4 ORTEP diagram at 50% probability for $[\text{Ni}^{\text{II}}(\text{L}^{\text{tBu}^{\text{A}}})_2]\cdot 2\text{CH}_3\text{OH}$ (7). Solvents and hydrogen atoms are excluded for clarity.....	31
Figure 3.5 ORTEP diagram at 50% probability for $[\text{Cu}^{\text{II}}(\text{HL}^{\text{tBu}^{\text{A}}})(\text{L}^{\text{tBu}^{\text{A}}})]\text{ClO}_4$ (8). Counterions and hydrogen atoms are excluded for clarity.....	32
Figure 3.6 ORTEP diagram at 50% probability for $[\text{Zn}^{\text{II}}(\text{HL}^{\text{tBu}^{\text{A}}})(\text{L}^{\text{tBu}^{\text{A}}})]\text{ClO}_4$ (9). Counterions and hydrogen atoms are excluded for clarity.....	33
Figure 3.7 UV–vis spectra of complexes 3 and 8 in dichloromethane, 1.0×10^{-4} M. Inset: 3 and 8 at 1.0×10^{-2} M.....	39
Figure 3.8 Selected MOs and spin density plot for the archetype 6	43
Figure 3.9 Selected molecular orbitals and spin-density plot for the optimized structures of the archetype 8 and model 3'	45
Figure 3.10 Langmuir–Blodgett isotherms of the metallosurfactants.....	47
Figure 3.11 Selected Brewster angle micrographs. For 1 : (a) before compression, (b) between $1\text{--}10 \text{ mN m}^{-1}$, (c) after 11 mN m^{-1} . For 2 : (d) before compression,	

(e) between 3–10 mN m ⁻¹ , (f) after 11 mN m ⁻¹ . For 3: (g) before compression, (h) between 2–12 mN m ⁻¹ , (i) after 13 mN m ⁻¹ . For 4: (j) before compression, (k) between 1–10 mN m ⁻¹ , and (l) after 11 mN m ⁻¹	49
Figure 4.1 Modular discoid species [Fe ^{II} (Fe ^{III} L ²) ₃] ²⁺	71
Figure 4.2 XANES region of the Fe K-edge XAS for [Fe ^{II} (Fe ^{III} L ²) ₃](PF ₆) ₂ (red) and [Fe ^{III} L ²] (blue). Inset: EXAFS region for [Fe ^{II} (Fe ^{III} L ²) ₃](PF ₆) ₂ . Data (red) and simulation (blue). Shell 1 (Fe–O): <i>n</i> = 2, <i>r</i> = 1.839(6) Å, σ^2 = 0.0048(13) Å ² . Shell 2 (Fe–N): <i>n</i> = 3, <i>r</i> = 1.960(3) Å, σ^2 = 0.0010(5) Å ² . Shell 3 (Fe–N): <i>n</i> = 1, <i>r</i> = 2.104(13) Å, σ^2 = 0.0030(2) Å ² . Shell 4 (Fe–C): <i>n</i> = 4, <i>r</i> = 2.919(6) Å, σ^2 = 0.0053(8) Å ² . <i>E</i> ^o = 7128.7 eV. ϵ^2 = 0.63.....	73
Figure 4.3 (a) ORTEP for [GaL ²], Ga–O(3) = 1.828(3), Ga–O(1) = 828(3), Ga–O(2) = 1.899(3), Ga–N(4) = 1.975(4), Ga–N(1) = 2.266(4) Å. (b) MM-UFF model for [Ga(GaL ²) ₃] ²⁺	76
Figure 4.4 CVs of [Fe ^{II} (phen) ₃](PF ₆) ₂ (top), [Fe ^{III} L ²] (middle), and [Fe ^{II} (Fe ^{III} L ²) ₃](PF ₆) ₂ (bottom) in dichloromethane, TBAPF ₆ vs Fc ⁺ /Fc.....	77
Figure 4.5 [Fe ^{II} (Fe ^{III} L ²) ₃](PF ₆) ₂ at the air/water interface: (a) isothermal compression. Selected BAM images at (b) 10–40 mN/m and (c) collapse.....	79
Figure 5.1 UV–visible spectra of pyridyl complexes 1 and 2 (top) and phenolate complexes 3 and 4 (bottom) in acetonitrile, 1.0 × 10 ⁻⁵ M.....	93
Figure 5.2 Emission spectra of pyridyl complexes 1 and 2.....	94
Figure 5.3 UV–visible spectra recorded for photodissociation of 2 in MeCN.....	96
Figure 5.4 CVs of 1–4 in acetonitrile, TBAPF ₆ , Potential (mV) versus Fc ⁺ /Fc.....	98
Figure 5.5 Relative molecular orbital energies.....	100
Figure 5.6 Orbital composition for 1' and 3'.....	102
Figure 5.7 Compression isotherms of the metallosurfactants.....	105

Figure 5.8 BAM images of complexes 1 and 2	107
Figure 5.9 BAM images of complexes 3 and 4	108
Figure 6.1 ORTEP diagram for [Co(L') ₂]•2MeCN showing 50% probability of the thermal ellipsoids. Solvent and hydrogen atoms are excluded, and the ^t Bu groups are truncated to the central quaternary carbon for clarity. Selected bond lengths (Å) and angles (°): Co(1)–N(1) 1.876(2), Co(1)–N(3) 1.887(2), Co(1)–O(1) 1.892(2), Co(1)–O(3) 1.899(2), Co(1)–N(2) 1.953(2), Co(1)–N(4) 1.956(2); N(2)–Co(1)–N(3) 104.83(8), N(2)–Co(1)–N(4) 92.64(8), O(1)–Co(1)–N(3) 86.55(7), O(1)–Co(1)–O(3) 91.35(7), O(1)–Co(1)–N(1) 84.80(7), O(1)–Co(1)–N(4) 89.33(7).....	124
Figure 6.2 Contour plots (0.05 au) for the singly occupied (top) and AF coupled (bottom) orbitals resulting from the corresponding orbital analysis. S _{αβ} is the overlap integral for the AF coupled corresponding orbitals.....	126
Figure 6.3 Experimental (solid) and simulated (dashed) UV–visible absorption spectrum of [^L S Co ^{III} (PhO [–] –N [–] –Phz [•])(PhO [•] –N [–] –Phz [•]) ₂] ⁰ in CH ₂ Cl ₂	127
Figure 6.4 CV trace in CH ₂ Cl ₂ , with 0.1 M TBAPF ₆ , and 1.0×10 ^{–3} M [^L S Co ^{III} (PhO [–] –N [–] –Phz [•])(PhO [•] –N [–] –Phz [•])], 150 mV s ^{–1} ; mV vs. Fc ⁺ /Fc. Insets are representations of the cathodic ligand redox events, with only one resonance structure shown for each.....	128
Figure 7.1 Perspective view ORTEP diagrams for 1 (top) and [2]•0.5CH ₃ CN•0.5CH ₂ Cl ₂ (bottom) showing 50% probability of the thermal ellipsoids. Non-coordinated solvents and hydrogen atoms are excluded for clarity. Selected bond distances (Å) for 1 : Ga(1)–O(2) 1.877(3), Ga(1)–O(1) 1.880(3), Ga(1)–N(1) 2.024(3), Ga(1)–N(2) 2.025(3), Ga(1)–Cl(1) 2.224(12), Ga(1)–O(3) 2.329(6). For 2 : Fe(1)–O(2) 1.942(11), Fe(1)–O(1) 1.948(11), Fe(1)–N(1) 2.022(13), Fe(1)–N(2) 2.044(13), Fe(1)–Cl(1) 2.220(5).....	141
Figure 7.2 Isodensity plot (0.002 au) for the spin density of the lowest energy computed Fe ^{III} species. Blue and white correspond to excess α and β density, respectively.....	147

Figure 7.3 Absorption spectra of complexes **1** (black) and **2** (grey/red) in dichloromethane, 1.0×10^{-5} M. Experimental absorption curves are solid, while TD-DFT fitted curves are dashed.....148

Figure 7.4 CVs of **1** and **2** in dichloromethane, TBAPF₆, vs Fc⁺/Fc..... 150

LIST OF TABLES

Table 3.1 Selected bond lengths (Å) and angles (°) for 5 , 6 , 7 , 8' , and 9	34
Table 3.2 UV–vis parameters for ligands and complexes.....	40
Table 3.3 Crystal data.....	53
Table 5.1 Photophysical Parameters for Complexes 1–4	92
Table 5.2 Cyclic Voltammetry Data for 1–4	99
Table 5.3 Experimental and Calculated HOMO-LUMO Gaps.....	104
Table 7.1 Structural comparison of the M–L and some intraligand bond lengths (Å).....	142
Table 7.2 Structural comparison between experiment and computation for the M–L and some intraligand bond lengths (Å). See Table 7.1 for numbering scheme.....	146
Table 7.3 UV-visible Parameters for Complexes 1 and 2	148
Table 7.4 Cyclic voltammetry data for 1 and 2	151
Table 7.5 Crystal Data.....	153

LIST OF SCHEMES

Scheme 3.1 The ligand HL^{tBuODA} , possible protonation status for metallosurfactants and archetypes studied.....	25
Scheme 3.2 The ligands HL^{tBuI} , HL^A , and HL^{tBuA} used in the archetypes.....	29
Scheme 5.1 Series of Pyridine- and Phenolate-Based Ruthenium(II)-Containing Amphiphiles 1–4	88
Scheme 5.2 Ru/Phenolate Orbital Interactions for 3' and 4'	103
Scheme 6.1 Formation of the mixed phenolate/phenoxazinyl radical species from H_4L	122
Scheme 7.1 Resonance isomers of H_4L	140

CHAPTER 1

INTRODUCTION

1.1. Overview

Considerable effort grasping the fundamental concepts of a broad scope of non-trivial challenges provides momentum to the extensive realm of transition metal coordination chemistry. The available amount of knowledge, along with the access that inorganic chemists have to a vast toolbox of materials and methods, has facilitated them to tackle relevant obstacles on the molecular level by applying conceptual approaches and strategies. The spectrum of contributions, for example, can range anywhere from biological cancer therapies to energy-related applications. Owing to the versatility of synthetic manipulation and controlled chemical design and reactivity, the insight gained from the comprehension of molecular interactions, functions, and mechanisms creates traction towards developing innovative solutions. As opposed to directly targeting instant applications, research in our group has been primarily motivated by probing the underlying principles of preserving the rich electrochemical, spectroscopic, and magnetic properties of coordination complex systems that demonstrate effective activity in solution-based analyses for ordered surface deposition onto solid interfaces.

Our approach has been dedicated to spearheading the design of coordinating ligands with amphiphilic functionalities that upon complexation with various transition metal centers may behave as amphiphilic precursors, also referred to as metallosurfactants (*i.e.*, surfactants containing metal ions). For the formation of highly ordered monolayers by means of Langmuir–Blodgett deposition techniques this amphiphilic behavior is the crucial aspect. Consequently, these monolayers may allow for

thin film formation in an attempt to guide the path toward device fabrication for future applications. Deriving from this idea, our group is concurrently seeking to address the challenge posed by the persisting, nearly inescapable energy crisis. The objective is to develop unprecedented thin film materials with the capacity to improve the current efficiencies of photosensitized water oxidation catalysts to sustain a hydrogen economy post fossil-fuel age. Mimicking the natural process of photosynthesis by way of artificially developing systems with the capability of photochemically splitting water has been extremely desired. Such a feat requires the investigation of multielectron chemical reactivity and controlling energy transfer events. The approach being explored focuses on the incorporation of light absorbing antennae, charge accumulation sites, and heterobimetallic catalytic cores in an organized extended Langmuir–Blodgett precursor modular film. In accord with our overall aim, this methodology would enable for the surface deposition of a small-footprint responsive film while conserving the properties observed in solution.

The multidisciplinary nature of our research relies on a concerted effort in synthetic protocols, electrochemical, spectroscopic, and photophysical characterizations, film formation techniques, and predictive or explanatory theoretical and computational methods. Largely, the group has focused on:

- (i) The synthesis and characterization of first-row or selected second-row redox-active transition metal coordination complexes containing ligands with the capability to stabilize organic radicals.
- (ii) Analyzing the mechanisms of metal/radical ground state switching.
- (iii) Tailoring species for surface deposition.

Our group has demonstrated different redox and collapse mechanisms in cobalt(II) films, incorporated magnetic μ -oxo-Cu₄ clusters in Langmuir–Blodgett films, studied the thermotropic mesomorphism of copper-containing amphiphiles, and investigated the structural and electronic effects on geometry in metallosurfactants containing various first-row transition metal ions with asymmetric ligands. The methodology followed in these studies focuses on the isolation and characterization of the distinct metallosurfactant precursors prior to surface deposition. Previous reports describe direct assembly at the air/water interface which leads to restricted reproducibility because of the limited control. The rationale behind our design strategy targets chelating phenolate-based ligands coordinated to selected metal ions due to its synthetic and redox flexibility. Stabilization of the oxidized phenolate into a phenoxyl radical requires *tert*-butyl substituents for improved redox behavior. However, we have experienced first-hand that enhanced electrochemical properties can negatively affect amphiphilic behavior, or vice versa, and we continue to make efforts towards solving this issue.

1.2. Research Statement

Contributions on my part towards these abovementioned group objectives are defined generally within the synthetic design and characterization of novel redox-active species and the evaluation of electronic and electrochemical responses of such systems. In particular, these goals entail furthering our main objective of designing candidates for the formation of redox-responsive monolayer films by:

- (i) Using an array of different metal ions to understand how coordination preference dictates amphiphilicity.

- (ii) Exploiting a modular, multi-step approach for synthesizing supramolecular, multimetallic amphiphiles of new differentiated topologies to optimize redox and amphiphilic behaviors.

The relevant impact made towards our objective of achieving solar photocatalytic water oxidation focuses on:

- (i) Addressing the basic principles underlying photosensitivity by integrating ruthenium(II) into our existing amphiphilic precursor ligands for the formation of prospective photoresponsive modular films.
- (ii) Introducing a more stable organic radical to our current systems to examine the appealing nature associated with multielectronic ligand-centered redox reactivity.

1.3. Research Goals

The strategies executed to address the outlined problems are presented as the following Research Goals, which will encompass **Chapters 3–7**. The basis for the sequence that the experimental results are presented coincide with the chronological development of the progressing group motivations.

Goal #1: *To develop responsive metal-containing surfactants that serve as precursors for Langmuir–Blodgett films.* Current approaches in the emerging field of responsive thin film materials ordinarily involve assembling metal/organic scaffolds at the air/water interface without the characterization of discrete precursors. The isolation of well defined metallosurfactant precursors allows for precise control in the surfactant-to-metal ratio and coordination

modes of the final structure of the material. In **Chapter 3**, my resulting contributions toward this goal are discussed in detail by concentrating primarily on monometallic complexes of early transition metals (d^8 -Ni^{II}, d^9 -Cu^{II}, and d^{10} -Zn^{II}) with four-, five-, and six-coordinate geometries. We establish the effect of coordination and protonation preferences in these metallosurfactants and further the knowledge of how these factors dictate the observed amphiphilic behavior.

Goal #2: To extend efforts toward developing redox-active homotetranuclear and heterodinuclear pentacoordinated M(III)M(II) amphiphiles of new topologies. The specific objective of this goal is based on our group observation that when *tert*-butyl substituents are incorporated into phenolate-based headgroups for enhanced metal/radical stabilization, the effect confers improved redox behavior and leads to compromised amphiphilic character. This occurrence is addressed in **Chapter 4** through the development of multimetallic film precursors using a modular synthetic approach. Metal inclusion not only assists in accommodating both the redox and amphiphilic properties, but permits the design of novel topologies that are not available to traditional organic-derived surfactants.

Goal #3: To achieve the integration of photo-responsive groups to the headgroups of metal-containing surfactants that serve as precursors for Langmuir–Blodgett films. A pertinent step towards designing metallosurfactant precursors for photo-active modular films to achieve artificial photosynthesis is

merging amphiphilic properties to antennae components. The significance of ruthenium bipyridyl complexes towards water oxidation catalysts prompted us to coordinate well-established bidentate amphiphilic ligands (earlier investigated with the Cu^{2+} ion in our group) to the photo-responsive $[\text{Ru}(\text{bpy})_2]^{2+}$ to yield metalloamphiphiles with rich electronic and electrochemical features. **Chapter 5** discusses in detail the target of preserving the amphiphilic and photophysical properties of these new ruthenium(II)-containing metallosurfactants while expanding the redox behavior with the presence of ligand moieties such as phenolates.

Goal #4: *To expand our current use of redox-active moieties by exploiting ligands containing amino-catechols.* Current motivations focus on bringing into play the capacity of noninnocent ligands to enhance the reaction chemistry of coordination compounds. With the ability to store electrons, such ligands can act as electron reservoirs in complexes containing inexpensive first-row transition metals to essentially eliminate the use of noble transition metals to mediate multielectron catalytic transformations. The amino-catecholate chemistry of **Chapters 6** and **7** was initiated by attempts to expand the electrochemical response of our previously used phenoxyl radical based systems by tailoring our phenanthroline ligand platforms to include a more air stable redox-active moiety.

CHAPTER 2

EXPERIMENTAL AND CHARACTERIZATION TECHNIQUES

2.1. General

Reagents and solvents were used as received from commercial sources. Methanol was distilled over CaH_2 . Infrared spectra were measured from 4000 to 400 cm^{-1} on a Tensor 27 FTIR spectrophotometer as KBr pellets. ^1H - and ^{13}C -NMR spectra were measured with Varian 300 and 400 MHz instruments. ESI(+) spectra were measured in a triple quadrupole Micromass QuattroLC mass spectrometer with ESCi source. A Bruker 7.0T ApexUltra FTMS with an Apollo 2 Dual Source was used to measure the ESI(+) spectrum of the $[\text{Fe}^{\text{II}}(\text{Fe}^{\text{III}}(\text{L}^2)_3](\text{PF}_6)_2$ species in **Chapter 4**. This sample was dissolved in methanol at a concentration of 1 mg/mL then diluted 1:100–1:1000, externally calibrated with NaTFA, and analyzed at a flow rate of 180 mL/min from m/z 300–3500. Elemental analyses were performed with the addition of V_2O_5 to ensure complete combustion by Midwest Microlab, Indianapolis, IN.

Absorption UV–visible spectroscopy from 1.0×10^{-2} to 5.0×10^{-6} M acetonitrile, dichloromethane, dimethylformamide, or dichloromethane/methanol (1:1) solutions were performed using a Cary 50 spectrometer within the 250 to 1100 nm range. Fluorescence excitation and emission spectra were measured on a Cary Eclipse fluorescence spectrophotometer. Lifetime measurements were recorded using a Hamamatsu R9220 type photomultiplier tube and decay traces were collected using a National Instruments PCI-5154 digitizer. Samples were excited using a Photochemical Research Associates Inc. nitrogen/dye laser combination LN1000 and LN107, respectively. Lifetimes were determined by single exponential fitting of the luminescence decay traces. Cyclic

voltammetry experiments were performed in 1.0×10^{-3} M dry acetonitrile or dichloromethane analyte solutions containing 0.1 M TBAPF₆ supporting electrolyte using a BAS 50W voltammetric analyzer at various scan rates (mV s^{-1}). A standard three-electrode cell was employed with a carbon or platinum working electrode, a platinum-wire auxiliary electrode, and an Ag/AgCl reference electrode (freshly coated) under an inert atmosphere at RT. All potentials are reported versus the Fc⁺/Fc internal standard reference couple.¹ The first derivative X-band EPR spectrum of a 1.0×10^{-3} M CH₂Cl₂/CH₃OH (1:1) solution was measured with a Bruker ESP 300 spectrometer at 115 K using a liquid N₂ cryostat. X-ray diffraction data were measured using a Bruker P4/CCD or a Bruker X8 APEX-II kappa geometry diffractometer with Mo radiation and a graphite monochromator.

Photolability studies were performed with a highly intense T-type halogen source (500 W) without use of an UV cutoff filter by irradiation of dissolved samples of the $[(L^{Py^I})Ru^{II}(bpy)_2](PF_6)_2$, $[(L^{Py^A})Ru^{II}(bpy)_2](PF_6)_2$, and $[(L^{PhBu^I})Ru^{II}(bpy)_2](PF_6)_2$ metalloamphiphiles in **Chapter 5**. Photoirradiation of each sample at 1.0×10^{-3} M concentrations occurred in a 25 mL round-bottom flask, fitted with a reflux condenser, under argon blanketing and stirring for a time period of 40 min while keeping constant the exposure intensity of irradiation. During this time period, aliquots were analyzed at times $t = 0, 3, 20,$ and 40 min by UV-visible spectroscopy and mass spectrometry.

Electronic structure calculations were carried out either by Dr. Marco M. Allard in the Verani Lab for **Chapters 3–5** or Dr. Richard L. Lord under the supervision of Prof. H. Bernhard Schlegel for **Chapters 6 and 7** with the Gaussian 09 suite of programs² using DFT. In general, calculations with the B3LYP^{3–5} functional employed the

LANL2DZ⁶ basis set and pseudopotential. Since all of the ground states were closed shell singlets, calculations were carried out with spin restricted methods. Tight self-consistent field (SCF) convergence (10⁻⁸ rms for the density) was used throughout. Geometries were fully optimized without symmetry constraints, and stationary points were verified via frequency analysis. Solvent effects in acetonitrile were estimated using the IEF-PCM polarizable continuum model.⁷⁻⁹ Molecular orbitals were plotted with GaussView.¹⁰

Isothermal compression and Brewster angle microscopy monolayer studies were performed in our lab by Dr. Sarmad S. Hindo for the compounds in **Chapter 3** or Rama Shanmugam for the complexes in **Chapters 4** and **5** using an automated KSV 200 mini trough at room temperature (23.0 ± 0.5 °C). Ultrapure water (Barnstead NANOpure) with a resistivity of about 18.2 MΩ/cm was used as the subphase in all of the experiments with the exception of compounds [(L^{PyI})Ru^{II}(bpy)₂](PF₆)₂ and [(L^{PyA})Ru^{II}(bpy)₂](PF₆)₂ in **Chapter 5**. These species were found to be partially soluble in the pure water subphase, therefore a 0.1 M NaCl solution (pH ≈ 5.0) was prepared using ultrapure water (Barnstead NANOpure) with a resistivity of about 18.2 MΩ·cm⁻¹ and was used as the subphase in each of the experiments. Universally, the surface of the subphase was cleaned by vacuum suction after barrier compression. Spreading solutions of a known concentration (1.0 mg·mL⁻¹) and a known quantity (30 μL), prepared in spectra grade chloroform, were then introduced on the clean aqueous subphase. The system was then allowed to equilibrate for 15 min before monolayer compression. The compression isotherms were obtained at a compression rate of 10 mm·min⁻¹. The surface pressure was measured using the Wilhelmy plate (paper plates 20 mm × 10 mm) method. The selected isotherms represent the average of at least three independent measurements with

excellent reproducibility. Brewster angle micrographs were taken simultaneously with the compression isotherms using a KSV–Optrel BAM 300 equipped with a HeNe laser (10 mW, 632.8 nm) and a CCD detector. The field of view was $800 \times 600 \mu\text{m}$ and the lateral resolution was about $1 \mu\text{m}$. Since these methods were extensively used in the experimental research to follow, a brief review of these methods is offered: Langmuir–Blodgett (LB) film preparation begins with the measurement of the amphiphilic behavior of the surfactant monolayer at the air/water interface. After spreading the amphiphile, the monolayer can be compressed by displacing moving barriers on a minitrough closer to each other. The KSV computer controlled minitrough operates with two compressing barriers. The compression isotherms for the novel amphiphiles described will be measured using the Wilhelmy plate technique, which plots surface pressure (π) vs. area occupied per molecule (A^2). The area A^2 can be accurately determined from the enclosed area between movable barriers and the concentration of the surfactant initially loaded. The knowledge of the 2D phase diagram for each molecular precursor is essential. It allows to access the desired 2D phase of the monolayer and to control the molecular order in the film. Furthermore, the compression isotherms yield fundamental information regarding the effect of the sub-phase aqueous solution on the organization of the monolayer, such as the limiting area per molecule (A_{lim}), the area at the collapse of the monolayer (A_c), and the collapse pressure (π_c). Similar to the behavior of liquid crystals, these monolayers can possess a large number of mesophases with different orientation or rotational degrees of freedom for the molecules. Brewster angle microscopy,^{11,12} is a complimentary technique that gives information about this phase behavior. A Brewster angle is associated with p-polarized light, where a reflectivity coefficient vanishes at the

Brewster angle with no light being reflected, and the typical domain size observed is between 20–200 micrometers. The air/water monolayers with the desired order and molecular patterns will be transferred onto solid substrates using LB deposition. The transfer ratio (area occupied by the monolayer on the water sub-phase *vs.* area of the transferred monolayer on the solid substrate) can be measured accurately, addressing the issue of how well the monolayers are transferred onto the substrates. A transfer ratio of 1.00 indicates full transfer. All films discussed here show total-reflectance between 0.98–1.05 Langmuir monolayers can be transferred reproducibly, with the transferred motif being a close representation of the monolayer at the air/water interface.

The X-ray absorption near edge structure (XANES) and extended X-ray absorption fine structure (EXAFS) data of solid samples of $[\text{Fe}^{\text{II}}(\text{Fe}^{\text{III}}(\text{L}^2)_3)(\text{PF}_6)_2$ and $[\text{Fe}^{\text{III}}(\text{L}^2)]$ in **Chapter 4** was collected by Prof. Jason M. Shearer (Department of Chemistry, University of Nevada, Reno, NV). The samples were diluted in nujol (final concentration of Fe \sim 0.5 M), ground into a fine homogeneous paste, and packed into aluminum sample holders with Kapton tape windows. Data were collected at the National Synchrotron Light Source (Brookhaven National Laboratories; Upton, NY) on beamline X3b. A focused Si(111) double monochromator was used for energy selection along with a low-angle Ni mirror for harmonic rejection. Energy calibrations were performed by recording a reference spectrum of Fe foil (first inflection point assigned to 7111.2 eV) simultaneously with the samples. All samples were maintained at 20 K throughout the data collection using a helium Displex cryostat. The spectra for the solid state samples were recorded in transmission mode ($\text{N}_2(\text{g})$ filled ionization chambers). For edge spectra, the primary hutch aperture height was set to 0.4 mm to obtain the maximum resolution

(theoretical maximum is ~ 0.7 eV) and data were obtained in 10 eV steps in the pre-edge region (6960–7100 eV), 0.3 eV steps in the edge region (7100–7126 eV), and 2.0 eV steps in the near-edge region. For EXAFS spectra, the primary hutch aperture was set to 0.8 mm and data were obtained in 5.0 eV steps in the pre-edge region (6950–7100 eV), 0.5 eV steps in the edge region (7100–7126 eV), 2.0 eV steps in the near-edge region (7126–7611 eV), and 5.0 eV steps in the far-edge region (7611 eV–15.5 k). All spectra represent the averaged sum of three data sets. Data analysis was performed with the XAS refinement package EXAFS123.¹³ Phase (α) and amplitude (f) functions were generated with FEFF 7.02 as previously described^{14,15} using crystallographic data from $[\text{Fe}^{\text{III}}(\text{L}^2)]$ and $[\text{Fe}^{\text{II}}(\text{phen})_3]^{2+}$. All of the nomenclature and error analysis used conforms to generally accepted usage based on the recommendations of the International Workshops on Standards and Criteria in XAFS.¹⁶

Standard spectrometric, spectroscopic, electrochemical, and diffraction methods mentioned used in the Verani Group for extensive characterization of inorganic species will not be discussed in further detail. Cyclic voltammetry (CV) warrants some discussion because of the emphasis placed on the redox response throughout the experimental research to follow. In addition, the aspect of emission spectroscopy becomes relevant with the investigation of the photoresponsive properties of ruthenium bipyridyl complexes and will also be described in some detail.

2.2. Cyclic Voltammetry

The electroanalytical technique of cyclic voltammetry (CV), or linear sweep voltammetry, is practical in the qualitative investigation of the electron transfer behavior of a solution system from the current-potential response within an electrochemical cell.

Widespread applications include the detailed mechanistic evaluation of reduction/oxidation properties associated with biomimetic enzymatic catalysts,¹⁷ the identity of reaction intermediates, ligand effects on redox potentials in metal-containing complexes,^{18,19} biosynthetic reaction pathways,²⁰ and the electrochemical formation of free radicals.²¹ In the course of a typical cyclic voltammetric experiment, a standard three-electrode potentiostat is employed with a working electrode, an auxiliary electrode, and a reference electrode all immersed in a purged supporting electrolyte solution containing a dissolved analyte species of interest. A cyclic voltammogram, as illustrated in **Figure 2.1** where one complete redox cycle is depicted, is generated from the ensuing current response that is measured while the applied potential at the working electrode is cycled at various scan rates.

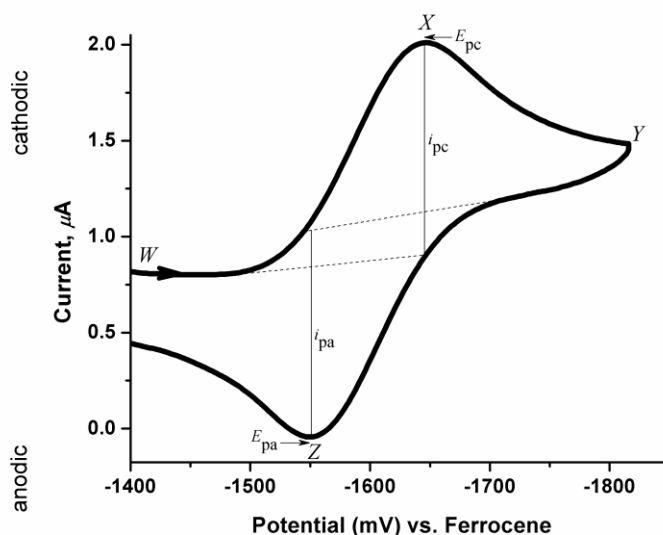


Figure 2.1. Sample cyclic voltammogram (adapted from reference 22)

At point *W*, the initial potential is applied to the example system and the forward negative scan of the potential advances until a cathodic current is reached for reduction to begin.

The observed current increases sharply to point *X* at which stage the electrode surface concentration of the original species is significantly lessened. As the species dissolved in solution surrounding the electrode surface convert to the fully reduced form, the current diminishes to point *Y*. At this potential only the reduced form of the initial species is present in solution and the reverse positive scan progresses until an anodic current is attained for oxidation to occur. The observed current decreases abruptly to point *Z* at which period the surface of the electrode is appreciably depleted of the reduced species. The current decays back to point *W* as the species dissolved in solution nearby the surface of the electrode revert back to the fully oxidized form.²²

In an overall electrochemical transfer, in which the observed current is dependent upon the variable rates of mass and electron transfer from the bulk solution to the surface of the electrode, the Nernst equation (**Equation 2.1**) relates the equilibrium of the concentrations of reduced (red) and oxidized (ox) analyte species.²³

$$E = E^{\circ'} - (0.05916/n) \ln([\text{red}]/[\text{ox}]) \quad \text{Eq. 2.1}$$

Here, E is the applied electrode potential, the formal reduction potential is $E^{\circ'}$, and n represents the amount of electrons transferred in each molecule. Labeled in the cyclic voltammogram (**Figure 2.1**) are the parameters necessary to quantify the electrochemical process in order to describe the behavior observed. These include, E_{pc} and E_{pa} , for the respective cathodic and anodic peak potentials, as well as i_{pc} and i_{pa} , which represent the cathodic and anodic peak currents, correspondingly. To define a redox couple as an electrochemically reversible process whereby efficient concentrations of reduced and

oxidized species are kept at equilibrium at the surface of the electrode: (i) the potential peak separation, $\Delta E_p = |E_{pa} - E_{pc}|$, is approximately $59/n$ mV at 25 °C for all scan rates with n number of electrons, (ii) the peak potentials remain unchanged when varying the scan rate, (iii) the cathodic and anodic peak currents are proportional to $\nu^{1/2}$, where ν is the scan rate,¹⁹ and (iv) the ratio of peak currents, $|i_{pa}/i_{pc}|$, is equal to 1.0 at all scan rates.²⁴ Voltages are tabulated as half-wave potentials, $E_{1/2} = \frac{1}{2}(E_{pa} + E_{pc})$, versus the Fc^+/Fc internal standard reference couple.¹

2.3. Photoluminescence Spectroscopy

The phenomenon of molecular photoluminescence is observed as either fluorescence or phosphorescence subsequent to the excitation of a molecule that has absorbed photons of electromagnetic radiation. Emission of a photon accompanies the deactivation process from an electronically excited state to the ground state, whereby a molecule exhibits luminescence. Molecular absorption of radiation happens on the order of 10^{-15} s, whereas the rate of emission, or lifetime, averages from less than 10^{-5} s for fluorescence and 10^{-4} to 10 s for phosphorescence.²² Differences between these forms of emission derive from distinct excited state spectroscopic multiplicities. As depicted in **Figure 2.2**, an electron can be promoted from the ground singlet state to an excited singlet state or triplet state.

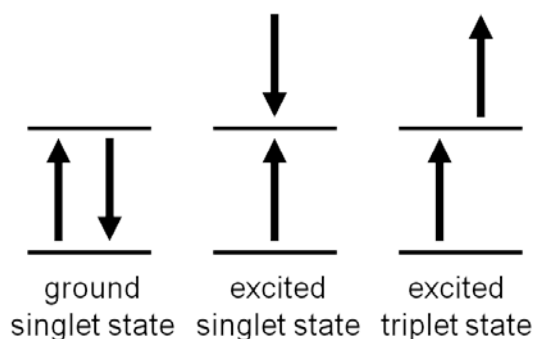


Figure 2.2. Electron spin and singlet/triplet excited states (adapted from reference 22)

For the case of the excited singlet state, the electron spins remain opposite and thus paired. The triplet state, in contrast, has unpaired electrons with equivalent spins. Fluorescence is shorter-lived because no change in multiplicity occurs and the singlet \rightarrow singlet transition is not forbidden. On the other hand, in the photo-active systems investigated in **Chapter 5**, phosphorescence becomes relevant and arises from the change in multiplicity. As illustrated in **Figure 2.3**, a molecule first absorbs photons of radiation and excitation from the ground singlet state, S_0 , to the excited singlet state, S_1 , proceeds.

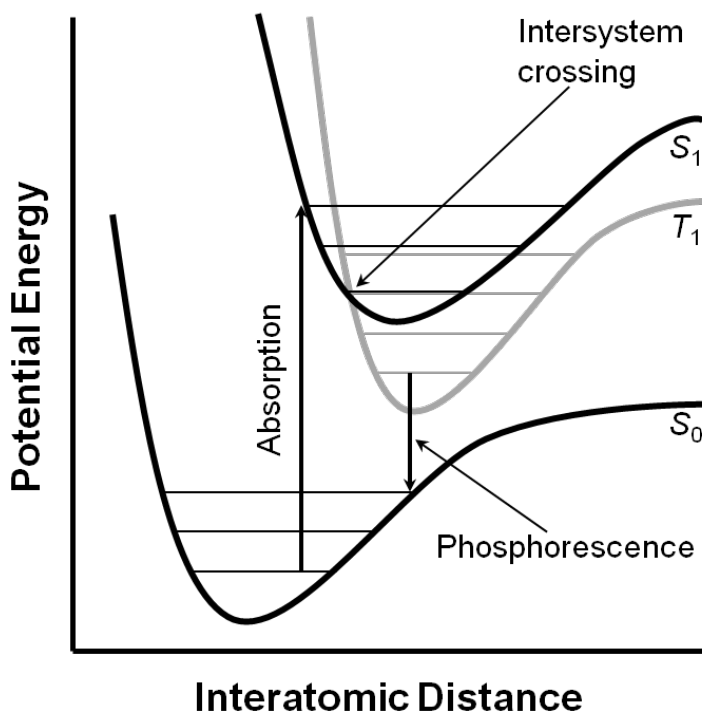


Figure 2.3. Potential-energy curve for phosphorescence (adapted from reference 25)

This S_1 excited state species can undergo intersystem crossing, or reversal of the spin of an excited electron, to the excited triplet state T_1 , where the S_1 and T_1 potential energy curves intersect. Such forbidden transitions in multiplicity become plausible because of spin-orbit coupling in the presence of heavy atoms, making the rate of these transitions

slower. The excited triplet species must once again change multiplicity in the return triplet \rightarrow singlet transition. It is in this process that a photon is emitted and phosphorescence occurs.^{23,25}

2.4. References

- 1 Gagne, R. R.; Koval, C. A.; Lisensky, G. C. "Ferrocene as an Internal Standard for Electrochemical Measurements." *Inorg. Chem.* **1980**, *19*, 2854.
- 2 Frisch, M. J.; Trucks, G. W.; Schlegel, H. B.; Scuseria, G. E.; Robb, M. A.; Cheeseman, J. R.; Scalmani, G.; Barone, V.; Mennucci, B.; Petersson, G. A.; Nakatsuji, H.; Caricato, M.; Li, X.; Hratchian, H. P.; Izmaylov, A. F.; Bloino, J.; Zheng, G.; Sonnenberg, J. L.; Hada, M.; Ehara, M.; Toyota, K.; Fukuda, R.; Hasegawa, J.; Ishida, M.; Nakajima, T.; Honda, Y.; Kitao, O.; Nakai, H.; Vreven, T.; Montgomery, J. A.; Peralta, J. E.; Ogliaro, F.; Bearpark, M.; Heyd, J.; Brothers, J. E.; Kudin, K. N.; Staroverov, V. N.; Kobayashi, R.; Normand, J.; Raghavachari, K.; Rendell, A.; Burant, J. C.; Iyengar, S. S.; Tomasi, J.; Cossi, M.; Rega, N.; Millam, J. M.; Klene, M.; Knox, J. E.; Cross, J. B.; Bakken, V.; Adamo, C.; Jaramillo, J.; Gomperts, R.; Stratmann, R. E.; Yazyev, O.; Austin, A. J.; Cammi, R.; Pomelli, C.; Ochterski, J. W.; Martin, R. L.; Morokuma, K.; Zakrzewski, V. G.; Voth, G. A.; Salvador, P.; Dannenberg, J. J.; Dapprich, S.; Parandekar, P. V.; Mayhall, N. J.; Daniels, A. D.; Farkas, O.; Foresman, J. B.; Ortiz, J. V.; Cioslowski, J.; Fox, D. J. *Gaussian G09*; Gaussian, Inc.: Wallingford, CT, **2009**.
- 3 Becke, A. D. "Density-Functional Thermochemistry. III. The Role of Exact Exchange." *J. Chem. Phys.* **1993**, *98*, 5648.
- 4 Lee, C.; Yang, W.; Parr, R. G. "Development of the Colle-Salvetti Correlation-Energy Formula into a Functional of the Electron Density." *Phys. Rev. B* **1988**, *37*, 785.

- 5 Miehlich, B.; Savin, A.; Stoll, H.; Preuss, H. "Results Obtained with the Correlation Energy Density Functionals of Becke and Lee, Yang and Parr." *Chem. Phys. Lett.* **1989**, *157*, 200.
- 6 Dunning, T. H.; Hay, P. J. *Modern Theoretical Chemistry*; Plenum: New York, **1976**; Vol. 3, pp 1–28.
- 7 Cossi, M.; Rega, N.; Scalmani, G.; Barone, V. "Energies, Structures, and Electronic Properties of Molecules in Solution with the C-PCM Solvation Model." *J. Comput. Chem.* **2003**, *24*, 669.
- 8 Miertus, S.; Scrocco, E.; Tomasi, J. "Electrostatic Interaction of a Solute with a Continuum. A Direct Utilization of ab Initio Molecular Potentials for the Prevision of Solvent Effects." *Chem. Phys.* **1981**, *55*, 117.
- 9 Miertus, S.; Tomasi, J. "Approximate Evaluations of the Electrostatic Free Energy and Internal Energy Changes in Solution Processes." *Chem. Phys.* **1982**, *65*, 239.
- 10 Whangbo, M.-H.; Schlegel, H. B.; Wolfe, S. "Molecular Orbitals from Group Orbitals. 3. Quantitative Perturbational Molecular Orbital Analysis of ab Initio SCF-MO Wave Functions." *J. Am. Chem. Soc.* **1977**, *99*, 1296.
- 11 Shakya, R.; Keyes, P. H.; Heeg, M. J.; Moussawel, A.; Heiney, P. A.; Verani, C. N. "Thermotropic Mesomorphism of Soft Materials Bearing Carboxylate-Supported μ_4 -Oxo Tetracupric Clusters." *Inorg. Chem.* **2006**, *45*, 7587.
- 12 Jayathilake, H. D.; Driscoll, J.; Bordenyuk, A.; Wu, L.; da Rocha, S. R. P.; Verani, C. N.; Benderskii, A. V. "Molecular Order in Langmuir–Blodgett Monolayers of Metal-Ligand Surfactants Probed by Sum Frequency Generation." *Langmuir* **2009**, *25*, 6880.

- 13 Egdal, R. K.; Hazell, A.; Larsen, F. B.; McKenzie, C. J.; Scarrow, R. C. A “Dihydroxo-Bridged Fe(II)-Fe(III) Complex: A New Member of the Diiron Diamond Core Family.” *J. Am. Chem. Soc.* **2003**, *125*, 32.
- 14 Ankudinov, A. L.; Rehr, J. J. “Relativistic Calculations of Spin-Dependent X-ray Absorption Spectra.” *Phys. Rev.* **1997**, *B56*, R1712 .
- 15 Scarrow, R. C.; Strickler, B. S.; Ellison, J. J.; Shoner, S. C.; Kovacs, J. A.; Cummings, J. G.; Nelson, M. J. “X-ray Spectroscopy of Nitric Oxide Binding to Iron in Inactive Nitrile Hydratase and a Synthetic Model Compound.” *J. Am. Chem. Soc.* **1998**, *120*, 9237.
- 16 Bunker, G.; Hasnain, S.; Sayers, D., Eds. *X-ray Absorption Fine Structure*; Hasnain, S. S., Ed.; Ellis Horwood: New York, **1991**.
- 17 Rice, C. A.; Spence, J. T. “New Molybdenum (IV) Complexes. Syntheses and Properties.” *Inorg. Chem.* **1980**, *19*, 2845.
- 18 Powers, M. J.; Meyer, T. J. “Medium and Distance Effects in Optical and Thermal Electron Transfer.” *J. Am. Chem. Soc.* **1980**, *102*, 1289.
- 19 Mabbott, G. A. “An Introduction to Cyclic Voltammetry.” *J. Chem. Educ.* **1983**, *60*, 697.
- 20 Bobbitt, J. M.; Wills, J. P. “Electrochemistry of Natural Products. 7. Oxidative Decarboxylation of Some Tetrahydro- β -Carbolinecarboxylic Acids.” *J. Org. Chem.* **1980**, *45*, 1978.
- 21 Nelsen, S. F.; Kessel, C. R.; Brien, D. J.; Weinhold, F. “J. 9-(9-Borabicyclo[3.3.1]nonyl)-9-Azabicyclo[3.3.1]Nonane Radical Cation: A Failure of Bredt's Rule Kinetic Stabilization.” *Org Chem.* **1980**, *45*, 2116.

- 22 Skoog, D. A.; Holler, F. J.; Nieman, T. A. *Principles of Instrumental Analysis*, 5th edition. Philadelphia: Saunders College Pub.; Orlando, FL: Harcourt Brace College Publishers, **1998**.
- 23 Willard, H. H.; Merritt, Jr., L. L.; Dean, J. A.; Settle, Jr., F. A. *Instrumental Methods of Analysis*, 7th edition. Wadsworth Publishing Company: Belmont California, **1988**.
- 24 Wang, J. *Analytical Electrochemistry*, Chapter 2, John Wiley and Sons, Inc: New York, **2000**.
- 25 Laidler, K. J; Meiser, J. H.; Sanctuary, B. C. *Physical Chemistry*, 4th edition. Houghton Mifflin Company: Boston, **2003**.

Chapter 3

ON THE EFFECT OF COORDINATION AND PROTONATION PREFERENCES IN THE AMPHIPHILIC BEHAVIOR OF METALLOSURFACTANTS WITH ASYMMETRIC HEADGROUPS

[03]

Eur. J. Inorg. Chem. 2009, 321–452

D 375

3/2009
3rd January Issue

Cover Picture
Cláudio N. Verani et al.
Metallosurfactants with Asymmetric Headgroups

Microreview
Pedro Tartaj
Supramagnetic Composites: Magnetism with No Memory

WILEY-VCH

www.eurjic.org

A Journal of
ChemPubSoc
Europe

0950-0804 (Print) • ISSN 1522-2675 (Online) • No. 3/2009

CHAPTER 3
ON THE EFFECT OF COORDINATION AND PROTONATION PREFERENCES
IN THE AMPHIPHILIC BEHAVIOR OF METALLOSURFACTANTS WITH
ASYMMETRIC HEADGROUPS

Frank D. Lesh, Sarmad Sahiel Hindo, Mary Jane Heeg, Marco M. Allard,

Prateek Jain, Bo Peng, Lew Hryhorczuk, and Cláudio N. Verani*

Reprinted with permission from *Eur. J. Inorg. Chem.* **2009**, 3, 345–356. Copyright 2009

WILEY-VCH Verlag GmbH & Co. KGaA, Weinheim.

Contributions to this work on my part included the synthetic, spectroscopic, and electrochemical characterizations along with the original draft of the manuscript.

3.1. Introduction

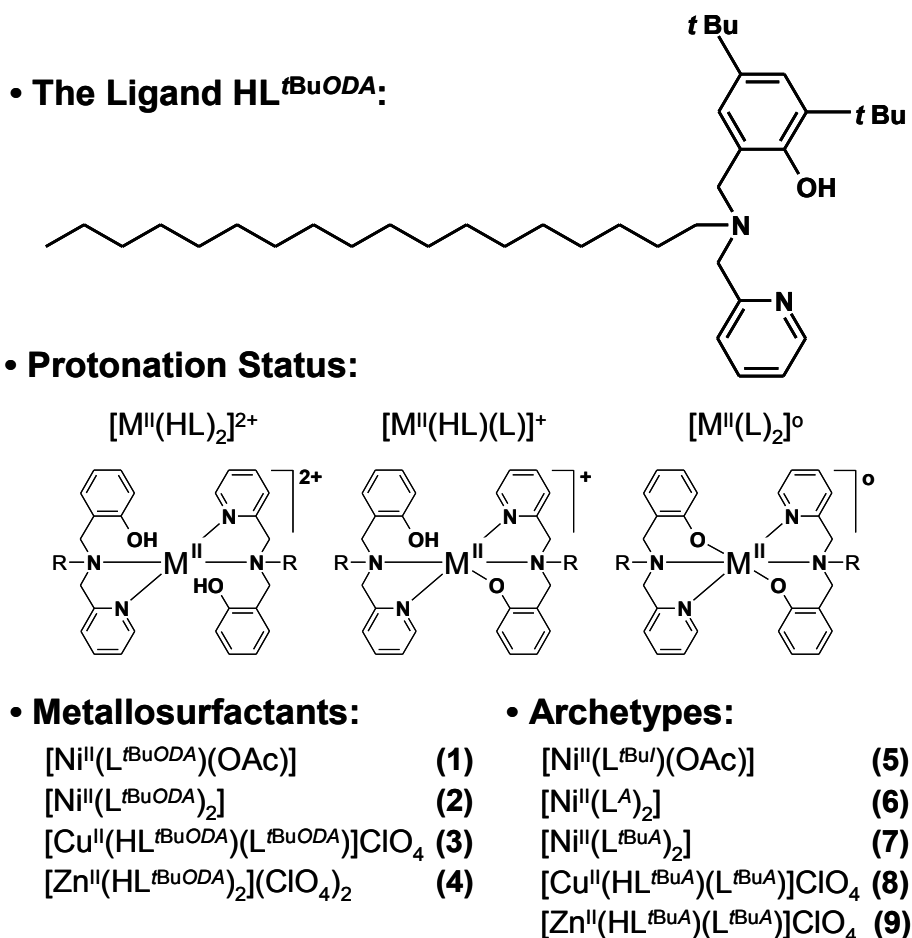
Molecular architectures displaying cooperativity among transition metals and amphiphilic organic scaffolds combine unique geometric, electronic, redox, and magnetic behavior¹⁻⁴ with distinctive ordering morphologies. The approach has been used with impressive results in the design of soft materials with thixotropic,⁵ mesogenic,⁶ ionophoric,⁷ luminescent,⁸ and micellar⁹ properties. This fact points out to the potential role of discrete metallosurfactant materials in the emerging field of responsive thin films.¹⁰⁻¹² However, metallosurfactants (*i.e.*, surfactants containing metal ions) are usually assembled at the air/water interface without isolation of the precursors. As a consequence, lack of precise control in (i) the surfactant-to-metal ratio, (ii) the coordination modes and the final structure of the material, and (iii) protonation preferences limit reproducibility leading to adventitious defects. Therefore having well defined, isolated, and characterized precursors is of paramount importance. Nevertheless,

the small body of work available on the isolation and air/water interface behavior of metallosurfactant precursors still poses a major drawback to the approach.^{13,14}

At the forefront of this area, our group has focused on synthetic, modeling, and surface protocols involving the incorporation of magnetic μ -oxo-Cu₄ clusters in Langmuir–Blodgett films,^{15,16} the observation of distinctive collapse mechanisms on cobalt(II) films,¹⁷ and the design of redox-active copper-containing amphiphiles.^{18,19} In a series of studies with iron(III),²⁰ cobalt(II/III),²¹ and gallium(III)²² we have demonstrated that structural and electronic effects can determine the preferential geometry of redox-active asymmetric NN'O ligands in [ML₂] metallosurfactants. Structural rigidity of the ligand takes precedence to the electronic configuration of the metal ion and favors *meridional* coordination when asymmetric amines and imines are compared. On the other hand, electronic configuration is a determining factor when flexible amines are involved; a *facial* coordination mode is preferred, and the metal dictates the preferential *cis* or *trans* orientation of equivalent phenolates and other donor sets in vicinal ligands. Consequently, 3d⁵ high-spin configuration leads to *cis*-arrangement while 3d⁶ low-spin and 3d⁷ high-spin ions support *trans*-orientation. Gallium(III), with 3d¹⁰ configuration, does not seem to exhibit a clear preference. These observations are serving as guidelines to the design of metal-containing amphiphiles for redox-responsive Langmuir–Blodgett films.

In this chapter, we describe the synthesis and amphiphilic behavior of nickel(II), copper(II), and zinc(II) complexes with an asymmetric NN'O ligand. Due to the 3d⁸⁻¹⁰ electronic configurations found in these bivalent metal ions, stoichiometric preferences, coordination modes, and ligand protonation status can lead to distinct [M^{II}(HL)X]²⁺,

$[M^{II}(L)X]^+$, $[M^{II}(L)_2]^0$, $[M^{II}(HL)(L)]^+$, and $[M^{II}(HL)_2]^{2+}$ products (**Scheme 3.1**). Because of the waxy texture of most of the resulting metallosurfactants, archetypical modeling (*i.e.*, the investigation of a series of discrete complexes that retain key structural and electronic attributes) was used to assess the nature of these products. A careful comparison between the stoichiometric and protonation status and the amphiphilic behavior is offered.



Scheme 3.1. The ligand HL^{tBuODA}, possible protonation status for metallosurfactants and archetypes studied.

3.2. The Ligands

Condensation of 1-octadecylamine with 2-pyridinecarboxaldehyde in methanol with subsequent reduction in the presence of sodium borohydride gave the amine

precursor that was treated with 2,4-di-*tert*-butyl-6-(chloromethyl)phenol to generate the ligand $\text{HL}^{\text{tBuODA}}$. Similarly, the archetypical ligands were synthesized with 80–85 % yields following literature procedures^{17,20,21} and characterized by means of ESI mass spectrometry, ¹H–NMR, and infrared spectroscopy.

3.3. The Metallosurfactants

Treatment of the ligand $\text{HL}^{\text{tBuODA}}$ with several metal salts yielded products with textures varying from waxy to solid. Compound $[\text{Ni}^{\text{II}}(\text{L}^{\text{tBuODA}})(\text{OAc})]$ (**1**) was isolated upon complexation in methanol of $\text{HL}^{\text{tBuODA}}$ with nickel(II) acetate tetrahydrate in a 1:1 ligand-to-metal ratio. Similarly, treatment of the ligand with hexahydrated perchlorate salts of nickel(II), copper(II), or zinc(II) in a 2:1 ratio yielded $[\text{Ni}^{\text{II}}(\text{L}^{\text{tBuODA}})_2]$ (**2**), $[\text{Cu}^{\text{II}}(\text{HL}^{\text{tBuODA}})(\text{L}^{\text{tBuODA}})]\text{ClO}_4 \cdot \text{CH}_3\text{OH}$ (**3**), and $[\text{Zn}^{\text{II}}(\text{HL}^{\text{tBuODA}})_2](\text{ClO}_4)_2$ (**4**), respectively. Triethylamine was used as a base to assist phenol deprotonation in all cases. The waxy constitution of compounds **1** and **2** precluded elemental analysis as a tool for characterization. The ESI mass analysis of **1** indicates the presence of peak clusters at $m/z = 635.4$ and $m/z = 695.4$ corresponding respectively to $[\text{Ni}(\text{L}^{\text{tBuODA}})]^+$ and $[\text{Ni}(\text{L}^{\text{tBuODA}})(\text{OAc}) + \text{H}]^+$. The former peak is favored at higher cone voltages, whereas the latter is more abundant at lower cone voltages. Similarly, **2** shows a peak cluster at $m/z = 1214.0$ providing evidence for species such as $[\text{Ni}(\text{L}^{\text{tBuODA}})_2 + \text{H}]^+$ or $[\text{Ni}(\text{HL}^{\text{tBuODA}})(\text{L}^{\text{tBuODA}})]^+$. The use of triethylamine in the synthetic procedure, as well as the absence of infrared peaks at 1090 cm^{-1} for perchlorate counterions, supports that the ligands are fully deprotonated and that the singly charged peak observed is formed in situ. The ESI mass analysis of **3** suggests the formation of the cationic species $[\text{Cu}^{\text{II}}(\text{HL}^{\text{tBuODA}})(\text{L}^{\text{tBuODA}})]^+$ with a peak cluster at $m/z = 1219.0$. Likewise, **4** shows a peak

cluster at $m/z = 1220.0$ implying the formation of the species $[\text{Zn}^{\text{II}}(\text{HL}^{\text{tBuODA}})(\text{L}^{\text{tBuODA}})]^+$. Additional interpretation of the fragmentation patterns suggests the existence of the species $[\text{Zn}^{\text{II}}(\text{HL}^{\text{tBuODA}})_2]^{2+}$, as confirmed by a prominent peak cluster at $m/z = 641.5$ for the species $[\text{Zn}^{\text{II}}(\text{HL}^{\text{tBuODA}})_2 + \text{CH}_3\text{OH}]^{2+}$. This dicationic species is particularly visible at low cone voltages. The peak clusters of interest were simulated and agree well in their patterns, positions, and isotopic distributions, and substantiate the behavior of the metal ions. These spectrometric profiles are shown in **Figure 3.1**.

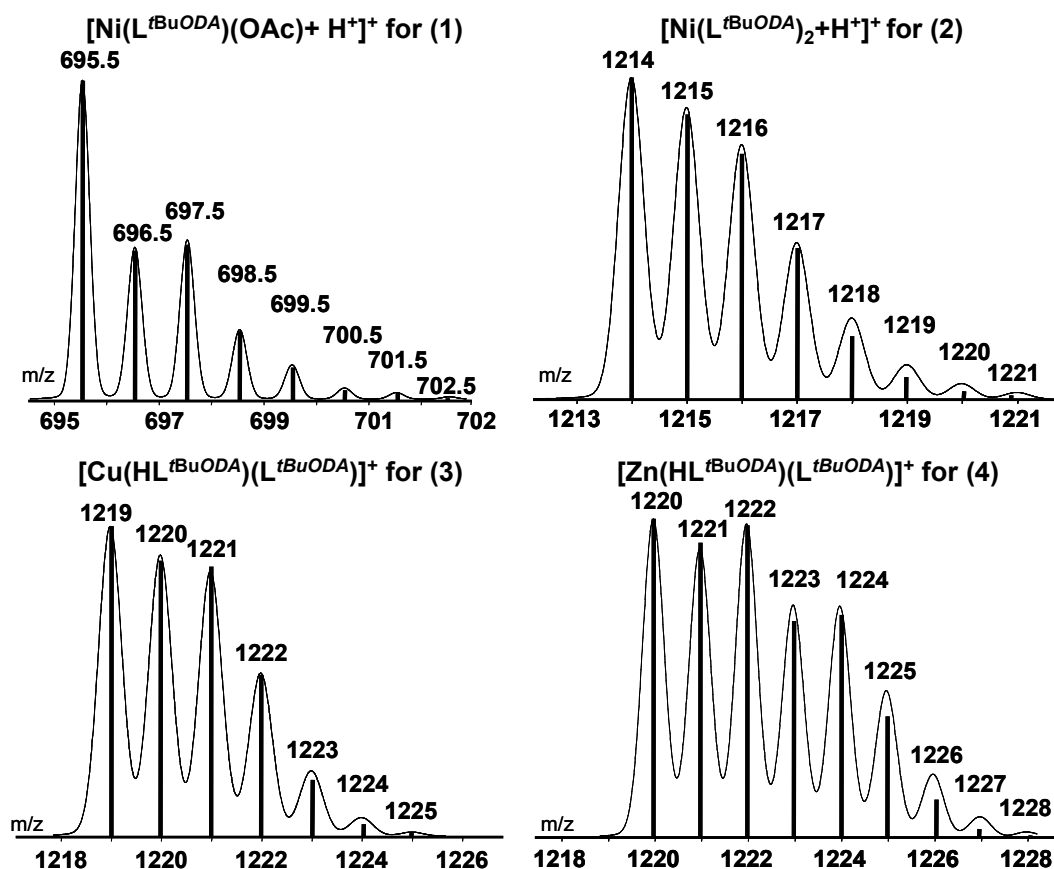


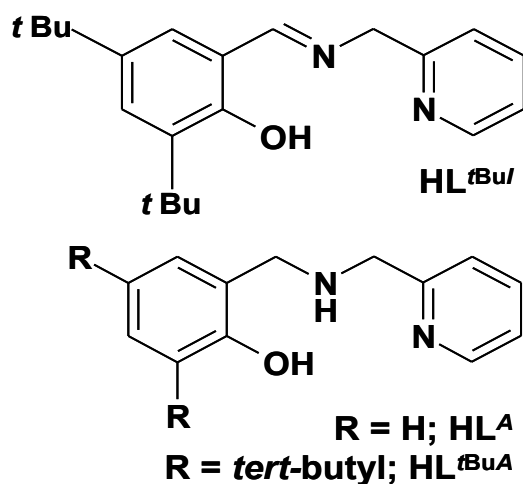
Figure 3.1. ESI(pos) peak clusters with experimental (bars) and simulated (continuum) isotopic distributions for 1–4. The relative abundance axis of each complex is omitted for clarity.

Infrared analysis further suggests metal coordination by the sharp doublet of the C=N bonds in pyridine rings between 1590–1570 cm^{-1} . These peaks are shown broadened and shifted in the spectra of the compounds, along with the presence of characteristic C–H stretching contribution of the alkyl chain and tertiary butyl groups from the ligand. Additionally, **1** shows an antisymmetric stretch at 1574 cm^{-1} for its coordinated acetate. While the neutral compound **2** lacks a perchlorate peak, **3** and **4** display strong Cl–O stretchings at ca. 1105 cm^{-1} , indicative of the presence of perchlorate counterions. Because precipitates were isolated for **3** and **4**, elemental analyses were carried out and are in good agreement with these formulations.

3.4. The Archetypes

Archetypical modeling was used in order to correlate the amphiphilic behavior observed for **1–4** with detailed structural information. A series of discrete complexes was studied in which the long alkyl chain is replaced by a hydrogen atom, whereas other key features like the chelating headgroup are left unchanged. These species were synthesized using perchlorate salts analogously to the metallosurfactants above, and are described as $[\text{Ni}^{\text{II}}(\text{L}^{\text{tBuI}})(\text{OAc})] \cdot \text{CH}_3\text{OH}$ (**5**), $[\text{Ni}^{\text{II}}(\text{L}^{\text{A}})_2] \cdot \text{CH}_3\text{OH} \cdot \text{H}_2\text{O}$ (**6**), $[\text{Ni}^{\text{II}}(\text{L}^{\text{tBuA}})_2] \cdot 2\text{CH}_3\text{OH}$ (**7**), $[\text{Cu}^{\text{II}}(\text{HL}^{\text{tBuA}})(\text{L}^{\text{tBuA}})]\text{ClO}_4$ (**8**), and $[\text{Zn}^{\text{II}}(\text{HL}^{\text{tBuA}})(\text{L}^{\text{tBuA}})]\text{ClO}_4$ (**9**). The archetypical ligands HL^{tBuI} , HL^{A} , and HL^{tBuA} are depicted in **Scheme 3.2**. Species **7** has been recently studied by Thomas *et al.*,²³ along with a series of related $[\text{Ni}^{\text{II}}(\text{NN}'\text{O})_2]$ complexes, but no X-ray structure was available. Elemental analyses of the compounds **5–9** are in excellent agreement with theoretical percentages, and the ESI(pos) mass spectra exhibit distinct $m/z = [\text{M}^{\text{II}}(\text{L})_2]^+$ and $[\text{M}^{\text{II}}(\text{HL})(\text{L})]^+$ peaks in methanol. Peak cluster simulation of these archetypes parallel those obtained for the metallosurfactants **1–4**, reinforcing the notion

that the expected ligand-to-metal ratios were achieved. The neutrality of the nickel(II) complexes, as well as the presence of protonated ligands, is once again confirmed by the respective absence or presence of a peak associated with the perchlorate counterion at around $1100\text{--}1090\text{ cm}^{-1}$ in their IR spectra.



Scheme 3.2. The ligands HL^{tBu} , HL^{A} , and HL^{tBuA} used in the archetypes.

3.5. Molecular Structures and Coordination Modes

Discrete mononuclear crystals of archetypes **5–9** were structurally resolved by X-ray diffraction. The ORTEP diagrams are displayed in **Figures 3.2–3.6**, and selected bond lengths and angles summarized in **Table 3.1**.

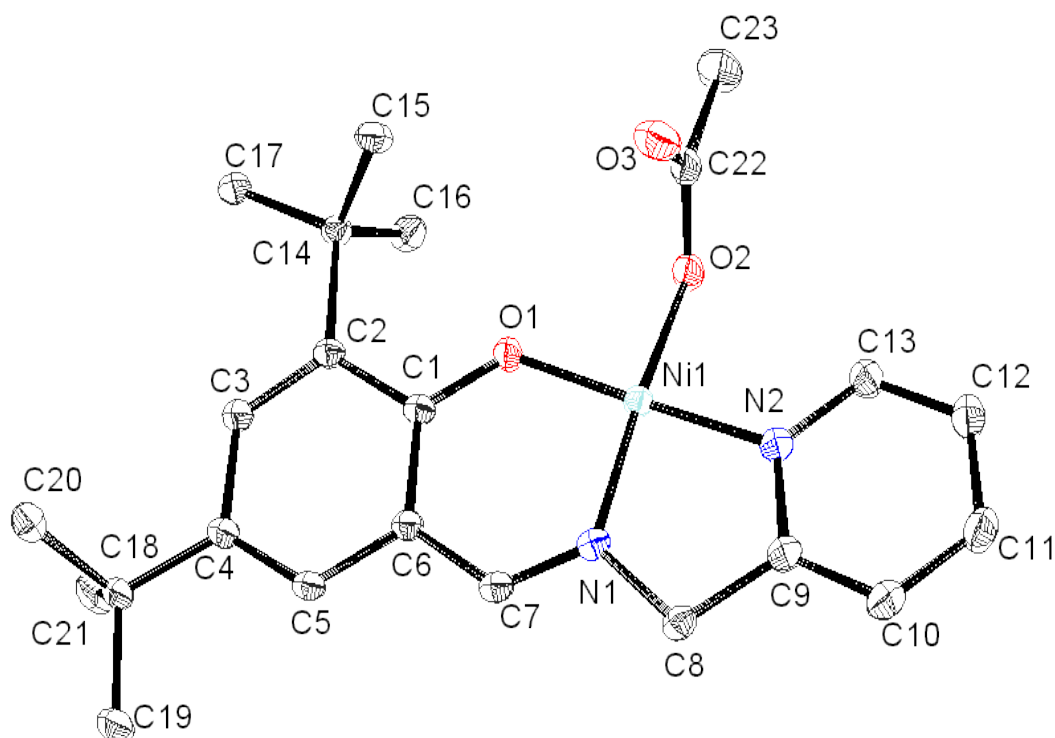


Figure 3.2. ORTEP diagram at 50% probability for [Ni^{II}(L^tBu)(OAc)]·CH₃OH (**5**). Solvent and hydrogen atoms are excluded for clarity.

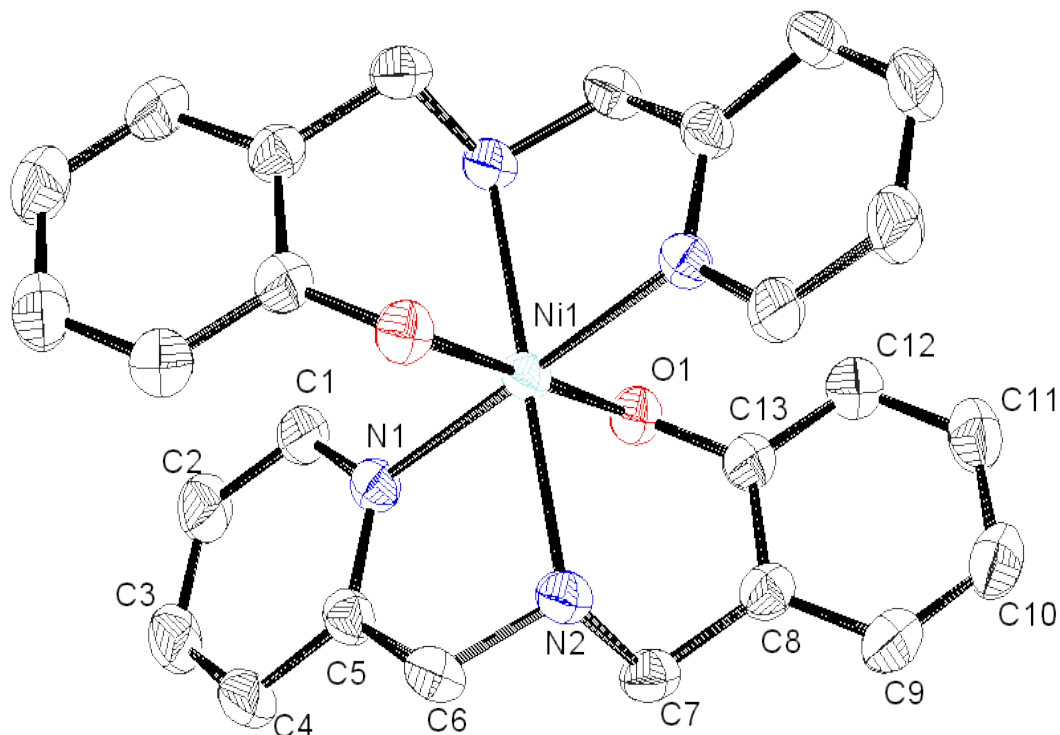


Figure 3.3. ORTEP diagram at 50% probability for $[\text{Ni}^{\text{II}}(\text{L}^4)_2] \cdot \text{CH}_3\text{OH} \cdot \text{H}_2\text{O}$ (**6**). Solvents and hydrogen atoms are excluded for clarity.

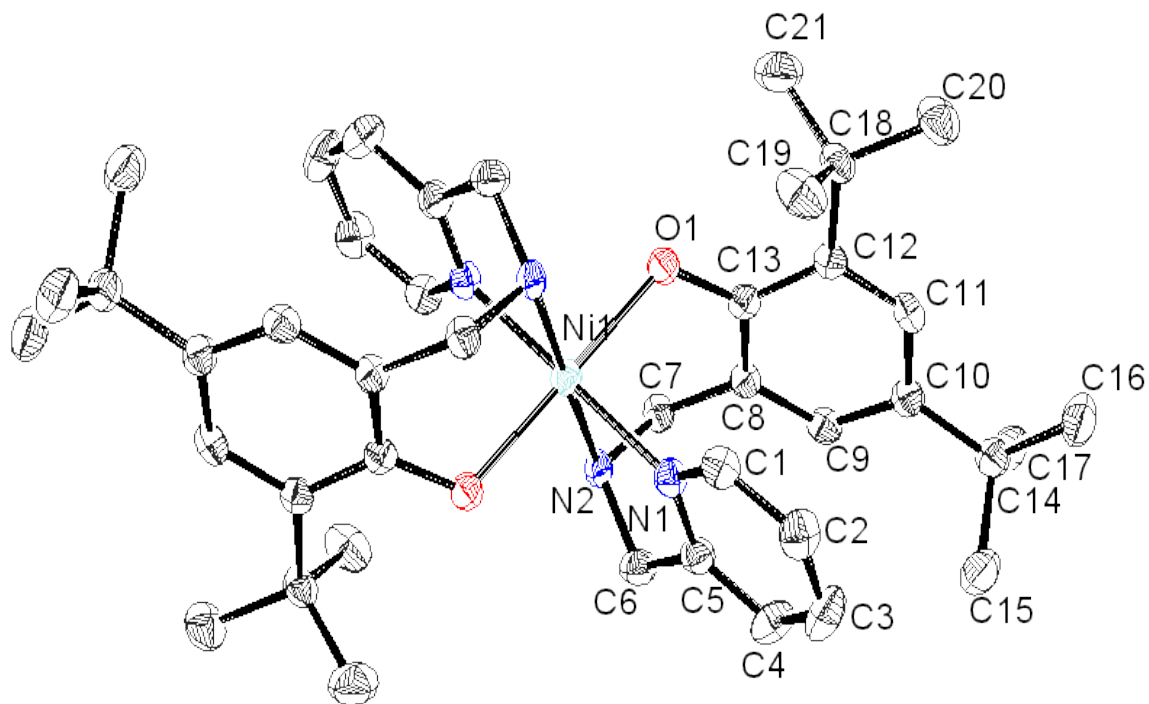


Figure 3.4. ORTEP diagram at 50% probability for $[\text{Ni}^{\text{II}}(\text{L}^{\text{tBuA}})_2] \cdot 2\text{CH}_3\text{OH}$ (**7**). Solvents and hydrogen atoms are excluded for clarity.

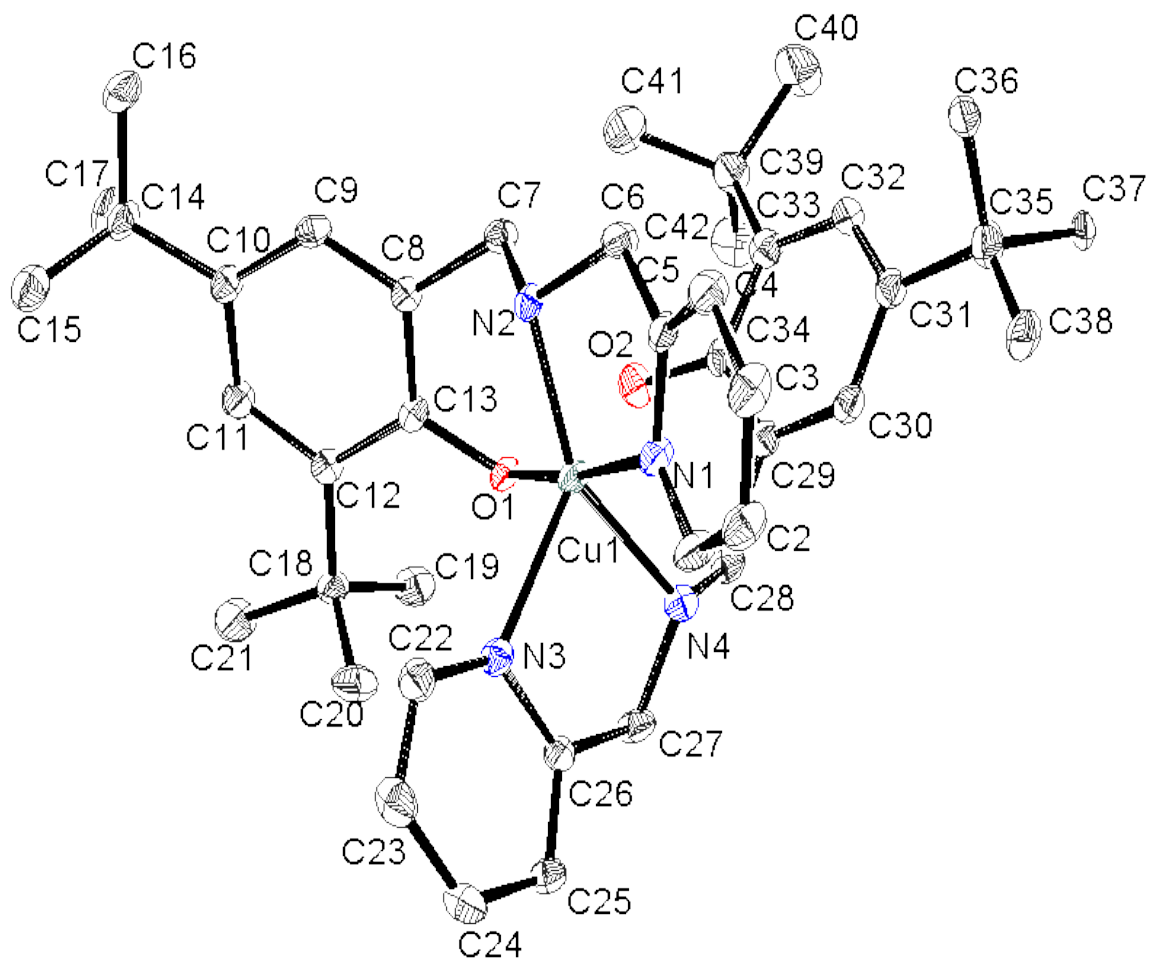


Figure 3.5. ORTEP diagram at 50% probability for $[\text{Cu}^{\text{II}}(\text{HL}^{\text{tBuA}})(\text{L}^{\text{tBuA}})]\text{ClO}_4$ (**8**). Counterions and hydrogen atoms are excluded for clarity.

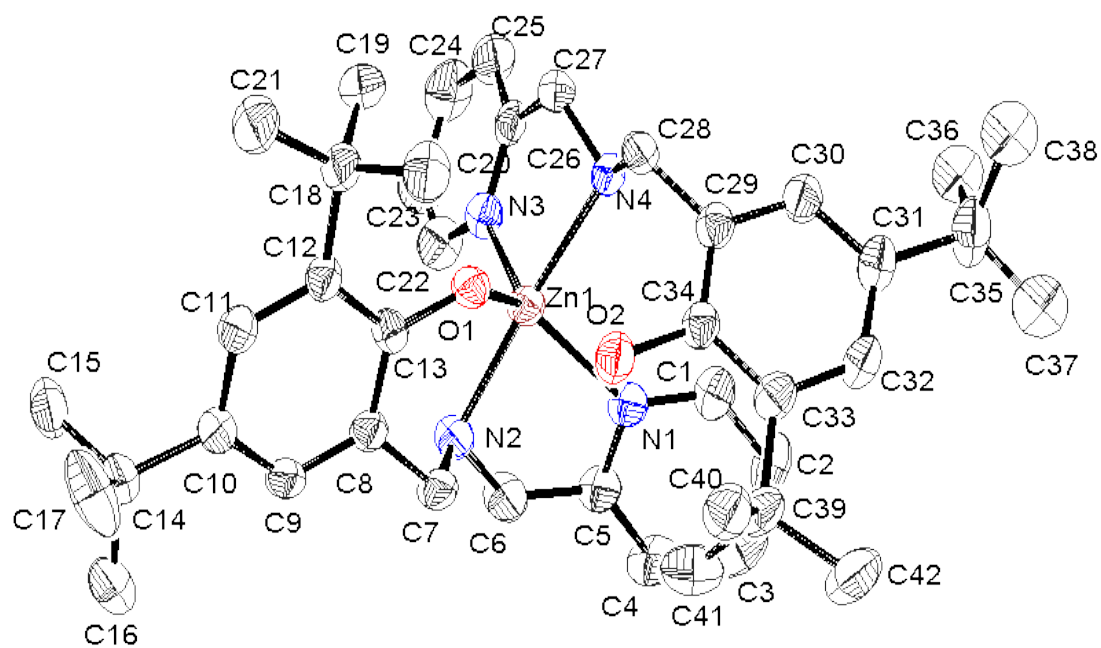


Figure 3.6. ORTEP diagram at 50% probability for [Zn^{II}(HL^{tBuA})(L^{tBuA})]ClO₄ (9). Counterions and hydrogen atoms are excluded for clarity.

Table 3.1. Selected bond lengths (Å) and angles (°) for **5**, **6**, **7**, **8'**, and **9**.

5	6	7	8'	9
Ni1-O1 1.8215(9) Ni1-N1 1.8416(10) Ni1-N2 1.8863(10) Ni1-O2 1.8840(8)	Ni1-O1 2.0916(17) Ni1-N1 2.0829(18) Ni1-N2 2.1119(19)	Ni1-O1 2.0869(13) Ni1-N1 2.1039(16) Ni1-N2 2.1117(17)	Cu1-O1 1.9501(15) Cu1-N2 1.9938(18) Cu1-N4 2.0419(19) Cu1-N1 2.0609(19) Cu1-N3 2.2708(19)	Zn1-O1 1.960(3) Zn1-N3 2.074(4) Zn1-N2 2.141(4) Zn1-N1 2.147(4) Zn1-N4 2.175(4)
Bite Angles	Bite Angles	Bite Angles	Bite Angles	Bite Angles
O1-Ni1-N1 94.87(4) N1-Ni1-N2 85.72(4)	O1-Ni1-N2 89.60(7) N1-Ni1-N2 79.86(7)	O1-Ni1-N2 89.66(6) N1-Ni1-N2 80.12(6)	O1-Cu1-N2 93.01(7) N2-Cu1-N1 81.02(7) N4-Cu1-N3 79.21(7)	O1-Zn1-N2 94.10(13) N2-Zn1-N1 78.96(15) N3-Zn1-N4 80.44(14)
Average Distances	Average Distances	Average Distances	Average Distances	Average Distances
Py C – C 1.3856(18) Py C – N 1.3534(15) Ph C – C 1.4081(16)	Py C – C 1.3835(3) Py C – N 1.3395(3) Py C – C 1.3933(4)	Py C – C 1.371(3) Py C – N 1.347(2) Ph C – C 1.3975(3)	Py C – C 1.381(3) Py C – N 1.345(3) Ph C – C 1.398(3)	Py C – C 1.374(8) Py C – N 1.346(6) Ph C – C 1.396(7)

3.5.1. The Nickel Archetypes 5, 6, and 7. The coordination environment for the nickel(II) metal center in complex **5** approximates a square-planar geometry with the deprotonated ligand $(L^{tBu})^-$ meridionally coordinated through an NN'O donor set of N_{imine} and $N_{pyridine}$, and $O_{phenolate}$ atoms, along with a deprotonated terminally coordinated acetate group occupying the fourth position. Both *trans* angles are smaller than 180° , thus confirming a distorted square-planar geometry. The bond angles and lengths at the metal center agree with literature values of mono-substituted imine complexes with similarly organized donor frameworks. For example, the Ni– $O_{phenolate}$, Ni– $O_{acetate}$, and Ni– N_{imine} bonds herein are 1.82, 1.88 and 1.84 Å, respectively, closely resembling the values found for the complex $[Ni(L)(OAc)]$, where L is the deprotonated form of the 6-[(*E*)-({[(2*S*)-1-benzylpyrrolidin-2-yl]methyl}imino)methyl]-2-*tert*-butyl-4-methylphenol.²⁴ Finally, it is noteworthy that the ligand $(L^{tBu})^-$ in **5** is definitely an imine, as evidenced by the short bond length between C7–N1 (1.30 Å). Even though the ligand $(L^{tBuODA})^-$ in **1** is more flexible than that in **5** and could possibly adopt a facial conformation in a tetrahedral coordination sphere, the preferential coordination modes of a low-spin $3d^8$ ion like nickel(II) should favor a square-planar geometry. Therefore, **5** provides an acceptable model for the coordination environment for the surfactant **1**.

Complexes **6** and **7** are intended to act as archetypical models for species **2**, which displays two fully deprotonated ligands $(L^{tBuODA})^-$ and neutral character. In fact the results observed for both archetypes with ligands $(L^A)^-$ for **6** and $(L^{tBuA})^-$ for **7** give consistent information about the coordination modes of NN'O ligands around nickel(II). The coordination geometries resemble those observed for cobalt(III/II) complexes recently reported by this group.^{17,21} These structures are arranged pseudo-octahedrally in

an approximate D_{2h} local symmetry about the nickel(II) center, coordinated by two deprotonated, facially coordinated ligands. Hence, **6** and **7** are described in BMT²⁵ notation as $[\text{Ni } \langle \text{N}_{\text{am}1} \text{N}_{\text{am}2} \rangle \langle \text{N}_{\text{py}1} \text{N}_{\text{py}2} \rangle \langle \text{O}_{\text{phen}1} \text{O}_{\text{phen}2} \rangle]$. The Ni–N_{amine} bond lengths consistently measure 2.11 Å, while the Ni–O_{phenolate} bond lengths are 2.09 Å and the Ni–N_{pyridine} bond lengths are 2.08 and 2.10 Å. The six-coordinate geometry and absorption spectra (*vide infra*) indicate the presence of a high spin 3d⁸ ion.^{23,26} On the basis of the structures of these two archetypes, an accurate picture of the coordination modes present in **2** can be drawn.

3.5.2. The Copper Archetype 8'. By means of counterion exchange, single crystals of the complex $[\text{Cu}^{\text{II}}(\text{HL}^{\text{tBuA}})(\text{L}^{\text{tBuA}})]\text{B}(\text{Ph})_4$ (**8'**) were obtained from the perchlorate parent species **8** to gather comparative information about the coordination modes and geometrical parameters of the copper-containing surfactant **3**. It contains a discrete $[\text{Cu}^{\text{II}}(\text{HL}^{\text{tBuODA}})(\text{L}^{\text{tBuODA}})]^+$ cation in which a single ligand is deprotonated, whereas another one remains protonated. Therefore, the coordination sphere around the copper(II) center in **8'**, and consequently in **8** and **3** as well, approximates a distorted $\text{N}_2\text{N}_2'\text{O}$ square-pyramidal geometry ($\tau = 0.34$)²⁷ in which the protonated O_{phenol} assumes a remote position (*viz.* Cu1⋯O2 > 3.80Å). The angles between adjacent corner atoms of the basal plane (O1–Cu1–N2 93.0°, O1–Cu1–N4 91.2°, N1–Cu1–N4 92.4°, and N2–Cu1–N1 81.0°) are consistent with pseudo-square pyramidal inter-plane angles approximating 90°, where the atoms O1, N4, N1, and N2 are situated on the vertices of the plane, while the pyridine nitrogen, N3, is apically coordinated to the copper center (2.27 Å). The *trans* amine nitrogen to opposing amine nitrogen bond angle is 152.4° and the *trans* phenolate oxygen to pyridine nitrogen bond angle is 173.0°, leaving the bond

angles comprising the apical pyridine nitrogen (O1–Cu1–N3 98.3°, N2–Cu1–N3 126.9°, N4–Cu1–N3 79.2°, and N1–Cu1–N3 88.2°) to reveal the degree of structural distortion. The increased copper to apical pyridine nitrogen bond length (2.27 Å) grants further evidence concerning the structure: the phenol group is neither bonded nor contributing structurally to the rigidity of the system. The other pyridine is situated *cis* to this apical pyridine with a Cu–N distance of 2.06 Å. Also occupying *cis* positions are the O_{phenolate} atom (Cu1–O1 1.95 Å) and the N_{amine} atom (Cu1–N2 2.0 Å) of the deprotonated ligand. In addition, the N_{amine} of the protonated ligand is positioned *trans* (Cu1–N4 2.04 Å) to its opposing N_{amine} of the deprotonated ligand. These bond lengths are in good agreement with reported values.^{28,29}

3.5.3. The Zinc Archetype 9. Analogous to the copper(II) center in the archetypical systems **8** and **8'**, the zinc(II) metal center in complex **9** bears ligand coordination through an N₂N₂'O donor set consisting of two tertiary amine and pyridine nitrogen atoms, and a single deprotonated phenolate oxygen atom. Similarly, the second phenol oxygen atom is protonated and lies 3.42 Å from the metal center. Calculation of the relative amount of trigonality reveals that the structural coordination geometry is more characteristic of trigonal bipyramidal geometry with a τ value of 0.79. The pseudo-trigonal bipyramidal geometry of the complex demonstrates facial ligand coordination organized in an approximate C_{2v} local symmetry, where the phenolate oxygen atom (Zn1–O1 1.96 Å) and pyridine nitrogen atoms (Zn1–N1 2.15, Zn1–N3 2.07 Å) are positioned on the vertices of the equatorial plane, and the *trans* tertiary amine nitrogen atoms are apically coordinated to the zinc center (Zn1–N2 2.14, Zn1–N4 2.17 Å). The angles at the zinc ion center around the equatorial plane are consistent with pseudo-

trigonal bipyramidal inter-plane angles approximating the ideal 120° ($O1-Zn1-N1$ 128.41° , $N1-Zn1-N3$ 114.29° , $N3-Zn1-O1$ 117.24°), while the $N2-Zn1-N4$ axial bond angle is 175.98° , deviating slightly from 180° linearity. The range for the pyridine nitrogen to amine nitrogen axial-to-equatorial bond angles containing the zinc ion center, $N_{ax}-Zn-N_{eq}$, is $80-100^\circ$, and the amine nitrogen to phenolate oxygen axial-to-equatorial bond angle range at the zinc ion center, $N_{ax}-Zn-O_{eq}$, is $89-94^\circ$. For purpose of contrast, it is interesting to consider the distinguishing features that exist between zinc complexes with local pseudo-trigonal bipyramidal geometries. For instance the cation $[Zn(TMPA)(OBz)]^+$,³⁰ where TMPA is tris[(2-pyridyl)methyl]amine and OBz is a benzoate ligand, is functionally comparable to **9**. The TMPA-based complex exhibits a slightly elongated Zn^{II} to axial N_{amine} bond length (2.26 \AA) along with shorter $Zn-N_{pyridine}$ distances, when compared to **9**. The axial $Zn-O_{benzoate}$ bond (1.95 \AA), on the other hand, is nearly equivalent to the equatorial $Zn-O_{phenolate}$ bond (1.96 \AA) in **9**. Equally relevant is the precise crystallographic work described by Neves *et al.*³¹⁻³³ on zinc-phenolate ligands. It has been postulated that both the nature of the phenol ring substituent and the geometry adopted around the metal play a crucial role in the length of the $Zn-O_{phenolate}$ bond. Unsubstituted ligands yield the longest bonds (2.15 \AA), whereas bromo- and *tert*-butyl-substituted phenolates yield comparable bonds reaching 1.90 to 1.96 \AA , respectively. This is in good agreement with the value observed for **9**. It is noteworthy that while most ligands yield $[ZnL_2]$ species, *tert*-butyl-substituted ligands are prone to form partially protonated $[Zn(HL)(L)]^+$ species. This has been observed even when zinc acetate, which fosters phenol deprotonation, is used. Unfortunately, **9** does not seem to be a valid archetypical model for **4**. The archetype possesses a single protonated ligand,

whereas elemental analysis and mass spectrometry support the presence of two protonated ligands in the surfactant. This is also consistent with an unusual collapse mechanism pattern observed in the Langmuir films of 4.

3.6. Electronic Spectroscopy

The electronic spectra of the ligands $\text{HL}^{\text{tBuODA}}$ and HL^{tBuA} , surfactant complexes 1–4, and archetypes 5–9 were measured either in dichloromethane or in 1:1 solutions of dichloromethane/methanol. The results are summarized in **Table 3.2** and selected spectra for the copper species 3 and 8 are shown in **Figure 3.7**. The ligands $\text{HL}^{\text{tBuODA}}$ and HL^{tBuA} show expected similarities in the ultraviolet region, assigned to intense intraligand $\sigma \rightarrow \pi^*$ and $\pi \rightarrow \pi^*$ bands.

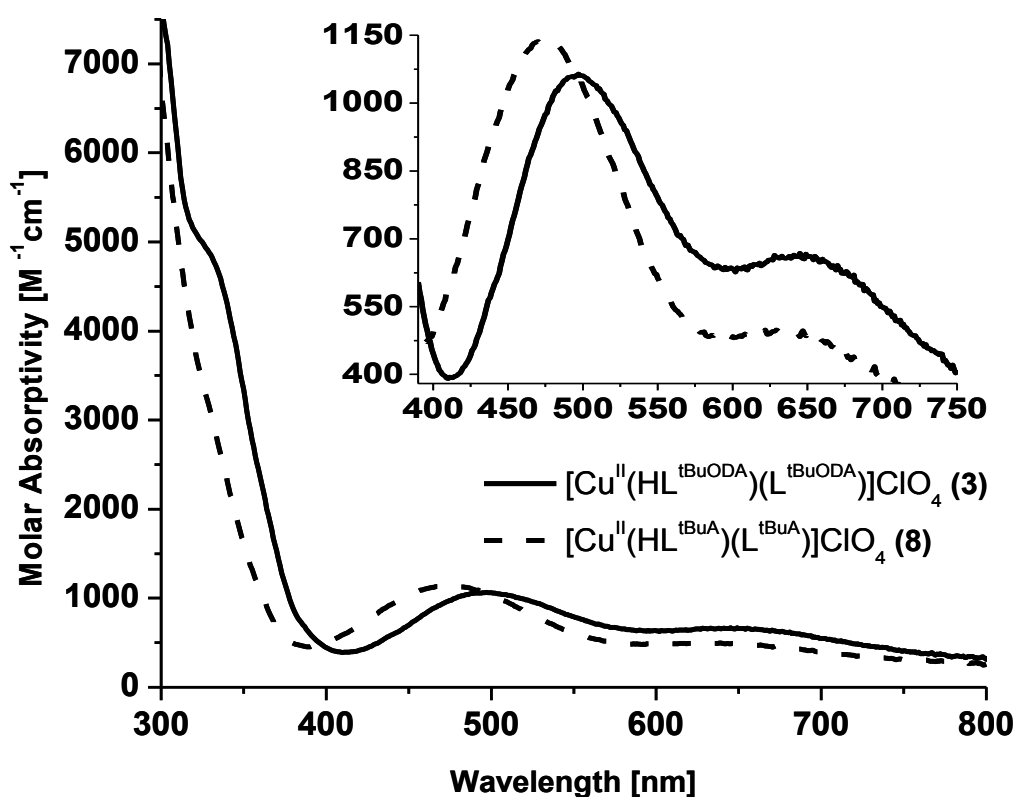


Figure 3.7. UV-vis spectra of complexes 3 and 8 in dichloromethane, 1.0×10^{-4} M. Inset: 3 and 8 at 1.0×10^{-2} M.

Table 3.2. UV–vis parameters for ligands and complexes.

Compounds ^[a]	λ (nm) / ϵ (Lmol ⁻¹ cm ⁻¹) ^[b]
<i>Ligands:</i> HL ^{tBuODA} HL ^{tBuA}	263 (7290), 268 (7200), 280 (5600) 262 (3750), 268 (3550), 282 (2990)
Nickel species	
[Ni ^{II} (L ^{tBuODA})(OAc)] (1) [Ni ^{II} (L ^{tBuA})(OAc)]·CH ₃ OH (5) [Ni ^{II} (L ^{tBuODA}) ₂] (2) [Ni ^{II} (L ^A) ₂]·2CH ₃ OH (6) [Ni ^{II} (L ^{tBuA}) ₂]·2CH ₃ OH (7)	288 (6180), 422 (860), 604 {11} ^[c] ; 965 {8} 261(6250), 348 sh (4030), 425, (915), 510 {10} 264 (9350), 620 {31}, 965 {12} 304 (8250), 605 {14}, 952 {5} 306 (9220), 610 {18}, 960 {8}
Copper species^[d]	
[Cu ^{II} (HL ^{tBuODA})(L ^{tBuODA})]ClO ₄ ·CH ₃ OH (3) [Cu ^{II} (HL ^{tBuA})(L ^{tBuA})]ClO ₄ (8)	247 (18200), 287 (9340), 328 sh (4900), 498 (1060), 651 (660) 241 (20900), 289 (9800), 474 (1140), 640 (490)
Zinc species	
[Zn ^{II} (HL ^{tBuODA}) ₂](ClO ₄) ₂ (4) [Zn ^{II} (HL ^{tBuA})(L ^{tBuA})]ClO ₄ (9)	263 (9540), 269 (8300), 290 (6340) 240 (12530), 289 (4600)

[a] Spectra measured in dichloromethane/methanol (1:1), unless otherwise noted. [b] Values for equivalent peaks within a similar group are sorted in columns.

[c] All solutions are 1.0×10^{-4} M, except for values indicated in curly brackets where 1.0×10^{-2} M solutions were used. [d] Spectra measured in dichloromethane.

Electronic information is also limited for **4** and **9** as a consequence of the intrinsic nature of the $3d^{10}$ zinc(II) ion. The interpretation of the spectra is restricted to the observation of comparable profile contours for the intraligand $\pi \rightarrow \pi^*$ bands in both species. Assessment of the differences in coordination geometry revealed by mass spectrometry and elemental analysis was not possible. The square-planar $3d^8$ low-spin ($S = 0$) nickel(II) complex **1** reveals its nature with a medium-intensity band at 422 nm, attributed to a $^1A_{1g} \rightarrow ^1A_{2g}$ spin-allowed d–d transition.³⁴ The archetype **5** displays a similar, albeit slightly more intense, band at 425 nm, along with a ill-defined shoulder at 348 nm. These features are less intense but comparable with those of low-spin $[Ni^{II}(\text{salen})]$,²⁶ and attributed respectively to charge transfer and $\pi\text{--}\pi^*$ transitions. The nickel-centered d–d transitions are also comparable at 510 nm. The pseudo-octahedral nickel(II) species **2**, **6**, and **7** do not display this band and are characterized by less intense signals around 605–620 nm, ($\epsilon \approx 20\text{--}30$) and 950–965 nm ($\epsilon \approx 5\text{--}15$), respectively attributed to $^3A_{2g} \rightarrow ^3T_{1g}(P)$ and $^3A_{2g} \rightarrow ^3T_{2g}$ spin-allowed d–d transitions.³⁵ This is in good agreement with the observation that lower wavelength absorption bands are associated with low-spin square planar electronic configurations, while higher wavelength bands are found for high-spin octahedral configurations.³⁶ The positions of the observed absorptions in **1**, **2**, **5–7** indicate that in solution, **1** and **5** remain low-spin and **2**, **6**, and **7** remain high-spin. The high-spin ($S = 1$) nature of these species can be inferred by the presence of broad and ill-defined H^1 –NMR peaks, but EPR detection is precluded due to the presence of an integer spin associated to the approximate $[e_g^2 t_{2g}^4]$ configuration (in an idealized O_h symmetry) for the Ni^{II} ion. Very recently Thomas et al.²³ have isolated a series of nickel compounds related to the archetypes **6**, and **7**

confirming the high-spin nature of pseudo-octahedral $[\text{Ni}^{\text{II}}(\text{NN}'\text{O})_2]$ systems. The most noticeable parallel between the nickel(II) surfactant **2** and the archetypes **6** and **7** is the similarity in shape and wavelength ranges for the two overlaid spectral curves. This validates further the use of archetypical complexes in providing direct insight to the coordination mode and local geometry of the metal center in architectures of higher complexity.

The agreement between the copper-containing surfactant **3** and archetype **8** is excellent. A broad band transition present at 498 and 474 nm, respectively in **3** and **8**, is attributed to a well characterized^{37–39} phenolate \rightarrow copper(II) charge-transfer transition. A lower intensity band centered at 640–650 nm is likely to have overlapping charge transfer and d–d band nature. The only evident deviation is the presence of a shoulder at 328 nm in the spectrum of **3** and absent in **8**. This shoulder is ascribed to a $\text{N}(\pi) \rightarrow \text{Cu}^{\text{II}}$ charge transfer observed for square-pyramidal copper(II) species.⁴⁰ It is possible to hypothesize that the alkyl group attached to the N_{amine} atom in **3** impinges a certain degree of distortion to the coordination environment around copper, thus causing bathochromic shifts. Indeed, all the charge-transfer bands in **3** seem to be red-shifted by about 10–20 nm. Therefore, the shoulder at 328 nm in **3** would be overlapped by more intense intraligand bands in **8**. Similar shifts have been observed by our group in phenolate-containing copper amphiphiles with distinct apolar chains.¹⁸

3.7. Electronic Structure Calculations

A series of electronic structure calculations were carried out on archetypical nickel-containing **6**, copper-containing **8**, and zinc-containing **9**, as well as on model **3'** (a model for the copper metallosurfactant **3** comprising of shortened alkyl chains). Attempts

to model **4** were made considering multiple different geometrical arrangements, but lack of convergence towards a satisfactory minimum preclude discussion at this time. Single point energy calculations on **6** were carried out with nuclear coordinates obtained directly from the crystallographic structure (see **Figure 3.3** above). The optimized geometries for structures of **8** and **9** are in good agreement with the crystallographic data presented above. Structural and electronic properties were evaluated to gain insight on the binding modes of the amphiphilic complexes. A recent study on **7**²³ supports the favorable *trans* facial coordination of the ligands over the meridional mode by ca. 5.0 kcal mol⁻¹ using a comparable level of theory. Similar values were obtained for **6** suggesting that the 3d⁸ ion favors *trans, fac* coordination.

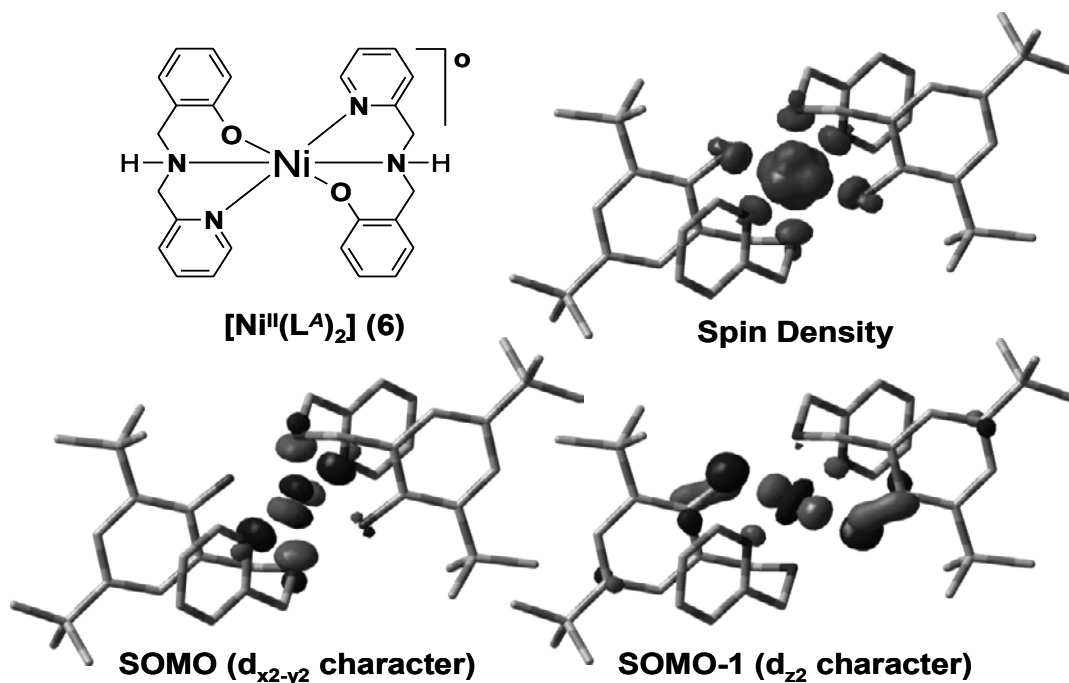


Figure 3.8. Selected MOs and spin density plot for the archetype **6**.

This is similar to the results observed for $3d^7$ ions, and in clear opposition to the preferred *cis, fac* observed for $3d^5$ ions. As shown in **Figure 3.8**, the spin density plot for the nickel archetype **6** is consistent with two unpaired electrons being arranged in the $d_{x^2-y^2}$ and d_{z^2} orbitals and resulting in an $S = 1$ ground state. This triplet state is expected for six-coordinate high-spin bivalent nickel ($3d^8$) complexes. The molecular orbital plots of the singly occupied orbitals, namely the SOMO ($d_{x^2-y^2}$) and SOMO-1(d_{z^2}) orbitals are also available. The dipole moment for **6** is small in magnitude, reaching 0.10 Debye. This is not unexpected if the high symmetry of the all-*trans* binding mode of the ligands is taken into account, as it becomes clear by inspection of the spin density plot.

The copper archetype **8** displays the SOMO consistent with a $d_{x^2-y^2}$ orbital in good agreement with the expected behavior of a bivalent copper ($3d^9$) ion in a five coordinate complex (**Figure 3.9**). Comparison between **8** and the model **3'** shows similar geometrical arrangement and comparable bond lengths and angles. An almost identical hydrogen-bonding mode between the phenolate-phenol oxygen atoms is also present. One noticeable difference is the presence of a longer Cu-N_{amine} bond length for **3'** (ca. 0.03 Å) as compared to that of **8**. This lengthening must be associated with the change from a secondary amine in **8** to a tertiary amine in **3'**, and corroborates with the observations from the UV-vis spectra. The model **3'** also displays a SOMO consistent with a $d_{x^2-y^2}$ orbital. The spin density plots reinforce this notion. Both **3'** and **8** have comparable dipole moments of 13.9 and 13.7 Debye, respectively. Overall, the archetypical **8** can be considered in excellent agreement with model **3'**, and therefore, with metallosurfactant **3**.

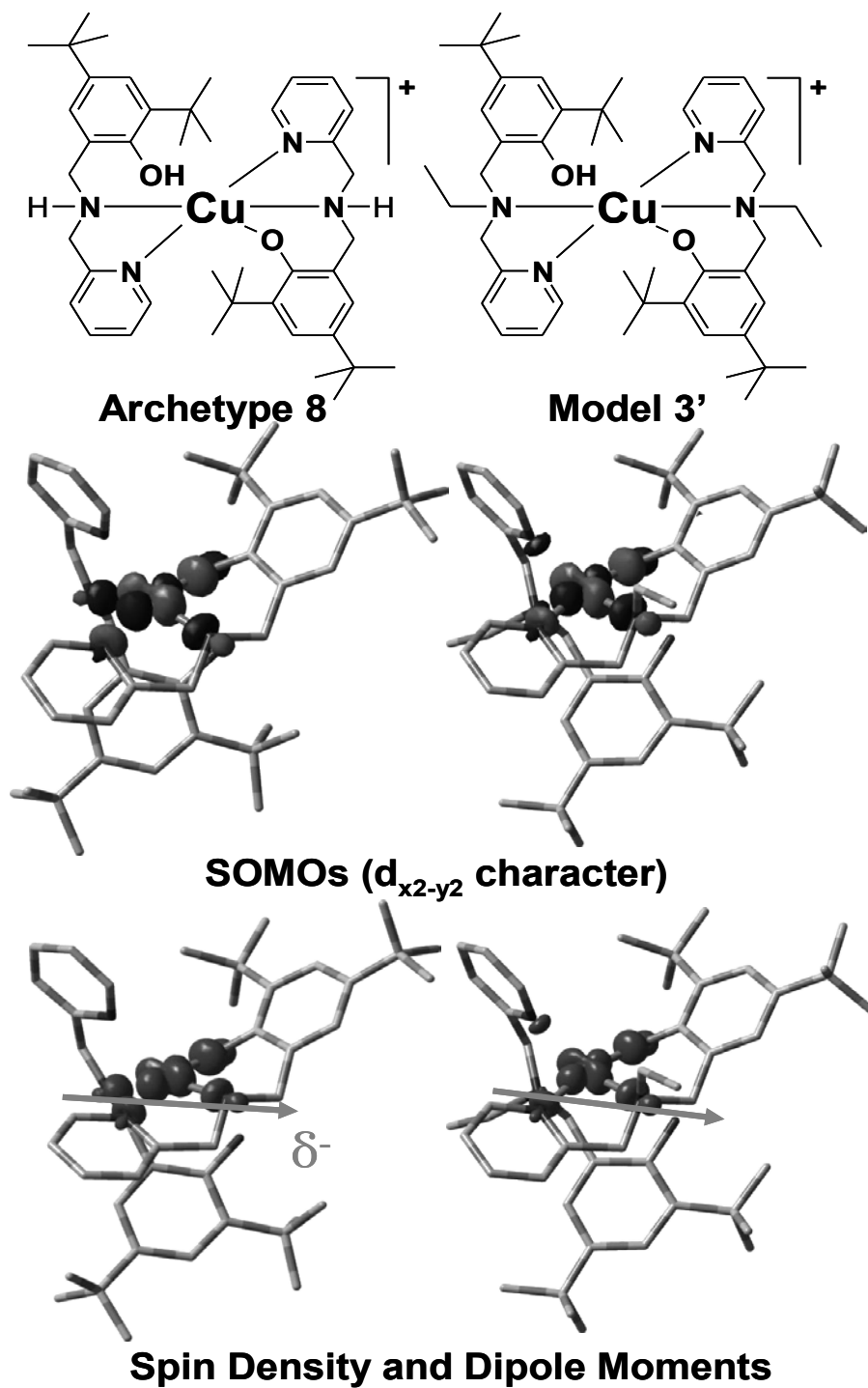


Figure 3.9. Selected molecular orbitals and spin-density plot for the optimized structures of the archetype 8 and model 3'.

Owing to their $3d^{10}$ configuration, the zinc complexes exhibit an $S = 0$ spin state. Consequently, **9** has no spin density plot and its frontier bonding orbitals are predominantly ligand-based (**Figure A.3.1**). This increase in ionic character can be reinforced by comparing the Mulliken charges in archetypes **8** and **9**. An increase is observed in the Mulliken charge from 0.84 for the copper center in **8** to 0.94 for the zinc center in **9**. Similarly, the copper-bound phenolate-oxygen shows a charge of -0.77 , compared to -0.80 in the zinc-bound phenolate-oxygen. The increasing charge separation in **9** corroborates with a decreased covalent character. The dipole moment of **9** is on the same order of magnitude as for **3'** and **8**, though slightly larger at 14.5 Debye. Refer to **Table A.3.1** for the Cartesian coordinates for all DFT calculations.

3.8. Amphiphilic Properties

The amphiphilic properties of species **1–4** were studied by way of compression isotherms⁴¹ plotting surface pressure (Π , mN m^{-1}) vs. average area per molecule [A (\AA^2)] and Brewster angle microscopy. Compression isotherms are performed in a minitrough with movable barriers and allow for two-dimensional activities that transpire at the air/water interface, which result in the formation of Langmuir films. The assessment of mono- or multilayers, collapse pressures (π_c), limiting areas per molecule (A_{lim}), and the area at the collapse of the monolayer (A_c) become evident. When the barriers of a minitrough are compressed, the tension (γ) of the amphiphile-containing air/water interface decreases as compared to that of the air/water interface only ($\gamma_0 = 72 \text{ mN m}^{-1}$ at $23 \text{ }^\circ\text{C}$), following in an increase in Π ($= \gamma_0 - \gamma$). When conducting compression isotherms in concert with Brewster angle microscopy, polarized light passes throughout media with

different refractive indexes at the air/water interface revealing agglomerates and domains, as well homogeneity in films.

Species 1–4 resemble structurally a series of *tert*-butyl-substituted phenolate-containing amphiphiles published recently by our group.¹⁸ The main difference is the presence of a methylpyridine arm attached to the N_{amine} atom. Similarly, the ligand $\text{HL}^{\text{tBuODA}}$ used in this article is related to the ligand HL^{IODA} with iodo groups occupying the 2nd and 4th position of the phenolate ring. This ligand stabilizes bivalent cobalt ions in the $[\text{Co}^{\text{II}}(\text{L}^{\text{IODA}})_2]$ species.¹⁷ A detailed comparison among these species will be provided. The isotherms for 1–4 are shown in **Figure 3.10** and present moderate collapse pressures.

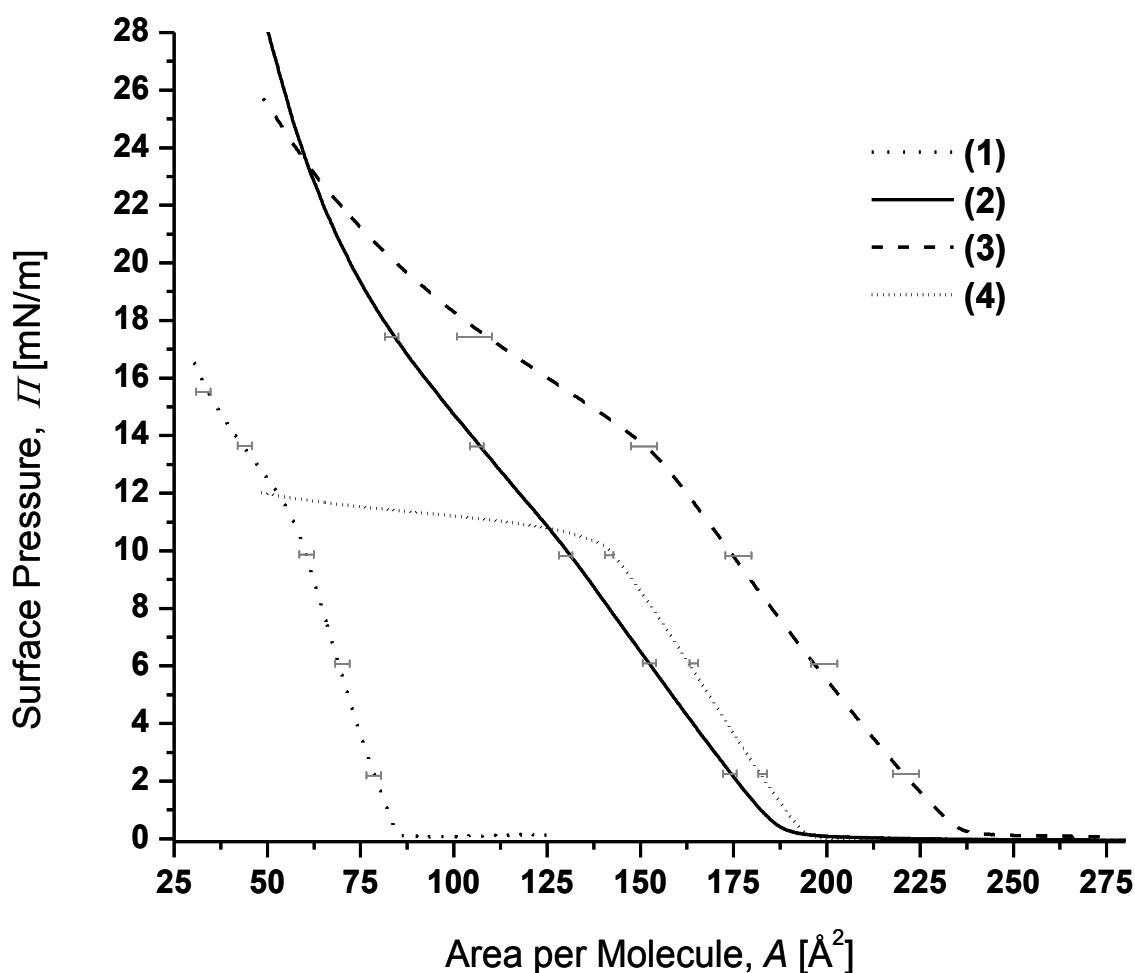


Figure 3.10. Langmuir–Blodgett isotherms of the metallocosurfactants.

For **1**, with a single alkyl chain and a higher dipole moment, the individual molecules start interacting at the air/water interface at around $85 \text{ \AA}^2 \text{ molecule}^{-1}$, whereas the molecules of **2**, **3**, and **4** interact at much higher areas of 185, 230, and $195 \text{ \AA}^2 \text{ molecule}^{-1}$, respectively. Hence, species **2–4** are characterized by large average areas per molecule reflecting the *trans* arrangement of the alkyl chains. At least partially, the high areas observed for **3** and **4** are also related to the presence of a cationic core. However, no clear pattern can be observed correlating an increase in average areas with increasing core charge, since the monocationic **3** displays higher areas than the dicationic **4**. In spite of the distinctive average areas, **1**, **3**, and **4** present similar profiles with an inflection point around $10\text{--}14 \text{ mN m}^{-1}$ followed by a less steep compression pattern. Interestingly, species **4** shows a much more accentuated decline, resembling the profile of a system with constant-pressure collapse,⁴² while **2** shows the opposite behavior, displaying a more steep isotherm after the inflection point at 18 mN m^{-1} . This led to the suspicion that in spite of a continuous compression profile and lack of traditional collapse, the inflection point in these systems may coincide with folding, bending, and breaking into multilayers proposed by the Ries mechanism.^{43,44} Brewster angle microscopy was used to evaluate the homogeneity of the films and corroborates with the idea that agglomerates similar to those expected in multilayers exist after the inflection points. The results are shown in **Figure 3.11**, where it can be seen that for **1–4** flat domains coexist before compression at low surface pressures. Upon compression, seemingly homogeneous films are observed up to pressures that precede the inflection points, when the appearance of multiple ring-shaped events predominates. These rings are multilayer granules formed from the

ejection of matter from the compressed monolayer when localized oscillations are present and account for the thermodynamic instability of the film.⁴⁵

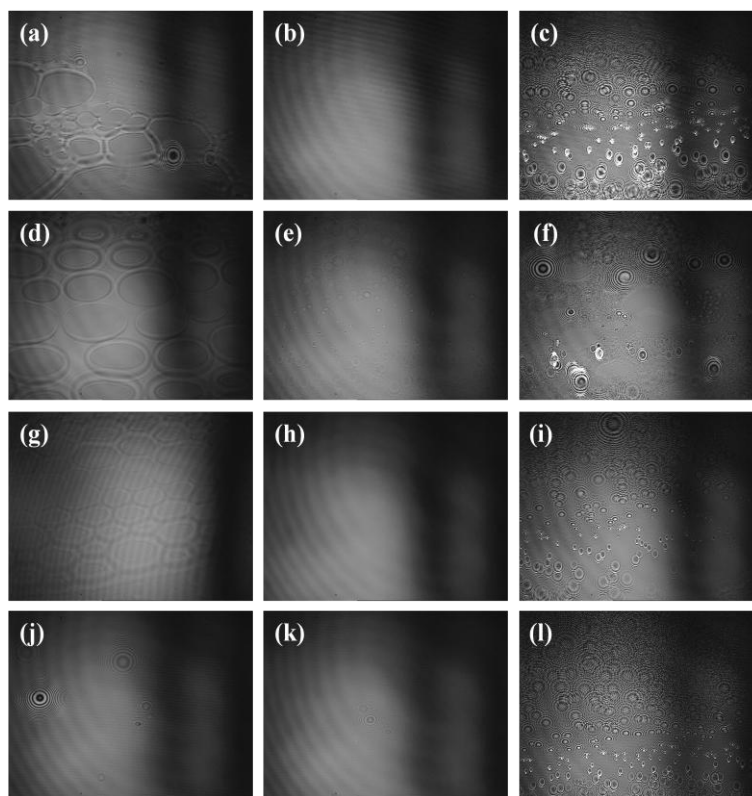


Figure 3.11. Selected Brewster angle micrographs. For **1**: (a) before compression, (b) between $1\text{--}10\text{ mN m}^{-1}$, (c) after 11 mN m^{-1} . For **2**: (d) before compression, (e) between $3\text{--}10\text{ mN m}^{-1}$, (f) after 11 mN m^{-1} . For **3**: (g) before compression, (h) between $2\text{--}12\text{ mN m}^{-1}$, (i) after 13 mN m^{-1} . For **4**: (j) before compression, (k) between $1\text{--}10\text{ mN m}^{-1}$, and (l) after 11 mN m^{-1} .

In an attempt to correlate structural and amphiphilic properties of **1–4**, as well as to compare with other similar metalloamphiphiles the following conclusions can be drawn: It is evident that **2–4** have roughly twice the area per molecule than **1**, this is due to the fact that **2–4** have two $\text{HL}^{\text{tBuODA}}$ ligands coordinated to the metal center, while **1** contains a single ligand. The areas observed for **2–4** are comparable to other *tert*-butyl-substituted phenolate-containing amphiphiles.¹⁸ Replacement of these substituents

by more polar groups, as well as the design of surfactants with a single alkyl chain as in **1**, seems to be necessary to achieve ordered films with higher collapse pressures. The nickel(II) complex **2** has a neutral octahedral core with two deprotonated (L^{tBuODA})⁻ ligands, while copper-containing **3** has a five-coordinate monocationic core associated with one protonated HL^{tBuODA} ligand, and zinc-containing **4** has a dicationic four-coordinate core with both HL^{tBuODA} ligands protonated. It seems that in moving from rigid octahedral cores as in **2** to more flexible cores in **3** and **4**, a tendency toward constant-pressure collapse can be observed. This is in excellent agreement with the behavior observed for cobalt amphiphiles,¹⁸ in which increased core-flexibility also led to a constant-pressure collapse mechanism. Finally, it is not clear why **2** and **4** display similar average areas per molecule, while **3** shows higher areas.

3.9. Summary and Conclusions

In this chapter, we have synthesized and characterized the metallosurfactants $[Ni^{II}(L^{tBuODA})(OAc)]$ (**1**), $[Ni^{II}(L^{tBuODA})_2]$ (**2**), $[Cu^{II}(HL^{tBuODA})(L^{tBuODA})]ClO_4 \cdot CH_3OH$ (**3**), and $[Zn^{II}(HL^{tBuODA})_2](ClO_4)_2$ (**4**). Due to the waxy texture of some of the metallosurfactants and due to the inability of getting crystal structures for **1–4**, archetypical modeling was used to assess the nature of these products. For this reason, species $[Ni^{II}(L^{tBuA})(OAc)] \cdot CH_3OH$ (**5**), $[Ni^{II}(L^A)_2] \cdot CH_3OH \cdot H_2O$ (**6**), $[Ni^{II}(L^{tBuA})_2] \cdot 2CH_3OH$ (**7**), $[Cu^{II}(HL^{tBuA})(L^{tBuA})]ClO_4$ (**8**), and $[Zn^{II}(HL^{tBuA})(L^{tBuA})]ClO_4$ (**9**) were synthesized. Careful analysis of **5–9** allowed us to evaluate the relationship between stoichiometric, coordination, and protonation preferences in metallosurfactants **1–4**, and therefore, draw structure/amphiphilic function relationships.

The nickel(II) complex **1** is square planar, whereas **2** has a neutral octahedral core with two deprotonated (L^{tBuODA})⁻ ligands. Copper-containing **3** has a five-coordinate monocationic core associated with one protonated HL^{tBuODA} ligand, whereas the zinc-containing **4** has a dicationic four-coordinate core with both HL^{tBuODA} ligands protonated. DFT calculations were used to identify the frontier orbitals, polarizability, and dipole moments. In an attempt to correlate structural and amphiphilic properties of **1–4**, as well as to compare with other similar metalloamphiphiles the following conclusions can be drawn: in Langmuir films of **1**, the average molecular area is approximately half of that needed for **2–4**. Nonetheless the areas observed for **2–4** are comparable to other *tert*-butyl-substituted phenolate-containing amphiphiles. The nature of the core, reflected by its flexibility and coordination number seems to foster distinctive collapse mechanisms. Flexible penta- and tetracoordinate cores show a tendency to support constant-pressure collapse mechanisms. This behavior was also observed for structurally related cobalt amphiphiles, but in that case, the coordination modes were kept constant while the ligand flexibility was variable. The results reported here suggest that (i) control of the surfactant-to-metal ratio, (ii) selection of the coordination modes and structural properties of the material, and (iii) understanding of the protonation preferences of the ligands can be achieved by careful choice of the metal ion. Awareness of this information will allow to push current limits in reproducibility of thin films of metallosurfactants and is expected to pave the way toward the development of metal-containing responsive films.

3.10. Experimental Section

Methods and materials used in this chapter are listed in **Section 2.1** of **Chapter 2**.

3.10.1. X-ray Structural Determinations. Diffraction data were measured using a Bruker P4/CCD or a Bruker X8 APEX-II kappa geometry diffractometer with Mo radiation and a graphite monochromator at 100 or 213 K. Frames were collected for 10 s and 0.2 or 0.3° between each frame. The frame data was indexed and integrated with the manufacturer's software.⁴⁶ SHELX-97 was used for refinement.⁴⁷ The collected crystal data for the five structures is shown in **Table 3.3**.

Table 3.3. Crystal data.

	5	6	7	8'	9
Formula	C ₂₄ H ₃₄ NiN ₂ O ₄	C ₂₇ H ₃₂ NiN ₄ O ₄	C ₄₄ H ₆₆ NiN ₄ O ₄	C ₆₇ H ₈₃ BCuN ₄ O ₃	C ₄₂ H ₅₉ ClZnN ₄ O ₆
<i>M</i>	473.24	535.28	773.72	1066.72	816.75
Space group	<i>P</i> 2 ₁ / <i>c</i>	<i>P</i> 1	<i>P</i> 2 ₁ / <i>c</i>	<i>P</i> 2 ₁ / <i>c</i>	<i>P</i> 1
<i>a</i> [Å]	14.8325(6)	9.4001(6)	13.864(3)	10.7795(5)	11.439(3)
<i>b</i> [Å]	7.0996(3)	11.7678(8)	12.596(3)	27.7798(10)	13.745(5)
<i>c</i> [Å]	22.2614(9)	11.8448(8)	12.297(3)	20.1353(9)	15.891(5)
α [°]		100.501(1)			96.456(8)
β [°]	94.382(2)	90.400(1)	105.450(4)	97.053(2)	110.106(5)
γ [°]		101.558(2)			108.547(4)
<i>V</i> [Å ³]	2337.38(17)	1260.9(2)	2069.8(7)	5983.9(4)	2154.3(11)
<i>Z</i>	4	2	2	4	2
<i>T</i> [K]	100(2)	213(2)	213(2)	100(2)	213(2)
λ [Å]	0.71073	0.71073	0.71073	0.71073	0.71073
<i>D</i> _{calcd.} [g cm ⁻³]	1.345	1.410	1.241	1.184	1.259
μ [mm ⁻¹]	0.862	0.810	0.515	0.413	0.681
<i>R</i> (<i>F</i>) (%) ^[a]	3.43	3.87	3.59	4.70	7.47
<i>Rw</i> (<i>F</i>) (%)	8.87	10.09	7.61	10.38	19.88

[a] $R(F) = \sum ||F_o| - |F_c|| / \sum |F_o|$ for $I > 2\sigma(I)$; $Rw(F) = [\sum w(F_o^2 - F_c^2)^2 / \sum w(F_o^2)^2]^{1/2}$ for $I > 2\sigma(I)$.

$[\text{Ni}(\text{C}_{23}\text{H}_{30}\text{N}_2\text{O}_3)] \cdot \text{CH}_3\text{OH}$ (**5**): Crystallized as red-amber rods, and a sample approximately $0.26 \times 0.20 \times 0.16 \text{ mm}^3$ was used for data collection. 6513 frames were collected, yielding 101662 reflections, of which 8947 were independent. Hydrogen positions were placed in calculated or observed positions. The asymmetric unit consists of one neutral complex, with one equivalent of methanol solvate. $[\text{Ni}(\text{C}_{26}\text{H}_{26}\text{N}_4\text{O}_2)] \cdot (\text{H}_2\text{O}) \cdot (\text{CH}_3\text{OH})$ (**6**) crystallized as pale violet rods. A sample $0.28 \times 0.12 \times 0.15 \text{ mm}^3$ was used for data collection. 1850 frames were collected, yielding 6605 reflections, of which 5292 were independent. Hydrogen positions were observed or calculated. The asymmetric unit contains two half coordination molecules, each with Ni occupying a crystallographic inversion center, and one equivalent each of solvents water and methanol.

$[\text{Ni}(\text{C}_{42}\text{H}_{58}\text{N}_4\text{O}_2)] \cdot 2\text{CH}_3\text{OH}$ (**7**) crystallized as pale yellow-green rods and plates. A sample $0.24 \times 0.18 \times 0.12 \text{ mm}^3$ was used for data collection. 1850 frames were collected, yielding 53411 reflections, of which 7392 were independent. Hydrogen positions were observed and refined. The dataset exhibited a rotated 180 degree twin about the (100) reciprocal axis, and corrections were made by use of CELL-NOW, SAINT-7, and TWINABS.^{46,47} The twin component refined to 41 % of the total diffraction. Within the coordination complex, Ni occupies a crystallographic inversion center. The asymmetric unit contains one half complex and one molecule of methanol solvate. $[\text{Cu}(\text{C}_{42}\text{H}_{59}\text{N}_4\text{O}_2)] \cdot \text{B}(\text{C}_6\text{H}_5)_4 \cdot \text{CH}_3\text{OH}$ (**8'**) crystallized as square, purple plates. The sample mounted measured $0.24 \times 0.22 \times 0.03 \text{ mm}^3$. 1397 frames were collected, yielding 51713 reflections, of which 14731 were unique. Hydrogen atoms were placed in observed or calculated positions. The asymmetric unit contains one cation, a

tetraphenylborate anion and one equivalent of methanol solvent. $[\text{Zn}(\text{C}_{42}\text{H}_{59}\text{N}_4\text{O}_2)](\text{ClO}_4)$ (**9**) presents as yellow plates. The sample used was $0.4 \times 0.2 \times 0.05 \text{ mm}^3$. 1850 frames yielded 11230 reflections, of which 8803 were unique. Hydrogen atoms were placed in observed or calculated positions. Partially occupied positions were assigned for disorder in the *tert*-butyl groups C15–17 and C36–38. In addition, C36–38 and C36'–38' were kept isotropic during refinement. Typical large thermal parameters were displayed by the perchlorate anion.

3.10.2. Syntheses. Preparation of the Ligands HL^A , $\text{HL}^{t\text{Bu}2A}$, $\text{HL}^{t\text{Bu}2I}$, and $\text{HL}^{t\text{Bu}2\text{ODA}}$. The ligands were synthesized according to the literature.^{17,20,21} Basic procedures are explained for the syntheses of the nickel, copper, and zinc complexes.

3.10.3. Preparation of the Metallosurfactant $[\text{Ni}^{\text{II}}(\text{L}^{t\text{BuODA}})(\text{OAc})]$ (1**).** A 10 mL MeOH solution of $\text{Ni}(\text{OAc})_2 \cdot 4\text{H}_2\text{O}$ (0.25 g, 1.0 mmol) was added dropwise to a 30 mL MeOH solution of $\text{HL}^{t\text{BuODA}}$ (0.58 g, 1.0 mmol). The solution was stirred and gently refluxed for 2 h, and then filtered to eliminate unreacted solids. Slow solvent evaporation after concentration to one-third of its original volume yielded a waxy, dark green film layer. Yield 0.50 g, 72 % for $[\text{C}_{41}\text{H}_{68}\text{N}_2\text{O}_3\text{Ni}_1]$ (1214.6). IR data (KBr): $\tilde{\nu} = 2933\text{--}2857$ (alkyl chain and *tert*-butyl C–H stretches), 1609 (C=N from pyridine), 1574 (antisym. acetate stretch), 1480 (C–O from phenyl) cm^{-1} . MS data (ESI⁺ in MeOH): $m/z = 695.4$ $[\text{Ni}(\text{L}^{t\text{BuODA}})(\text{OAc}) + \text{H}]^+$.

3.10.4. Preparation of the Metallosurfactants $[\text{Ni}^{\text{II}}(\text{L}^{t\text{BuODA}})_2]$ (2**), $[\text{Cu}^{\text{II}}(\text{HL}^{t\text{BuODA}})(\text{L}^{t\text{BuODA}})]\text{ClO}_4$ (**3**), and $[\text{Zn}^{\text{II}}(\text{HL}^{t\text{BuODA}})_2](\text{ClO}_4)_2$ (**4**).** **CAUTION!** *Although no difficulties were experienced, species 3–4 and 8–9 were isolated as their perchlorate salts, and therefore they should be handled as potentially explosive.* A 10 mL

MeOH solution containing the salts $\text{Ni}(\text{ClO}_4)_2 \cdot 6\text{H}_2\text{O}$ (0.18 g, 0.5 mmol), $\text{Cu}(\text{ClO}_4)_2 \cdot 6\text{H}_2\text{O}$ (0.185 g, 0.5 mmol), or $\text{Zn}(\text{ClO}_4)_2 \cdot 6\text{H}_2\text{O}$ (0.186 g, 0.5 mmol) was added dropwise to a 30 mL MeOH solution containing $\text{HL}^{\text{tBuODA}}$ (0.58 g, 1.0 mmol) and Et_3N (0.14 mL, 1.0 mmol). In each case the resulting solutions were stirred under mild reflux for 1–2 h and then filtered while warm. The solvent was removed by rotary evaporation and the crude products were dissolved in 50 mL dichloromethane and washed with 4×50 mL of saturated brine solution in a separation funnel. The dichloromethane phase was then dried with Na_2SO_4 and concentrated to one third of its original volume. Slow solvent evaporation yielded a brown thick oil for **2**, a brownish green waxy solid for **3** and an off-white solid for **4**.

2: Yield 0.42 g, 70 % for $[\text{C}_{78}\text{H}_{130}\text{N}_4\text{O}_2\text{Ni}_1]$ (1214.6). IR data (KBr): $\tilde{\nu} = 2958\text{--}2854$ (alkyl chain and *tert*-butyl C–H stretches), 1610 (C=N from pyridine), 1467 (C–O from phenyl) cm^{-1} . MS data (ESI⁺ in MeOH): $m/z = 1214$ $[\text{Ni}(\text{L}^{\text{tBuODA}})_2 + \text{H}]^+$. The consistency of the material precludes elemental analysis.

3: Yield 0.46 g, 68 %. $\text{C}_{79}\text{H}_{135}\text{ClCuN}_4\text{O}_7$ (1351.9): calcd. C 70.18, H 10.02, N 4.14; found C 69.66, H 9.84, N 3.97. IR data (KBr): $\tilde{\nu} = 2922\text{--}2856$ (alkyl chain and *tert*-butyl C–H stretches), 1611 (C=N from pyridine), 1467 (C–O from phenyl), 1104 (Cl–O from ClO_4^-) cm^{-1} . MS data (ESI⁺ in MeOH): $m/z = 1219.0$ $[\text{Cu}(\text{HL}^{\text{tBuODA}})(\text{L}^{\text{tBuODA}})]^+$.

4: Yield 0.50 g, 70 %. $\text{C}_{78}\text{H}_{132}\text{Cl}_2\text{N}_4\text{O}_{10}\text{Zn}$ (1422.2): calcd. C 65.87, H 9.36, N 3.94; found C 66.12, H 9.34, N 4.00. IR data (KBr): $\tilde{\nu} = 2923\text{--}2851$ (alkyl chain and *tert*-butyl C–H stretches), 1608 (C=N from pyridine), 1472 (C–O from phenyl), 1116 (Cl–O from ClO_4^-) cm^{-1} . MS data (ESI⁺ in MeOH): $m/z = 1220.0$ $[\text{Zn}(\text{HL}^{\text{tBuODA}})(\text{L}^{\text{tBuODA}})]^+$ and 641.5 $[(m/2) + \text{CH}_3\text{OH}]$.

3.10.5. Preparation of the Archetype $[\text{Ni}^{\text{II}}(\text{L}^{\text{tBuI}})(\text{OAc})]\cdot\text{CH}_3\text{OH}$ (5). The synthesis of this complex similarly follows that of **1**. The crude red powder product obtained after roto-evaporation was recrystallized using a 1:1 dichloromethane/methanol solvent combination to give needle-like crystals. Yield 0.65 g, 77%. $\text{C}_{24}\text{H}_{34}\text{N}_2\text{NiO}_4$ (473.2): calcd. C 60.81, H 7.24, N 5.92; found C 59.92, H 7.26, N 6.18. IR data (KBr): $\tilde{\nu}$ = 1600 (C=N from pyridine), 1570 (antisym. acetate stretch) cm^{-1} . 1487 (C–O from phenyl), 2957–2869 (C–H). MS data (ESI⁺ in MeOH): m/z = 413.4 $[\text{Ni}(\text{L}^{\text{tBuI}}) + \text{CH}_3\text{OH}]^+$.

3.10.6. Preparation of the Archetypes $[\text{Ni}^{\text{II}}(\text{L}^{\text{A}})_2]\cdot\text{H}_2\text{O}\cdot\text{CH}_3\text{OH}$ (6), $[\text{Ni}^{\text{II}}(\text{L}^{\text{tBuA}})_2]\cdot 2\text{CH}_3\text{OH}$ (7), $[\text{Cu}^{\text{II}}(\text{HL}^{\text{tBuA}})(\text{L}^{\text{tBuA}})]\text{ClO}_4$ (8), $[\text{Zn}^{\text{II}}(\text{HL}^{\text{tBuA}})(\text{L}^{\text{tBuA}})]\text{ClO}_4$ (9). A general synthetic approach was followed for the archetypical complexes. A 10 mL solution of $\text{Ni}(\text{ClO}_4)_2\cdot 6\text{H}_2\text{O}$ (0.366 g, 1.0 mmol) for **6** and **7**, $\text{Cu}(\text{ClO}_4)_2\cdot 6\text{H}_2\text{O}$ (0.370 g, 1 mmol) for **8**, or $\text{Zn}(\text{ClO}_4)_2\cdot 6\text{H}_2\text{O}$ (0.372 g, 1 mmol) for **9** was added dropwise to a 30 mL MeOH solution containing 2.0 mmol of the appropriate ligand (HL^{A} for **6** and $\text{HL}^{\text{tBuODA}}$ for **7–9**) and 2 equiv. of Et_3N (0.28 mL, 2.0 mmol). In each reaction, the resulting solution was stirred and warmed gently for 1 h. The metal complexes were recovered either by precipitation or by slow evaporation and were collected by filtration and washed with diethyl ether. Recrystallization in MeOH afforded suitable crystals for X-ray analysis for **6**, **7**, **8**, and **9** after slow solvent evaporation.

6: Yield 0.53 g, 79%. $\text{C}_{27}\text{H}_{32}\text{N}_4\text{NiO}_4$ (535.3): calcd. C 60.65, H 6.03, N 10.48; found C 60.23, H 6.17, N 10.21. IR data (KBr): $\tilde{\nu}$ = 3291 (N–H), 2924 (C–H stretches), 1606, 1593 (C=N from pyridine), 1486 (C–O from phenyl) cm^{-1} . MS data (ESI⁺ in MeOH): m/z = 484.1 $[\text{Ni}(\text{L}^{\text{A}})_2 + \text{H}]^+$.

7: Yield 0.59 g, 76 %. $C_{44}H_{66}N_4NiO_4$ (773.7): calcd. C 68.35, H 8.61, N 7.25; found C 68.23, H 8.74, N 7.20. IR data (KBr): $\tilde{\nu} = 3322$ (N–H), 2950 (C–H), 1607 (C=N from pyridine), 1469 (C–O from phenyl) cm^{-1} . MS data (ESI⁺ in MeOH): $m/z = 709.3$ $[Ni(L^{tBuA})_2 + H]^+$.

8: Yield 0.68 g, 82 %. $C_{42}H_{61}ClCuN_4O_7$ (832.9): calcd. C 60.56, H 7.38, N 6.73; found C 60.05, H 7.36, N 6.81. IR data (KBr): $\tilde{\nu} = 3439$ (OH), 3259 (N–H), 2954 (C–H), 1603 (C=N from pyridine), 1443 (C–O from phenyl), 1120 (Cl–O from ClO_4^-) cm^{-1} . MS data (ESI⁺ in MeOH): $m/z = 714.4$ $[Cu(HL^{tBuA})(L^{tBuA})]^+$. **Note:** X-ray quality crystals were generated through counterion exchange using a 3-fold excess of tetraphenylboron sodium salt in 50 mL methanol.

9: Yield 0.60 g, 73 %. $C_{42}H_{59}ClN_4O_6Zn$ (816.8): calcd. C 61.76, H 7.28, N 6.86; found C 61.84, H 7.32, N 6.90. IR data (KBr): $\tilde{\nu} = 3290$ (N–H), 2957–2869 (C–H), 1608 (C=N from pyridine), 1474 (C–O from phenyl), 1097 (Cl–O from ClO_4^-) cm^{-1} . MS data (ESI⁺ in MeOH): $m/z = 715.2$ $[Zn^{II}(HL^{tBuA})(L^{tBuA})]^+$.

3.11. References

- 1 Park, J.; Pasupathy, A. N.; Goldsmith, J. I.; Chang, C.; Yaish, Y.; Petta, J. R.; Rinkoski, M.; Sethna, J. P.; Abruña, H. D.; McEuen, P. L.; Ralph, D. C. "Coulomb Blockade and the Kondo Effect in Single-Atom Transistors." *Nature* **2002**, *417*, 722.
- 2 (a) Zhang, J.; Chu, B. W.-K.; Zhu, N.; Yam, V. W.-W. "Synthesis, Characterization, Langmuir–Blodgett Film-Forming Property, and Second-Order Nonlinear Optical Study of Rhenium(I) and Ruthenium(II) Diimine Complexes." *Organometallics* **2007**, *26*, 5423. (b) Yam, V. W.-W.; Li, B.; Yang, Y.; Chu, B. W.-K.; Wong, K. M.-C.; Cheung, K.-K. "Preparation, Photoluminescence and Electroluminescence Behavior of Langmuir–Blodgett Films of Bipyridylrhenium(I) Surfactant Complexes." *Eur. J. Inorg. Chem.* **2003**, 4035. (c) Chu, B. W.-K.; Yam, V. W.-W. "Synthesis, Characterization, Langmuir–Blodgett Film-Forming Properties, and Second-Harmonic-Generation Studies of Ruthenium(II) Complexes with Long Hydrocarbon Chains." *Inorg. Chem.* **2001**, *40*, 3324.
- 3 (a) Binnemans, K.; Lodewyckx, K.; Donnio, B.; Guillon, D. "Mixed Copper-Lanthanide Metallomesogens." *Chem. Eur. J.* **2002**, *8*, 1101. (b) Binnemans, K.; Galyametdinov, Y. G.; Van Deun, R.; Bruce, D. W.; Collinson, S. R.; Polishchuk, A. P.; Bikchantaev, I.; Haase, W.; Prosvirin, A. V.; Tinchurina, L.; Litvinov, I.; Gubajdullin, A.; Rakhmatullin, A.; Uytterhoeven, K.; Van Meervelt, L. "Rare-Earth-Containing Magnetic Liquid Crystals." *J. Am. Chem. Soc.* **2000**, *122*, 4335.

- 4 (a) Rueff, J.-M.; Masciocchi, N.; Rabu, P.; Sironi, A.; Skoulios, A. "Structure and Magnetism of a Polycrystalline Transition Metal Soap - Co^{II} $[\text{OOC}(\text{CH}_2)_{10}\text{COO}](\text{H}_2\text{O})_2$." *Eur. J. Inorg. Chem.* **2001**, 2843. (b) Rueff, J.-M.; Masciocchi, N.; Rabu, P.; Sironi, A.; Skoulios, A. "Synthesis, Structure and Magnetism of Homologous Series of Polycrystalline Cobalt Alkane Mono- and Dicarboxylate Soaps." *Chem. Eur. J.* **2002**, 08, 1813.
- 5 Beck, J. B.; Rowan, S. J. "Multistimuli, Multiresponsive Metallo-Supramolecular Polymers." *J. Am. Chem. Soc.* **2003**, 125, 13922.
- 6 Hayami, S.; Danjobara, K.; Shigeyoshi, Y.; Inoue, K.; Ogawa, Y.; Maeda, Y. "Crystal Structure and Mesogenic Property of an Iron(II) Complex with a Terpyridine Derivative Ligand." *Inorg. Chem. Commun.* **2005**, 8, 506.
- 7 Lednev, I. K.; Petty, M. C. "Langmuir Monolayers and Langmuir-Blodgett Multilayers Containing Macrocyclic Ionophores." *Adv. Mater.* **1996**, 8, 615.
- 8 Vergeer, F. W.; Chen, X.; Lafolet, F.; De Cola, L.; Fuchs, H.; Chi, L. "Ultrathin Luminescent Films of Rigid Dinuclear Ruthenium(II) Trisbipyridine Complexes." *Adv. Funct. Mater.* **2006**, 16, 625.
- 9 (a) Griffiths, P. C.; Fallis, I. A.; Chuenpratoom, T.; Watanesk, R. "Metallosurfactants: Interfaces and Micelles." *Adv. Colloid Interf. Sci.* **2006**, 122, 107. (b) Griffiths, P. C.; Fallis, I. A.; Willock, D. J.; Paul, A.; Barrie, C. L.; Griffiths, P. M.; Williams, G. M.; King, S. M.; Heenan, R. K.; Goergl, R. "The Structure of Metallomicelles." *Chem. Eur. J.* **2004**, 10, 2022.

- 10 Chen, X.; Lenhert, S.; Hirtz, M.; Lu, N.; Fuchs, H.; Chi, L. "Langmuir–Blodgett Patterning: A Bottom-Up Way to Build Mesostructures over Large Areas." *Acc. Chem. Res.* **2007**, *40*, 393.
- 11 Yang, L.; Peng, H.; Huang, K.; Mague, J. T.; Li, H.; Lu, Y. "Hierarchical Assembly of Organic/Inorganic Building Molecules with π - π Interactions." *Adv. Funct. Mater.* **2008**, *18*, 1526.
- 12 Brabec, C. J.; Sariciftci, N. S.; Hummelen, J. C. "Plastic Solar Cells." *Adv. Funct. Mater.* **2001**, *11*, 15.
- 13 (a) Jaeger, D. A.; Peacock, M. F.; Bohle, D. S. "A Surfactant Transition Metal Chelate." *Langmuir* **2003**, *19*, 4859. (b) Arulsamy, N.; Bohle, D. S.; Goodson, P. A.; Jaeger, D. A.; Reddy, V. B. "Synthesis, Structure, and Stereochemistry of Double-Chain Surfactant Co(III) Complexes." *Inorg. Chem.* **2001**, *40*, 836.
- 14 (a) Choi, H. J.; Suh, M. P. "Nickel(II) Macrocyclic Complexes with Long Alkyl Pendant Chain: Synthesis, X-ray Structure, and Anion Exchange Property in the Solid State." *Inorg. Chem.* **2003**, *42*, 1151. (b) Ryan, M. F.; Metcalfe, R. A.; Lever, A. B. P.; Haga, M.-A. "A Novel Ruthenium Surfactant: Electronic Spectra, ZINDO Analysis and Langmuir–Blodgett Studies of Trans-Dichloro(6,6'-bis(N-dodecylbenzimidazol-2-yl)-2,2'-bipyridine)ruthenium(II)." *J. Chem. Soc., Dalton Trans.* **2000**, 2357. (c) Wang, K.; Haga, M.-A.; Monjushiro, H.; Akiba, M.; Sasaki, Y. "Luminescent Langmuir–Blodgett Films of Platinum(II) Complex [Pt(L₁₈)Cl](PF₆) (L₁₈ = 2,6-Bis(1-octadecylbenzimidazol-2-yl)pyridine)." *Inorg. Chem.* **2000**, *39*, 4022.

- 15 Shakya, R.; Keyes, P. H.; Heeg, M. J.; Moussawel, A.; Heiney, P. A.; Verani, C. N. "Thermotropic Mesomorphism of Soft Materials Bearing Carboxylate-Supported μ_4 -Oxo Tetracupric Clusters." *Inorg. Chem.* **2006**, *45*, 7587.
- 16 Shakya, R.; Hindo, S. S.; Wu, L.; Ni, S.; Allard, M.; Heeg, M. J.; da Rocha, S. R. P.; Yee, G. T.; Hratchian, H. P.; Verani, C. N. "Amphiphilic and Magnetic Properties of a New Class of Cluster-Bearing $[L_2Cu_4(\mu_4-O)(\mu_2\text{-carboxylato})_4]$ Soft Materials." *Chem. Eur. J.* **2007**, *13*, 9948.
- 17 Shakya, R.; Hindo, S. S.; Wu, L.; Allard, M. M.; Heeg, M. J.; Hratchian, H. P.; McGarvey, B. R.; da Rocha, S. R. P.; Verani, C. N. "Archetypical Modeling and Amphiphilic Behavior of Cobalt(II)-Containing Soft-Materials with Asymmetric Tridentate Ligands." *Inorg. Chem.* **2007**, *46*, 9808.
- 18 Hindo, S. S.; Shakya, R.; Rannulu, N. S.; Allard, M. M.; Heeg, M. J.; Rodgers, M. T.; da Rocha, S. R. P.; Verani, C. N. "Synthesis, Redox, and Amphiphilic Properties of Responsive Salicylaldehyde-Copper(II) Soft Materials." *Inorg. Chem.* **2008**, *47*, 3119.
- 19 Driscoll, J. A.; Allard, M. M.; Wu, L.; Heeg, M. J.; da Rocha, S. R. P.; Verani, C. N. "Interfacial Behavior and Film Patterning of Redox-Active Cationic Copper(II)-Containing Surfactants." *Chem. Eur. J.* **2008**, *14*, 9665.
- 20 Imbert, C.; Hratchian, H. P.; Lanznaster, M.; Heeg, M. J.; Hryhorczuk, L. M.; McGarvey, B. R.; Schlegel, H. B.; Verani, C. N. "Influence of Ligand Rigidity and Ring Substitution on the Structural and Electronic Behavior of Trivalent Iron and Gallium Complexes with Asymmetric Tridentate Ligands." *Inorg. Chem.* **2005**, *44*, 7414.

- 21 Shakya, R.; Imbert, C.; Hratchian, H. P.; Lanznaster, M.; Heeg, M. J.; McGarvey, B. R.; Allard, M.; Schlegel, H. B.; Verani, C. N. "Structural, Spectroscopic, and Electrochemical Behavior of Trans-Phenolato Cobalt(III) Complexes of Asymmetric NN'O Ligands as Archetypes for Metallomesogens." *Dalton Trans.* **2006**, 2517.
- 22 Shakya, R.; Peng, F.; Liu, J.; Heeg, M. J.; Verani, C. N. "Synthesis, Structure, and Anticancer Activity of Gallium(III) Complexes with Asymmetric Tridentate Ligands: Growth Inhibition and Apoptosis Induction of Cisplatin-Resistant Neuroblastoma Cells." *Inorg. Chem.* **2006**, *45*, 6263.
- 23 Rotthaus, O.; Labet, V.; Philouze, C.; Jarjays, O.; Thomas, F. "Pseudo-Octahedral Schiff Base Nickel(II) Complexes: Does Single Oxidation Always Lead to the Nickel(III) Valence Tautomer?" *Eur. J. Inorg. Chem.* **2008**, 4215.
- 24 Khandar, A. A.; Hosseini-Yazdi, S. A.; Zarei, S. A. "Synthesis, Characterization and X-ray Crystal Structures of Copper(II) and Nickel(II) Complexes with Potentially Hexadentate Schiff Base Ligands." *Inorg. Chim. Acta* **2005**, *358*, 3211.
- 25 BMT stems for Bailar, Missler and Tarr notation, where $\langle A_1B_2 \rangle$ indicates that A is *trans* to B, with A and B corresponding to the pyridine (N_{py}) amine (N_{am}), or phenolato (O_{phen}) groups. Subscripts 1 and 2 designate respectively the first and the second ligand. This concise notation saves space and was adapted by G. Miessler and D. Tarr, in *Inorganic Chemistry*, Pearson-Prentice Hall, p. 311–315, **2004** from the original work by John Bailar, Jr. "The Numbers and Structures of Isomers of Sexicovalent Complexes." *J. Chem. Educ.* **1957**, *34*, 334 and 623. The

- link to Prof. Bailar's work has been explained by Prof. Miessler in a personal communication to C.N.V.
- 26 Rotthaus, O.; Thomas, F.; Jarjayes, O.; Philouze, C.; Saint-Aman, E.; Pierre, J.-L. "Valence Tautomerism in Octahedral and Square-Planar Phenoxy-Nickel(II) Complexes: are Imino Nitrogen Atoms Good Friends?" *Chem. Eur. J.* **2006**, *12*, 6953.
- 27 Addison, A. W.; Rao, T. N.; Reedijk, J.; Van Rijn, J.; Verschoor, G. C. "Synthesis, Structure, and Spectroscopic Properties of Copper(II) Compounds Containing Nitrogen-Sulfur Donor Ligands: The Crystal and Molecular Structure of Aqua [1,7- bis (N- methylbenzimidazol- 2'- yl)- 2,6- dithiaheptane] copper(II) Perchlorate." *J. Chem. Soc., Dalton Trans.* **1984**, 1349.
- 28 Neves, A.; Verani, C. N.; de Brito, M. A.; Vencato, I.; Mangrich, A.; Oliva, G.; Souza, D. D. H. F.; Batista, A. A. "Copper(II) Complexes with (2-hydroxybenzyl-2-pyridylmethyl)amine-Hbpa: Syntheses, Characterization and Crystal Structures of the Ligand and [Cu(II)(Hbpa)₂](ClO₄)₂·2H₂O." *Inorg. Chim. Acta* **1999**, *290*, 207.
- 29 Kaizer, J.; Pap, J.; Speier, G.; Parkanyi, L.; Korecz, L.; Rockenbauer, A. "Synthesis, Structure and Catecholase Activity of Dinuclear Copper and Zinc Complexes with an N₃-Ligand." *J. Inorg. Biochem.* **2002**, *91*, 190.
- 30 Adams, H.; Bailey, N. A.; Fenton, D. E.; He, Q.-Y. "Mononuclear Zinc(II), Homodinuclear Zinc(II) and Heterodinuclear Zinc(II)-Copper(II) Complexes Derived from Tris[(2-pyridyl)methyl]amine." *J. Chem. Soc., Dalton Trans.* **1997**, 1533.

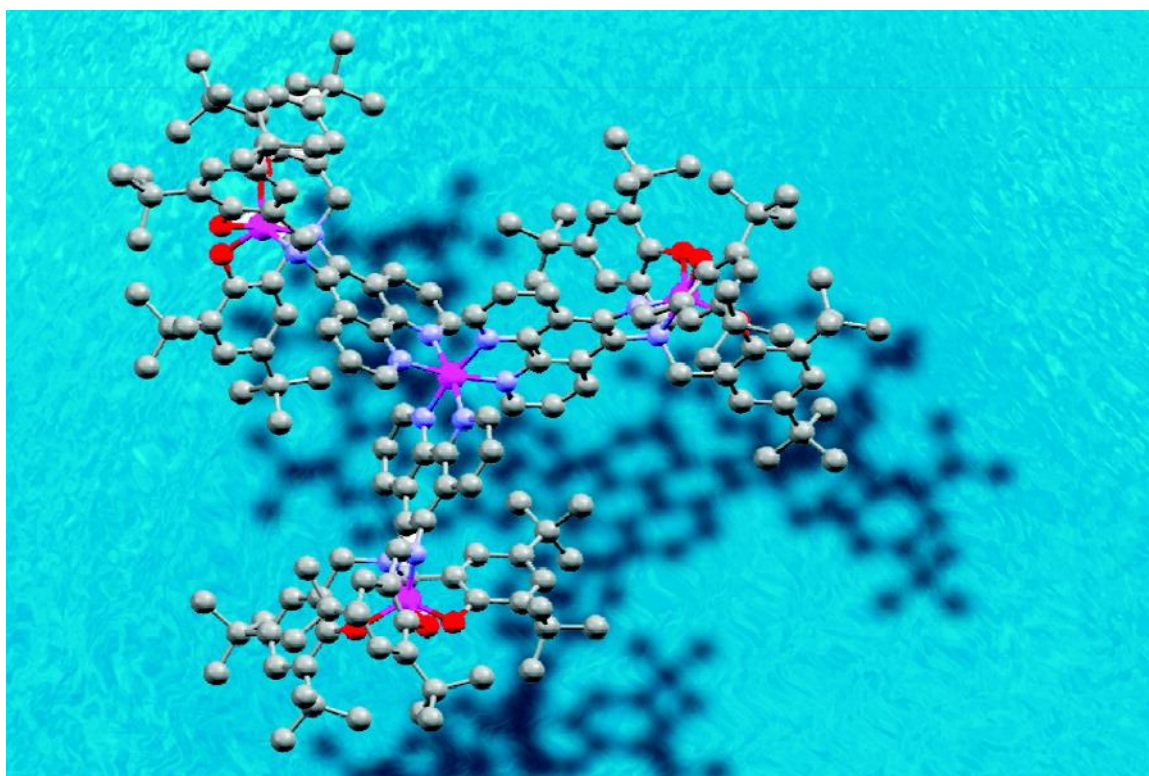
- 31 Lanznaster, M.; Neves, A.; Vencato, I.; Bortoluzzi, A. J.; Gallardo, H.; Machado, S. P.; Assumpcao, A. M. C. "Synthesis, Structure and Molecular Modeling of a ZnII-Phenolate Complex as a Model for Zn^{II}-Containing Tyrosinate Metalloenzymes." *J. Braz. Chem. Soc.* **2006**, *17*, 289.
- 32 dos Anjos, A.; Bortoluzzi, A. J.; Szpoganicz, B.; Caro, M. S. B.; Friedermann, G. R.; Mangrich, A. S.; Neves, A. "Synthesis, Characterization and Structure of a New Zinc(II) Complex Containing the Hexadentate N,N',N,N'-bis[(2-hydroxy-3,5-di-*tert*-butylbenzyl)(2-pyridylmethyl)]ethylenediamine Ligand: Generation of Phenoxy Radical Species." *Inorg. Chim. Acta* **2005**, *358*, 3106.
- 33 Neves, A.; Vencato, I.; Verani, C. N. "The Synthesis and Characterization of the Novel Pseudo-Octahedral Complex Bis [(2- hydroxybenzyl) (2-pyridylmethyl) amine] zinc(II), [Zn^{II}(bpa)₂].2H₂O as a Model for Astacin." *J. Braz. Chem. Soc.* **1997**, *8*, 265.
- 34 Lever, A. B. P. *Inorganic Electronic Spectroscopy*, 2nd ed., Elsevier Science, Amsterdam, **1984**.
- 35 Mukhopadhyay, S.; Mandal, D.; Ghosh, D.; Goldberg, I.; Chaudhury, M. "Equilibrium Studies in Solution Involving Nickel(II) Complexes of Flexidentate Schiff Base Ligands: Isolation and Structural Characterization of the Planar Red and Octahedral Green Species Involved in the Equilibrium." *Inorg. Chem.* **2003**, *42*, 8439.
- 36 Ohtsu, H.; Tanaka, K. "Equilibrium of Low- and High-Spin States of Ni(II) Complexes Controlled by the Donor Ability of the Bidentate Ligands." *Inorg. Chem.* **2004**, *43*, 3024.

- 37 (a) Viswanathan, R.; Palaniandavar, M.; Balasubramanian, T.; Muthiah, P. T. "Synthesis, Structure, Spectra and Redox Chemistry of Iron(III) Complexes of Tridentate Pyridyl and Benzimidazolyl Ligands." *J. Chem. Soc., Dalton Trans.* **1996**, 2519. (b) Rajendran, U.; Viswanathan, R.; Palaniandavar, M.; Lakshminarayanan, M. "An Unusual Axial Coordination of Phenolate Oxygen to Copper(II): Crystal Structure of Chloro{2-[bis(2-pyridylmethyl)aminomethyl]-4-nitrophenolato}copper(II)." *J. Chem. Soc., Dalton Trans.* **1992**, 3563.
- 38 (a) Bill, E.; Mueller, J.; Weyhermueller, T.; Wieghardt, K. "Intramolecular Spin Interactions in Bis(phenoxy)metal Complexes of Zinc(II) and Copper(II)." *Inorg. Chem.* **1999**, 38, 5795. (b) Auerbach, U.; Eckert, U.; Wieghardt, K.; Nuber, B.; Weiss, J. "Synthesis and Coordination Chemistry of the Hexadentate Ligands 1,4,7-tris(2-hydroxybenzyl)-1,4,7-triazacyclononane (H_3L^1) and 1,4,7-tris(3-tert-butyl-2-hydroxybenzyl)-1,4,7-triazacyclononane (H_3L^2). Crystal Structures of $[HL^1Cu^{II}]$ and $[L^2Fe^{III}]acacH$." *Inorg. Chem.* **1990**, 29, 938.
- 39 (a) Jazdzewski, B. A.; Holland, P. L.; Pink, M.; Young Jr., V. G.; Spencer, D. J. E.; Tolman, W. B. "Three-Coordinate Copper(II)-Phenolate Complexes." *Inorg. Chem.* **2001**, 40, 6097. (b) Halfen, J. A.; Jazdzewski, B. A.; Mahapatra, S.; Berreau, L. M.; Wilkinson, E. C.; Que Jr., L.; Tolman, W. B. "Synthetic Models of the Inactive Copper(II)-Tyrosinate and Active Copper(II)-Tyrosyl Radical Forms of Galactose and Glyoxal Oxidases." *J. Am. Chem. Soc.* **1997**, 119, 8217.
- 40 (a) Carvalho, S.; Delgado, R.; Drew, M. G. B.; Felix, V. "Dicopper(II) Complexes of a New Di-para-xylyldioxatetraazamacrocyclic and Cascade Species with Dicarboxylate Anions: Thermodynamics and Structural Properties." *Dalton*

- Trans.* **2007**, 2431. (b) VanOrman, C. A.; Reddy, K. V.; Sayre, L. M.; Urbach, F. L. "Dicopper(II) Complexes with Flexible Binucleating Ligands Containing Two Tridentate Coordination Sites." *Polyhedron* **2001**, *20*, 541. (c) Hegg, E. L.; Mortimore, S. H.; Cheung, C. L.; Huyett, J. E.; Powell, D. R.; Burstyn, J. N. "Structure-Reactivity Studies in Copper(II)-Catalyzed Phosphodiester Hydrolysis." *Inorg. Chem.* **1999**, *38*, 2961.
- 41 Petty, M. C. *Langmuir-Blodgett Films*, Cambridge University Press, New York, **1996**, pp. 65.
- 42 (a) Kundu, S.; Datta, A.; Hazra, S. "Growth of a Collapsing Langmuir Monolayer." *Phys. Rev. E: Stat., Nonlinear, Soft Matter Phys.* **2006**, *73*, 051608/051601–051608/051607. (b) Kundu, S.; Datta, A.; Hazra, S. "Effect of Metal Ions on Monolayer Collapses." *Langmuir* **2005**, *21*, 5894.
- 43 Ybert, C.; Lu, W.; Moller, G.; Knobler, C. M. "Kinetics of Phase Transitions in Monolayers: Collapse." *J. Phys.: Condens. Matter* **2002**, *14*, 4753.
- 44 Ries Jr., H. E. "Stable Ridges in a Collapsing Monolayer." *Nature* **1979**, *281*, 287.
- 45 Galvan-Miyoshi, J.; Ramos, S.; Ruiz-Garcia, J.; Castillo, R. "Localized Oscillations and Fraunhofer Diffraction in Crystalline Phases of a Monolayer." *J. Chem. Phys.* **2001**, *115*, 8178.
- 46 *APEX-II*, SMART, SAINT, SAINT-7, SADABS and TWINABS collection and processing programs are distributed by the manufacturer. Bruker AXS, Inc., Madison WI, USA **2001**.
- 47 (a) Sheldrick, H. *SHELX-97 and CELL-NOW*, University of Göttingen, Germany, **1997**. (b) Sheldrick, G. M. *Acta Crystallogr., Sect. A* **2008**, *64*, 112.

Chapter 4

A MODULAR APPROACH TO REDOX-ACTIVE MULTIMETALLIC HYDROPHOBES OF DISCOID TOPOLOGY



CHAPTER 4

**A MODULAR APPROACH TO REDOX-ACTIVE MULTIMETALLIC
HYDROPHOBES OF DISCOID TOPOLOGY**

Frank D. Lesh, Rama Shanmugam, Marco M. Allard, Maurício Lanznaster, Mary Jane Heeg, M. T. Rodgers, Jason M. Shearer, and Cláudio N. Verani*

Reprinted with permission from *Inorg. Chem.* **2010**, *49*, 7226–7228. Copyright 2010 American Chemical Society.

Contributions to this work on my part included the synthetic, spectroscopic, and electrochemical characterizations along with the original draft of the manuscript.

4.1. Introduction

The combination of amphiphilic properties with controllable and tunable behavior of transition metal complexes leads to metal-containing surfactants that exhibit interfacial organization, along with variable geometric, charge, redox, optical, and magnetic properties.¹ Considerable progress has been made toward the understanding of this metal ion/amphiphile cooperativity in supramolecular assemblies.² Potential high-end uses of metallosurfactants include films for optoelectronics³ and logic and memory operations⁴ and micellar luminescence and electron transfer.⁵ Our group is developing precursor metallosurfactants, aiming at the inclusion of ligand- and metal-centered redox activity while preserving the ability to organize into well-ordered films.⁶ The current approach involves incorporation of selected metal ions into a phenolate-based headgroup of a designer amphiphile. The phenolate can then be oxidized into a phenoxyl radical. However, because the stabilization of radicals requires the incorporation of *tert*-butyl

groups into the headgroup, it has been observed that improved redox properties lead to decreased amphiphilic character and vice versa. Therefore, the development of new topologies that can accommodate both properties becomes highly relevant. Recently, we reported on an $[\text{Fe}^{\text{III}}\text{L}^1]$ species ($(\text{L}^1)^{3-}$ is a phenylene-diamine/triphenolate ligand) in which five-coordinate iron(III) centers seem to enhance the formation and reversibility of three consecutive phenolate/phenoxy processes on the cyclic voltammetric time scale.⁷ The related species $[\text{Fe}^{\text{III}}\text{L}^2]$, where $(\text{L}^2)^{3-}$ describes a similar phenanthrolinediamine/trisphenolate ligand, served as a module for $[\text{Fe}^{\text{III}}(\text{L}^2)\text{Cu}^{\text{II}}(\text{Cl})_2(\text{MeOH})]$. The redox responses in this bimetallic species are based on controlled oxidations and reductions of its fundamental components, *i.e.*, the metal centers and the electroactive arms of the ligand.⁸ Specific potentials trigger definite spin ground-state changes, as observed by EPR spectroscopy.

In this chapter, we describe the synthesis and characterization of the tetrametallic $[\text{Fe}^{\text{II}}(\text{Fe}^{\text{III}}\text{L}^2)_3](\text{PF}_6)_2$ (**Figure 4.1**), along with studies on its electrochemical and surfactant properties.

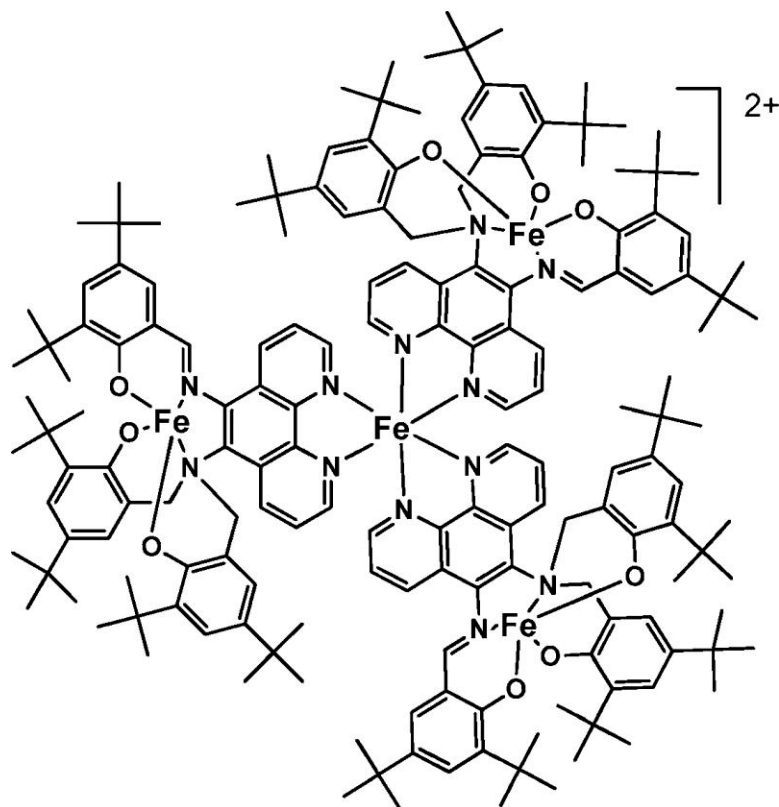


Figure 4.1. Modular discoid species $[\text{Fe}^{\text{II}}(\text{Fe}^{\text{III}}\text{L}^2)_3]^{2+}$.

4.2. Results and Discussion

This discoid molecule (oblate spheroid with $x = y > z$) is a first example that reconciles the use of *tert*-butyl groups to promote redox activity and surfactancy by enhancement of the species hydrophobic character. Thus, it supports the development of a modular approach to discoid multimetallic film precursors. Treatment of $[\text{Fe}^{\text{III}}\text{L}^2]$ with anhydrous FeCl_2 in a 3:1 ratio in methanol and under argon yielded the tetrametallic species $[\text{Fe}^{\text{II}}(\text{Fe}^{\text{III}}\text{L}^2)_3](\text{PF}_6)_2$ as a homogeneous microcrystalline solid. In spite of the apparent simplicity of the preparation, several attempts under aerobic conditions led to the formation of undesirable side products. This compound, as presently synthesized, was characterized by means of exact ESI mass spectrometry and elemental analysis.⁹ Further characterization was obtained by comparative infrared, UV–visible, and XANES/EXAFS

spectroscopies and electrochemical data between $[\text{Fe}^{\text{II}}(\text{Fe}^{\text{III}}\text{L}^2)_3](\text{PF}_6)_2$, the module $[\text{Fe}^{\text{III}}\text{L}^2]$, and the compound $[\text{Fe}^{\text{II}}(\text{phen})_3](\text{PF}_6)_2$ (phen = 1,10-phenanthroline). The exact ESI-MS for the tetrametallic species (2802.3976 Da) in methanol exhibits peaks at $m/z = 1401.69970$ related to the bivalent cation $[\text{Fe}^{\text{II}}(\text{Fe}^{\text{III}}\text{L}^2)_3]^{+2}$ and 916.49504 associated with the module $[(\text{Fe}^{\text{III}}\text{L}^2)_3 + \text{H}^+]^+$. Comparison of the features present in the UV-visible spectra of $[\text{Fe}^{\text{II}}(\text{Fe}^{\text{III}}\text{L}^2)_3](\text{PF}_6)_2$, $[\text{Fe}^{\text{III}}\text{L}^2]$, and $[\text{Fe}^{\text{II}}(\text{phen})_3](\text{PF}_6)_2$ in CH_2Cl_2 also permits one to ascertain the nature of the multimetallic species. The module $[\text{Fe}^{\text{III}}\text{L}^2]$ shows the expected intraligand $\pi \rightarrow \pi^*$ and $\text{N} \rightarrow \text{Fe}$ charge transfer bands at 281 and 333 nm (115 900 and 69 000 $\text{L mol}^{-1}\text{cm}^{-1}$), respectively. The phenolate-to-metal charge transfer bands¹⁰ ($p\pi \rightarrow d\sigma^*$ and $p\pi \rightarrow d\pi^*$) appear at 411 and 463 nm (both at 27 500 $\text{L mol}^{-1}\text{cm}^{-1}$), thus unusually close to each other. This proximity is attributed to the five-coordination of the metal. The $[\text{Fe}^{\text{II}}(\text{Fe}^{\text{III}}\text{L}^2)_3](\text{PF}_6)_2$ species presents the analogous processes at 279 (249 700), 336 (96 000), and 486 nm (50 300 $\text{L mol}^{-1}\text{cm}^{-1}$), along with a new band at 525 nm (51 700 $\text{L mol}^{-1}\text{cm}^{-1}$). This new process is comparable to the metal-to-phenanthroline charge transfer present in $[\text{Fe}^{\text{II}}(\text{phen})_3](\text{PF}_6)_2$ at 511 nm (9390 $\text{L mol}^{-1}\text{cm}^{-1}$), thus indicating the presence of all expected chromophores.¹¹ The IR spectrum of $[\text{Fe}^{\text{II}}(\text{Fe}^{\text{III}}\text{L}^2)_3](\text{PF}_6)_2$ presents peaks at 2870–2960 and 1605 cm^{-1} associated, respectively, with the *tert*-butyl and C=N groups in the module $[\text{Fe}^{\text{III}}\text{L}^2]$. Peaks associated with the counterion PF_6^- appear at 840 cm^{-1} . An equally prominent peak related to the out-of-plane deformation of the phenanthroline rings and enhanced through coordination is observed at 558 cm^{-1} . The XANES/EXAFS spectra of $[\text{Fe}^{\text{II}}(\text{Fe}^{\text{III}}\text{L}^2)_3](\text{PF}_6)_2$ and the module $[\text{Fe}^{\text{III}}\text{L}^2]$ are compared in **Figure 4.2**.

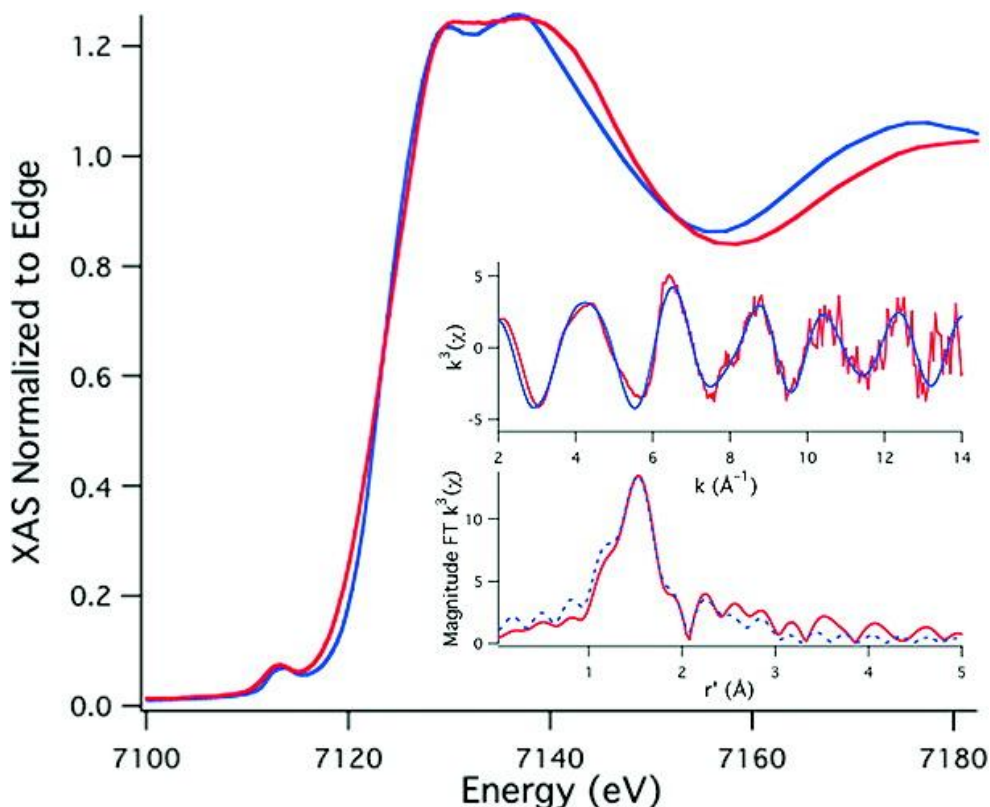


Figure 4.2. XANES region of the Fe K-edge XAS for $[\text{Fe}^{\text{II}}(\text{Fe}^{\text{III}}\text{L}^2)_3](\text{PF}_6)_2$ (red) and $[\text{Fe}^{\text{III}}\text{L}^2]$ (blue). Inset: EXAFS region for $[\text{Fe}^{\text{II}}(\text{Fe}^{\text{III}}\text{L}^2)_3](\text{PF}_6)_2$. Data (red) and simulation (blue). Shell 1 (Fe–O): $n = 2$, $r = 1.839(6)$ Å, $\sigma^2 = 0.0048(13)$ Å². Shell 2 (Fe–N): $n = 3$, $r = 1.960(3)$ Å, $\sigma^2 = 0.0010(5)$ Å². Shell 3 (Fe–N): $n = 1$, $r = 2.104(13)$ Å, $\sigma^2 = 0.0030(2)$ Å². Shell 4 (Fe–C): $n = 4$, $r = 2.919(6)$ Å, $\sigma^2 = 0.0053(8)$ Å². $E^\circ = 7128.7$ eV. $\epsilon^2 = 0.63$.

The edge position of $[\text{Fe}^{\text{II}}(\text{Fe}^{\text{III}}\text{L}^2)_3](\text{PF}_6)_2$ occurs at a slightly lower energy than that of $[\text{Fe}^{\text{III}}\text{L}^2]$ (7121.8(3) vs 7122.2(2) eV). A reduction from Fe(III) to Fe(II) should result in a lowering of the edge energy by $\sim 2\text{--}3$ eV. This small shift in edge energy is, therefore, consistent with the presence of both trivalent and bivalent oxidation states, where the Fe(III) state is predominant. A pre-edge peak in the XANES of $[\text{Fe}^{\text{II}}(\text{Fe}^{\text{III}}\text{L}^2)_3](\text{PF}_6)_2$ occurs at 7113.0(1) eV, which corresponds to the parity-forbidden Fe(1s \rightarrow 3d) transitions and has an area of 0.16(1) eV relative to the edge. These transitions gain intensity in noncentrosymmetric coordination environments through a dipole mechanism and are thus more intense in five- vs six-coordinate environments.¹²

The Fe(1s \rightarrow 3d) transition of $[\text{Fe}^{\text{III}}\text{L}^2]$ at 7113.2(1) eV has an area of 0.21(1) eV relative to the edge. Therefore, the average iron coordination environment is slightly more symmetric in $[\text{Fe}^{\text{II}}(\text{Fe}^{\text{III}}\text{L}^2)_3](\text{PF}_6)_2$ than in $[\text{Fe}^{\text{III}}\text{L}^2]$, suggesting that the multimetallic species contains both five- and six-coordinate iron centers. The EXAFS region of $[\text{Fe}^{\text{II}}(\text{Fe}^{\text{III}}\text{L}^2)_3](\text{PF}_6)_2$ was best modeled with iron surrounded by nitrogen and oxygen donors. Three shells are resolvable: one shell containing two short Fe–O scatterers at 1.84 Å, one shell containing three Fe–N or Fe–O scatterers at 1.96 Å, and one shell containing a single long Fe–N scatterer at 2.10 Å. This is consistent with the average iron environment predicted for $[\text{Fe}^{\text{II}}(\text{Fe}^{\text{III}}\text{L}^2)_3](\text{PF}_6)_2$.

In spite of several attempts, the determination of the molecular structure for $[\text{Fe}^{\text{II}}(\text{Fe}^{\text{III}}\text{L}^2)_3](\text{PF}_6)_2$ via X-ray diffraction was not possible. The structure of the molecule $[\text{Fe}^{\text{III}}\text{L}^2]$ was published recently,⁸ but attempts to use it as a starting point for calculations has proven to be nontrivial due to the large number of unpaired electrons at the iron centers.

Therefore, we obtained a crystal structure for the analogous compound $[\text{Ga}^{\text{III}}\text{L}^2]$.¹³ The ORTEP representation is shown in **Figure 4.3(a)** with selected bond lengths. The similar nature of the gallium and iron structures is inferred by their neutral character, the identity of the ligand showing a monosubstituted amine N4 with a single phenolate appended, whereas the vicinal amine N1 exhibits two of these groups. Furthermore, both species display a short bond length characteristic of a C=N imine group and a metal center that is five-coordinated in a N_2O_3 environment. On the basis of these similarities, a model $[\text{Ga}^{\text{III}}(\text{Ga}^{\text{III}}\text{L}^2)_3]^{3+}$ was built and its geometry minimized using the molecular mechanics UFF force field¹⁴ available in the Gaussian 03 software package.¹⁵ This model

describes one possible isomer, shown in **Figure 4.3(b)**, in which one module displays the singly appended phenolate pointing upward while the two other modules point downward. Although several isomers are possible,¹⁶ the one displayed is more stable by *ca.* 20 kcal/mol when compared to three other calculated geometries.

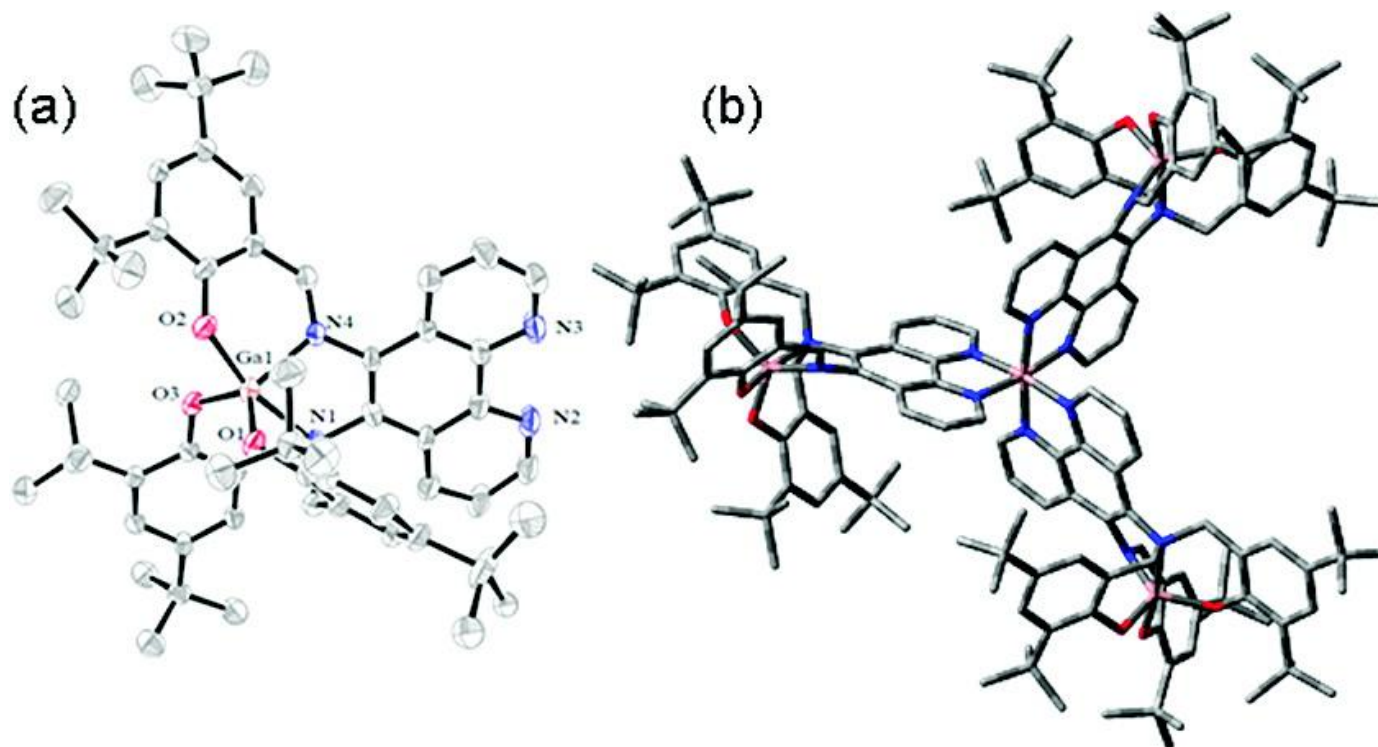


Figure 4.3. (a) ORTEP for [GaL²], Ga-O(3) = 1.828(3), Ga-O(1) = 1.828(3), Ga-O(2) = 1.899(3), Ga-N(4) = 1.975(4), Ga-N(1) = 2.266(4) Å. (b) MM-UFF model for [Ga(GaL²)₃]²⁺.

In all cases, the models provide evidence for the discoid nature of the multimetallic species. On the basis of the similar ionic radii of gallium(III) (0.76 Å) and iron_{1s}(II) (0.75 Å), as well as in the already established similarities between the complexes of both metals coordinated to these pentadentate ligands, an estimated geometric radius from the central metal to the periphery is calculated to lie between 9.0 and 11.0 Å. Examination of the positions occupied by the *tert*-butyl groups attached to each phenolate reveals that the majority of these groups point outward conferring an enhanced hydrophobic cushioning which prevents the charged and hydrophilic discoid core from sinking into water and leads to a differentiated topology. The redox responsivity of $[\text{Fe}^{\text{II}}(\text{Fe}^{\text{III}}\text{L}^2)_3](\text{PF}_6)_2$ was assessed by cyclic voltammetry (CV, vs Fc^+/Fc). Comparison with the $[\text{Fe}^{\text{III}}\text{L}^2]$ module and with $[\text{Fe}^{\text{II}}(\text{phen})_3](\text{PF}_6)_2$ allowed for attributions to the origin of the observed processes (**Figure 4.4**).

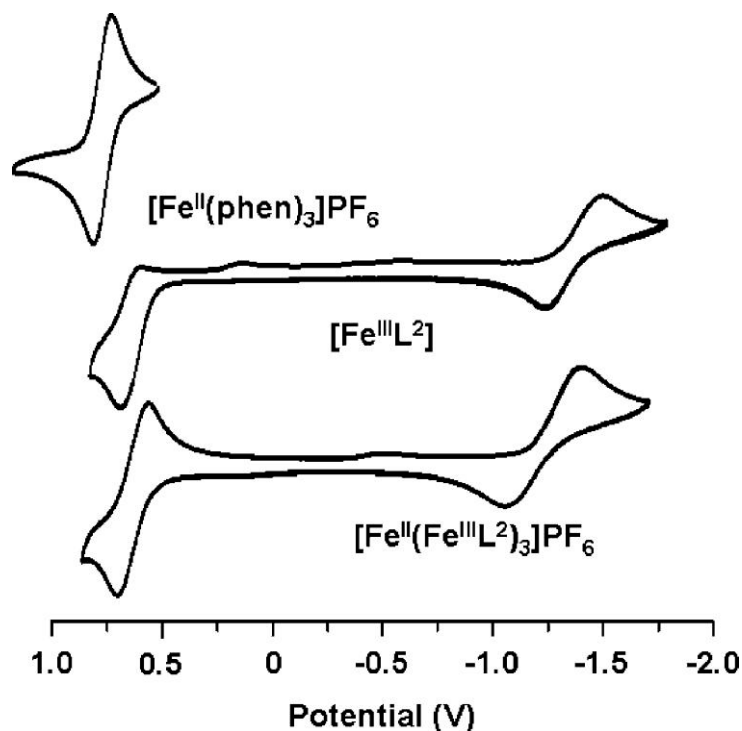


Figure 4.4. CVs of $[\text{Fe}^{\text{II}}(\text{phen})_3](\text{PF}_6)_2$ (top), $[\text{Fe}^{\text{III}}\text{L}^2]$ (middle), and $[\text{Fe}^{\text{II}}(\text{Fe}^{\text{III}}\text{L}^2)_3](\text{PF}_6)_2$ (bottom) in dichloromethane, TBAPF_6 vs Fc^+/Fc .

The CVs for the multimetallic species and the module display a cathodic wave for the process ascribed to the $\text{Fe}^{\text{III}}/\text{Fe}^{\text{II}}$ couple. This process is anodically shifted in the tetrametallic species to $E_{1/2} = -1.24$ V and is less reversible ($\Delta E_p = 0.33$ V; $|I_{pc}/I_{pa}| = 1.8$) than that of the module at $E_{1/2} = -1.37$ ($\Delta E_p = 0.25$ V; $|I_{pc}/I_{pa}| = 1.4$). The phenolate/phenoxy oxidative process occurs for both $[\text{Fe}^{\text{II}}(\text{Fe}^{\text{III}}\text{L}^2)_3](\text{PF}_6)_2$ and $[\text{Fe}^{\text{III}}\text{L}^2]$ at *ca.* $E_{1/2} = 0.64$ V. Interestingly, an enhanced reversibility is observed in the multimetallic complex, as indicated by $|I_{pc}/I_{pa}| = 0.8$, compared to a value of 0.2 observed for the module. This profile might be associated with—or at least influenced by—the $\text{Fe}(\text{II})$ –phenanthroline core, because the metal-centered process for the unsubstituted $[\text{Fe}^{\text{II}}(\text{phen})_3](\text{PF}_6)_2$ appears at $E_{1/2} = 0.77$ V ($\Delta E_p = 0.08$ V; $|I_{pc}/I_{pa}| = 1.1$). To evaluate the efficacy of the discoid design to act in hydrophobic precursors for film formation, compression isotherms plotted as surface pressure (mN/m) vs average molecular area (\AA^2) were recorded at the air/water interface in a Langmuir–Blodgett trough at 23 °C, as shown in **Figure 4.5(a)**. The quality of the films was monitored during compression using Brewster angle microscopy (BAM), **Figure 4.5(b)**. The molecules of $[\text{Fe}^{\text{II}}(\text{Fe}^{\text{III}}\text{L}^2)_3](\text{PF}_6)_2$ start to interact with each other at the subphase at *ca.* 320 $\text{\AA}^2/\text{molecule}$. The BAM images display a highly homogeneous film from 10 to *ca.* 40 mN/m, when a decrease in the slope of the isotherm coincides with the formation of linearly oriented Newton rings,¹⁷ suggestive of a formal constant pressure collapse mechanism.¹⁸ The average limiting area per molecule is 280 $\text{\AA}^2/\text{molecule}$, thus with a radius of *ca.* 9.5 \AA , in excellent agreement with the estimated radius of the $[\text{Ga}^{\text{III}}(\text{Ga}^{\text{III}}\text{L}^2)_3]^{3+}$ model.

Methods and materials used in this chapter are listed in **Section 2.1 of Chapter 2**. All synthetic details, X-ray structural determinations, molecular mechanics calculations, ESI-MS exact mass, infrared, UV-visible spectra, and electrochemical data can be found in **Appendix B**.

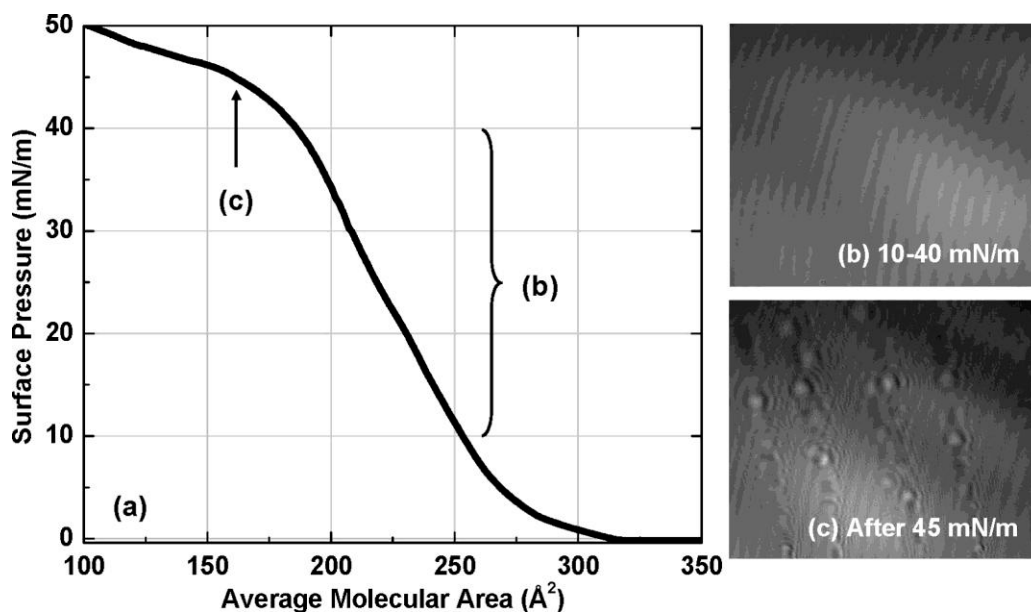


Figure 4.5. $[\text{Fe}^{\text{II}}(\text{Fe}^{\text{III}}\text{L}^2)_3](\text{PF}_6)_2$ at the air/water interface: (a) isothermal compression. Selected BAM images at (b) 10–40 mN/m and (c) collapse.

4.3. Conclusions

In summary, we have reported on the tetrametallic complex $[\text{Fe}^{\text{II}}(\text{Fe}^{\text{III}}\text{L}^2)_3](\text{PF}_6)_2$ of discoid topology. The presence of metallic centers and ligand moieties such as phenolates and coordinated phenanthrolines extends the redox capabilities of this species. Along with its hydrophobic character, this species is a strong candidate for the formation of redox-responsive monolayer films. To the best of our knowledge, this is the first example of a discoid tetrametallic species in which the presence of *tert*-butyl groups concomitantly enforces redox activity *and* surfactancy. This result points to a general strategy in which a modular approach can be used to develop redox-active homo- and

heterometallic film precursors of discoid topology. The synthetic approach and film transfer onto solid substrates are under investigation in our laboratories.

4.4. References

- 1 (a) Bodenthin, Y.; Pietsch, U.; Moehwald, H.; Kurth, D. G. "Inducing Spin Crossover in Metallo-Supramolecular Polyelectrolytes through an Amphiphilic Phase Transition." *J. Am. Chem. Soc.* **2005**, *127*, 3110. (b) Talham, D. R. "Conducting and Magnetic Langmuir–Blodgett Films." *Chem. Rev.* **2004**, *104*, 5479.
- 2 (a) Hoogenboom, R.; Fournier, D.; Schubert, U. S. "Asymmetrical Supramolecular Interactions as Basis for Complex Responsive Macromolecular Architectures." *Chem. Commun.* **2008**, 155. (b) Verani, C. "Efforts Toward Mono and Multimetallic Redox-Active Amphiphiles." *McGraw-Hill Yearb. Sci. Technol.* **2010**, 142.
- 3 Zhang, J.; Chu, B. W.-K.; Chu, Z. N.; Yam, V. W.-W. "Synthesis, Characterization, Langmuir–Blodgett Film-Forming Property, and Second-Order Nonlinear Optical Study of Rhenium(I) and Ruthenium(II) Diimine Complexes." *Organometallics* **2007**, *26*, 5423.
- 4 (a) Wassel, R. A.; Gorman, C. B. "Molecular Electronics: Establishing the Molecular Basis for Molecular Electronics." *Angew. Chem., Int. Ed.* **2004**, *43*, 5120. (b) Low, P. J. "Metal Complexes in Molecular Electronics: Progress and Possibilities." *Dalton Trans* **2005**, 2821.
- 5 (a) Guerrero-Martinez, A.; Vida, Y.; Dominguez-Gutierrez, D.; Albuquerque, R. Q.; De Cola, L. "Tuning Emission Properties of Iridium and Ruthenium Metallosurfactants in Micellar Systems." *Inorg. Chem.* **2008**, *47*, 9131. (b) Wang, K.; Haga, M.-A.; Monjushiro, H.; Akiba, M.; Sasaki, Y. "Luminescent Langmuir–

- Blodgett Films of Platinum(II) Complex $[\text{Pt}(\text{L}^{18})\text{Cl}](\text{PF}_6)$ ($\text{L}^{18} = 2,6\text{-Bis}(1\text{-octadecylbenzimidazol-2-yl})\text{pyridine}$).” *Inorg. Chem.* **2000**, *39*, 4022.
- 6 (a) Hindo, S. S.; Shakya, R.; Rannulu, N. S.; Allard, M. M.; Heeg, M. J.; Rodgers, M. T.; da Rocha, S. R. P.; Verani, C. N. “Synthesis, Redox, and Amphiphilic Properties of Responsive Salicylaldehyde-Copper(II) Soft Materials.” *Inorg. Chem.* **2008**, *47*, 3119. (b) Shakya, R.; Imbert, C.; Hratchian, H. P.; Lanznaster, M.; Heeg, M. J.; McGarvey, B. R.; Allard, M.; Schlegel, H. B.; Verani, C. N. “Structural, Spectroscopic, and Electrochemical Behavior of Trans-Phenolato Cobalt(III) Complexes of Asymmetric NN'O Ligands as Archetypes for Metallomesogens.” *Dalton Trans.* **2006**, 2517.
- 7 Lanznaster, M.; Hratchian, H. P.; Heeg, M. J.; Hryhorczuk, L. M.; McGarvey, B. R.; Schlegel, H. B.; Verani, C. N. “Structural and Electronic Behavior of Unprecedented Five-Coordinate Iron(III) and Gallium(III) Complexes with a New Phenol-Rich Electroactive Ligand.” *Inorg. Chem.* **2006**, *45*, 955.
- 8 Lanznaster, M.; Heeg, M. J.; Yee, G. T.; McGarvey, B. R.; Verani, C. N. “Design of Molecular Scaffolds Based on Unusual Geometries for Magnetic Modulation of Spin-Diverse Complexes with Selective Redox Response.” *Inorg. Chem.* **2007**, *46*, 72.
- 9 Elemental analyses gave lower than expected carbon contents for $[\text{Fe}^{\text{II}}(\text{Fe}^{\text{III}}\text{L}^2)_3](\text{PF}_6)_2$. Best results were obtained for $[\text{Fe}^{\text{II}}(\text{Fe}^{\text{III}}\text{L}^2)_3](\text{ClO}_4)_2$ ($\text{C}_{171}\text{H}_{213}\text{Cl}_2\text{Fe}_4\text{N}_{12}\text{O}_{17}$, MW = 3002.88) with C (calcd/exptl), 68.40/68.63; H, 7.15/7.27; N, 5.60/5.68.

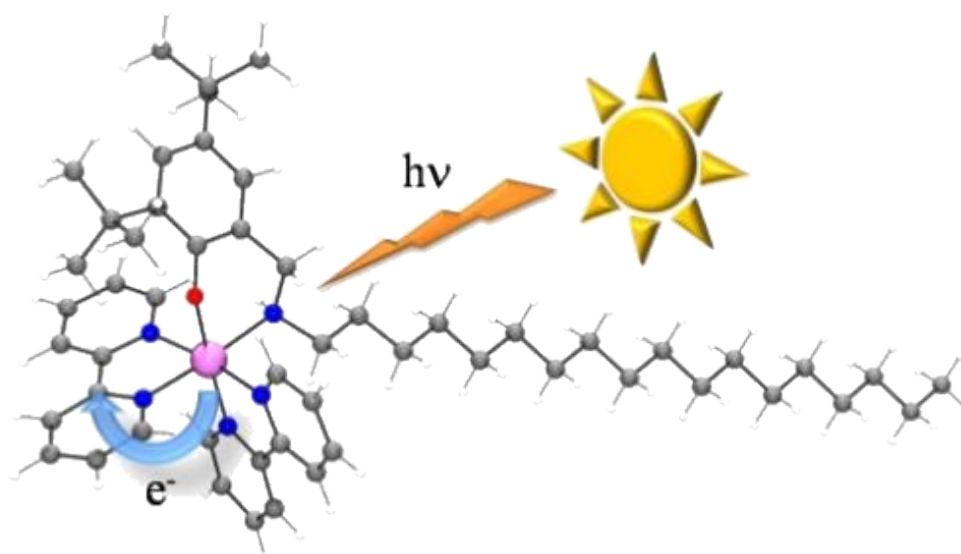
- 10 Davis, M. I.; Orville, A. M.; Neese, F.; Zaleski, J. M.; Lipscomb, J. D.; Solomon, E. I. "Spectroscopic and Electronic Structure Studies of Protocatechuate 3,4-Dioxygenase: Nature of Tyrosinate-Fe(III) Bonds and Their Contribution to Reactivity." *J. Am. Chem. Soc.* **2002**, *124*, 602.
- 11 All expected chromophores: Braterman, P. S.; Song, J.-I.; Peacock, R. D. "Electronic Absorption Spectra of the Iron(II) Complexes of 2,2'-bipyridine, 2,2'-bipyrimidine, 1,10-phenanthroline, and 2,2':6',2"-terpyridine and Their Reduction Products." *Inorg. Chem.* **1992**, *31*, 555.
- 12 (a) Roe, A. L.; Schneider, D. J.; Mayer, R. J.; Pyrz, J. W.; Widom, J. L.; Que, L., Jr. "X-ray Absorption Spectroscopy of Iron-Tyrosinate Proteins." *J. Am. Chem. Soc.* **1984**, *106*, 1676. (b) Westre, T. E.; Kennepohl, P.; DeWitt, J. G.; Hedman, B.; Hodgson, K. O.; Solomon, E. I. "A Multiplet Analysis of Fe K-Edge 1s \rightarrow 3d Pre-Edge Features of Iron Complexes." *J. Am. Chem. Soc.* **1997**, *119*, 6297.
- 13 [Ga^{III}L²]: C₆₃H₈₀GaN₇O₃, $M = 1053.06$ Bruker P4/CCD (Mo/graphite), $T = 208(2)$ K, triclinic, $P(-1)$, $a = 13.5969(18)$, $b = 14.763(2)$, $c = 15.893(2)\text{\AA}$, $\alpha = 113.395(4)$, $\beta = 92.907(4)$, $\gamma = 93.361(4)^\circ$, $V = 2913.5(7)\text{\AA}^3$, $Z = 2$, $D_{\text{calc}} = 1.200\text{ Mg/m}^3$, abs. coeff = 0.522 mm^{-1} , 15444 refls collected, 12319 unique [R(int) = 0.042], $\theta = 2.04\text{--}28.31^\circ$, $R1 = 0.0754$, $wR2 = 0.1707$, GOF $F^2 = 0.896$ [$I > 2\sigma(I)$].
- 14 Rappé, A. K.; Casewit, C. J.; Colwell, K. S.; Goddard, W. A., III; Skiff, W. M. "UFF, A Full Periodic Table Force Field for Molecular Mechanics and Molecular Dynamics Simulations." *J. Am. Chem. Soc.* **1992**, *114*, 10024.
- 15 Frisch, M. J.; Trucks, G.W.; Schlegel, H. B.; Scuseria, G. E.; Robb, M. A.; Cheeseman, J. R.; Montgomery, J. A.; Vreven, T.; Kudin, K. N.; Burant, J. C.;

- Millam, J.M.; Iyengar, S. S.; Tomasi, J.; Barone, V.; Mennucci, B.; Cossi, M.; Scalmani, G.; Rega, N.; Petersson, G. A.; Nakatsuji, H.; Hada, M.; Ehara, M.; Toyota, K.; Fukuda, R.; Hasegawa, J.; Ishida, M.; Nakajima, T.; Honda, Y.; Kitao, O.; Nakai, H.; Klene, M.; Li, X.; Knox, J. E.; Hratchian, H. P.; Cross, J. B.; Bakken, V.; Adamo, C.; Jaramillo, J.; Gomperts, R.; Stratmann, R. E.; Yazyev, O.; Austin, A. J.; Cammi, R.; Pomelli, C.; Ochterski, J. W.; Ayala, P. Y.; Morokuma, K.; Voth, G. A.; Salvador, P.; Dannenberg, J. J.; Zakrzewski, V. G.; Dapprich, S.; Daniels, A. D.; Strain, M. C.; Farkas, O.; Malick, D. K.; Rabuck, A. D.; Raghavachari, K.; Foresman, J. B.; Ortiz, J. V.; Cui, Q.; Baboul, A. G.; Clifford, S.; Cioslowski, J.; Stefanov, B. B.; Liu, G.; Liashenko, A.; Piskorz, P.; Komaromi, I.; Martin, R. L.; Fox, D. J.; Keith, T.; Al-Laham, M. A.; Peng, C. Y.; Nanayakkara, A.; Challacombe, M.; Gill, P. M. W.; Johnson, B.; Chen, W.; Wong, M. W.; Gonzalez, C.; Pople, J. A. *03, GAUSSIAN*, Gaussian, Inc., C. T. Wallingford, **2003**.
- 16 Bergman, S. D.; Frantz, R.; Gut, D.; Kol, M.; Lacour, J. "Effective Chiral Recognition Among Ions in Polar Media." *Chem. Commun.* **2006**, 850.
- 17 Galvan-Miyoshi, J.; Ramos, S.; Ruiz-Garcia, J.; Castillo, R. "Localized Oscillations and Fraunhofer Diffraction in Crystalline Phases of a Monolayer." *J. Chem. Phys.* **2001**, 115, 8178.

- 18 (a) Kundu, S.; Datta, A.; Hazra, S. "Effect of Metal Ions on Monolayer Collapses." *Langmuir* **2005**, *21*, 5894. (b) Kundu, S.; Datta, A.; Hazra, S. "Growth of a Collapsing Langmuir Monolayer." *Phys. Rev. E* **2006**, *73*, 051608.

Chapter 5

INVESTIGATION OF THE ELECTRONIC, PHOTOSUBSTITUTION, REDOX, AND SURFACE PROPERTIES OF NEW RUTHENIUM(II)-CONTAINING AMPHIPHILES



CHAPTER 5

INVESTIGATION OF THE ELECTRONIC, PHOTOSUBSTITUTION, REDOX,
AND SURFACE PROPERTIES OF NEW RUTHENIUM(II)-CONTAINING
AMPHIPHILES

Frank D. Lesh, Marco M. Allard, Rama Shanmugam, Lew M. Hryhorczuk,
John F. Endicott, H. Bernhard Schlegel, and Cláudio N. Verani*

Reprinted with permission from *Inorg. Chem.* **2011**, *50*, 969–977. Copyright 2011
American Chemical Society. This article figured among the “top accessed” papers in
March 2011 for *Inorganic Chemistry*.

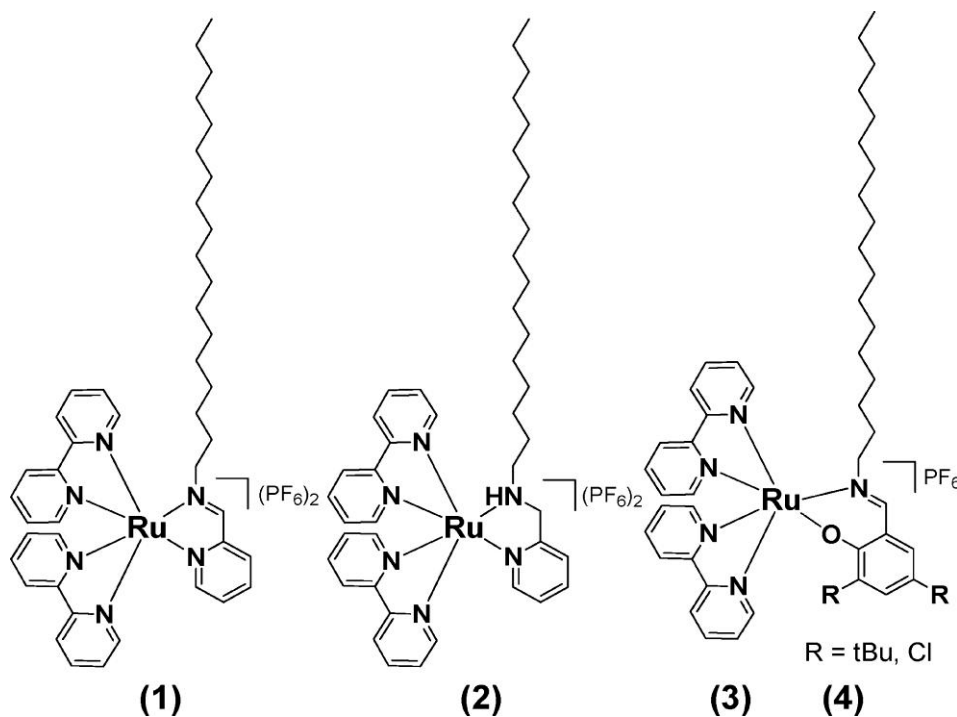
Contributions to this work on my part included the synthetic, spectroscopic, and
electrochemical characterizations along with the original draft of the manuscript.

5.1. Introduction

Metallosurfactants comprise a new class of coordination compounds that combine metal properties such as geometric control, redox, optical, and magnetic behavior^{1,2} with amphiphilicity.³ These materials are increasingly relevant for high-end applications involving optoelectronics,⁴ logic and memory operations,^{5,6} and micellar luminescence and electron transfer.^{7,8} Therefore, the integration of amphiphilic properties to antennae constituents is a relevant step toward the development of metallosurfactant precursors for photoresponsive modular films for artificial photosynthesis. In this regard, ruthenium bipyridyl complexes such as the $[\text{Ru}^{\text{II}}(\text{bpy})_2]^{2+}$ have received considerable attention because of their superior photosensitizing properties and consequent relevance toward water oxidation.

In recent years, our group has spearheaded a comprehensive effort toward redox active precursors for Langmuir–Blodgett films. We have established a wide range of differentiated scaffold designs,^{9,10} studied redox and collapse mechanisms,¹¹ and demonstrated how coordination and protonation preferences dictate amphiphilic behavior.¹²

We have envisioned the integration of the photoresponsive $[\text{Ru}^{\text{II}}(\text{bpy})_2]^{2+}$ to bidentate amphiphilic ligands containing aminomethyl-pyridine and -phenol headgroups, and in this article, we evaluate a new family of asymmetric $[\text{LRu}(\text{bpy})_2]^{+/2+}$ metalloamphiphiles, namely, $[(\text{L}^{\text{PyI}})\text{Ru}^{\text{II}}(\text{bpy})_2](\text{PF}_6)_2$ (**1**), $[(\text{L}^{\text{PyA}})\text{Ru}^{\text{II}}(\text{bpy})_2](\text{PF}_6)_2$ (**2**), $[(\text{L}^{\text{PhBu}})\text{Ru}^{\text{II}}(\text{bpy})_2](\text{PF}_6)$ (**3**), and $[(\text{L}^{\text{PhCl}})\text{Ru}^{\text{II}}(\text{bpy})_2](\text{PF}_6)$ (**4**) (Scheme 5.1), where *Py* = pyridine and *Ph* = phenolate, *I* = imine and *A* = amine, and *Bu* or *Cl* indicates the *ortho*- and *para*-substituted *tert*-butyl or chloro groups in the phenolate complexes.



Scheme 5.1. Series of Pyridine- and Phenolate-Based Ruthenium(II)-Containing Amphiphiles 1–4

We interrogate the electrochemical properties of these systems to evaluate the nature of the redox processes, the optical and electronic properties to evaluate the photostability and excitability (emission) of these species, and the amphiphilic properties to evaluate the potential for formation of ordered LB films. In particular, we evaluate (a) how the presence of C18 alkyl groups allow for formation of high-quality Langmuir films at the air/water interface, (b) the difference in related species (imino versus amino) for L^{Py} and (*tert*-butyl versus chloro) for L^{Ph} , and (c) whether density functional theory (DFT) calculations can model and account for the observed redox responses. These concerns are addressed using a host of synthetic, spectrometric, spectroscopic, and computational- and surface-dedicated methods, and we attempt to correlate these properties to assess the viability of these species as precursors for photoresponsive LB films.

5.2. Results and Discussion

5.2.1. Syntheses and Characterizations. Design Rationale. The rationale behind our design strategy involves the combination of distinct donor sets built into photoresponsive $[Ru^{II}(bpy)_2]^{2+}$ moieties by means of bidentate chelating ligands containing hydrophobic alkyl tails. This design is based on our previously described pyridyl-¹³⁻¹⁵ and phenol-based¹⁶ ligands coordinated to the Cu(II) dication and bears resemblance to some of the work by Yam et al.^{4,17,18} and Keyes et al.^{19,20} We aim at extending efforts toward the relatively more inert bivalent Ru^{2+} ion, targeting the electrochemical redox behavior of species **1-4**, while preserving their amphiphilic and photoresponsive character. Along with the ligands L^{PyI} and L^{PyA} present in **1** and **2**, we recognized phenolato-based complexes as less prevalent. This prompted us to merge

well-established amphiphilic ligands such as HL^{PhBuA} and HL^{PhClA} with $[\text{Ru}(\text{bpy})_2]^{2+}$ to yield the imines **3** and **4** with extended spectroscopic and electrochemical features.¹⁹

5.2.2. Ligands. Condensation of 1-octadecylamine with 2-pyridinecarboxyaldehyde in methanol gave the imine surfactant ligand precursor L^{PyI} which was subsequently reduced in the presence of sodium borohydride to yield the amine ligand precursor L^{PyA} .¹⁵ The phenol-containing surfactant ligands HL^{PhBuA} and HL^{PhClA} were generated from 1-octadecylamine in reaction with 3,5-di-*tert*-butyl-2-hydroxybenzaldehyde or 3,5-dichloro-2-hydroxybenzaldehyde, respectively, followed by reduction to generate the amine precursors.¹⁶ These ligands were characterized by means of ¹H-NMR and infrared (IR) spectroscopies and electrospray ionization (ESI-MS) mass spectrometry with generally 80–85% overall yields.

5.2.3. Complexes. The Ru(II) pyridine complexes **1–2** were obtained by adapting general synthetic approaches for analogous compounds by treatment of equimolar ratios of *cis*- $[\text{Ru}(\text{bpy})_2\text{Cl}_2]\cdot 2\text{H}_2\text{O}$ with the ligands L^{PyI} and L^{PyA} in absolute ethanol.^{4,17} The Ru(II) phenol-containing metallosurfactants **3–4** were achieved upon complexation of the ligands HL^{PhBuA} and HL^{PhClA} with $\text{Ru}(\text{bpy})_2(\text{CF}_3\text{SO}_3)_2$ in isopropanol or acetone, respectively, using triethylamine as a base for phenol deprotonation. Because previous attempts using *cis*- $[\text{Ru}(\text{bpy})_2\text{Cl}_2]\cdot 2\text{H}_2\text{O}$ led to undesirable side products, $\text{Ru}(\text{bpy})_2(\text{CF}_3\text{SO}_3)_2$ was chosen for complexation with the phenolate-containing ligands. This route took advantage of the excellent leaving group properties of the triflate ion. It should be pointed out that compounds **3** and **4** encompass imine ligands formed from in situ oxidation of the parent amine ligands. Such conversion has been reported in similar systems.²¹

All complexes were precipitated with ammonium hexafluorophosphate and purified by column chromatography to yield microcrystalline powders which were characterized by IR, elemental analyses, ESI⁺ mass spectrometry, and electrochemical methods. Elemental analyses for **1–4** were in excellent agreement with theoretical percentages. The ESI⁺ mass analyses of **1** and **2** in methanol indicate the presence of signature peak clusters with general formulas $[(L^{PyX})Ru^{II}(bpy)_2]^{2+}$ and $[(L^{PyX})Ru^{II}(bpy)_2PF_6]^+$. The phenolate species **3** and **4**, being composed of a charged ligand, showed single mass patterns corresponding to the monovalent $[(L^{PhBuI})Ru^{II}(bpy)_2]^+$ ion species. A differential isotopic distribution was observed for **4** due to the contributing chloride isotopes. The pertinent *m/z* peak clusters are shown in **Appendix C, Figures C.5.1–C.5.4** and were simulated in good agreement with their patterns, positions, and isotopic distributions.

Complex formation was further observed by the presence of vibrational modes attributed to the ligand, particularly the characteristic strong C–H stretching contribution of the alkyl chain appearing at 2851–2924 cm⁻¹, and the strong stretch at 840–846 cm⁻¹ (ν_{P-F}) due to the totally symmetric vibration frequency of hexafluorophosphate counterion.

5.2.4. Electronic Absorption Spectroscopy. Electronic absorption spectral data for complexes **1–4** were measured in 10⁻³ to 10⁻⁵ M acetonitrile solutions. **Table 5.1** lists relevant absorption maxima and molar extinction coefficients, and spectra are displayed in **Figure 5.1**. Intense intraligand $\sigma \rightarrow \pi^*$ and $\pi \rightarrow \pi^*$ processes dominate the ultraviolet region of the spectrum for **1–4** with two maxima centered about 245 and 290 nm. Appreciably larger absorptivities have been observed for the phenolato-based **3** and **4**.

Table 5.1. Photophysical Parameters for Complexes 1–4

complex	absorption λ_{abs} (nm)/ ϵ ($\text{L mol}^{-1} \text{cm}^{-1}$) ^a	emission λ_{em} /nm; cm^{-1} ^{b,c}	lifetime τ_0 (ns) ^c
1	239 (17,330); 243 (17,530); 255 (16,030); 287 (44,120); 345 sh (4,460); 432 sh (8,940); 462 (11,080)	715; 13,986	77
2	245 (18,120); 291 (43,850); 342 (7,450); 424 sh (4,540); 472 (7,070)	641; 15,601	193
3	248 (50,260); 294 (59,200); 377 (13,870); 476 sh (7,950); 521 (8,550)		
4	247 (37,910); 295 (60,860); 363 (10,570); 519 (8,380)		

^a Spectra measured in 1.0×10^{-3} M acetonitrile solution. ^b Emission maxima are corrected values. ^c Excitation wavelength at 460 nm for **1** and 470 nm for **2**.

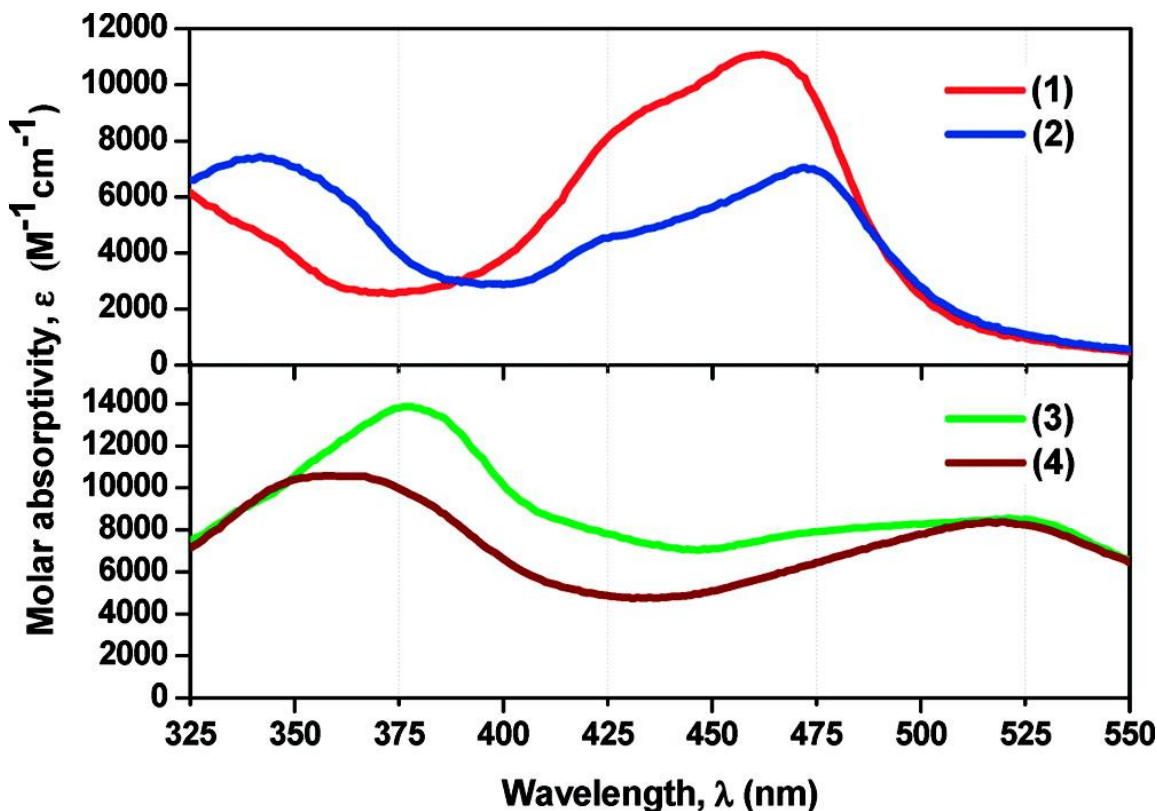


Figure 5.1. UV–visible spectra of pyridyl complexes **1** and **2** (top) and phenolate complexes **3** and **4** (bottom) in acetonitrile, 1.0×10^{-5} M.

Additionally, a third less intense intraligand absorption band is positioned near 342 nm for the pyridyl-based ligand compounds. A shoulder is seen for **1**; the equivalent band for compounds **3** and **4** is red-shifted to the vicinity of 370 nm. Previously Meyer et al.²² have isolated and investigated the related $[\text{Ru}(\text{bipy})_2(\text{AMPy})](\text{ClO}_4)_2$, where (AMPy) is 2-(aminomethyl)-pyridine, analogous to **1**–**2**. A matching absorption profile can be drawn between that species and **2**, allowing to infer that the alkyl chain plays a negligible electronic role to the overall spectroscopic properties of these species. Both the complex $[\text{Ru}(\text{bipy})_2(\text{AMPy})](\text{ClO}_4)_2$ and **2** exhibit an ill-defined shoulder at 425 nm, absent in the pyridyl-imine **1**, where this corresponding shoulder is slightly shifted to 432 nm. On the basis of other related compounds,^{4,17,18,22} we tentatively ascribe this band to a composite

of allowed intraligand $\pi \rightarrow \pi^*$ and $d\pi(\text{Ru}^{\text{II}}) \rightarrow \pi^*(\text{bpy})$ metal-to-ligand charge transfer transitions. The second feature of importance in the visible region is a broad band transition at 462 nm for **1**. This transition band is attributed to the $d\pi(\text{Ru}^{\text{II}}) \rightarrow \pi^*(\text{iminomethylpyridine})$ metal-to-ligand charge transfer transition,^{4,17,18,22} which in the pyridyl-amine **2** is red-shifted to 472 nm with distinctly lower absorptivity. The overall smaller ligand-field strengths of the σ -donating phenolato ligands present comparatively red-shifted, markedly broad low-energy metal-to-ligand charge-transfer (MLCT) or intraligand CT bands for complexes **3** and **4**, relative to **1** and **2** containing the π -acceptor pyridyl ligands. These charge transfer transitions are observed at 519–521 nm ($\epsilon = 8380\text{--}8550 \text{ L mol}^{-1} \text{ cm}^{-1}$) for both **3** and **4**, thus consistent with the behavior observed for other RuN_5O chromophores in similar ligand-donor environments.^{23,24}

5.2.5. Emission Spectroscopy. Room temperature (RT) excitation of **1** and **2** in acetonitrile at $\lambda > 460$ nm induces emission at 715 and 641 nm, respectively (**Figure 5.2**).

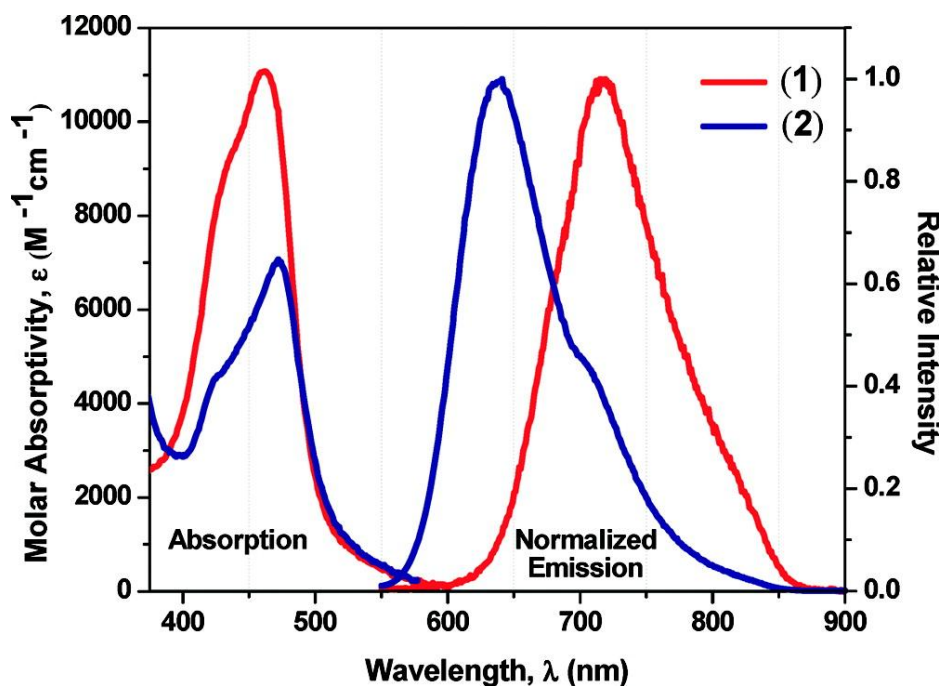


Figure 5.2. Emission spectra of pyridyl complexes **1** and **2**.

The pseudo-Stokes shift for **1** (ca. 7700 cm⁻¹) is about 2100 cm⁻¹ larger than that observed for **2** (ca. 5600 cm⁻¹). Species **2** showed a room-temperature lifetime 2.5 times longer than that of **1**. These observations lead to the inference that the lowest energy triplet MLCT states originate from different chromophores, as will be supported by the electrochemical data and density functional theory (DFT) calculations. Further studies are necessary for a definitive assignment. The phenolate-based **3** and **4** seem non-emissive in the UV–visible range accessible to the detector at room-temperature in acetonitrile. The [Ru(bpy)₂(AMPy)](PF₆)₂ compound was prepared according to the protocol published by Meyer.²² This species is analogous to the above-mentioned pyridyl-amine complex **2** but lacks the octadecyl chain. The response for both compounds is identical in position and intensity.

5.2.6. Photolability Studies. Owing to the commonly observed photoactive nature of ruthenium-containing complexes, we examined the relative photolability of **1–3**. Samples were prepared in dry acetonitrile or dichloromethane to distinguish between the effects of coordinating versus non-coordinating solvents on the apparent photolability of the ruthenium complex. Clear photochemical conversion was observed in complex **2** by the disappearance of peaks at 342 and 472 nm, along with the appearance of a new peak at 427 nm. The observations indicate that **2** was converted into the [(MeCN)₂Ru^{II}(bpy)₂]²⁺ species in acetonitrile (**Figure 5.3**).

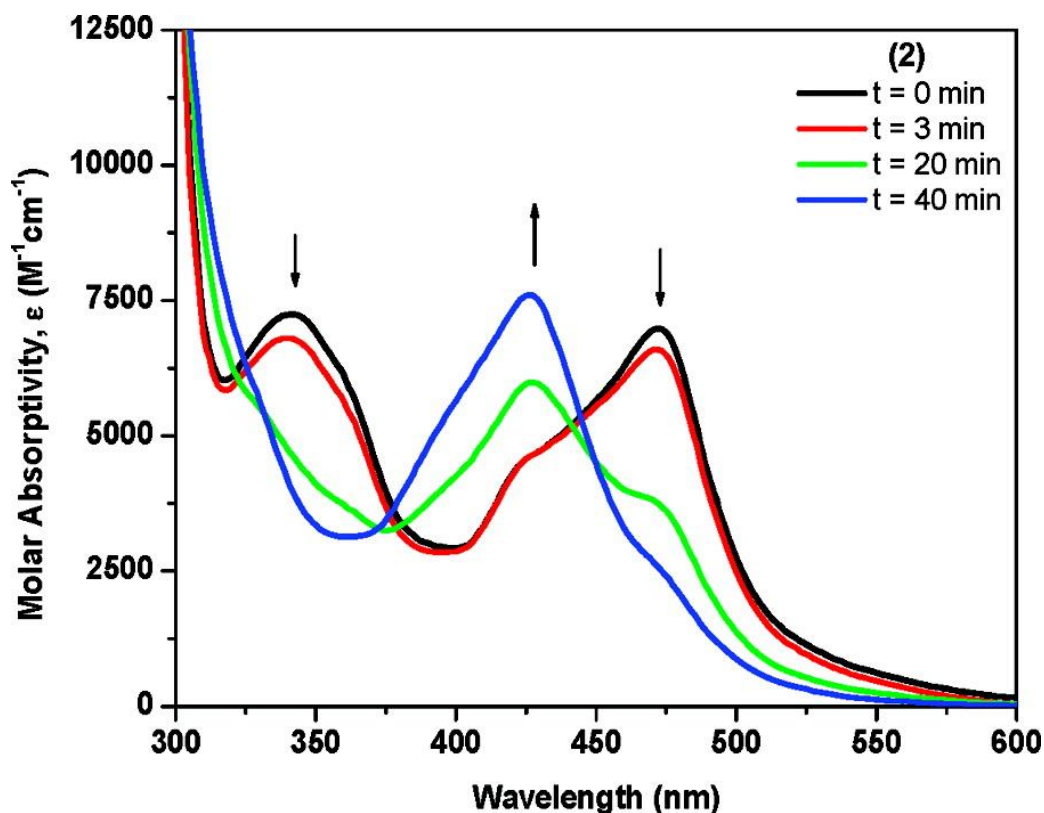


Figure 5.3. UV-visible spectra recorded for photodissociation of **2** in MeCN.

ESI⁺ mass spectrometry supports these results with the appearance of a new peak at $m/z = 248.2$ associated with the dicationic species $[(\text{MeCN})_2\text{Ru}^{\text{II}}(\text{bpy})_2]^{2+}$. Peaks of interest for **2** and $[(\text{MeCN})_2\text{Ru}^{\text{II}}(\text{bpy})_2]^{2+}$ were monitored at different cone voltages (5, 20, and 40 V) and times (0, 3, 20, 40 min). At low cone voltages (5 V), the peak at $m/z = 248.2$ increased over time to 100% intensity. Other relevant peaks appeared after 20 min irradiation at $m/z = 641.2$ for $[(\text{MeCN})_2\text{Ru}^{\text{II}}(\text{bpy})_2 + \text{PF}_6]^+$ and $m/z = 361.6$ for $[\text{L}^{\text{PyA}} + \text{H}]^+$, concomitant to a decreased intensity for $m/z = 919.7$ associated with $[\mathbf{2} - \text{PF}_6]^+$ and $m/z = 387$ from $[\mathbf{2} - (\text{PF}_6)_2]^{2+}$. The $[\mathbf{2} - (\text{PF}_6)]^+$ ion disappears after 40 min of photoirradiation. The observed isotopic fingerprint clusters were in good agreement with the nature and charge of the ions present.

The mass spectroscopic results from the photosubstitution experiments for **1–2** in acetonitrile were plotted as percentage intensity counts versus time (minutes). For **2**, the decrease in percentage abundance of the $[(L^{PyA})Ru^{II}(bpy)_2 + (PF_6)]^+$ species at a cone voltage of 5 V followed concurrent increase in formation for the $[(MeCN)_2Ru^{II}(bpy)_2]^{2+}$ photoproduct (**Appendix C, Figure C.5.5**). A viable photodissociative mechanism has been proposed by Matsuo et al.²⁵ using online electrospray MS, and seems to involve formation of monodentate intermediates of **2** before the ligand L^{PyA} is fully exchanged by coordinating acetonitrile molecules.

When the non-coordinating dichloromethane was used, no significant changes in the UV–visible and ESI⁺ features of **2** were observed (**Appendix C, Figure C.5.6**). Furthermore, both **1** and **3** revealed excellent photostability in acetonitrile and dichloromethane. The stability of **3** is tentatively associated to the strong σ -donor nature of the phenolate moiety.²⁰

5.2.7. Electrochemistry. The cyclic voltammograms (CVs) of **1–4** demonstrate two successive cathodic waves, ranging between $E_{1/2} = -1.78$ and -2.27 V, for the one-electron processes attributed to the classical bipyridine reduction couples (**Figure 5.4**). Complex **1** reveals a third ligand-centered reductive process at $E_{1/2} = -2.22$ V versus Fc^+/Fc . The process observed at $E_{1/2} = -1.63$ V versus Fc^+/Fc is tentatively ascribed to the reduction of the L^{PyI} imine-based ligand, which appears at the least negative potential of all complexes. A single quasi-reversible one-electron metal-centered Ru^{II}/Ru^{III} couple appears at $E_{1/2} = 0.93$ V ($\Delta E_p = 0.08$ V; $|I_{pc}/I_{pa}| = 1.31$) versus Fc^+/Fc . The pyridyl-amine based complex **2** displays an irreversible metal-centered oxidative process credited to the Ru^{II}/Ru^{III} couple, as an anodic wave observed at $E_{1/2} = 0.68$ V versus Fc^+/Fc , where ΔE_p

= 0.12 V. Additionally, this complex shows a ligand-based process due to the oxidation of the ligand from aminomethylpyridine to its imine counterpart. This oxidative dehydrogenation mechanism was investigated by Keene et al.^{22,26,27} The conversion of an amine into an imine is catalyzed by the coordination to the ruthenium ion, and its reversibility seems highly dependent on the scan rate.

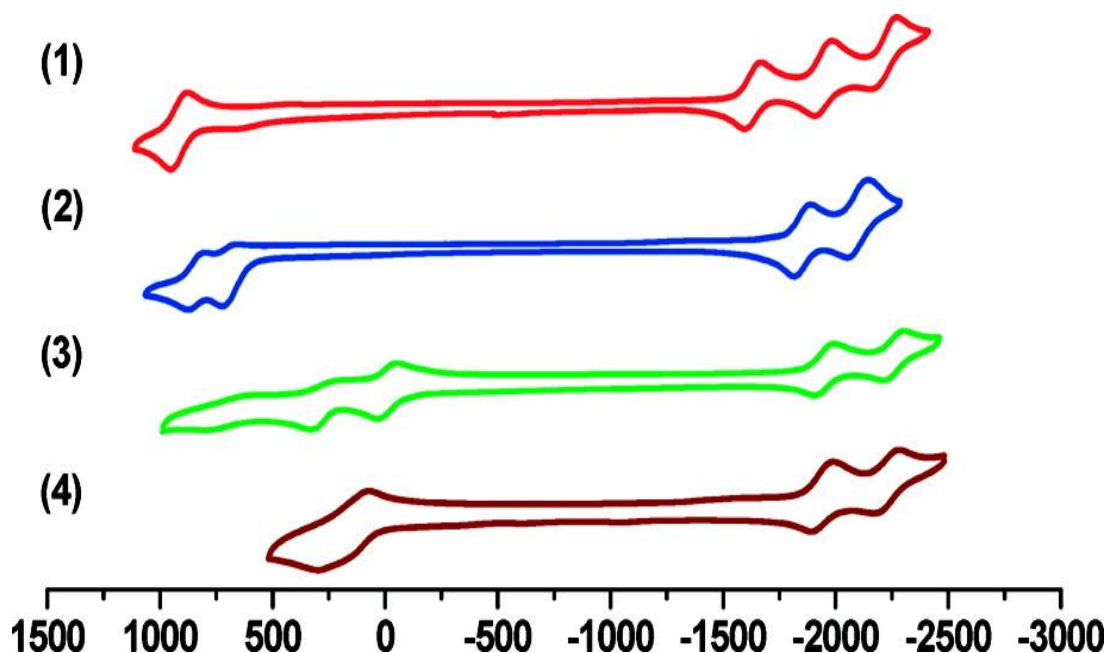


Figure 5.4. CVs of **1–4** in acetonitrile, TBAPF₆, Potential (mV) versus Fc⁺/Fc.

Complexes **3** and **4** present more negative potentials for the reductive bipyridine couples, in contrast to the pyridyl-based complexes **1** and **2**. The averaged reduction potentials are $E_{1/2} = -1.94$ and -2.25 V versus Fc⁺/Fc, and are comparable in reversibility to those containing aminomethylpyridine ligands. The metal-based Ru^{II/III} oxidation couple and the phenolate/phenoxyl radical ligand oxidative processes are associated with the anodic waves observed for complexes **3** and **4**. These waves have not been assigned conclusively and heavy orbital-interaction between redox centers is most likely a major

complicating factor for these oxidative type processes. The chloro-substituted complex **4** displays narrowly overlapping oxidative processes. This indicates some destabilization effects on the phenolate-to-phenoxy oxidation when compared to the *tert*-butyl-substituted complex **3**. **Table 5.2** summarizes the results with potentials reported versus the Fc^+/Fc couple. The correlation of the observed spectroscopic and electrochemical data to the frontier orbitals was explored by means of DFT calculations to understand the origin of these processes.

Table 5.2. Cyclic Voltammetry Data for **1–4**^a

complex	$E_{1/2} (\Delta E_p)$ [V], $ I_{pc}/I_{pa} $	oxidations ^c
	reductions ^b	
1	–1.63 (0.09), 1.57 ; –1.94 (0.09), 1.56 ;	0.93 (0.08), 1.31
2	–2.22 (0.1)	0.68 (0.12); 0.93 (0.08)
3	–1.78 (0.06), 0.66 ; –2.03 (0.06), 0.91	–0.01 (0.08); 0.28 (0.10); 0.71
4	–1.95 (0.09), 1.34 ; –2.27 (0.08), 2.02 –1.93 (0.09), 1.65 ; –2.23 (0.09), 1.51	(0.18), 1.44 ~ 0.18 (0.20); 0.25 ^{ox}

^a CVs of **1–4** at 1.0×10^{-3} mol L⁻¹ in MeCN with 0.1 M TBAPF₆ supporting electrolyte using 150 mV s⁻¹ scan rate at RT in an inert atmosphere. ^b Potentials listed as the cathodic peak potential E_{pc} versus Fc^+/Fc . ^c Potentials listed as the anodic peak potential E_{pa} versus Fc^+/Fc . ox = oxidation only

5.2.8. Electronic Structure Calculations. Representative models **1'**, **2'**, **3'**, and **4'** composed of shortened propyl chains were designed to offer insight into the electronic and structural properties of **1–4** (**Appendix C, Figure C.5.7**). The models are in good agreement with corresponding structural data of pyridyl- and phenol-based $[\text{Ru}^{\text{II}}(\text{bpy})_2]$ complexes previously reported.^{24,26,28–30} Similar approaches in our group^{9,11,12,14,16,31} have been instructive to provide information of the binding modes of metal-containing amphiphilic compounds.

5.2.9. Nature of the HOMOs and LUMOs. Frontier orbitals for **1'–4'** were calculated for correlation to and probing of the origin of the observed electrochemical

(redox) and spectroscopic (optical) properties.²⁸ Relative Molecular Orbital (MO) energies are displayed in **Figure 5.5**, and **Appendix C (Table C.5.1 and Figure C.5.8)**.

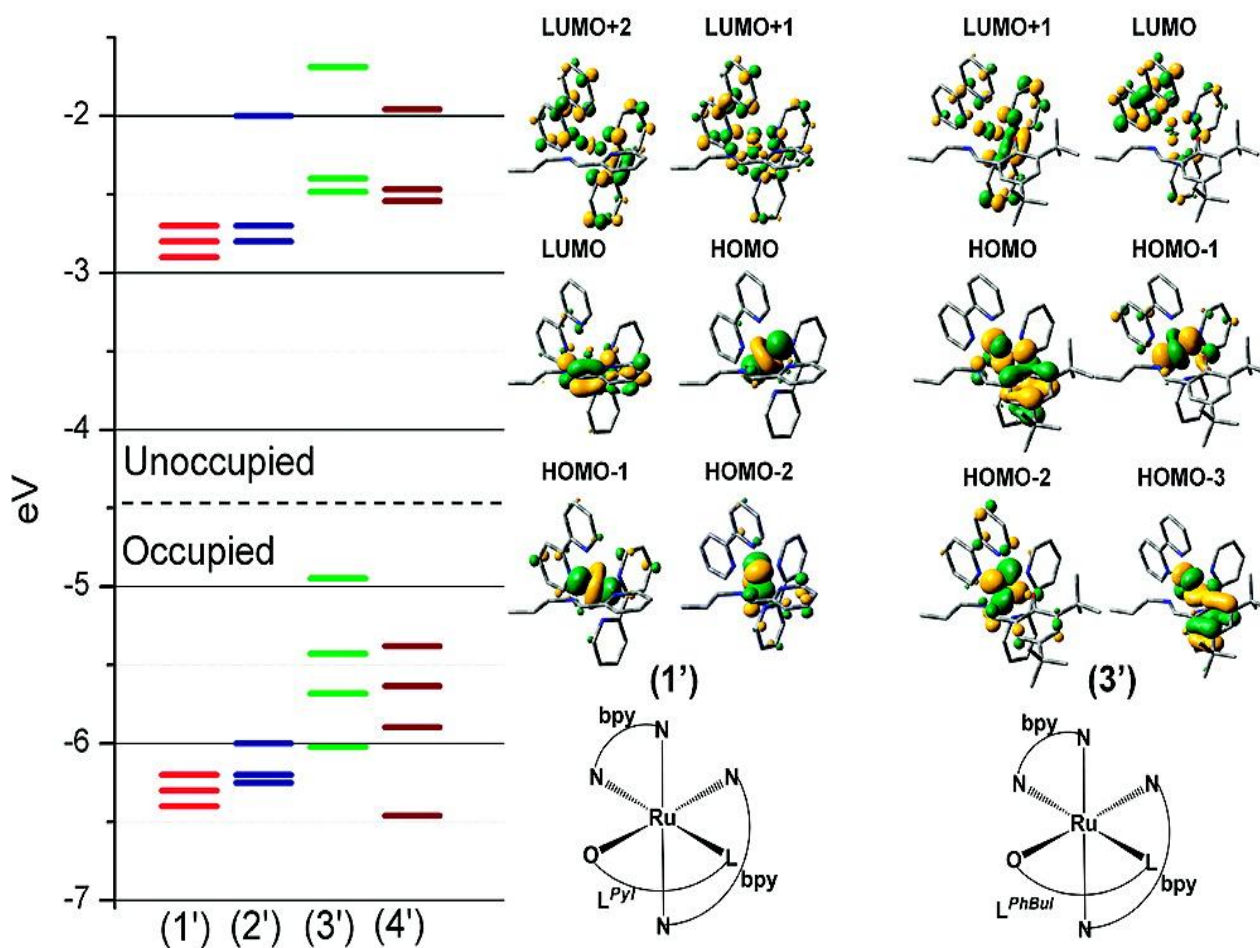
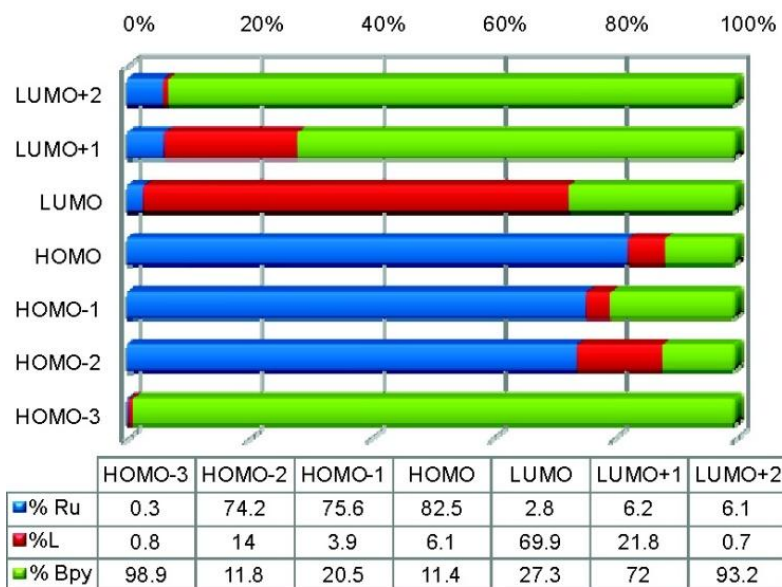


Figure 5.5. Relative molecular orbital energies.

As ordinarily observed for polypyridyl complexes, the contributions from the first three occupied orbitals for the pyridyl-imine based model **1'** can be assigned to the $Ru_{d\pi}$ orbitals. More specifically, the highest occupied molecular orbital (HOMO), HOMO-1, and HOMO-2 are comparatively similar in energy with 74–83% localization on the metal ion. Although the orientation of HOMO-2 is slightly different, the HOMO, HOMO-1, and HOMO-2 orbitals for **2'** are quite consistent to the arrangement observed for **1'**. Interestingly, the three lowest unoccupied molecular orbitals (LUMOs) for **1'** are

distinctly unique among the presented series. These three orbitals display similar energy, rather than the typical set of symmetrical and unsymmetrical combinations for bipyridines. The LUMO is dominated by 70% localized contribution of the pyridine-imine ligand, while the LUMO+1 and LUMO+2 are, respectively, the antisymmetric and symmetric combinations of the bipyridine orbitals. In contrast, the LUMO and LUMO+1 for **2'** are ascribed to the conventional antisymmetric and symmetric combinations of the bipyridine orbitals. The model complexes containing phenolato-based ligands (**3'** and **4'**) behave in a generally comparable manner to one another. However, these complexes consist of different occupied orbital compositions relative to **1'** and **2'**. The HOMO for **3'** is 63% localized on the phenolate-imine based ligand and 31% contribution is coming from a ruthenium-based orbital. The result is a largely mixed metal–ligand orbital. Moreover, the HOMO-1 and HOMO-2 are chiefly $Ru_{d\pi}$ -based orbitals with 76% and 69% contributions, respectively, possessing unsuited spatial orientation for overlap with the phenolate $p\pi$ -type orbital. Percent compositions of representative MOs are shown in **Figure 5.6** and the **Appendix C, Figure C.5.9**.

(1')



(3')

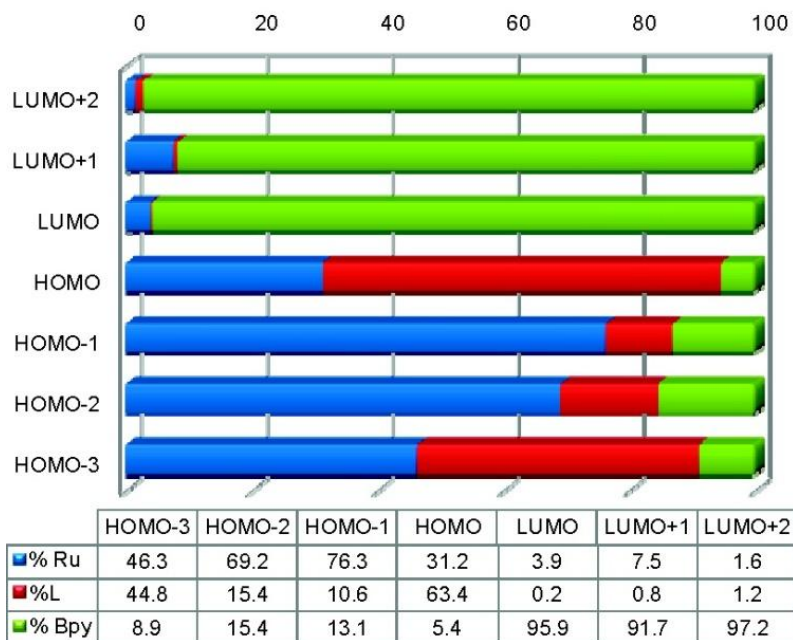
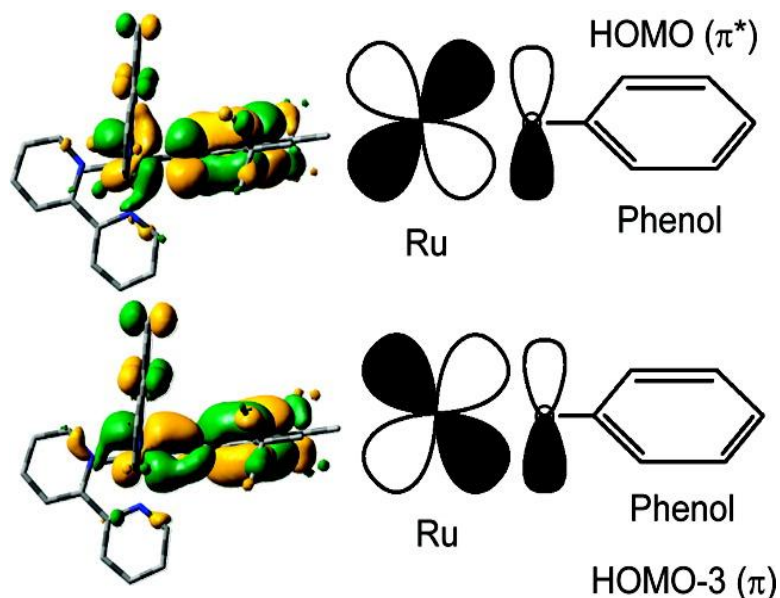


Figure 5.6. Orbital composition for 1' and 3'.

The HOMO and HOMO-3 appear to be the result of π interactions where the HOMO-3 (45: 46% phenolate-to-metal) is the bonding orbital and the HOMO is described by an antibonding arrangement (**Scheme 5.2**).



Scheme 5.2. Ru/Phenolate Orbital Interactions for 3' and 4'.

5.2.10. Correlations to Spectroscopic and Electrochemical Data. Considerable differences in the behavior of 1–4 have been observed experimentally. Frontier orbital arguments invoking 1'–4' can be helpful to infer which MOs are related to redox and spectroscopic processes. This approach should be used with caution, considering that orbitals are determined without nuclear relaxation while electrochemistry is an equilibrium measurement. Further complexity is brought to this picture when multiple redox centers are involved. The electrochemical and the DFT-calculated HOMO–LUMO gap are tabulated in **Table 5.3** and plotted in the **Appendix C, Figure C.5.10**. The experimental data agrees well with the theoretically calculated trend where $3' < 4' < 2' \approx 1'$. The *tert*-butyl-phenolate species presents the lowest HOMO–LUMO gap ($\Delta E_{\text{calc}} = 2.5$ eV, $\Delta E_{\text{exp}} = 1.94$ V), and both of the pyridyl-based complexes demonstrate comparable energy values. The differences observed can be directly attributed to the HOMO orbital associated with the anodic oxidation potential. Thus, the oxidative processes must be described as involving heavily mixed Ru-phenolato processes, rather than as formal

Ru^{II}/Ru^{III} or phenolate/phenoxy redox couples. This interpretation is supported by the MLCT bands of **3** and **4** between 500 and 550 nm, where a similar trend is observed as a consequence of a small HOMO–LUMO energy difference. Cartesian coordinates for the optimized structures can be found in **Appendix C, Table C.5.2**.

Table 5.3. Experimental and Calculated HOMO–LUMO Gaps

complex	experimental redox gap (V) ^a	model	calculated HOMO–LUMO gap (eV) ^b
1	2.56	1'	3.3
2	2.46	2'	3.3
3	1.94	3'	2.5
4	2.11	4'	2.8

^a Difference between half-wave potentials for oxidation and reduction. ^b B3LYP/LANL2DZ with IEF-PCM MeCN.

5.2.11. Amphiphilic Properties. The amphiphilic behavior of the metallosurfactants **1–4** was analyzed by means of compression isotherms³² (**Figure 5.7**) and Brewster angle microscopy (BAM).^{33,34} Langmuir film formation is monitored following the spreading of solutions of the amphiphiles, dissolved in an immiscible organic solvent, onto the aqueous subphase of a minitrough with moveable barriers. As these barriers move closer to each other, compression isotherms plotting surface pressure (Π , mN·m⁻¹) versus average molecular area (A , Å²) grant fundamental information concerning the two-dimensional molecular organization of the monolayer at the air/water interface, collapse pressures (π_c), limiting areas per molecule (A_{lim}), and monolayer collapse areas (A_c). Simultaneously Brewster angle microscopy evaluates film homogeneity, domain and agglomerate formation upon passing vertically polarized light through media possessing different refractive indexes.

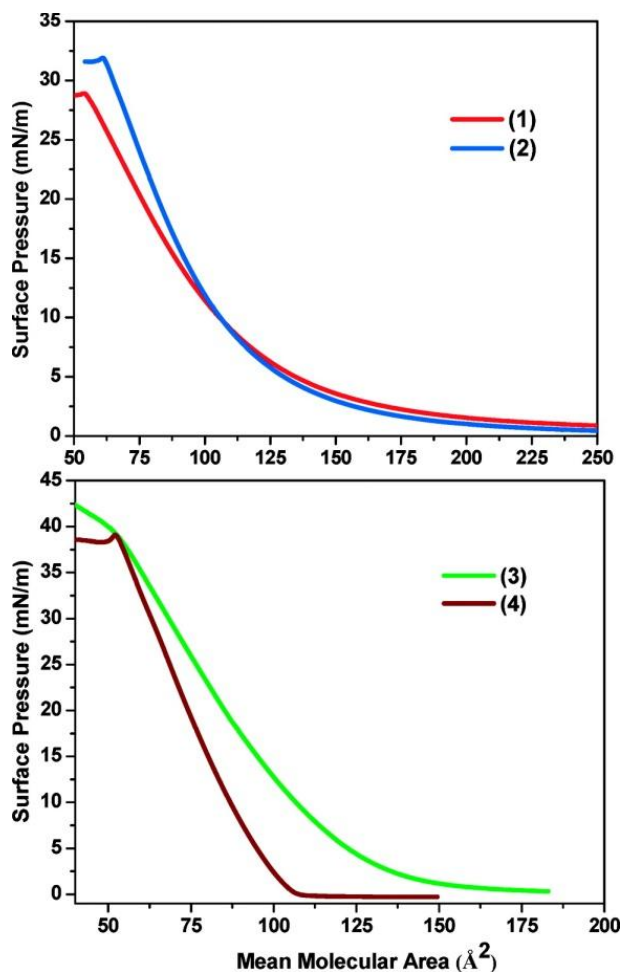


Figure 5.7. Compression isotherms of the metallosurfactants.

Given that the pyridyl-containing ruthenium amphiphiles **1** and **2** showed some solubility in water, complex dissolution was prevented by using a 0.1 M NaCl aqueous subphase with increased ionic strength. The compression isotherms measured for **1** and **2** indicate the formation of well-defined condensed phase regions and distinct collapse pressures; properties characteristic of the formation of stable monolayer films. The individual molecules of both pyridyl-containing amphiphiles start interacting at the air/water interface at an area of about $235 \text{ \AA}^2 \cdot \text{molecule}^{-1}$ to form an expanded phase. No phase transitions were observed, and **1** presents a collapse pressure of about $29 \text{ mN} \cdot \text{m}^{-1}$, while **2** shows a collapse pressure of about $32 \text{ mN} \cdot \text{m}^{-1}$. Amphiphiles **1** and **2** both

demonstrate a sudden decrease in surface pressures, which is a trait typical of constant-area collapse mechanisms.^{35,36} Collapse areas for these species were obtained by extrapolating the steepest portion of the isotherm to zero pressure, which have been determined to be 125 and 120 Å²·molecule⁻¹ for **1** and **2**, respectively. Close structural resemblances can be attributed to the similar interactions observed by the molecules of both complexes at the air/water interface.

Isothermal compressions for the phenolato-containing ruthenium amphiphiles **3** and **4** were recorded in a 0.1 M NaCl aqueous subphase. Although these species are insoluble in water, this subphase was selected to keep consistency. Single molecules of the *tert*-butyl-substituted **3** start interacting at the air/water interface at about 170 Å²·molecule⁻¹, whereas the molecules of the chloro-substituted **4** interact at a lower area of about 107 Å²·molecule⁻¹. These species do not show distinct phase transitions and display well-defined condensed phase regions until the collapse pressure is reached. Similar surface collapse pressures of about 39 mN·m⁻¹ were observed for **3** and **4**. However, the *tert*-butyl-substituted **3** shows an isothermal profile akin to a constant-pressure collapse mechanism, and the chloro-substituted counterpart **4** presents a constant-area collapse mechanism. Both mechanisms follow the Ries sequence^{37,38} of folding, bending, and breaking into multilayers. Amphiphile **4** confers a moderately sharp area of interaction relative to the other complexes in this series. The limiting areas per molecule for **3** and **4** reach about 120 and 100 Å²·molecule⁻¹, respectively. The similar limiting areas per molecule for **1–4** are greater than the expected values and can be accounted for by the increased ionic strength of the subphase, suggesting some tilting of the alkyl-chains.¹³

Representative Brewster angle micrographs have been recorded simultaneously along with the isothermal compressions for **1–4** (**Figures 5.8** and **5.9**). Complexes **1** and **2** reveal multiple domains before compression and at pressures lower than $4 \text{ mN}\cdot\text{m}^{-1}$. The pyridyl-imine complex **1** exhibits a smooth and homogeneous film throughout compression. Formation of minor domains at about $29 \text{ mN}\cdot\text{m}^{-1}$ suggest collapse, directly correlating to the isothermal compression data. Likewise, the pyridyl-amine complex **2** shows a homogeneous monolayer until collapse is reached at about $32 \text{ mN}\cdot\text{m}^{-1}$. The molecules of the phenolate-containing **3** and **4** form random domains before compression and evolve to smooth, non-corrugated films. At a pressure of about $35 \text{ mN}\cdot\text{m}^{-1}$ collapse is evident via the formation of several spots interpreted as either Newton rings or vesicles suggestive of thermodynamic film instability.³⁹

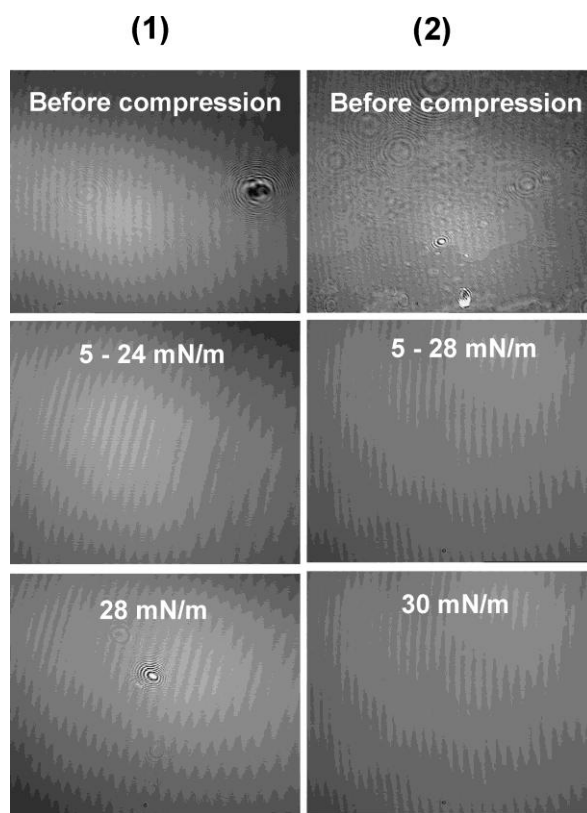


Figure 5.8. BAM images of complexes **1** and **2**.

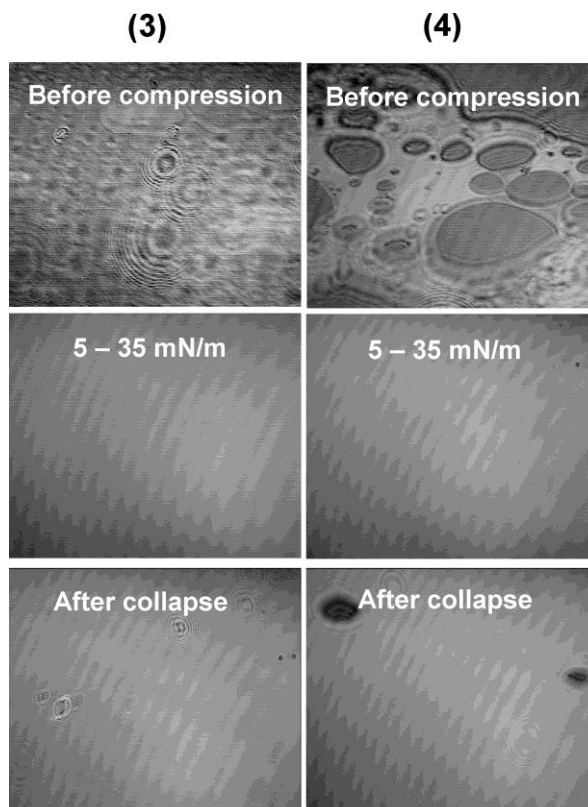


Figure 5.9. BAM images of complexes **3** and **4**.

5.3. Overview and Conclusions

In this chapter, we have described the synthesis and characterization of the new family of pyridyl- and phenolato-containing amphiphiles described as $[(L^{PyI})Ru^{II}(bpy)_2](PF_6)_2$ (**1**), $[(L^{PyA})Ru^{II}(bpy)_2](PF_6)_2$ (**2**), $[(L^{PhBuI})Ru^{II}(bpy)_2](PF_6)$ (**3**), and $[(L^{PhClI})Ru^{II}(bpy)_2](PF_6)$ (**4**). The viability of these species as precursors for photoresponsive Langmuir–Blodgett films was evaluated by addressing (i) the electronic properties to assess the photostability and excitability (emission), (ii) the electrochemical properties to evaluate the nature of the redox processes, and (iii) the amphiphilic properties to investigate the potential for formation of ordered Langmuir–Blodgett films.

(i) Electronic Properties. Absorption spectral data show the visible region dominated by $d\pi(Ru^{II}) \rightarrow \pi^*(bpy)$ MLCT transitions for **1** and **2**, along with $d\pi(Ru^{II}) \rightarrow$

π^* (iminomethylpyridine) processes for **1**. The pyridyl-amine **2** shows a red-shifted band at 472 nm. The phenolato complexes **3** and **4** present less intense and red-shifted MLCT observed between 519–521 nm. Emission spectral data show that species **1** and **2** emit at 715 and 641 nm, respectively, with the second species having a lifetime 2.5 times longer than the first. The relative photolability of these species was examined. Clear photochemical conversion was observed for **2** in acetonitrile, but not in dichloromethane. On the basis of ESI⁺ mass spectrometric methods, we suggested that **2** was converted into [(MeCN)₂Ru^{II}(bpy)₂]²⁺. The imines **1**, **3**, and **4** do not show evidence of photodissociation.

(ii) Electrochemical Properties. Species **1–4** showed rich redox chemistry, where two successive cathodic waves were attributed to bipyridine reduction. More negative potentials for these processes were observed for **3** and **4**, whereas an additional process was observed for **1** and ascribed to the reduction of the imine-based L^{PyI} ligand. Anodic waves were associated to metal oxidation in **1–4** and the formation of phenoxyl radicals for **3** and **4**. DFT calculations based on models **1'–4'** with shortened propyl chains have helped in the interpretation of the experimental electronic and redox behavior of **1–4**. The calculated HOMO–LUMO energy differences correlate well with the observed electrochemical potentials as follows: (a) the energy differences observed for **1** and **2** when compared to **3** and **4**, are directly attributed to the HOMO orbital associated with the oxidation processes, (b) the distinctive three low-lying unoccupied LUMO orbitals for **1'** seem consistent with the electrochemical and emission spectroscopy results, and (c) for **3** and **4**, the oxidative processes are based on heavily mixed Ru-phenolate based MOs that correlate to broad low energy MLCT bands.

(iii) Amphiphilic Properties. Species **1–4** are surface-active and are strong candidates for the formation of monolayer films, as characterized by compression isotherms and Brewster angle microscopy. The collapse pressures are fairly high at about 29–32 mN·m⁻¹ for **1** and **2** and about 39 mN·m⁻¹ for **3** and **4**. Relative solubility in water for **1** and **2** requires the presence of a NaCl aqueous subphase for proper film formation.

Knowledge gained from this effort provides relevant insight toward the integration of amphiphilic properties in the design of photoresponsive precursors for modular films aimed at artificial photosynthetic processes. Our laboratories are currently working on the deposition of Langmuir–Blodgett (LB) films and their photophysical characterization. Integration of [catalytic centers/antennae] into LB films is also under development.

5.4. Experimental Section

Methods and materials used in this chapter are listed in **Section 2.1** of **Chapter 2**.

5.4.1. Syntheses. Preparation of the Ligands L^{PyI}, L^{PyA}, HL^{PhBuA}, and HL^{PhClA}.

The ligands were synthesized according to the literature or used as purchased from the commercial source.^{15,16} General synthetic approaches for complexes **1–4** followed modifications of previously published procedures.^{4,14,17} The starting complex Ru(bpy)₂(CF₃SO₃)₂ was prepared according to the reported procedure.⁴⁰

5.4.2. Preparation of the Metallosurfactants [(L^{PyI})Ru^{II}(bpy)₂](PF₆)₂ (1**) and [(L^{PyA})Ru^{II}(bpy)₂](PF₆)₂ (**2**).** A 10 mL EtOH solution of *cis*-[Ru(bpy)₂Cl₂]·2H₂O (0.520 g, 1.0 mmol) was added dropwise to a 30 mL EtOH solution containing either L^{PyI} (0.394 g, 1.1 mmol) or L^{PyA} (0.397 g, 1.1 mmol). In each instance, the resulting mixtures were stirred under mild reflux overnight (24 h) under an argon blanketing atmosphere and

protected from light. The solution was filtered while warm to eliminate unreacted solids, and the filtrate was concentrated to half of the original volume by rotary evaporation. Slow solvent evaporation after the addition of a saturated solution of NH_4PF_6 in MeOH precipitated the crude product which was filtered and washed with cold distilled water. The compound was purified by column chromatography using a neutral alumina column with toluene-acetonitrile (2:1) as eluent. The solvent was removed, and the product was dissolved in acetone. Slow solvent evaporation yielded an isolable dark red crystalline powder after drying under vacuum.

1. Yield: 76%. Elemental anal. calcd for $[\text{C}_{44}\text{H}_{58}\text{F}_{12}\text{N}_6\text{P}_2\text{Ru}_1]$: C, 49.76, H, 5.50, N, 7.91%. Found: C, 49.83, H, 5.44, N, 7.89%. IR data (KBr, cm^{-1}): 3084(w) (C-H_{arom}); 2920(s), 2851(s) (alkyl chain C-H stretches); 1606(m) (C=N_{pyr}); 1466(s) (C=C_{arom}); 1162(m) (-C-N-); 846(s) (PF_6^-). UV-visible data (ACN, 1.0×10^{-5} M): 239 (17 330), 243 (17 530), 255 (16 030), 287 (44 120), 345 sh (4460), 432 sh (8940), 462 (11 080). $^1\text{H-NMR}$ (400 MHz, CDCl_3): δ 8.97 (d, 4H), 8.42 (d, 1H), 8.34 (d, 4H), 7.96 (d, 1H), 7.71–7.63 (m, 6H), 7.58 (s, 1H), 7.41 (t, 4H), 1.25 (m, 34H), 0.88 (t, 3H). MS data (ESI⁺ in MeOH): $m/z = 386$ (100%) for $[(\text{L}^{\text{PyI}})\text{Ru}^{\text{II}}(\text{bpy})_2]^{2+} + 2$, $m/z = 917$ for $[(\text{L}^{\text{PyI}})\text{Ru}^{\text{II}}(\text{bpy})_2 + (\text{PF}_6^-)]^+$, and $m/z = 771$ for $[(\text{L}^{\text{PyI}})\text{Ru}^{\text{II}}(\text{bpy})_2]^{2+} - \text{H}^+$.

2. Yield: 79%. Elemental anal. calcd for $[\text{C}_{44}\text{H}_{60}\text{F}_{12}\text{N}_6\text{P}_2\text{Ru}_1]$: C, 49.67, H, 5.68, N, 7.90%. Found: C, 49.21, H, 5.68, N, 7.95%. IR data (KBr, cm^{-1}): 3670(w), 3287(w) (N-H); 3086(w) (C-H_{arom}); 2924(s), 2853(s) (alkyl chain C-H stretches); 1604(m) (C=N_{pyr}); 1467(s), 1446(s) (C=C_{arom}); 1162(m) (-C-N-); 840(s) (PF_6^-). UV-visible data (ACN, 1.0×10^{-5} M): 245 (18 120), 291 (43 850), 342 (7450), 424 sh (4540), 472 (7070). $^1\text{H-NMR}$ (400 MHz, CDCl_3): δ 9.06 (d, 4H), 8.50–8.42 (m, 5H), 8.35 (m, 5H), 8.06 (d,

1H), 7.52 (t, 1H), 7.40 (t, 4H), 4.44 (s, 2H), 1.97 (t, 2H), 1.74 (s, 1H), 1.24 (m, 32H), 0.88 (t, 3H). MS data (ESI⁺ in MeOH): $m/z = 387$ (100%) for $[(L^{PyA})Ru^{II}(bpy)_2]^{2+}/+2$, $m/z = 919$ for $[(L^{PyA})Ru^{II}(bpy)_2 + (PF_6^-)]^+$, and $m/z = 773$ for $[(L^{PyA})Ru^{II}(bpy)_2]^{2+} - H^+$.

5.4.3. Preparation of the Metallosurfactants $[(L^{PhBuI})Ru^{II}(bpy)_2](PF_6)$ (3) and $[(L^{PhClI})Ru^{II}(bpy)_2](PF_6)$ (4). A 10 mL isopropanol or acetone solution of $Ru(bpy)_2(CF_3SO_3)_2$ (0.356 g, 0.5 mmol) was added dropwise to a 30 mL isopropanol or acetone solution containing either HL^{PhBuA} (0.244 g, 0.5 mmol) or HL^{PhClA} (0.222 g, 0.5 mmol), respectively, and Et_3N as base (0.076 g, 0.75 mmol) for deprotonation. Isolation and purification procedures were similar to those of **1** and **2**.

3. Yield: 72%. Elemental anal. calcd for $[C_{53}H_{74}F_6N_5O_1P_1Ru_1]$: C, 61.02, H, 7.15, N, 6.71%. Found: C, 61.25, H, 7.35, N, 6.69%. IR data (KBr, cm^{-1}): 3120(w), 3078(w) (C–H_{arom}); 2922(s), 2857(s) (alkyl chain and *tert*-butyl C–H stretches); 1602(m) (C=N_{pyr}); 1465(s), 1442(s), 1423(s) (C=C_{arom}); 1260(m), 1234(m) (C–O); 1161(m) (–C–N–); 841(s) (PF_6^-). UV–visible data (ACN, 1.0×10^{-5} M): 248 (50 260), 294 (59 200), 377 (13 870), 476 sh (7950), 521 (8550). ¹H–NMR (400 MHz, $CDCl_3$): δ 8.71 (d, 4H), 8.22 (d, 4H), 8.05 (s, 1H), 7.83 (t, 4H), 7.75–7.73 (s, 2H), 7.41 (t, 4H), 3.15 (t, 2H), 1.24 (m, 50H), 0.88 (t, 3H). MS data (ESI⁺ in MeOH): $m/z = 898$ (100%) for $[(L^{PhBuI})Ru^{II}(bpy)_2]^+$.

4. Yield: 70%. Elemental anal. calcd for $[C_{48}H_{64}Cl_2F_6N_5O_2P_1Ru_1]$: C, 54.39, H, 6.09, N, 6.61%. Found: C, 54.60, H, 6.05, N, 6.25%. IR data (KBr, cm^{-1}): 3121(w), 3077(w) (C–H_{arom}); 2923(s), 2852(s) (alkyl chain C–H stretches); 1602(w) (C=N_{pyr}); 1459(s), 1442(s), 1418(s) (C=C_{arom}); 1262(m) (C–O); 1172(m) (–C–N–); 842(s) (PF_6^-). UV–visible data (ACN, 1.0×10^{-5} M): 247 (37 910), 295 (60 860), 363 (10 570), 519

(8380). $^1\text{H-NMR}$ (400 MHz, CDCl_3): δ 8.62 (d, 4H), 8.36 (d, 4H), 8.19 (s, 1H), 8.11 (t, 4H), 7.92–7.84 (s, 2H), 7.45 (t, 4H), 3.67 (t, 2H), 1.25 (m, 32H), 0.88 (t, 3H). MS data (ESI⁺ in MeOH): $m/z = 856$ (100%) for $[(\text{L}^{\text{PhCl}})\text{Ru}^{\text{II}}(\text{bpy})_2]^+$.

5.5. References

- 1 Bodenthin, Y.; Pietsch, U.; Mohwald, H.; Kurth, D. G. "Inducing Spin Crossover in Metallo-Supramolecular Polyelectrolytes through an Amphiphilic Phase Transition." *J. Am. Chem. Soc.* **2005**, *127*, 3110.
- 2 Talham, D. R. "Conducting and Magnetic Langmuir–Blodgett Films." *Chem. Rev.* **2004**, *104*, 5479.
- 3 Hoogenboom, R.; Fournier, D.; Schubert, U. S. "Asymmetrical Supramolecular Interactions as Basis for Complex Responsive Macromolecular Architectures." *Chem. Commun.* **2008**, 155.
- 4 Zhang, J.; Chu, B. W. K.; Zhu, N.; Yam, V. W.-W. "Synthesis, Characterization, Langmuir–Blodgett Film-Forming Property, and Second-Order Nonlinear Optical Study of Rhenium(I) and Ruthenium(II) Diimine Complexes." *Organometallics* **2007**, *26*, 5423.
- 5 Low, P. J. "Metal Complexes in Molecular Electronics: Progress and Possibilities." *Dalton Trans.* **2005**, 2821.
- 6 Wassel, R. A.; Gorman, C. B. "Molecular Electronics: Establishing the Molecular Basis for Molecular Electronics." *Angew. Chem.* **2004**, *43*, 5120.
- 7 Guerrero-Martinez, A.; Vida, Y.; Dominguez-Gutierrez, D.; Albuquerque, R. Q.; De Cola, L. "Tuning Emission Properties of Iridium and Ruthenium Metallosurfactants in Micellar Systems." *Inorg. Chem.* **2008**, *47*, 9131.
- 8 Wang, K.; Haga, M.; Monjushiro, H.; Akiba, M.; Sasaki, Y. "Luminescent Langmuir–Blodgett Films of Platinum(II) Complex [Pt(L₁₈)Cl](PF₆) (L₁₈ = 2,6-Bis(1-octadecylbenzimidazol-2-yl)pyridine)." *Inorg. Chem.* **2000**, *39*, 4022.

- 9 Shakya, R.; Hindo, S. S.; Wu, L.; Ni, S.; Allard, M.; Heeg, M. J.; da Rocha, S. R.; Yee, G. T.; Hratchian, H. P.; Verani, C. N. "Amphiphilic and Magnetic Properties of a New Class of Cluster-Bearing $[L_2Cu_4(\mu_4-O)(\mu_2\text{-carboxylato})_4]$ Soft Materials." *Chem.—Eur. J.* **2007**, *13*, 9948.
- 10 Shakya, R.; Keyes, P. H.; Heeg, M. J.; Moussawel, A.; Heiney, P. A.; Verani, C. N. "Thermotropic Mesomorphism of Soft Materials Bearing Carboxylate-Supported μ_4 -Oxo Tetracupric Clusters." *Inorg. Chem.* **2006**, *45*, 7587.
- 11 Shakya, R.; Hindo, S. S.; Wu, L.; Allard, M. M.; Heeg, M. J.; Hratchian, H. P.; McGarvey, B. R.; da Rocha, S. R.; Verani, C. N. "Archetypical Modeling and Amphiphilic Behavior of Cobalt(II)-Containing Soft-Materials with Asymmetric Tridentate Ligands." *Inorg. Chem.* **2007**, *46*, 9808.
- 12 Lesh, F. D.; Hindo, S. S.; Heeg, M. J.; Allard, M. M.; Jain, P.; Peng, B.; Hryhorczuk, L.; Verani, C. N. "On the Effect of Coordination and Protonation Preferences in the Amphiphilic Behavior of Metallosurfactants with Asymmetric Headgroups." *Eur. J. Inorg. Chem.* **2009**, 345.
- 13 Driscoll, J. A.; Allard, M. M.; Wu, L. B.; Heeg, M. J.; da Rocha, S. R. P.; Verani, C. N. "Interfacial Behavior and Film Patterning of Redox-Active Cationic Copper(II)-Containing Surfactants." *Chem.—Eur. J.* **2008**, *14*, 9665.
- 14 Driscoll, J. A.; Keyes, P. H.; Heeg, M. J.; Heiney, P. A.; Verani, C. N. "Influence of the Apical Ligand in the Thermotropic Mesomorphism of Cationic Copper-Based Surfactants." *Inorg. Chem.* **2008**, *47*, 7225.
- 15 Jayathilake, H. D.; Driscoll, J. A.; Bordenyuk, A. N.; Wu, L. B.; da Rocha, S. R. P.; Verani, C. N.; Benderskii, A. V. "Molecular Order in Langmuir–Blodgett

- Monolayers of Metal-Ligand Surfactants Probed by Sum Frequency Generation.” *Langmuir* **2009**, *25*, 6880.
- 16 Hindo, S. S.; Shakya, R.; Rannulu, N. S.; Allard, M. M.; Heeg, M. J.; Rodgers, M. T.; da Rocha, S. R.; Verani, C. N. “Synthesis, Redox, and Amphiphilic Properties of Responsive Salicylaldehyde-Copper(II) Soft Materials.” *Inorg. Chem.* **2008**, *47*, 3119.
- 17 Chu, B. W.; Yam, V. W.-W. “Synthesis, Characterization, Langmuir–Blodgett Film-Forming Properties, and Second-Harmonic-Generation Studies of Ruthenium(II) Complexes with Long Hydrocarbon Chains.” *Inorg. Chem.* **2001**, *40*, 3324.
- 18 Yam, V. W.-W.; Lee, V. W. M. “Synthesis, Emission, Electrochemistry and Cation-Binding Studies of Ruthenium(II)-Diimine-Crown and -Terpyridine-Crown Complexes.” *J. Chem. Soc., Dalton Trans.* **1997**, 3005.
- 19 Keyes, T. E.; Leane, D.; Forster, R. J.; Coates, C. G.; McGarvey, J. J.; Nieuwenhuyzen, M. N.; Figgemeier, E.; Vos, J. G. “Redox and Spectroscopic Orbitals in Ru(II) and Os(II) Phenolate Complexes.” *Inorg. Chem.* **2002**, *41*, 5721.
- 20 Leane, D.; Keyes, T. E. “Electronic Coupling and Photochemical Stability of O,N Bound Mononuclear Ru(II) and Os(II)-Hydroquinone Complexes.” *Inorg. Chim. Acta.* **2006**, *359*, 1627.
- 21 Lanznaster, M.; Heeg, M. J.; Yee, G. T.; McGarvey, B. R.; Verani, C. N. “Design of Molecular Scaffolds Based on Unusual Geometries for Magnetic Modulation

- of Spin-Diverse Complexes with Selective Redox Response.” *Inorg. Chem.* **2007**, *46*, 72.
- 22 Brown, G. M.; Weaver, T. R.; Keene, F. R.; Meyer, T. J.; Kenan, W. R., Jr. “Oxidation of Coordinated Diamines in Bis(2,2'-bipyridine) Complexes of Ruthenium.” *Inorg. Chem.* **1976**, *15*, 190.
- 23 Chakraborty, S.; Walawalkar, M. G.; Lahiri, G. K. “Ruthenium(II)/(III) Bipyridine Heterochelates Incorporating Phenolato Imine Functionalities. Synthesis, Crystal Structure, Spectroscopic and Electron-Transfer Properties and Solution Reactivities.” *J. Chem. Soc., Dalton Trans.* **2000**, 2875.
- 24 Holligan, B. M.; Jeffery, J. C.; Norgett, M. K.; Schatz, E.; Ward, M. D. “The Coordination Chemistry of Mixed Pyridine-Phenol Ligands; Spectroscopic and Redox Properties of Mononuclear Ruthenium Complexes with (pyridine)_{6-x}(phenolate)_x Donor Sets (x = 1 or 2).” *J. Chem. Soc., Dalton Trans.* **1992**, 3345.
- 25 Arakawa, R.; Tachiyashiki, S.; Matsuo, T. “Detection of Reaction Intermediates: Photosubstitution of (Polypyridine) Ruthenium(II) Complexes Using Online Electrospray Mass Spectrometry.” *Anal. Chem.* **1995**, *67*, 4133.
- 26 Keene, F. R.; Ridd, M. J.; Snow, M. R. “Investigations of the Nature of Dehydrogenation of the α -carbon Atom in the Oxidation of Amines Coordinated to Ruthenium.” *J. Am. Chem. Soc.* **1983**, *105*, 7075.
- 27 Ridd, M. J.; Keene, F. R. “Mechanism of Oxidation of an Amine Coordinated to Ruthenium.” *J. Am. Chem. Soc.* **1981**, *103*, 5733.
- 28 Allard, M. M.; Odongo, O. S.; Lee, M. M.; Chen, Y.-J.; Endicott, J. F.; Schlegel, H. B. “Effects of Electronic Mixing in Ruthenium(II) Complexes with Two

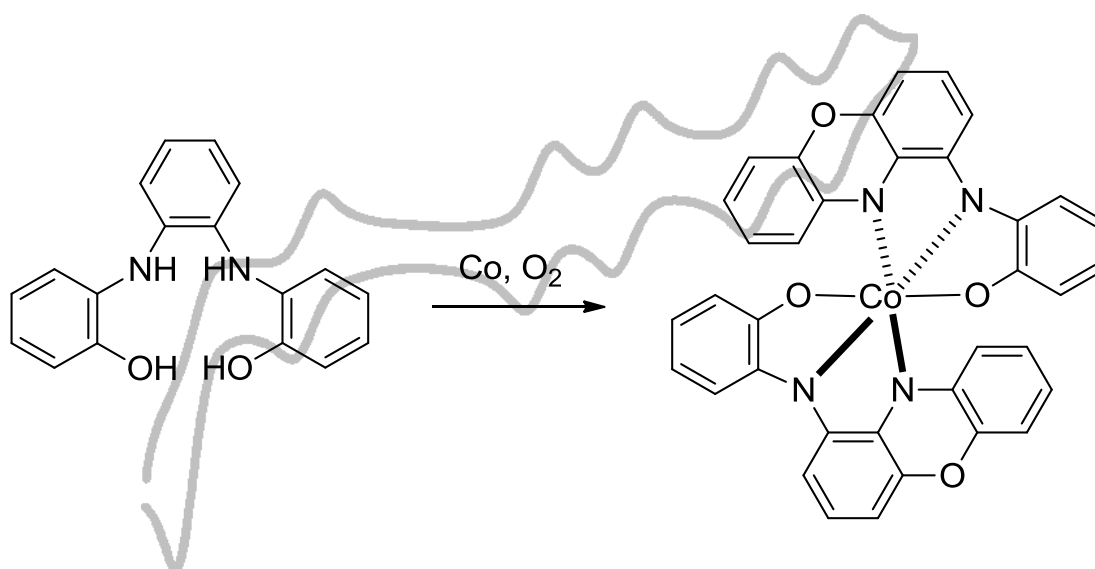
- Equivalent Acceptor Ligands. Spectroscopic, Electrochemical, and Computational Studies.” *Inorg. Chem.* **2010**, *49*, 6840.
- 29 Cai, P.; Li, M. X.; Duan, C. Y.; Lu, F.; Guo, D.; Meng, Q. J. “Syntheses, Crystal Structure and Electrochemical Properties of Dinuclear Ruthenium Complexes Containing Saturated and Unsaturated Spacers.” *New J. Chem.* **2005**, *29*, 1011.
- 30 Chakraborty, S.; Walawalkar, M. G.; Lahiri, G. K. “Ruthenium-Mediated Selective Cleavage of Nitrogen-Carbon Bond of the Diimine Function. Synthesis, Spectroscopic and Redox Properties of the Complexes $[\text{Ru}(\text{L})_2\{-\text{OC}_6\text{H}_4\text{C}(\text{CH}_3)\text{:N-H}\}][\text{ClO}_4]$ (L = 2,2'-bipyridine and 1,10-phenanthroline) and the Crystal Structure of the Bipyridine Derivative.” *Polyhedron* **2001**, *20*, 1851.
- 31 Shakya, R.; Imbert, C.; Hratchian, H. P.; Lanznaster, M.; Heeg, M. J.; McGarvey, B. R.; Allard, M.; Schlegel, H. B.; Verani, C. N. “Structural, Spectroscopic, and Electrochemical Behavior of Trans-Phenolato Cobalt(III) Complexes of Asymmetric NN'O Ligands as Archetypes for Metallomesogens.” *Dalton Trans.* **2006**, 2517.
- 32 Petty, M. C. *Langmuir–Blodgett Films: An Introduction*; Cambridge University Press: Cambridge, **1996**.
- 33 Mobius, D. “Morphology and Structural Characterization of Organized Monolayers by Brewster Angle Microscopy.” *Curr. Opin. Colloid Interface Sci.* **1998**, *3*, 137.
- 34 Vollhardt, D. “Morphology and Phase Behavior of Monolayers.” *Adv. Colloid Interface Sci.* **1996**, *64*, 143.

- 35 Kundu, S.; Datta, A.; Hazra, S. "Growth of a Collapsing Langmuir Monolayer." *Phys. Rev. E* **2006**, *73*, 051608/1.
- 36 Vaknin, D.; Bu, W.; Satija, S. K.; Travesset, A. "Ordering by Collapse: Formation of Bilayer and Trilayer Crystals by Folding Langmuir Monolayers." *Langmuir* **2007**, *23*, 1888.
- 37 Ries, H. E., Jr. "Stable Ridges in a Collapsing Monolayer." *Nature* **1979**, *281*, 287.
- 38 Ybert, C.; Lu, W.; Moller, G.; Knobler, C. M. "Kinetics of Phase Transitions in Monolayers: Collapse." *J. Phys.: Condens. Matter* **2002**, *14*, 4753.
- 39 Galvan-Miyoshi, J.; Ramos, S.; Ruiz-Garcia, J.; Castillo, R. "Localized Oscillations and Fraunhofer Diffraction in Crystalline Phases of a Monolayer." *J. Chem. Phys.* **2001**, *115*, 8178.
- 40 Greaney, M. A.; Coyle, C. L.; Harmer, M. A.; Jordan, A.; Stiefel, E. I. "Synthesis and Characterization of Mononuclear and Dinuclear Bis(2,2'-bipyridine) Ruthenium(II) Complexes Containing Sulfur-Donor Ligands." *Inorg. Chem.* **1989**, *28*, 912.

Chapter 6

UNEXPECTED FORMATION OF A COBALT(III)

PHENOXAZINYLATE ELECTRON RESERVOIR



CHAPTER 6

UNEXPECTED FORMATION OF A COBALT(III) PHENOXAZINYLATE
ELECTRON RESERVOIRFrank D. Lesh, Richard L. Lord, Mary Jane Heeg, H. Bernhard Schlegel, and
Cláudio N. Verani*

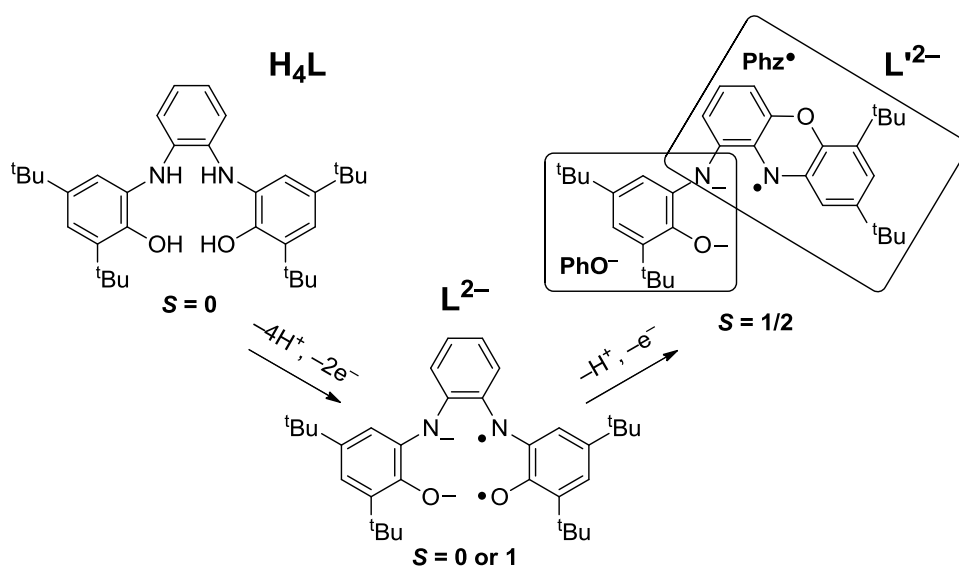
Reprinted with permission from *Eur. J. Inorg. Chem.* **2012**, 3, 463–466. Copyright 2012 WILEY-VCH Verlag GmbH & Co. KGaA, Weinheim. This article appears within a special cluster issue entitled “Cooperative & Redox Non-Innocent Ligands in Directing Organometallic Reactivity.”

Contributions to this work on my part included the synthetic, spectroscopic, and electrochemical characterizations along with the original draft of the manuscript.

6.1. Introduction

There is considerable interest in the development and characterization of redox-active ligands with finely tuned potentials that act as electron reservoirs during catalytic processes.¹ Among an ever growing group of such redox-active ligands, the species *N,N'*-bis(3,5-di-*tert*-butyl-2-hydroxyphenyl)-1,2-diamine (H_4L) has received substantial attention.²⁻⁵ Coordination compounds with this ligand demonstrate catalytic behavior in pseudooctahedral complexes with early transition metals and square planar complexes with late transition metals. Such metal complexes mediate reductive bond formation³⁻⁵ and bioinspired aerobic oxidation,² respectively, partially due to five ligand-based discrete oxidation levels. When complexed to metals, the most commonly observed ligand oxidation state is 2– ($H_4L \rightarrow L^{2-} + 4H^+ + 2e^-$, **Scheme 6.1** left), which can be

written with both closed shell² and diradical electron configurations (only one shown). To our knowledge, however, similar adducts with middle 3d-metals (Mn, Fe, Co) have not received similar attention, despite the intriguing combination of this ligand with redox rich metals.^{1,6-8} Towards this goal, we report here an unprecedented ligand transformation of L^{2-} whereby one of the phenolate/phenoxy arms has cyclized to form a mixed phenolate/phenoxy radical species, which we denote L'^{2-} ($L^{2-} \rightarrow L'^{2-} + H^+ + e^-$, **Scheme 6.1** right).



Scheme 6.1. Formation of the mixed phenolate/phenoxy radical species from H_4L .

Phenoxazines, found in nature as potent chromophores,⁹⁻¹¹ demonstrate efficient electron transfer and high luminescence quantum yields required for organic light-emitting diodes and dye-sensitized solar cells.¹² Pierpont *et al.* observed a related transformation involving cyclization of a Schiff base biquinone ligand to confer a phenoxazinylate radical anion.^{13,14} Defining a ligand shorthand for this new ligand is complicated by the fact that the bridging amide can conjugate with both arms. In the past, there has been reference to imino and diimino catecholate/semiquinonate redox behavior

when it was straightforward to group this nitrogen with a single arm of the ligand, *e.g.* phenolate or phenoxazinylate, respectively. We prefer to discuss the ligand as three fragments (**Scheme 6.1**, right): (i) the phenolate (PhO^- , left box), (ii) the bridging amide (N^- , overlap between boxes), and (iii) the phenoxazinyl radical (Phz^\bullet , right box). Thus, L^{2-} is abbreviated $\text{PhO}^- - \text{N}^- - \text{Phz}^\bullet$. While this description is inherently too localized a description, it emphasizes correctly whether the phenoxazinyl or phenolate arm is the major contributor to a given redox process.¹⁵ Herein, we describe the synthesis and characterization of the species $[\text{Co}(\text{L}')_2]^0$ along with its rich redox chemistry.

6.2. Results and Discussion

Condensation of 3,5-di-*tert*-butylcatechol and *o*-phenylenediamine (2:1) together with Et_3N in *n*-heptane generates H_4L after four days of stirring at ambient temperature under aerobic conditions.^{2,4} Equimolar treatment of H_4L with anhydrous CoCl_2 in the presence of Et_3N under aerobic conditions in acetonitrile afforded a microcrystalline precipitate of $[\text{Co}(\text{L}')_2]^0$. This stoichiometry does not seem to be affected by 1:1 vs. 2:1 $\text{H}_4\text{L}:\text{Co}^{\text{II}}$ loadings or by the equivalents of added base (see **Appendix D**). Dark green crystals suitable for X-ray analysis were obtained by slow evaporation from a $\text{CH}_2\text{Cl}_2:\text{CH}_3\text{CN}$ mixture (1:1), and the unanticipated bisligated structure, with each ligand coordinated in a $[\text{O}-\text{N}-\text{N}']$ ($\text{O1}-\text{N1}-\text{N2}$ / $\text{O3}-\text{N3}-\text{N4}$) meridional fashion, is presented in **Figure 6.1**. It is tempting to assign this neutral species as $[\text{Co}^{\text{II}}(\text{L}'^{-})_2]^0$ based on the fairly similar bond lengths within each of the two ligands (see **Appendix D**), however, averaged metal–ligand bond lengths of 1.896 ± 0.004 , 1.882 ± 0.006 , and 1.955 ± 0.002 Å for Co–O, Co–N, and Co–N', respectively, strongly imply a low-spin cobalt(III) ($^{\text{LS}}\text{Co}^{\text{III}}$) metal center.¹⁶⁻¹⁸

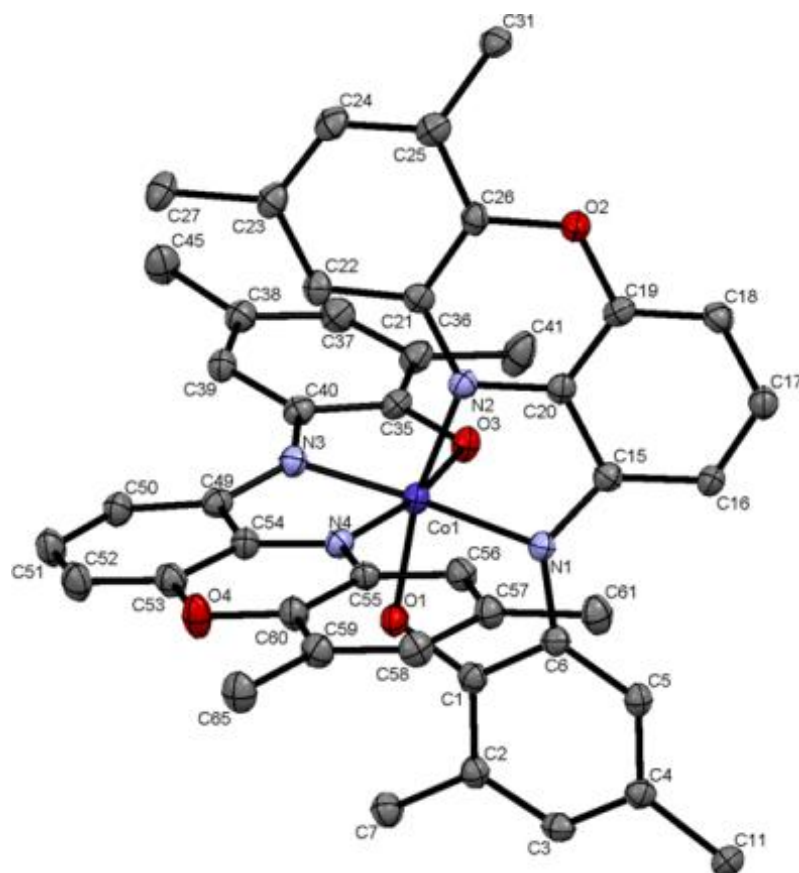


Figure 6.1. ORTEP diagram for $[\text{Co}(\text{L}')_2] \cdot 2\text{MeCN}$ showing 50% probability of the thermal ellipsoids. Solvent and hydrogen atoms are excluded, and the ^tBu groups are truncated to the central quaternary carbon for clarity. Selected bond lengths (\AA) and angles ($^\circ$): $\text{Co}(1)\text{--N}(1)$ 1.876(2), $\text{Co}(1)\text{--N}(3)$ 1.887(2), $\text{Co}(1)\text{--O}(1)$ 1.892(2), $\text{Co}(1)\text{--O}(3)$ 1.899(2), $\text{Co}(1)\text{--N}(2)$ 1.953(2), $\text{Co}(1)\text{--N}(4)$ 1.956(2); $\text{N}(2)\text{--Co}(1)\text{--N}(3)$ 104.83(8), $\text{N}(2)\text{--Co}(1)\text{--N}(4)$ 92.64(8), $\text{O}(1)\text{--Co}(1)\text{--N}(3)$ 86.55(7), $\text{O}(1)\text{--Co}(1)\text{--O}(3)$ 91.35(7), $\text{O}(1)\text{--Co}(1)\text{--N}(1)$ 84.80(7), $\text{O}(1)\text{--Co}(1)\text{--N}(4)$ 89.33(7).

The formation of phenoxazinyl rings is known to occur in a basic, oxidizing medium for some aminocatechols.¹⁹ It is noteworthy that we have observed this ligand transformation in the presence of cobalt, but not manganese or iron ions under similar basic, oxidizing conditions.²⁰ One plausible difference between these metals is that the Co^{II} ion is capable of reducing dioxygen to superoxide.²¹ Anaerobic mixing of H_4L and the cobalt salt affords the uncyclized metal-ligand adduct in a 2:1 ratio $[\text{Co}^{\text{II}}(\text{HL})_2]^0$, similar to the

manganese species, as suggested by ESI mass spectrometric methods (see **Appendix D**). Pursuit of mechanistic details and the possible role of superoxide are ongoing, but are beyond the scope of this communication.

In order to understand the oxidation and spin states of the metal ion and ligands in the $[\text{Co}^{\text{III}}(\text{L}')_2]$ species, we investigated multiple electronic structures with density functional theory (DFT) calculations.²² Two low energy structures were identified that are best described as a $^{\text{LS}}\text{Co}^{\text{III}}$ species with one unpaired electron, $S = 1/2$ (see **Appendix D** for structural details and comparison to X-ray structure). One has ligands in different oxidation states, 2- and 1-, while the other is symmetric and has formal charges of 1.5- for each ligand. We present the former because it does not invoke fractional electron charges, but it is important to note these species are isoenergetic suggesting multiple resonance forms are accessible. A corresponding orbital analysis²³ of this localized species suggests that one ligand is in the $\text{PhO}^- - \text{N}^- - \text{Phz}^\bullet$ oxidation state with an unpaired α electron (**Figure 6.2** top), while the other ligand is in the $\text{PhO}^\bullet - \text{N}^- - \text{Phz}^\bullet$ oxidation state with two antiferromagnetically coupled radicals (**Figure 6.2** bottom). The overlap of the antiferromagnetically coupled orbitals is quite large at 0.8, and may suggest a closed-shell description. However, all attempts to compute a structure with a closed-shell, localized 1- ligand collapsed to the delocalized structure with fractional ligand charges. The EPR derived g -value of 2.0 is consistent with the assignment of an organic radical, and despite the known shortcomings for predicting spin states of transition metal complexes *a priori*, DFT seems to capture correctly the physicochemical properties of $[\text{Co}^{\text{III}}(\text{PhO}^- - \text{N}^- - \text{Phz}^\bullet)(\text{PhO}^\bullet - \text{N}^- - \text{Phz}^\bullet)]^0$.^{24,25} The unpaired electrons in the $\text{PhO}^- - \text{N}^- - \text{Phz}^\bullet$ and $\text{PhO}^\bullet - \text{N}^- - \text{Phz}^\bullet$ ligands should demonstrate diagnostic intra- or inter-ligand

charge transfer bands, and we therefore measured the absorption spectrum to probe further the electronic structure.

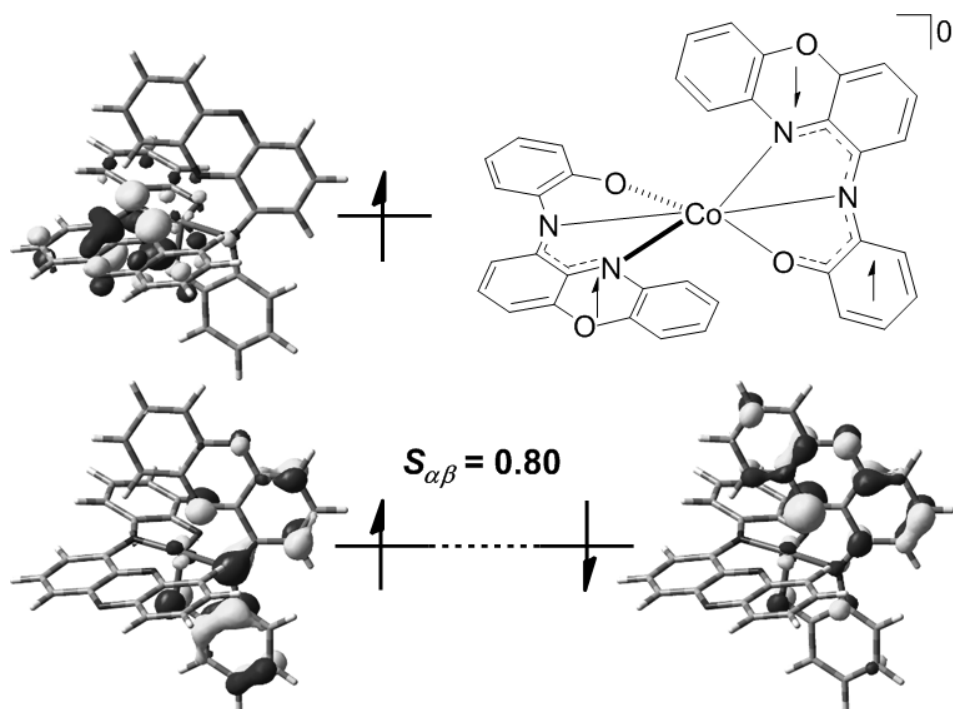


Figure 6.2. Contour plots (0.05 au) for the singly occupied (top) and AF coupled (bottom) orbitals resulting from the corresponding orbital analysis. $S_{\alpha\beta}$ is the overlap integral for the AF coupled corresponding orbitals.

The UV-visible spectrum of $[\text{Co}^{\text{III}}(\text{PhO}^- - \text{N}^- - \text{Phz}^*)(\text{PhO}^- - \text{N}^- - \text{Phz}^*)]$ was collected in CH_2Cl_2 (see **Figure 6.3**). Prominent $\sigma \rightarrow \pi^*$ and $\pi \rightarrow \pi^*$ transition bands positioned at 271 nm ($88,770 \text{ L mol}^{-1} \text{ cm}^{-1}$) are succeeded by less intense shoulders at 387 and 474 nm ($16,630$ and $9,660 \text{ L mol}^{-1} \text{ cm}^{-1}$). Just beyond the visible region is a broad, low-energy band centered at 871 nm ($9,690 \text{ L mol}^{-1} \text{ cm}^{-1}$). TD-DFT calculations corroborate the existence of a broad absorption feature around 1,000 nm with an intensity of $\sim 10,000 \text{ L mol}^{-1} \text{ cm}^{-1}$, which comprises transitions mostly corresponding to intra- and inter-ligand charge transfers.²⁶ This assignment is consistent with earlier reports

containing single and multiple phenoxazinolates,^{11,27-28} and with our hypothesis of one or more ligand-based radicals.

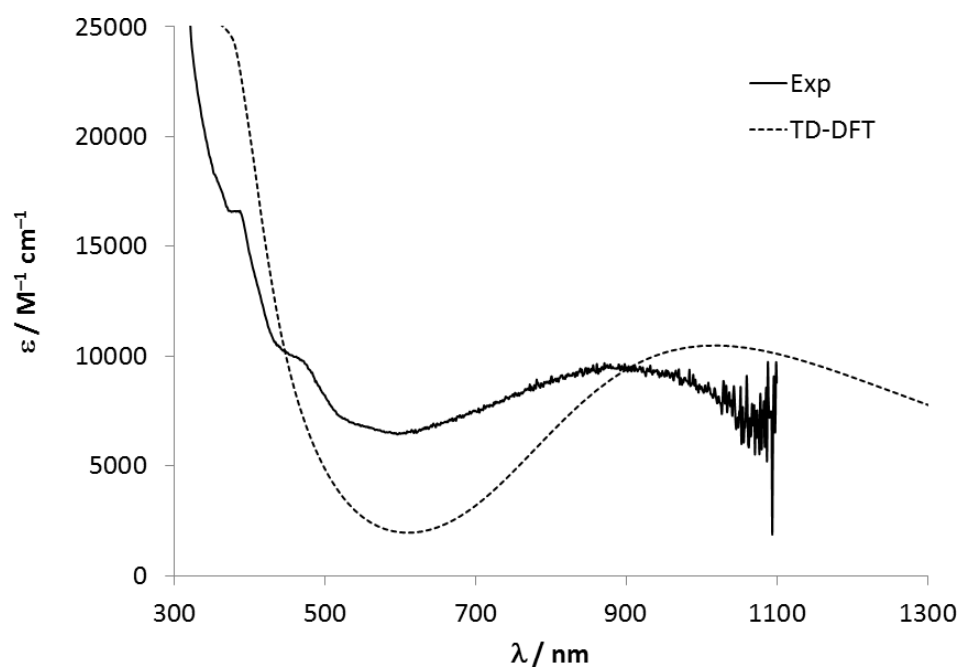


Figure 6.3. Experimental (solid) and simulated (dashed) UV-visible absorption spectrum of $[\text{L}^{\text{S}}\text{Co}^{\text{III}}(\text{PhO}^{\ominus}\text{-N}^{\ominus}\text{-Phz}^{\bullet})(\text{PhO}^{\bullet}\text{-N}^{\ominus}\text{-Phz}^{\bullet})_2]^0$ in CH_2Cl_2 .

Because the ligand can accommodate multiple oxidation levels in the ground state of the cobalt(III) complex, we investigated the redox behavior of $[\text{L}^{\text{S}}\text{Co}^{\text{III}}(\text{PhO}^{\ominus}\text{-N}^{\ominus}\text{-Phz}^{\bullet})(\text{PhO}^{\bullet}\text{-N}^{\ominus}\text{-Phz}^{\bullet})]$ by cyclic voltammetric methods in CH_2Cl_2 with TBA(tetra-*n*-butylammonium) PF_6 as supporting electrolyte. As **Figure 6.4** demonstrates, five quasi-reversible electrochemical responses are observed between 800 and -1300 mV vs. Fc^+/Fc as the internal reference. The two redox couples at -1090 and -870 mV correspond to $\text{PhO}^{\bullet}\text{-N}^{\ominus}\text{-Phz}^{\bullet}/\text{PhO}^{\ominus}\text{-N}^{\ominus}\text{-Phz}^{\ominus}$,²⁷⁻²⁹ and are consistent with the phenoxazinolate being more electron rich than phenolate in the fully reduced $\text{PhO}^{\ominus}\text{-N}^{\ominus}\text{-Phz}^{\ominus}$ state. The first two cathodic processes are followed at more positive potentials (-500 and -260 mV) by phenolate oxidation, $\text{PhO}^{\bullet}\text{-N}^{\ominus}\text{-Phz}^{\bullet}/\text{PhO}^{\ominus}\text{-N}^{\ominus}\text{-Phz}^{\bullet}$.³⁰⁻³² This description supports

qualitatively the proposed electronic structure, which has two phenoxazinyl-based radicals and one phenoxy-based radical. The redox process at 370 mV is presumably the formal oxidation of the amide ($\text{PhO}^{\bullet}\text{-N}^{\bullet}\text{-Phz}^{\bullet}/\text{PhO}^{\bullet}\text{-N}^{\bullet}\text{-Phz}^{\bullet}$), though the remaining charge may be quite delocalized. One further oxidation is observed at 650 mV, though this process is highly irreversible and seems to correspond to transfer of more than one electron. If correct, this scheme suggests that the $[\text{LS}^{\text{III}}\text{Co}^{\text{III}}(\text{PhO}^{\bullet}\text{-N}^{\bullet}\text{-Phz}^{\bullet})(\text{PhO}^{\bullet}\text{-N}^{\bullet}\text{-Phz}^{\bullet})]$ complex can access oxidation states ranging from 2+ to 3- with no metal-based redox events. We are currently pursuing a detailed experimental and computational characterization of the intermediate oxidation states within this redox series, aiming to compare them to the redox behavior of the manganese species with uncyclized ligands, $[\text{Mn}(\text{HL})_2]$.

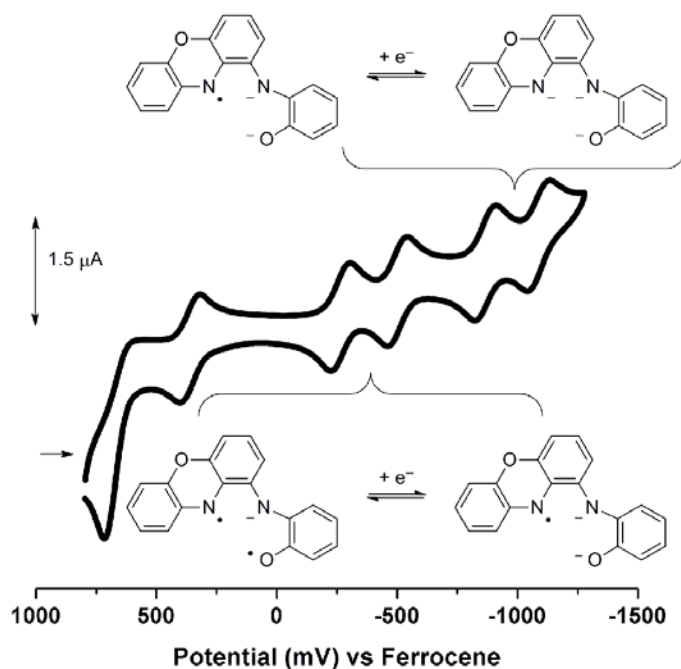


Figure 6.4. CV trace in CH_2Cl_2 , with 0.1 M TBAPF_6 , and 1.0×10^{-3} M $[\text{LS}^{\text{III}}\text{Co}^{\text{III}}(\text{PhO}^{\bullet}\text{-N}^{\bullet}\text{-Phz}^{\bullet})(\text{PhO}^{\bullet}\text{-N}^{\bullet}\text{-Phz}^{\bullet})]$, 150 mV s^{-1} ; mV vs. Fc^+/Fc . Insets are representations of the cathodic ligand redox events, with only one resonance structure shown for each.

6.3. Conclusions

In summary, we have reported a serendipitous functionalization of the redox-active ligand H₄L in the presence of a cobalt(II) salt affording the new mixed phenoxazinylate/phenoxyate ligand L'. Multiple oxidation levels were accessible within this ligand when templated to a ^{LS}Co^{III} metal center in a 2:1 ratio, which DFT describes as [^{LS}Co^{III}(L¹⁻)(L²⁻)]. We anticipate the rich redox chemistry exhibited by this bisligated complex, with five reversible, one-electron responses, to be an important electron reservoir motif towards our ultimate goal of multimetallic catalytic assemblies.

6.4. Experimental Section

Methods and materials used in this chapter are listed in **Section 2.1 of Chapter 2**.

6.4.1. Syntheses. Preparation of the H₄L ligand. H₄L was prepared as described by Chaudhuri *et al.*,² incorporating the purification steps recommended by Heyduk and co-workers⁴ to result in *ca.* 50% overall yield.

6.4.2. Preparation of [^{LS}Co^{III}(PhO⁻-N⁻-Phz')(PhO[•]-N⁻-Phz')]. Anhydrous CoCl₂ (0.130 g, 1 mmol) and Et₃N (0.2 mL) were added to a solution of H₄L (0.517 g, 1 mmol) in CH₃CN (25 mL) and the resultant mixture was refluxed for 1 h followed by stirring at ambient temperature for 4 h while exposed to air. A dark brown microcrystalline solid was collected by filtration and washed with CH₃CN. Yield: 40%. Elemental analysis calcd (%) for [C₆₈H₈₆CoN₄O₄]: C 75.18, H 8.35, N 5.16; found: C 74.90, H 8.05, N 5.10. IR data (KBr, cm⁻¹): 2955, 2906, 2869 (νC-H, ^tBu), 1528, 1479, 1457 (νC-O/νC-N, Phz/PhO). UV-visible (CH₂Cl₂, 1.0 × 10⁻³ M): 271 (88,770); 387 sh (16,630); 474 sh (9,660); 871 (9,690). ESI⁺-MS data (in CH₂Cl₂): *m/z* = 1082.61 (100%) for [M + H]⁺.

6.4. References

- 1 Dzik, W. I.; van der Vlugt, J. I.; Reek, J. N. H.; de Bruin, B. "Ligands that Store and Release Electrons during Catalysis." *Angew. Chem. Int. Ed.* **2011**, *50*, 3356.
- 2 Chaudhuri, P.; Hess, M.; Müller, J.; Hildenbrand, K.; Bill, E.; Weyhermüller, T.; Wieghardt, K. "Oxidation of Primary Alcohols (Including Methanol) by Copper(II)- and Zinc(II)-Phenoxy Radical Catalysts." *J. Am. Chem. Soc.* **1999**, *121*, 9599.
- 3 Blackmore, K. J.; Lal, N.; Ziller, J. W.; Heyduk, A. F. "Catalytic Reactivity of a Zirconium(IV) Redox-Active Ligand Complex with 1,2-Diphenylhydrazine." *J. Am. Chem. Soc.* **2008**, *130*, 2728.
- 4 Blackmore, K. J.; Lal, N.; Ziller, J. W.; Heyduk, A. F. "Group IV Coordination Chemistry of a Tetradentate Redox-Active Ligand in Two Oxidation States." *Eur. J. Inorg. Chem.* **2009**, *6*, 735.
- 5 Zelikoff, A. L.; Kopilov, J.; Goldberg, I.; Coates, G. W.; Kol, M. "New Facets of an Old Ligand: Titanium and Zirconium Complexes of Phenylenediamine Bis(phenolate) in Lactide Polymerisation Catalysis." *Chem. Commun.* **2009**, 6804.
- 6 Chirik, P. J.; Wieghardt, K. "Radical Ligands Confer Nobility on Base-Metal Catalysts." *Science* **2010**, *327*, 794.
- 7 Smith, A. L.; Hardcastle, K. I.; Soper, J. D. "Redox-Active Ligand-Mediated Oxidative Addition and Reductive Elimination at Square Planar Cobalt(III): Multielectron Reactions for Cross-Coupling." *J. Am. Chem. Soc.* **2010**, *132*, 14358.

- 8 Ivakhnenko, E. P.; Starikov, A. G.; Minkin, V. I.; Lyssenko, K. A.; Antipin, M. Y.; Simakov, V. I.; Korobov, M. S.; Borodkin, G. S.; Knyazev, P. A. "Synthesis, Molecular and Electronic Structures of Six-Coordinate Transition Metal (Mn, Fe, Co, Ni, Cu, and Zn) Complexes with Redox-Active 9-Hydroxyphenoxazin-1-one Ligands." *Inorg. Chem.* **2011**, *50*, 7022.
- 9 Gegiou, D.; Huber, J. R.; Weiss, K. "Photochemistry of Phenoxazine. Flash-Photolytic Study." *J. Am. Chem. Soc.* **1970**, *92*, 5058.
- 10 Barry, C. E.; Nayar, P. G.; Begley, T. P. "Phenoxazinone Synthase: Enzymatic Catalysis of an Aminophenol Oxidative Cascade." *J. Am. Chem. Soc.* **1988**, *110*, 3333.
- 11 Mukherjee, C.; Weyhermüller, T.; Bothe, E.; Rentschler, E.; Chaudhuri, P. A. "Tetracopper(II)-Tetraradical Cuboidal Core and Its Reactivity as a Functional Model of Phenoxazinone Synthase." *Inorg. Chem.* **2007**, *46*, 9895.
- 12 Karlsson, K. M.; Jiang, X.; Eriksson, S. K.; Gabrielsson, E.; Rensmo, H.; Hagfeldt, A.; Sun, L. "Phenoxazine Dyes for Dye-Sensitized Solar Cells and Relationship Between Molecular Structure and Electron Lifetime." *Chem. Eur. J.* **2011**, *17*, 6415.
- 13 DeLearie, L. A.; Haltiwanger, R. C.; Pierpont, C. G. "Divalent Rhenium Coordination to Two Radical Schiff-base Quinone Ligands." *Inorg. Chem.* **1989**, *28*, 644.
- 14 Simpson, C. L.; Boone, S. R.; Pierpont, C. G. "Charge Distribution in Transition-Metal Complexes of a Schiff Base Biquinone Ligand. Structural and

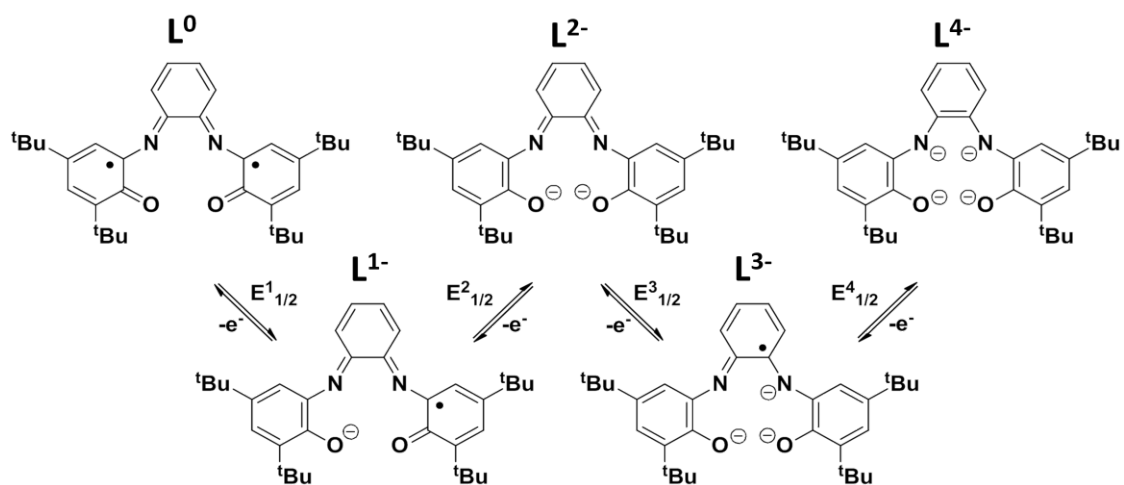
- Electrochemical Properties of the $M^{\text{II}}(\text{Cat-N-BQ})_2M^{\text{III}}(\text{Cat-N-BQ})(\text{Cat-N-SQ})M^{\text{IV}}(\text{Cat-N-SQ})_2$ Tautomeric Series.” *Inorg. Chem.* **1989**, 28, 4379.
- 15 See **Appendix D** for a Scheme outlining all oxidation states of L' in terms of PhO, N, and Phz.
- 16 Jeffery, J. C.; Schatz, E.; Ward, M. D. “The Coordination Chemistry of Mixed Pyridine-Phenol Ligands; Synthesis of 6-(2-Hydroxyphenyl)-2,2'-bipyridine (HL) and the Crystal Structures of $[\text{Cu}_2\text{L}_2(\mu\text{-MeCO}_2)][\text{PF}_6] \cdot 1.5\text{CH}_2\text{Cl}_2$ and $[\text{CoL}_2][\text{PF}_6] \cdot \text{MeCN}$.” *J. Chem. Soc., Dalton Trans.* **1992**, 1921.
- 17 Verani, C. N.; Gallert, S.; Bill, E.; Weyhermuller, T.; Wieghardt, K.; Chaudhuri, P. “[Tris(*o*-Iminosemiquinone)Cobalt(III)] - A Radical Complex with an $S_t = 3/2$ Ground State.” *Chem. Commun.* **1999**, 1747.
- 18 Shakya, R.; Imbert, C.; Hratchian, H. P.; Lanznaster, M.; Heeg, M. J.; McGarvey, B. R.; Allard, M.; Schlegel, H. B.; Verani, C. N. “Structural, Spectroscopic, and Electrochemical Behavior of *trans*-Phenolato Cobalt(III) Complexes of Asymmetric NN'O Ligands as Archetypes for Metallomesogens.” *Dalton Trans.* **2006**, 2517.
- 19 Stegmann, H. B.; Scheffler, K. “Electron Spin Resonance Studies of a Model Phenoxazine Synthesis.” *Chem. Ber.* **1968**, 101, 262.
- 20 Monoligated Fe and bisligated Mn complexes of uncyclized H_4L have been synthesized and characterized structurally. ORTEP diagrams for each may be found in **Chapter 7** and **Appendix D**, respectively.
- 21 Busch, D. H.; Alcock, N. W. “Iron and Cobalt “Lacunar” Complexes as Dioxygen Carriers.” *Chem. Rev.* **1994**, 94, 585.

- 22 Calculations at the B3LYP/6-31G(d,p) level of theory were conducted on a model where ^tBu groups have been replaced by H for computational efficiency. See **Appendix D** for full details.
- 23 Neese, F. J. "Definition of Corresponding Orbitals and the Diradical Character in Broken Symmetry DFT Calculations on Spin Coupled Systems." *Phys. Chem. Solids* **2004**, *65*, 781.
- 24 Paulsen, H.; Trautwein, A. X. *Spin Crossover in Transition Metal Compounds*; Springer-Verlag: Berlin, **2004**; vol. 235, p 197.
- 25 Lord, R. L.; Schultz, F. A.; Baik, M.-H. "Spin Crossover-Coupled Electron Transfer of $[M(\text{tacn})_2]^{3+/2+}$ Complexes (tacn = 1,4,7-Triazacyclononane; M = Cr, Mn, Fe, Co, Ni)." *J. Am. Chem. Soc.* **2009**, *131*, 6189.
- 26 TD-B3LYP/6-311+G(d,p)//B3LYP/6-31G(d,p) with IEF-PCM/CH₂Cl₂. See **Appendix D** for transition assignments. An error of 130 nm seems large, but this is only 0.2 eV on an energy scale and consistent with the accuracy of the methodology.
- 27 Whalen, A. M.; Bhattacharya, S.; Pierpont, C. G. "Iminoquinone Complexes of Iron and Nickel. Structural, Magnetic, and Electrochemical Properties of Complexes Containing the Phenoxazinolate Semiquinone Radical." *Inorg. Chem.* **1994**, *33*, 347.
- 28 Speier, G.; Whalen, A. M.; Csihony, J.; Pierpont, C. G. "Iminosemiquinone Complexes of Copper, Structural, Magnetic, and Electrochemical Characterization of Complexes of the Phenoxazinolate Semiquinone Radical." *Inorg. Chem.* **1995**, *34*, 1355.

- 29 Bhattacharya, S.; Pierpont, C. G. "Semiquinone Imine Complexes of Ruthenium. Coordination and Oxidation of the 1-Hydroxy-2,4,6,8-tetra-*tert*-butylphenoxazinyl Radical." *Inorg. Chem.* **1992**, *31*, 2020.
- 30 Chaudhuri, P.; Verani, C. N.; Bill, E.; Bothe, E.; Weyhermüller, T.; Wieghardt, K. "Electronic Structure of Bis(*o*-iminobenzosemiquinonato)metal Complexes (Cu, Ni, Pd). The Art of Establishing Physical Oxidation States in Transition-Metal Complexes Containing Radical Ligands." *J. Am. Chem. Soc.* **2001**, *123*, 2213.
- 31 Sik Min, K.; Weyhermüller, T.; Wieghardt, K. "Coordination Chemistry of 2-(8-aminoquinolino)-4,6-di-*tert*-butylphenol with Manganese(IV), Iron(III), and Cobalt(II/III): N,O-coordinated *o*-Iminobenzosemiquinonate(1-) Pi Radical Monoanions vs. *o*-Iminophenolate(2-) Dianions." *Dalton Trans.* **2004**, 178.
- 32 Mukherjee, S.; Weyhermüller, T.; Bill, E.; Wieghardt, K.; Chaudhuri, P. "Tuning of Spin Transition in Radical-Containing Iron(III) Complexes by Remote Ligand Substituents." *Inorg. Chem.* **2005**, *44*, 7099.

Chapter 7

THE RICH ELECTRON TRANSFER BEHAVIOR OF IRON(III) AND GALLIUM(III) COMPLEXES WITH A REDOX-ACTIVE BIS(PHENOLATE) PHENYLENEDIAMINE LIGAND



CHAPTER 7

THE RICH ELECTRON TRANSFER BEHAVIOR OF IRON(III) AND
GALLIUM(III) COMPLEXES WITH A REDOX-ACTIVE BIS(PHENOLATE)
PHENYLENEDIAMINE LIGAND

Frank D. Lesh, Richard L. Lord, Mary Jane Heeg, H. Bernhard Schlegel, and
Cláudio N. Verani*

The iron and gallium results described here are in preparation for submission to
Inorganic Chemistry as a full paper.

Contributions to this work on my part included the synthetic, spectroscopic, and
electrochemical characterizations along with the original draft of the manuscript.

7.1. Introduction

Ligand platforms capable of forming radical species when coordinated to transition metals cooperatively merge distinctive electronic, redox, and spectroscopic behavior. Extensive attention has been focused on the design of redox-active ligands to enhance the reaction chemistry of coordination compounds with early transition metals to induce noble-transition-metal reactivity.¹⁻³ Of these, one intriguing example that has left a substantial impact is the prevalently investigated *N,N'*-bis(3,5-di-*tert*-butyl-2-hydroxyphenyl)-1,2-phenylenediamine ligand, denoted as H₄L. The widespread attention that this ligand has received is based on the rich electrochemical and spectroscopic responses observed when bound to various metal centers. Multiple oxidation levels, with distinctly associated spin states, are energetically available to such systems that offer the capacity to act as electron reservoirs.³ The peculiar electronic nature inherent to redox-

active transition metal complexes merely complicates the proper assignment and identification of the diverse redox states observed.⁴

Owing to the appealing multi-electron reactivity derived from the intrinsic ligand-centered phenomena, prior studies have exploited this robust H₄L framework for its catalytic behavior. Initially, square planar complexes of Cu(II) and Zn(II) were prepared as effective catalyst models for the selective aerobic oxidation capability of the metalloenzyme galactose oxidase.⁵ Recent accounts establish the viability of d⁰ group IV metal centers coordinated to this ligand precursor for active multi-electron catalysis supported by ligand-based valence changes, including disproportionation of diphenylhydrazine and hetero-selective polymerization of *rac*-lactide.⁶⁻⁸ In parallel, considerable interest has been focused on the implication of semiquinonate, catecholate, and diimine scaffolds for serving as candidates for such dynamic concepts of spin-crossover and bistable molecular information storage given the capacity for interconversion between degenerated electronic states.⁹⁻¹¹

Thus far, only 1:1 complexes of L²⁻ (H₄L → L²⁻ + 2e⁻ + 2H⁺) with early (d⁹-Cu^{II}, d¹⁰-Zn^{II}) and late (d⁰-Ti^{IV}, d⁰-Zr^{IV}) transition metals have been described. In this chapter, the H₄L ligand is reacted with selected trivalent (d⁵-Fe^{III}, d¹⁰-Ga^{III}) metal ions to consequently lead to five- and six-coordinate complexes, respectively. Herein we spotlight an unprecedented oxidation state of L²⁻ when complexed to a metal ion and discuss the distinct structural and spectroscopic features observed.

7.2. Results and Discussion

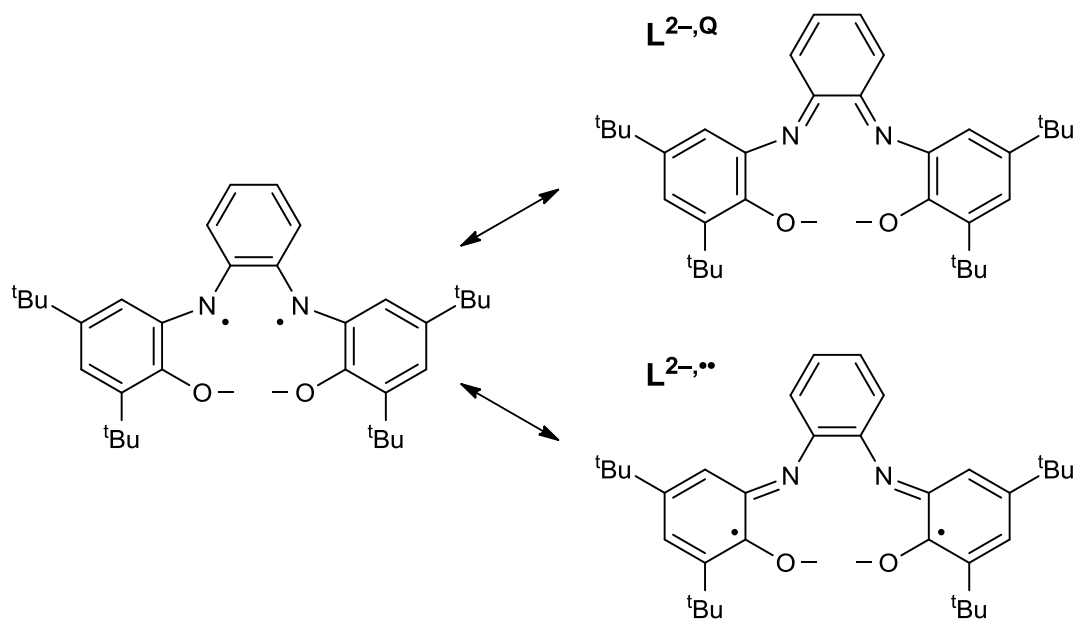
7.2.1. Syntheses and Characterizations. As established by Chaudhuri and co-workers,⁵ the condensation of 3,5-di-*tert*-butylcatechol and *o*-phenylenediamine (2:1)

together with a catalytic amount of Et₃N in *n*-heptane generates the ligand *N,N'*-bis(3,5-di-*tert*-butyl-2-hydroxyphenyl)-1,2-phenylenediamine, H₄L, after 4 days of stirring at ambient temperature under aerobic conditions. Purification steps described by Blackmore *et al.*⁷ were incorporated. Experimental analyses of H₄L are in agreement with the prior published data. General synthetic methodologies^{12,13} were tailored for complexation of H₄L with select trivalent metal chloride salts. Reaction of GaCl₃ with the H₄L ligand (1:1) employing Schlenk conditions in dry CH₃OH with a catalytic amount of Et₃N produced a pink-colored solution. Exposure to compressed O₂ yielded a dark violet solution from which a dark microcrystalline solid of [Ga(L)(Cl)(CH₃OH)] (**1**) resulted. Equimolar treatment of FeCl₃·6H₂O with H₄L in the presence of Et₃N under aerobic conditions in CH₃CN affords a blue-green microcrystalline precipitate of [Fe(L)(Cl)] (**2**).

Characterization of compounds **1** and **2** consisted of electrospray ionization (ESI⁺) mass spectrometry, elemental analysis, cyclic voltammetry, variable-temperature magnetic susceptibility measurements, as well as infrared, UV–visible, and electron paramagnetic resonance (EPR) spectroscopies. Density functional theory (DFT) calculations provided valuable insight to assist in the interpretation of the electronic structures of these species (see Appendix E for details). Elemental analyses of **1** and **2** show excellent agreement to the theoretical percentages, and the ESI⁺ mass spectra exhibit the pertinent *m/z* peak clusters for the compositions correlating to [Ga(C₃₄H₄₄N₂O₂)(CH₃OH) – Cl]⁺ for **1** and [Fe(C₃₄H₄₄N₂O₂) – Cl]⁺ for **2** in CH₂Cl₂. The absence of characteristic frequency bands beyond 3300 cm⁻¹ in the infrared spectra further establishes complex formation for each case. These bands are ascribed to the ν(N–H) and ν(O–H) vibrational modes that appear only in the spectrum of the protonated form

of the ligand. $^1\text{H-NMR}$ spectroscopy suggests species **1** is diamagnetic and species **2** is paramagnetic. Crystals of **1** and **2** suitable for X-ray diffractometry were recrystallized from 1:1 mixtures of $\text{CH}_2\text{Cl}_2:\text{CH}_3\text{OH}$ and $\text{CH}_2\text{Cl}_2:\text{CH}_3\text{CN}$, respectively.

7.2.2. Molecular and Electronic Structures. Previous work with H_4L led to the synthesis, isolation, and characterization of 1:1 complexes of L^{2-} ($\text{H}_4\text{L} \rightarrow \text{L}^{2-} + 2\text{e}^- + 2\text{H}^+$) with early and late transition metals to afford four-coordinate ($d^9\text{-Cu}^{\text{II}}$, $d^{10}\text{-Zn}^{\text{II}}$) and six-coordinate ($d^0\text{-Ti}^{\text{IV}}$, $d^0\text{-Zr}^{\text{IV}}$) species, respectively. Cyclic voltammetry suggests five redox states are accessible to the coordinated ligand. In the isolated examples of these complexes, the ligand is usually in a 2- oxidation state. Starting from the reduced and fully deprotonated ligand, L^{4-} , oxidation should occur at anionic N before O due to differences in electronegativity (**Scheme 7.1**, left). From this canonical starting point, one can envision resonance isomers representing an *o*-diiminoquinone at the phenylenediamine moiety (**Scheme 7.1**, top right) or an *o*-diiminocatechol bridge with two phenolate radicals (**Scheme 7.1**, bottom right). Herein we distinguish these as $\text{L}^{2-\text{Q}}$ and $\text{L}^{2-\text{C}}$, respectively. We have only drawn one of the possible phenolate radical resonance isomers. The conjugation pattern at the top right of **Scheme 7.1** was deduced from extensive experimental characterization for the known ML complexes.



Scheme 7.1. Resonance isomers of H_4L .

Our structures serve to fill the gap between M^{II} and M^{IV} complexes to see how binding of this ligand changes with metal oxidation state. The ORTEP diagrams for **1** and **2** are presented in **Figure 7.1**, and selected bond lengths and angles are listed in **Table 7.1** with comparisons to the previously known L^{2-} adducts. More extensive lists of bond lengths and angles for **1** and **2** may be found in **Appendix E (Table E.7.1)**. Gallium is unquestionably in the d^{10} - Ga^{III} oxidation state, however, iron has multiple oxidation and spin states available.

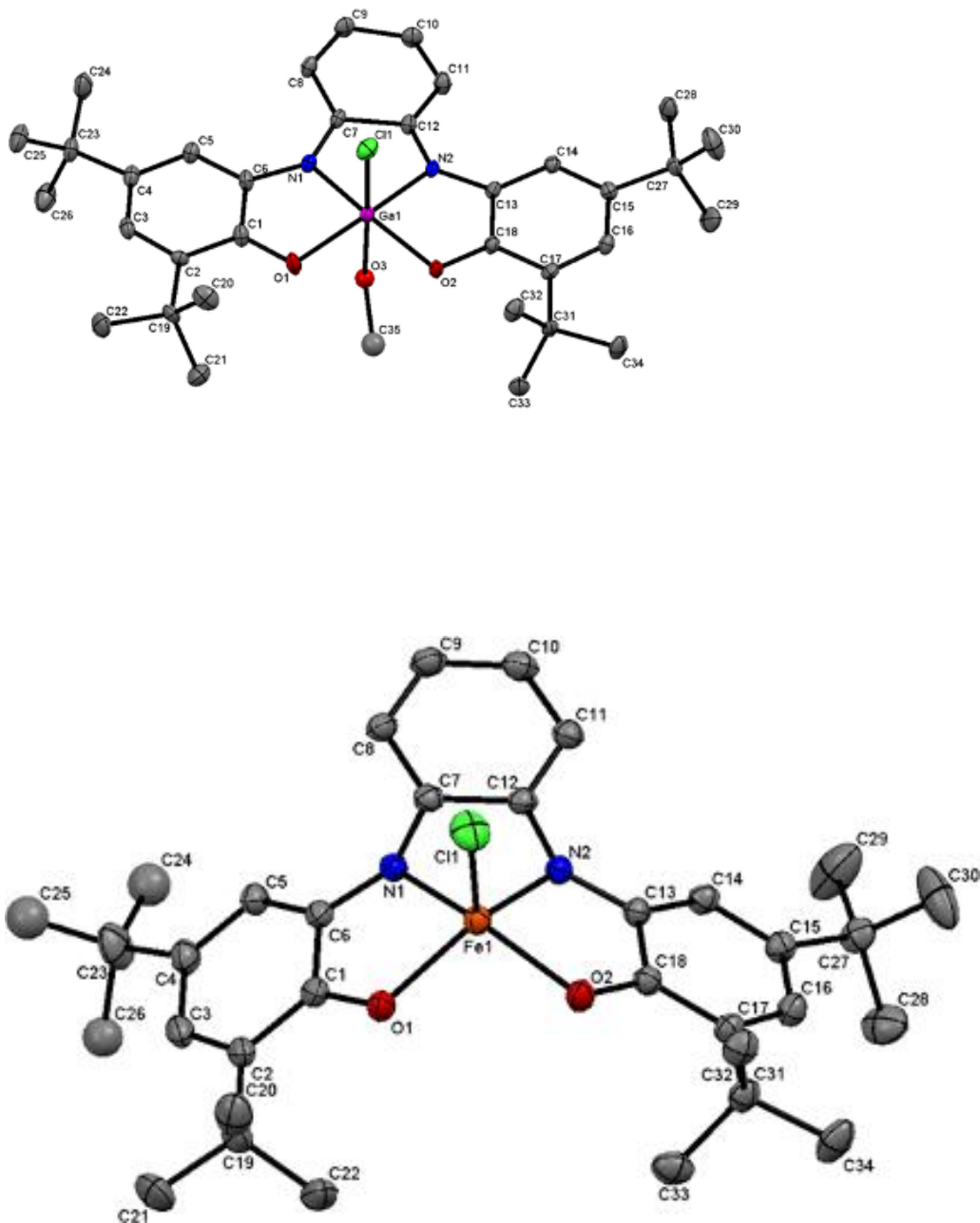
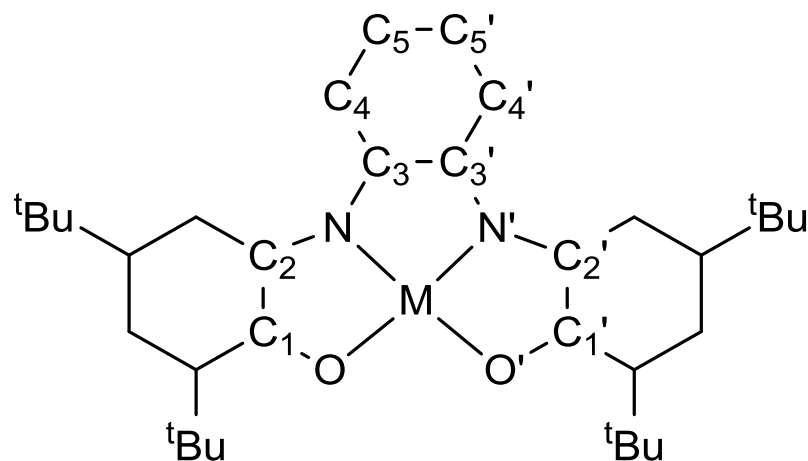


Figure 7.1. Perspective view ORTEP diagrams for **1** (top) and **[2]·0.5CH₃CN·0.5CH₂Cl₂** (bottom) showing 50% probability of the thermal ellipsoids. Non-coordinated solvents and hydrogen atoms are excluded for clarity. Selected bond distances (Å) for **1**: Ga(1)-O(2) 1.877(3), Ga(1)-O(1) 1.880(3), Ga(1)-N(1) 2.024(3), Ga(1)-N(2) 2.025(3), Ga(1)-Cl(1) 2.224(12), Ga(1)-O(3) 2.329(6). For **2**: Fe(1)-O(2) 1.942(11), Fe(1)-O(1) 1.948(11), Fe(1)-N(1) 2.022(13), Fe(1)-N(2) 2.044(13), Fe(1)-Cl(1) 2.220(5).

Table 7.1. Structural comparison of the M–L and some intraligand bond lengths (Å).



Å	M–O	M–N	O–C1	C1–C2	C2–N	N–C3	C3–C3'	C3–C4	C4–C5	C5–C5'	O–C1
Ga^{III}	1.88	2.02	1.32	1.44	1.38	1.32	1.49	1.43	1.35	1.43	1.32
Fe^{III}	1.95	2.03	1.30	1.45	1.34	1.39	1.42	1.40	1.39	1.39	1.30
^a Cu^{II}	1.93	1.94	1.31	1.45	1.37	1.34	1.47	1.43	1.36	1.42	1.31
^a Zn^{II}	1.93	1.94	1.32	1.45	1.37	1.34	1.48	1.43	1.36	1.43	1.32
^b Ti^{IV}	1.87	2.11	1.33	1.42	1.39	1.34	1.48	1.43	1.35	1.44	1.33
^c Zr^{IV}	2.09	2.30	1.33	1.42	1.39	1.34	1.46	1.42	1.36	1.42	1.33
^d Avg.	--	--	1.33	1.44	1.38	1.34	1.48	1.43	1.36	1.43	1.33

^a reference 5; ^b reference 7; ^c reference 6; ^d Averages of Ti, Zr, Zn an Cu structures

The coordination environment for the gallium(III) center in the neutral molecular structure of **1** is approximately octahedral, where the fully deprotonated ligand is equatorially coordinated through an N₂O₂ donor set and the axial positions are occupied by a chlorido ligand (Ga–Cl 2.22 Å) and a bound solvent molecule of methanol (Ga–O_{MeOH} 2.33 Å). We assign this ligand as methanol versus methoxide based on the 2.33 Å bond length that falls outside the range of Ga^{III}–O_{alkoxide} distances (1.91–2.10 Å).¹⁴ The N₂O₂ macrocycle is approximately planar as evidenced by a side-on, in-plane view of **1** (**Figure E.7.1**). Moreover, the gallium(III) ion sits slightly above the equatorial plane positioned towards the apical chlorido ligand. Within the macrocyclic pocket the Ga–O and Ga–N bond lengths of 1.88 and 2.03 Å¹⁵ indicate that the metal is off-centered towards the oxygens. This is further supported by the interplane angles composed of adjacent corner atoms of the GaN₂O₂ core (N–Ga–N' 79.5°, O'–Ga–N' 83.9°, O'–Ga–O 105.0°, and O–Ga–N 83.6°). Based on these coordination sphere metrics, we conclude that we have Ga^{III}, Cl⁻, CH₃OH, and L²⁻.

Within the coordinated ligand L²⁻, characteristic localized double bonds are found for N–C3 (1.32 Å) and C4–C5 (1.35 Å) while single bonds are observed for C2–N (1.38 Å), C3–C3' (1.49 Å), C3–C4 (1.43 Å), and C5–C5' (1.43 Å). These values match well with the averaged intraligand bond lengths for previously reported structures (**Table 7.1**): N–C3 (1.34 Å), C4–C5 (1.36 Å), C2–N (1.38 Å), C3–C3' (1.48 Å), C3–C4 (1.43 Å), and C5–C5' (1.43 Å). Bond lengths within the phenolate arms are also consistent with earlier reports, but they are not diagnostic (*vide infra*). The bonding pattern in the bridging unit is representative of an *o*-diiminoquinone¹⁶ moiety allowing us to conclude that species **1** contains L^{2-,Q}.

X-ray crystallographic structural determination of $[2] \cdot 0.5\text{CH}_3\text{CN} \cdot 0.5\text{CH}_2\text{Cl}_2$ shows a monoligated iron center in an approximate square pyramidal geometry (**Figure 7.1**, $\tau = 0.13^{17}$) with an apical chlorido ligand (Fe–Cl 2.22 Å). An approximate vertical plane of symmetry (σ_v) bisects the basal plane through this chlorido ligand. Angles containing adjacent vertex atoms of the basal plane (N–Fe–N' 75.9°, O'–Fe–N' 78.9°, O'–Fe–O 101.5°, and O–Fe–N 79.2°) reveal a deviation from the expected interplane angles of 90° for a perfect square pyramidal coordination sphere. Thus, five-coordinate iron allows for considerable distortion of the N₂O₂ donor set environment from planarity, in contrast to the six-coordinate gallium(III) species (see **Figure E.7.1** for comparative side-on views). The bond distances of 1.95 and 2.03 Å for Fe–O and Fe–N, respectively, are in agreement with analogous N₂O₂ imino-catecholate donor frameworks and suggest a high-spin d⁵ ferric ion (^{HS}Fe^{III}) in **2**.^{12,18,19} Based on the structural parameters of the ^{HS}Fe^{III} coordination environment and reinforcement by DFT studies (*vide infra*), we assign the ligand oxidation state as 2–. The ligand electronic structure differs from that of all other metal adducts characterized to date.

In our gallium(III) species and the previously reported structures, a characteristic localized bonding pattern in the phenylenediamine moiety, including a short N–C3 and long C2–N bond, points to an *o*-diiminoquinone oxidation state of the bridge (L^{2-,Q}). By contrast, species **2** demonstrates delocalized C–C bonds (1.39–1.42 Å) within the phenylenediamine bridge moiety.¹⁶ More importantly, the N–C3 and C2–N bond lengths of 1.39 and 1.34 Å, respectively, are in direct contrast to previously observed bond lengths (**Table 7.1**). These data indicate collectively that the bridging moiety in **2** should be considered an *o*-diiminocatechol, thereby placing radicals on the phenolate arms and

therefore $L^{2-,**}$. Unfortunately, bonding within the phenolate arms is not diagnostic for the presence or absence of radicals because all C–C bond lengths are ~ 1.4 Å regardless of metal identity (**Table E.7.2**). While the O–C1 bond length in the $^{HS}Fe^{III}$ species is shorter than for Ga^{III} , the difference of only 0.02 Å (1.30 vs. 1.32 Å) is ambiguous. We turned to DFT calculations to test this proposed electronic structure of a $^{HS}Fe^{III}$ ion complexed to a ligand with two phenolate radicals.

Calculations were performed at the B3LYP/6-31G(d,p) level of theory employing the IEF-PCM continuum solvation model in a development version of Gaussian. The tBu groups on the phenolate rings are critical experimentally because of their steric protection for the phenolate radicals. We are not likewise restricted computationally, and because tBu and Me groups are almost equally electron donating ($\sigma_{para} = -0.17$ and -0.20 , respectively)²⁰ we simplify our computational models for efficiency. We confirm the electronic structure for the six-coordinate Ga^{III} species by calculating: (i) an overall $S = 0$ state that should converge to an electronic structure similar to $L^{2-,Q}$ and (ii) an open-shell $S = 1$ electronic structure which should correspond to the diradical form $L^{2-,**}$. As the metrics in **Table 7.2** demonstrate, the intraligand bond lengths in $Ga^{III}-L^{2-,Q}$ are more consistent with the X-ray structure than those for $Ga^{III}-L^{2-,**}$, especially the ordering of $C2-N > N-C3$ for $L^{2-,Q}$ but $C2-N < N-C3$ for $L^{2-,**}$ and the more localized bonding of the C–C bonds in the bridging unit. The largest discrepancy between the values in **Table 7.2** for the computed $Ga^{III}-L^{2-,Q}$ structure and experiment is in the Ga–O bond lengths ($\Delta = \sim 0.04$ Å), but still consistent with the methodology accuracy.

Table 7.2. Structural comparison between experiment and computation for the M–L and some intraligand bond lengths (Å). See **Table 7.1** for numbering scheme.

Å	M–O	M–N	O–C1	C1–C2	C2–N	N–C3	C3–C3'	C3–C4	C4–C5	C5–C5'
$\text{Ga}^{\text{III}}_{\text{exp}}\text{-L}^{2-}$	1.88	2.02	1.32	1.44	1.38	1.32	1.49	1.43	1.35	1.43
$\text{Ga}^{\text{III}}_{\text{calc}}\text{-L}^{2-,Q}, S=0$	1.92	2.03	1.32	1.45	1.37	1.33	1.49	1.43	1.37	1.43
$\text{Ga}^{\text{III}}_{\text{calc}}\text{-L}^{2-,**}, S=1$	1.94	2.00	1.31	1.46	1.35	1.38	1.45	1.40	1.39	1.40
$\text{Fe}^{\text{III}}_{\text{exp}}$	1.95	2.03	1.30	1.45	1.34	1.39	1.42	1.40	1.39	1.39
$\text{Fe}^{\text{III}}_{\text{calc}}, S=3/2$	1.96	2.06	1.30	1.46	1.34	1.39	1.44	1.40	1.39	1.40

Multiple oxidation and spin states were tested as guess wavefunctions for the Fe species. The lowest energy neutral species is best described as having a $^{\text{HS}}\text{Fe}^{\text{III}}$ ion antiferromagnetically (AF) coupled to the ligand with an oxidation state consistent with $\text{L}^{2-\bullet}$. The spin density plot of this species is shown in **Figure 7.2**, where excess α density is shaded blue and excess β density is shaded white. Most of the α density is concentrated at Fe/Cl, while the β density is located primarily on the phenolate rings and not the phenylenediamine backbone. Structurally, excellent agreement between the computed and experimental structures is found with the largest deviation being 0.03 Å for the comparatively weak Fe–N bonds, and 0.02 Å within the ligand for C3–C3’.

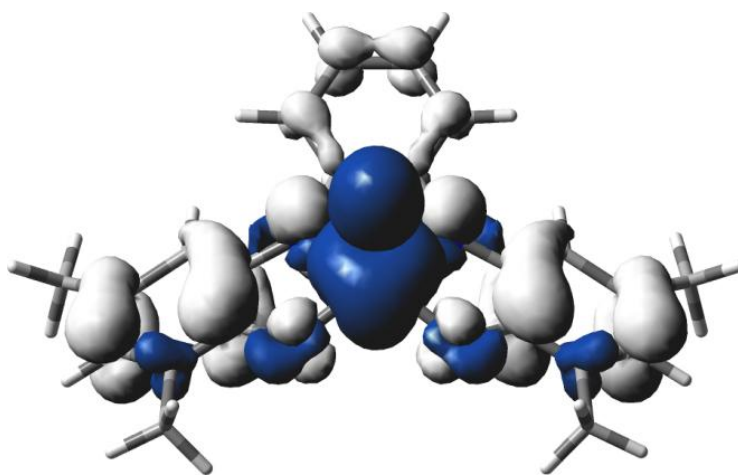


Figure 7.2. Isodensity plot (0.002 au) for the spin density of the lowest energy computed Fe^{III} species. Blue and white correspond to excess α and β density, respectively.

7.2.3. Electronic Spectroscopy. It stands to reason that species **2** should have an electronic absorption spectrum more similar to *o*-iminosemiquinone complexes than species **1** and the other known $\text{L}^{2-\text{Q}}$ metal species. In fact, UV–visible spectroscopic characterization helped distinguish between the different accessible oxidation levels of

single O,N-coordinated *o*-iminophenolate, *o*-iminobenzosemiquinonate, and *o*-iminobenzoquinone ligands.¹⁶ Thus, we measured the UV–visible spectra in 10^{-3} to 10^{-5} M CH_2Cl_2 solutions. Pertinent absorption maxima and molar extinction coefficients are listed in **Table 7.3**. Experimental (solid) and calculated (dashed) absorption spectra for **1** (black) and **2** (grey/red) between 300–1100 nm are shown in **Figure 7.3**. Overall excellent agreement is observed, though the calculated intensities are consistently overestimated.

Table 7.3. UV–visible Parameters for Complexes **1** and **2**.

Complex	Absorption, λ_{abs} (nm) / ϵ ($\text{Lmol}^{-1} \text{cm}^{-1}$) ^a
1	270 (28,450); 334 (14,730); 459 (3,890); 572 (4,990); 697 sh (4,970); 999 (15,980)
2	277 (89,890); 340 (16,950); 455 (7,830); 500 (7,120); 641 (5,600); 856 sh (4,620)

^a Spectra measured in 1.0×10^{-5} M dichloromethane solution.

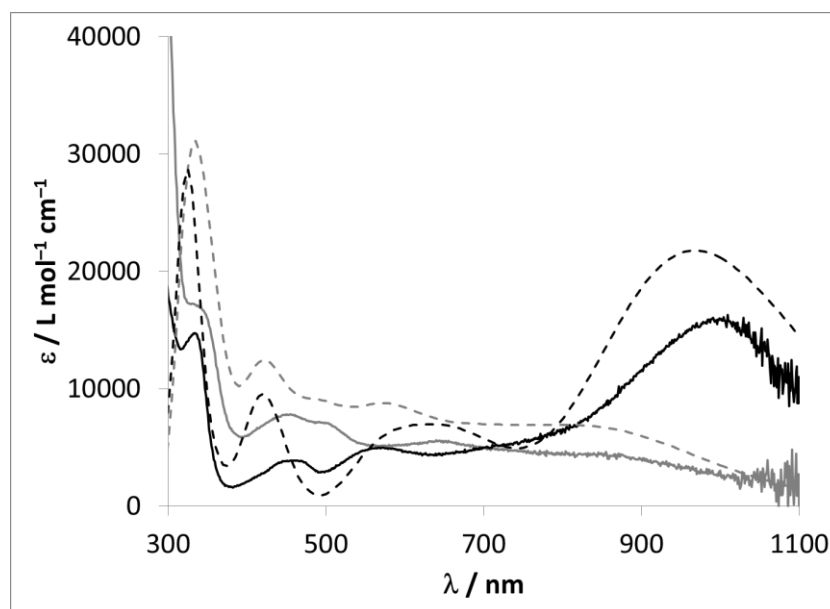


Figure 7.3. Absorption spectra of complexes **1** (black) and **2** (grey) in dichloromethane, 1.0×10^{-5} M. Experimental absorption curves are solid, while TD-DFT fitted curves are dashed.

The ultraviolet region of the spectra for both **1** and **2** demonstrate intraligand $\sigma \rightarrow \pi^*$ and $\pi \rightarrow \pi^*$ bands with maxima centered near 275 and 335 nm. For **1**, the low-energy region of the spectrum is dominated by an intense band at ~ 1000 nm ($15980 \text{ L mol}^{-1} \text{ cm}^{-1}$). This absorption band has likewise been observed in for Zn^{II} ⁵ and group IV metal complexes⁷ containing $\text{L}^{2-\text{Q}}$, but is noticeably absent for the iron species **2**. TD-DFT calculations show a transition at ~ 970 nm corresponding to a phenolate $\pi \rightarrow o$ -diiminoquinone π^* transition (HOMO \rightarrow LUMO), and thus explaining the absence of such a transition for $^{\text{HS}}\text{Fe}^{\text{III}}\text{-L}^{2-\text{Q}}$ which lacks the diiminoquinone functionality. Orbital excitations for the principle components of the absorption bands may be found in **Table E.7.3** of **Appendix E**. The bands observed at 459, 572, and 697(sh) nm (3890 , 4990 , and $4970 \text{ L mol}^{-1} \text{ cm}^{-1}$, respectively) are also assigned to phenolate $\pi \rightarrow o$ -diiminoquinone π^* transitions involving lower lying occupied orbitals (HOMO-3 to HOMO-1) based on computed transitions at 423, 576, and 673 nm. Four maxima are observed for **2** between 450-900 nm with relatively low intensity molar absorptivities ($\epsilon < 10^4 \text{ M}^{-1} \text{ cm}^{-1}$). This fingerprint agrees well with earlier reports of $^{\text{HS}}\text{Fe}^{\text{III}}$ complexes with *o*-imino-semiquinonate ligands.¹⁶ These bands arise from a complicated mixture of ligand-to-metal charge transfer (LMCT) and intraligand excitations. The shoulder at 856 nm ($4620 \text{ L mol}^{-1} \text{ cm}^{-1}$) comprises nearly equal contributions of both types based on a computed transition at 880 nm. The band at 641 nm ($5600 \text{ L mol}^{-1} \text{ cm}^{-1}$) is mostly MLCT based on a computed band at 683 nm. Peaks at 455 and 500 nm (7830 and $7120 \text{ L mol}^{-1} \text{ cm}^{-1}$) are intraligand $\pi \rightarrow \pi^*$ transitions with up to 30% MLCT character, based on computed peaks at 422 and 497 nm, respectively.

7.2.4. Electrochemistry. The cyclic voltammogram (CV) of **2** in CH₂Cl₂ with 0.1 M TBA(tetra-*n*-butylammonium)PF₆ supporting electrolyte at a scan rate of 100 mV s⁻¹ exhibits a single one-electron-transfer anodic wave and two one-electron-transfer cathodic process with potentials referenced versus the ferrocenium/ferrocene Fc⁺/Fc couple (Figure 7.4).

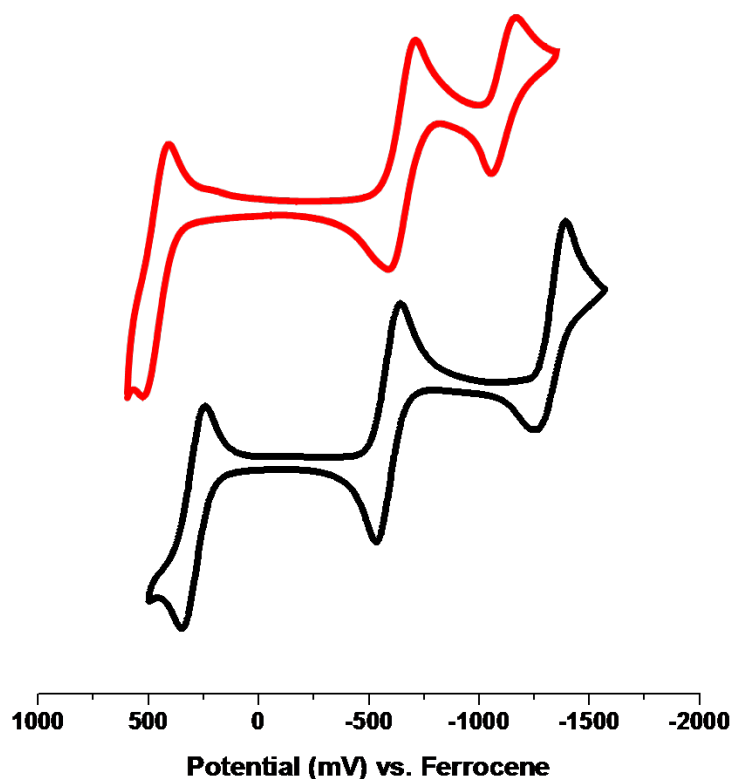


Figure 7.4. CVs of **1** and **2** in dichloromethane, TBAPF₆, vs Fc⁺/Fc.

Of the three successive redox waves, the first two are associated with reversible oxidative couples and the third corresponds to a quasi-reversible reductive process. All of these redox couples are ascribed to be ligand-centered processes based on the potential values comparable to those observed in **1** (Table 7.4).

Table 7.4. Cyclic voltammetry data for **1** and **2**.^[a]

Complex	Reductions ^[b]	Oxidations ^[c]
	$E_{1/2} (\Delta E_p)$ [V], $ I_{pc}/I_{pa} $	$E_{1/2} (\Delta E_p)$ [V], $ I_{pc}/I_{pa} $
1	-1.13 (0.10), 1.50 ; -0.66 (0.12), 1.05	0.47 (0.09), 0.12
2	-1.33 (0.12), 2.07 ; -0.59 (0.11), 1.00	0.30 (0.10), 0.70

^[a] CVs of **1** and **2** at 1.0×10^{-3} mol L⁻¹ in dichloromethane with 0.1 M TBAPF₆ supporting electrolyte using a scan rate of 100 mV s⁻¹ for **1** and **2** at RT in an inert atmosphere. ^[b] Potentials listed as the cathodic peak potential E_{pc} versus Fc⁺/Fc. ^[c] Potentials listed as the anodic peak potential E_{pa} versus Fc⁺/Fc.

It has been previously demonstrated that complexes of the H₄L ligand,⁵ and other related systems,¹⁶ display similar redox potentials irrespective of the nature of the coordinated metal. The observed redox equilibria in **2** is nearly consistent with analogous complexes containing three O,N-coordinated *o*-iminobenzosemiquinonate(1-) π radical anions (L^{ISQ})⁻ about a central iron(III) metal ion.^{21,22} Therefore, the processes occurring at $E_{1/2} = 0.30$ V ($\Delta E_p = 0.10$; $|I_{pc}/I_{pa}| = 0.70$) and -0.59 V ($\Delta E_p = 0.11$; $|I_{pc}/I_{pa}| = 1.00$) vs. Fc⁺/Fc can be tentatively assigned to the respective *o*-iminobenzosemiquinonate/*o*-iminobenzoquinone oxidative couples observed. Accordingly, the wave appearing at $E_{1/2} = -1.33$ V ($\Delta E_p = 0.12$; $|I_{pc}/I_{pa}| = 2.07$) vs. Fc⁺/Fc is suggestive of the complementary *o*-iminobenzosemiquinonate/*o*-imino-phenolate reductive process.

8.3. Summary

Based on the evidence gathered to this point, we conclude that **1** can be best described as the six-coordinate [Ga^{III}(L^{2-,Q})(CH₃OH)(Cl)] complex containing the previously documented *o*-diiminoquinone oxidation state of the phenylenediamine bridge moiety. Preliminary magnetic and EPR measurements were made to test the prediction of a strongly antiferromagnetically coupled system for compound **2**. The magnetic data corroborate an overall spin state of $S = 3/2$ derived from two $S = 1/2$ organic radicals

strongly antiferromagnetically coupled to the iron(III) center with $S = 5/2$. From the collective structural, computational, magnetic, and EPR data, we deduce that **2** is best described as the five-coordinate $[\text{HSFe}^{\text{III}}(\text{L}^{2-,\bullet\bullet})(\text{Cl})]$ species comprised of the *o*-diiminocatechol form of the bridging moiety with radicals on the phenolate arms.

8.4. Experimental Section

Methods and materials used in this chapter are listed in **Section 2.1** of **Chapter 2**.

8.4.1. X-ray Structural Determinations for 1 and 2. Diffraction data were measured on a Bruker *X8 APEX-II* kappa geometry diffractometer with Mo radiation and a graphite monochromator. Frames were collected at 100 K with the detector at 40 mm and 0.3 degrees between each frame and were recorded for 10 s unless otherwise noted. *APEX-II*²³ and *SHELX*²⁴ software were used in the collection and refinement of the models. **Table 7.5** shows the collected crystal data for structures **1** and **2**.

Compound $[\text{Ga}(\text{L})(\text{Cl})(\text{CH}_3\text{OH})]$ (**1**) crystallized as colorless dark green plates. Harvested were 38062 hkl data points, which averaged to 8161 data ($R_{\text{int}} = 0.053$). Hydrogen atoms were calculated or observed. The solvent region contains a disordered molecule of methanol, distributed into 2 half-occupancy positions which were kept isotropic during refinement. Crystals of $[\text{Fe}(\text{L})(\text{Cl})] \cdot 0.5\text{CH}_3\text{CN} \cdot 0.5\text{CH}_2\text{Cl}_2$ (**2**) appeared as dark flat parallelepipeds. Measured were 109464 reflections, yielding 13859 unique data ($R_{\text{int}} = 0.060$). Hydrogen atoms were placed in calculated positions. Two sets of *tert*-butyl groups were described on C23 with positional disorder, refined using partial occupancy sites and held isotropic. The solvent region was also disordered and appears to be $\frac{1}{2}$ acetonitrile and $\frac{1}{2}$ dichloromethane per equivalent of iron complex. The density

from this solvent region was added via the *SQUEEZE* program in the *PLATON* suite of software.²⁵

Table 7.5. Crystal Data^a

	[Ga(L)(Cl)(CH ₃ OH)] (1)	[Fe(L)(Cl)]·0.5CH ₃ CN·0.5CH ₂ Cl ₂ (2)
Formula	C ₃₅ H ₄₈ ClGa ₂ N ₂ O ₃	C _{35.50} H _{46.50} Cl ₂ FeN _{2.50} O ₂
<i>M</i>	649.92	667.00
Space group	C2/c	P(2 ₁)/c
<i>a</i> / Å	32.4909(12)	14.8640(5)
<i>b</i> / Å	9.2772(3)	19.0928(7)
<i>c</i> / Å	24.1691(10)	12.4873(4)
<i>α</i> / °		
<i>β</i> / °	113.752(3)	91.310(2)
<i>γ</i> / °		
<i>V</i> / Å³	6668.1(4)	3542.9(2)
<i>Z</i>	8	4
<i>T</i> / K	100(2)	100(2)
<i>λ</i> / Å	0.71073	0.71073
<i>D</i>_{calc} / g cm⁻³	1.295	1.250
<i>μ</i> / mm⁻¹	0.941	0.609
<i>R</i>(<i>F</i>) (%)	7.23	5.35
<i>Rw</i>(<i>F</i>) (%)	16.99	13.87

$$^a R(F) = \sum \| |F_o| - |F_c| \| / \sum |F_o| \text{ for } I > 2\sigma(I); R_w(F) = [\sum w(F_o^2 - F_c^2)^2 / \sum w(F_o^2)^2]^{1/2} \text{ for } I > 2\sigma(I).$$

8.4.2. Syntheses. Preparation of the Ligand *N,N'*-Bis(3,5-di-*tert*-butyl-2-hydroxyphenyl)-1,2-phenylenediamine (H₄L). The previously reported procedure by Wieghardt⁵ was followed for the synthesis of the H₄L ligand and the recommended purification steps suggested by Heyduk⁷ were integrated to result in an overall 45% yield. Characterization by means of ¹H-NMR spectroscopy and electrospray ionization (ESI-MS) mass spectrometry are in accord with the literature data.

8.4.3. Preparation of the Complexes. Complex 1 [Ga(L)(Cl)(MeOH)]. The ligand H₄L (0.517 g, 1 mmol) was dissolved in anhydrous methanol (30 mL) and treated with GaCl₃ (0.176 g, 1 mmol) under an argon atmosphere. Distilled Et₃N (0.2 mL) was added to the resulting solution and the mixture was stirred under reflux for 1 h.

Compressed O₂ was introduced to the pink solution, which turned dark violet, and for an additional 2 h was stirred at ambient temperature. Concentration of the suspension to one-fourth of its initial volume yielded a dark microcrystalline solid isolated by filtration and washed with cold CH₃OH. Recrystallization by slow evaporation from a CH₂Cl₂/CH₃OH (1:1) solvent mixture afforded suitable crystals for X-ray analysis. Yield: 71%. Elemental anal. calcd for [C₃₅H₄₈ClGa₂N₂O₃]: C, 64.68, H, 7.44, N, 4.31 %. Found: C, 64.84, H, 7.31, N, 4.57 %. IR data (KBr, cm⁻¹): 2955, 2906, 2867, 1499, 1387, 1361, 1311, 1288, 1256, 1165, 1132, 1113, 1025, 983, 913, 852, 747, 659, 593. UV-visible data (DCM, 1.0 x 10⁻⁵ M): 270 (28,450); 334 (14,730); 459 (3,890); 572 (4,990); 697 sh (4,970); 999 (15,980). MS data (ESI⁺ in CH₂Cl₂): *m/z* = 613.29 (100%) for [M - Cl]⁺.

8.4.4. Complex 2 [Fe(L)(Cl)]. A 25 mL MeCN solution of the ligand H₄L (0.517 g, 1 mmol) was treated with FeCl₃·6H₂O (0.270 g, 1 mmol) and Et₃N (0.2 mL). The resulting solution was stirred for 1 h at room temperature in the presence of air. Separating from this solution was a blue-green microcrystalline solid which was filtered and washed with acetonitrile. Recrystallization by slow solvent evaporation from a CH₂Cl₂/CH₃CN (1:1) mixture yielded X-ray quality crystals. Yield: 75%. Elemental anal. calcd for [C₃₄H₄₄ClFeN₂O₂]: C, 67.61, H, 7.34, N, 4.64 %. Found: C, 67.91, H, 7.39, N, 4.77 %. IR data (KBr, cm⁻¹): 2959, 2868, 1734, 1586, 1522, 1469, 1413, 1388, 1363, 1259, 1202, 1173, 1106, 1025, 994, 909, 889, 852, 779, 755, 645, 595. UV-visible data (DCM, 1.0 x 10⁻⁵ M): 277 (89,890); 340 (16,950); 455 (7,830); 500 (7,120); 641 (5,600); 856 sh (4,620). MS data (ESI⁺ in CH₂Cl₂): *m/z* = 568.27 (100%) for [M - Cl]⁺.

7.5. References

- 1 Chirik, P. J.; Wieghardt, K. "Radical Ligands Confer Nobility on Base-Metal Catalysts." *Science* **2010**, *327*, 794.
- 2 Smith, A. L.; Hardcastle, K. I.; Soper, J. D. "Redox-Active Ligand-Mediated Oxidative Addition and Reductive Elimination at Square Planar Cobalt(III): Multielectron Reactions for Cross-Coupling." *J. Am. Chem. Soc.* **2010**, *132*, 14358.
- 3 Dzik, W. I.; van der Vlugt, J. I.; Reek, J. N. H.; de Bruin, B. "Ligands that Store and Release Electrons during Catalysis." *Angew. Chem.* **2011**, *50*, 3356.
- 4 Kaim, W. "Manifestations of Noninnocent Ligand Behavior." *Inorg. Chem.* **2011**, *50*, 9752.
- 5 Chaudhuri, P.; Hess, M.; Müller, J.; Hildenbrand, K.; Bill, E.; Weyhermüller, T.; Wieghardt, K. "Aerobic Oxidation of Primary Alcohols (Including Methanol) by Copper(II)- and Zinc(II)-Phenoxy Radical Catalysts." *J. Am. Chem. Soc.* **1999**, *121*, 9599.
- 6 Blackmore, K. J.; Lal, N.; Ziller, J. W.; Heyduk, A. F. "Catalytic Reactivity of a Zirconium(IV) Redox-Active Ligand Complex with 1,2-Diphenylhydrazine." *J. Am. Chem. Soc.* **2008**, *130*, 2728.
- 7 Blackmore, K. J.; Lal, N.; Ziller, J. W.; Heyduk, A. F. "Group IV Coordination Chemistry of a Tetradentate Redox-Active Ligand in Two Oxidation States." *Eur. J. Inorg. Chem.* **2009**, *6*, 735.
- 8 Zelikoff, A. L.; Kopilov, J.; Goldberg, I.; Coates, G. W.; Kol, M. "New Facets of an Old Ligand: Titanium and Zirconium Complexes of Phenylenediamine

- Bis(phenolate) in Lactide Polymerisation Catalysis.” *Chem. Commun.* **2009**, *44*, 6804.
- 9 Pierpont, C. G.; Buchanan, R. M. “Transition Metal Complexes of *o*-Benzoquinone, *o*-Semiquinone, and Catecholate Ligands.” *Coord. Chem. Rev.* **1981**, *38*, 45.
- 10 Dei, A.; Gatteschi, D.; Sangregorio, C.; Sorace, L. “Quinonoid Metal Complexes: Toward Molecular Switches.” *Acc. Chem. Res.* **2004**, *37*, 827.
- 11 Sato, O.; Tao, J.; Zhang, Y.-Z. “Control of Magnetic Properties through External Stimuli.” *Angew. Chem. Int. Ed.* **2007**, *46*, 2152.
- 12 Mukherjee, C.; Weyhermüller, T.; Bothe, E.; Chaudhuri, P. “Targeted Oxidase Reactivity with a New Redox-Active Ligand Incorporating N₂O₂ Donor Atoms. Complexes of Cu(II), Ni(II), Pd(II), Fe(III), and V(V).” *Inorg. Chem.* **2008**, *47*, 11620.
- 13 Chaudhuri, P.; Bill, E.; Wagner, R.; Pieper, U.; Biswas, B.; Weyhermüller, T. “Radical-Ligand-Derived C-N Coupling, Ga(III)-Radical vs. Low-Spin Co(III)-Radical Reactivity.” *Inorg. Chem.* **2008**, *47*, 5549.
- 14 Carmalt, C. J.; King, S. J. “Gallium(III) and Indium(III) Alkoxides and Aryloxides.” *Coord. Chem. Rev.* **2006**, *250*, 682.
- 15 Lesh, F. D.; Shanmugam, R.; Allard, M. M.; Lanznaster, M.; Heeg, M. J.; Rodgers, M. T.; Shearer, J. M.; Verani, C. N. “A Modular Approach to Redox-Active Multimetallic Hydrophobes of Discoid Topology.” *Inorg. Chem.* **2010**, *49*, 7226.

- 16 Chaudhuri, P.; Verani, C. N.; Bill, E.; Bothe, E.; Weyhermüller, T.; Wieghardt, K. "Electronic Structure of Bis(*o*-iminobenzosemiquinonato)metal Complexes (Cu, Ni, Pd). The Art of Establishing Physical Oxidation States in Transition-Metal Complexes Containing Radical Ligands." *J. Am. Chem. Soc.* **2001**, *123*, 2213.
- 17 Addison, A. W.; Rao, T. N.; Reedijk, J.; Van Rijn, J.; Verschoor, G. C. "Synthesis, Structure, and Spectroscopic Properties of Copper(II) Compounds Containing Nitrogen-Sulfur Donor Ligands: The Crystal and Molecular Structure of Aqua [1,7- bis (*N*-methylbenzimidazol- 2'- yl)- 2,6- dithiaheptane] copper(II) Perchlorate." *J. Chem. Soc., Dalton Trans.* **1984**, 1349.
- 18 Chun, H.; Weyhermüller, T.; Bill, E.; Wieghardt, K. "Tuning the Electronic Structure of Halidobis(*o*-iminobenzosemiquinonato)iron(III) Complexes." *Angew. Chem., Int. Ed.* **2001**, *40*, 2489.
- 19 Chun, H.; Bill, E.; Weyhermüller, T.; Wieghardt, K. " $S = 3/2 \leftrightarrow S = 1/2$ Spin Crossover Behavior in Five-Coordinate Halido- and Pseudohalido-bis(*o*-iminobenzosemiquinonato)iron(III) Complexes." *Inorg. Chem.* **2003**, *42*, 5612.
- 20 Hammett, L. P. "Effect of Structure upon the Reactions of Organic Compounds. Benzene Derivatives." *J. Am. Chem. Soc.* **1937**, *59*, 96.
- 21 Chun, H.; Verani, C. N.; Chaudhuri, P.; Bothe, E.; Bill, E.; Weyhermüller, T.; Wieghardt, K. "Molecular and Electronic Structure of Octahedral *o*-Aminophenolato and *o*-Iminobenzosemiquinonato Complexes of V(V), Cr(III), Fe(III), and Co(III). Experimental Determination of Oxidation Levels of Ligands and Metal Ions." *Inorg. Chem.* **2001**, *40*, 4157.

- 22 Mukherjee, S.; Weyhermüller, T.; Bill, E.; Wieghardt, K.; Chaudhuri, P. "Tuning of Spin Transition in Radical-Containing Iron(III) Complexes by Remote Ligand Substituents." *Inorg. Chem.* **2005**, *44*, 7099.
- 23 *APEX II* collection and processing programs are distributed by the manufacturer. Bruker AXS Inc., Madison WI, USA, 2009.
- 24 Sheldrick, G.M. "A Short History of SHELX." *Acta Cryst.* **2008**, *A64*, 112.
- 25 Spek, A. L. "Single-Crystal Structure Validation with the Program PLATON." *J. Appl. Cryst.* **2003**, *36*, 7.

CHAPTER 8

CONCLUSIONS AND PERSPECTIVES

8.1. Overall Conclusions

The research of our group has been predominantly concerned with gaining insight into the underlying principles of preserving the rich electrochemical, spectroscopic, and magnetic properties of coordination complex systems that demonstrate effective activity in solution-based analyses for ordered surface deposition onto solid interfaces. Investigating the fundamental concepts of the specific objectives of (i) designing candidates for the formation of redox-responsive monolayer films, and (ii) achieving solar photocatalytic water oxidation are actively being undertaken in our laboratories by applying conceptual approaches and strategies. The research projects presented in this dissertation have afforded significant impacts toward these targets, in which my efforts were mainly concentrated on modulating the observed responsivity by synthetically enhancing our systems, either by controlling through the selection of metal incorporation or by tuning the ligand framework design. As outlined below, numerous metal ions and diverse ligand platforms have been deliberately integrated into our systems to serve distinct functions.

In **Chapter 3**, the first Research Goal of *developing responsive metal-containing surfactants that serve as precursors for Langmuir–Blodgett films* has been addressed through the synthesis and characterization of the metallosurfactants $[\text{Ni}^{\text{II}}(\text{L}^{\text{tBuODA}})(\text{OAc})]$, $[\text{Ni}^{\text{II}}(\text{L}^{\text{tBuODA}})_2]$, $[\text{Cu}^{\text{II}}(\text{HL}^{\text{tBuODA}})(\text{L}^{\text{tBuODA}})]\text{ClO}_4 \cdot \text{CH}_3\text{OH}$, and $[\text{Zn}^{\text{II}}(\text{HL}^{\text{tBuODA}})_2](\text{ClO}_4)_2$ {where $\text{HL}^{\text{tBuODA}} = 2,4$ - di- *tert*- butyl- 6- [(octadecyl (pyridine-2-ylmethyl) amino) methyl] phenol} in an attempt to establish how coordination modes and protonation

preferences relate to amphiphilic behavior. The archetypical compounds $[\text{Ni}^{\text{II}}(\text{L}^{\text{tBuI}})(\text{OAc})]\cdot\text{CH}_3\text{OH}$, $[\text{Ni}^{\text{II}}(\text{L}^{\text{A}})_2]\cdot\text{CH}_3\text{OH}\cdot\text{H}_2\text{O}$, $[\text{Ni}^{\text{II}}(\text{L}^{\text{tBuA}})_2]\cdot 2\text{CH}_3\text{OH}$, $[\text{Cu}^{\text{II}}(\text{HL}^{\text{tBuA}})(\text{L}^{\text{tBuA}})]\text{ClO}_4$, and $[\text{Zn}^{\text{II}}(\text{HL}^{\text{tBuA}})(\text{L}^{\text{tBuA}})]\text{ClO}_4$ were synthesized to model the stoichiometric, coordination, and protonation chemistry in the waxy metallosurfactants. Detailed data analysis and comparison between the metallosurfactants and the archetypes involved mass spectrometric and spectroscopic methods along with crystallographic determination of the archetypes. DFT calculations were used to identify the frontier orbitals, polarizability, and dipole moments. Metallosurfactant species had their compression isotherms measured and monitored by means of Brewster angle microscopy. The $[\text{Ni}^{\text{II}}(\text{L}^{\text{tBuODA}})(\text{OAc})]$ species is square planar, while $[\text{Ni}^{\text{II}}(\text{L}^{\text{tBuODA}})_2]$ has a neutral octahedral core with two deprotonated ligands. The five-coordinate $[\text{Cu}^{\text{II}}(\text{HL}^{\text{tBuODA}})(\text{L}^{\text{tBuODA}})]\text{ClO}_4\cdot\text{CH}_3\text{OH}$ complex has a monocationic core associated with one protonated ligand, whereas the dicationic $[\text{Zn}^{\text{II}}(\text{HL}^{\text{tBuODA}})_2](\text{ClO}_4)_2$ has a four-coordinate core with protonated ligands. It was observed that Langmuir films of $[\text{Ni}^{\text{II}}(\text{L}^{\text{tBuODA}})(\text{OAc})]$ display approximately half of the average molecular area observed for $[\text{Ni}^{\text{II}}(\text{L}^{\text{tBuODA}})_2]$, $[\text{Cu}^{\text{II}}(\text{HL}^{\text{tBuODA}})(\text{L}^{\text{tBuODA}})]\text{ClO}_4\cdot\text{CH}_3\text{OH}$, and $[\text{Zn}^{\text{II}}(\text{HL}^{\text{tBuODA}})_2](\text{ClO}_4)_2$ and that the flexibility and coordination number of the cores foster distinctive collapse mechanisms. Therefore, careful choice of the metal ion leads to control of surfactant-to-metal ratio, selection of coordination modes and structural properties, and the understanding of the protonation preferences of the ligands. This information will play an important role in the development of metal-containing responsive films.

The second Research Goal is detailed in **Chapter 4**, in which we have *extended efforts toward developing redox-active homotetranuclear and heterodinuclear pentacoordinated M(III)M(II) amphiphiles of new topologies* with the aim to control the magnetic behavior toward ground-state switching in heterospin metal/radical systems and to incorporate amphiphilic properties. A new modular $[\text{Fe}^{\text{II}}(\text{Fe}^{\text{III}}\text{L}^2)_3](\text{PF}_6)_2$ species was synthesized and characterized with discoid (disk-like) topology and found to exhibit redox and surfactant properties. These findings point to a new approach for developing redox-active multimetallic Langmuir film precursors.

Chapter 5 describes the results towards the third Research Goal of *achieving the integration of photo-responsive groups to the headgroups of metal-containing surfactants that serve as precursors for Langmuir–Blodgett films*. A series of pyridine- and phenol-based ruthenium(II)-containing amphiphiles with bidentate ligands of the following types are reported: $[(\text{L}^{\text{PyI}})\text{Ru}^{\text{II}}(\text{bpy})_2](\text{PF}_6)_2$, $[(\text{L}^{\text{PyA}})\text{Ru}^{\text{II}}(\text{bpy})_2](\text{PF}_6)_2$, $[(\text{L}^{\text{PhBuI}})\text{Ru}^{\text{II}}(\text{bpy})_2](\text{PF}_6)$, and $[(\text{L}^{\text{PhClI}})\text{Ru}^{\text{II}}(\text{bpy})_2](\text{PF}_6)$. The pyridine-based species are obtained by treatment of $[\text{Ru}(\text{bpy})_2\text{Cl}_2]$ with the ligands L^{PyI} (*N*-(pyridine-2-ylmethylene)octadecan-1-amine) and L^{PyA} (*N*-(pyridine-2-ylmethyl)octadecan-1-amine). The imine phenol-based species are synthesized by reaction of $[\text{Ru}(\text{bpy})_2(\text{CF}_3\text{SO}_3)_2]$ with the amine ligands HL^{PhBuA} (2,4-di-*tert*-butyl- 6-((octadecylamino) methyl) phenol), and HL^{PhClA} (2,4-dichloro- 6-((octadecylamino) methyl) phenol). All compounds are characterized by means of electrospray ionization (ESI⁺) mass spectrometry, elemental analyses, as well as electrochemical methods, infrared and UV–visible absorption and emission spectroscopies. The cyclic voltammograms (CVs) of the pyridine-based complexes are marked by two successive processes around -1.78 and -2.27 V versus Fc^+/Fc attributed

to bipyridine reduction. A further ligand-centered reductive process is seen for $[(L^{Py})Ru^{II}(bpy)_2](PF_6)_2$. The Ru^{II}/Ru^{III} couple appears at 0.93 V versus Fc^+/Fc . The phenolato-containing $[(L^{PhBu})Ru^{II}(bpy)_2](PF_6)$ and $[(L^{PhCl})Ru^{II}(bpy)_2](PF_6)$ species present relatively lower reduction potentials and more reversible redox behavior, along with $Ru^{II/III}$ and phenolate/phenoxy oxidations. The interpretation of observed redox behavior is supported by density functional theory (DFT) calculations. All complexes are surface-active as characterized by compression isotherms and Brewster angle microscopy. The pyridine-based complexes show collapse pressures of about 29–32 $mN \cdot m^{-1}$, and are strong candidates for the formation of redox-responsive monolayer films. Our target was to extend the electrochemical redox behavior of these species with the presence of ligand moieties such as phenolates, while preserving the amphiphilic and photophysical character of these ruthenium(II)-containing metallocsurfactants. We have addressed questions regarding electrochemical, optical, electronic, and amphiphilic properties using synthetic, spectrometric, spectroscopic, computational, and surface-dedicated methods and attempted to correlate these properties to assess the viability of these species as precursors for photo-responsive LB films.

The fourth Research Goal seeks to address the *expansion of current redox-active moieties by exploiting ligands containing amino-catechols*, as shown in **Chapters 6** and **7**. Extensive attention has been focused on the design of redox-active ligands to enhance the reaction chemistry of coordination compounds with early transition metals to induce noble-transition-metal reactivity. Of these, one intriguing example that has left a substantial impact is the prevalently investigated *N,N'*-bis(3,5-di-*tert*-butyl-2-hydroxyphenyl)-1,2-phenylenediamine ligand. We have isolated and characterized

species between this ligand and manganese(II), iron(III), cobalt(II), and gallium(III). Stoichiometric reactions resulted in mono-ligated species for iron and gallium, and pseudo-octahedral bis-ligated species for manganese and cobalt. An unforeseen aerobic cyclization of the ligand occurs in the presence of cobalt(II) to form a new mixed phenolate/phenoxazinylate radical species. The peculiar electronic nature inherent to these redox-active transition metal complexes merely complicates the proper assignment and identification of the diverse redox states observed. Experimental and computational evidence merge to elucidate the multiple oxidation levels accessible to these systems.

8.2. Perspectives

Although my contribution towards our group objectives have mainly focused on effectively adapting our previous systems to target enhanced electrochemical and spectroscopic responses, the next step that must be taken is to demonstrate ordered surface deposition onto solid surfaces to confirm that the observed solution-based response is in fact conserved. Towards this aim, members of our group have recently gained information regarding long chain orientation and headgroup arrangement of monolayers transferred onto gold with a variable angle reflection accessory that allows for infrared reflection-absorption spectroscopy (IRRAS). Nevertheless, the novel precursors described in **Chapters 3–5** display efficient amphiphilic behavior to presumably function as well-organized thin films once transferred onto solid substrates. The methodology exploited in the design of the $[\text{Fe}^{\text{II}}(\text{Fe}^{\text{III}}\text{L}^2)_3](\text{PF}_6)_2$ species of discoid topology has certainly paved a foundation for assembling extended modular films containing heterometallic cores based on Robson macrocycles and Asato-like ligands, whereby controlling subphase parameters, such as counterion choice, compression rate,

subphase pH, and temperature, may perhaps play an important factor in optimizing film quality.

The amino-catecholate chemistry of **Chapters 6** and **7** was initiated by attempts to expand the electrochemical response of our currently used phenoxyl radical based systems by tailoring our phenanthroline ligand platforms to include a more air stable redox-active moiety. Synthetically adapting these frameworks proved to be significantly more challenging than projected as a result of insolubility and air sensitivity with the diamine precursor. As a starting point, the analogous *N,N'*-bis(3,5-di-*tert*-butyl-2-hydroxyphenyl)-1,2-phenylenediamine ligand was investigated to familiarize ourselves with the particularly unique reaction conditions required. We ascertained that the impressive electrochemical response observed with both redox-active metal centers and the redox inert gallium(III) ion was derived from various ligand-centered oxidations. Specifically, the unexpected formation of the phenoxazinylate-type ligand in the presence of cobalt(II) ion is of paramount curiosity given the serendipitous observation of multiple accessible oxidation levels. The rich redox chemistry illustrated by this ligand motif evokes relevance towards potential catalytic avenues to be explored. Ligands with the capacity to store electrons can essentially eliminate the use of noble transition metals to mediate two-electron reductive elimination and oxidative addition catalytic processes, thus taking advantage of less expensive first-row transition metals to accomplish such transformations. Imperative targets to pursue involve determining the critical role of the cobalt(II) ion in the formation of the cyclized ligand, in addition to isolating the phenoxazinylate ligand for further incorporation with different metal ions and ligand scaffolds.

APPENDIX A

Supplementary Information for Chapter 3

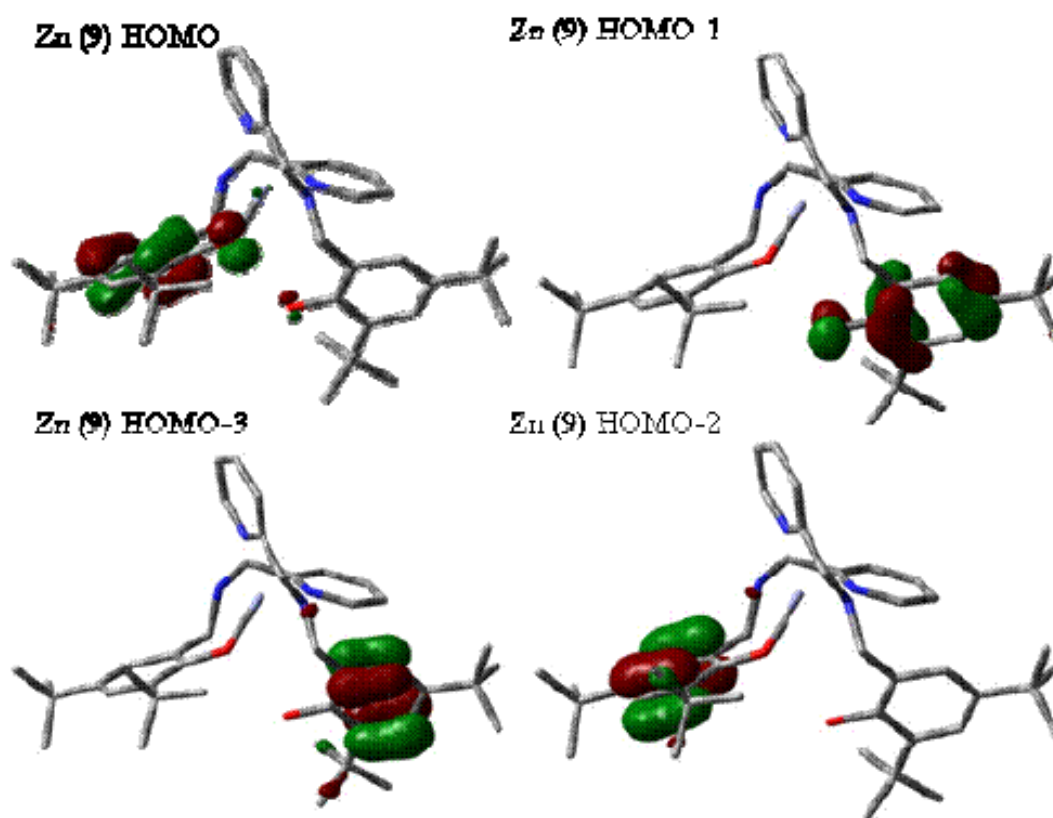


Figure A.3.1. Selected MOs for 9.

Table A.3.1. Optimized Structures Cartesian Coordinates:

(3') Cu: E(UB+HF-LYP) = -3802.91151977

H 0.27567400 -5.46607900 -1.05651100
 H -1.85909700 -6.35420700 -1.42554600
 H 0.07381400 -4.15478000 -2.22992000
 C -0.04623500 -4.42480600 -1.17834300
 H -2.29044600 -5.10780400 -2.60913100
 H 0.63088900 -3.79507600 -0.59789100
 H -1.12664400 -5.71737200 0.91781500
 C -2.31067200 -5.36251200 -1.54379900
 C -1.51609400 -4.31961300 -0.71440500
 H -3.35832600 -5.43967900 -1.23792700
 C -1.56359800 -4.72141500 0.78052600
 H -2.58531700 -4.75152600 1.17370500
 H -0.98782300 -4.01843700 1.39536000
 H 4.72249600 -4.29665100 1.47120900
 H 2.88359200 -0.77900300 -3.75790500
 C -2.19372200 -2.93146000 -0.89104000
 H 6.44546800 -4.58724100 1.19773600
 H 5.36038800 -4.31736800 -0.17980500
 O -0.24881900 -1.75854000 -1.67934400
 H -4.03308300 -3.73526900 -0.17261600
 C 5.57880500 -4.01272900 0.84979900
 H 2.75089100 0.87773900 -4.37189600
 C 2.68010600 0.25822600 -3.46924800
 H 5.34088900 -0.38817100 -3.35094500
 C -3.55595300 -2.84527900 -0.56885100
 C -1.58123100 -1.74749800 -1.37304500
 H 1.65573100 0.30161300 -3.09541600
 H 0.18054000 -0.89481900 -1.46848900
 H 5.34635900 -2.33431900 3.06306600
 H 5.11747800 1.25482000 -3.95650400
 C 5.09598900 0.63675100 -3.05198500
 H -0.80334600 0.27960400 -2.78773300
 H 7.05522900 -2.67111700 2.75843400
 H 5.59176200 -0.75935200 -1.20442900
 C 5.87270500 -2.49537100 0.92835200
 C -2.35268800 -0.58298400 -1.59997800
 C -4.35072700 -1.70506400 -0.74679900
 C 6.18545200 -2.11163900 2.39449900
 C 3.69771600 0.73866300 -2.40677100
 C 4.66245100 -0.85467100 -0.66287400
 H 0.23523200 -1.73062000 0.63207100
 C 4.64044800 -1.70916900 0.44536000
 C 3.56124500 -0.11814200 -1.12895800
 H -2.39438800 0.92132100 -3.12322400
 C 3.41508600 -1.83676200 1.10581400
 H 3.31872400 -2.51370000 1.95171000
 H 5.88828000 1.00253900 -2.38941000
 C -1.72961500 0.60011500 -2.31008900
 C -3.72089900 -0.58913000 -1.29763800
 C 2.34098400 -0.23569200 -0.40604200
 C 2.28807800 -1.13233000 0.68949400
 O 1.20169500 0.41316200 -0.77091000
 H 1.06083900 -2.12913200 2.14002300
 H 7.97377200 -2.77865600 0.46908200
 C 0.96488200 -1.36580200 1.35807200
 H 6.98744700 -2.49265600 -0.96743900
 H 6.41027800 -1.04226000 2.48151400

C 7.12570600 -2.20442500 0.08064500
 H 3.50146800 2.83957400 -2.97648500
 H -4.30352900 0.29349200 -1.53477900
 C 3.46433800 2.22711300 -2.06655900
 H 0.33304300 2.02897500 -2.59856100
 H 2.49763800 2.37162600 -1.58659500
 H -1.52340400 -0.92544400 1.66228700
 H 7.40446700 -1.14478200 0.11181600
 N -1.38917700 1.78449400 -1.45394700
 H 4.24195300 2.59357000 -1.38561300
 N 0.38532000 -0.11788100 1.94554700
 Cu 0.08732500 1.32421100 0.48474400
 C -0.45772500 2.66293700 -2.18649400
 H -0.93314800 3.17456700 -3.03496300
 C -0.98356600 -0.37948500 2.44678300
 H -0.98440500 -1.01575500 3.33997600
 C 0.21300900 3.68538300 -1.29568000
 N 0.58990600 3.27183100 -0.06849700
 C -1.67091300 0.93217100 2.72152100
 N -1.28688400 1.94709400 1.91750200
 H 0.18026800 5.28225000 -2.73602300
 C 0.50686700 4.97320700 -1.74812600
 H -2.89929400 0.26022800 4.35284400
 C -2.61707400 1.10289500 3.72977200
 C 1.28535000 4.11209800 0.71920200
 C -1.80592200 3.16857700 2.13641900
 H -1.44041300 3.96554500 1.49980300
 H 1.56947300 3.72972300 1.69563200
 C 1.22847700 5.84008900 -0.93069700
 C 1.63201200 5.40063500 0.33034100
 C -3.17590900 2.36373100 3.92773500
 C -2.75097800 3.42144200 3.12403500
 H 1.47169300 6.84192900 -1.27176500
 H 2.19983300 6.03786900 0.99965000
 H -3.91483000 2.52179200 4.70743200
 H -3.13748000 4.42587300 3.25864900
 C -5.84332600 -1.73356300 -0.36812200
 C -6.54801000 -0.39792800 -0.67288200
 H -6.10075200 0.43726300 -0.12005400
 H -6.52123100 -0.15658500 -1.74162200
 H -7.60093000 -0.45994500 -0.37773200
 C -6.56576000 -2.84762900 -1.16247500
 H -6.14483300 -3.83714600 -0.95667100
 H -7.62893600 -2.87825300 -0.89628600
 H -6.49051900 -2.67099000 -2.24116400
 C -5.98028600 -2.01512600 1.14720700
 H -5.49300000 -1.22909200 1.73749100
 H -7.03696700 -2.04999200 1.43775200
 H -5.52764900 -2.97256400 1.42580500
 C -2.60373800 2.53581200 -1.03122100
 H -2.25641300 3.37807400 -0.42831300
 H -3.16868200 1.88152900 -0.36298600
 C -3.53479600 3.08549900 -2.12282200
 H -4.34075700 3.64849200 -1.63945200
 H -3.02718400 3.77343500 -2.80671400
 H -4.00390300 2.30062800 -2.72228200
 C 1.28478700 0.47514500 2.99157000
 H 2.22815300 0.69212800 2.48311000
 H 0.84576500 1.42942900 3.29669300
 C 1.55961700 -0.38015500 4.23110900
 H 2.22173300 0.18153300 4.89825600
 H 0.65210500 -0.61284900 4.79763600

H 2.06574900 -1.31699200 3.98456300

(8) Cu: E(UB+HF-LYP) = -3645.68926619

H -1.58296300 -5.81942400 -1.65412100
 H -3.11853100 -6.08061200 0.22702100
 H -2.71713600 -4.75072500 -2.49631600
 C -1.88503900 -4.77324700 -1.78324200
 H -4.32983900 -5.06511000 -0.55557100
 H -1.04469700 -4.22611700 -2.21532800
 H -0.90877200 -5.35144300 0.75752000
 C -3.46932600 -5.04863400 0.12217500
 C -2.31605800 -4.17792700 -0.41891900
 H -3.81312500 -4.71874200 1.10984100
 C -1.14525800 -4.29474500 0.58588300
 H -0.24458200 -3.80608800 0.21204300
 H -1.41461300 -3.85720500 1.55631900
 H 5.86075700 -4.05363300 0.56752400
 H 2.89332100 -1.73454200 -3.38350600
 C -2.74776000 -2.70614100 -0.62346900
 H 7.50466700 -3.60818000 1.06424400
 H 6.78044900 -2.86473800 -0.36711700
 O -0.56089300 -2.07688100 -1.37768300
 H -4.73845800 -3.02455700 0.06827600
 C 6.56800500 -3.22032400 0.64654200
 H 2.72762900 -0.26827000 -4.36297200
 C 2.65981700 -0.66470200 -3.34234900
 H 5.34782400 -1.16397200 -3.08253300
 C -4.06155000 -2.29613000 -0.35372000
 C -1.86235400 -1.73080300 -1.14928100
 H 1.62997900 -0.56068300 -2.99733800
 H 0.05022200 -1.30548000 -1.26079400
 H 5.10706600 -3.52178500 2.96269500
 H 5.05607800 0.28469800 -4.04899900
 C 5.05745300 -0.10913800 -3.02664400
 H -0.59963500 0.06305800 -2.66015900
 H 6.75881700 -3.03393100 3.35298700
 H 5.61512400 -0.98033600 -0.88048200
 C 6.00245800 -2.09651600 1.54764900
 C -2.34687900 -0.44969300 -1.49370200
 C -4.55947100 -1.01031700 -0.61455600
 C 5.80135400 -2.67355500 2.96186300
 C 3.65280100 0.07567900 -2.41481800
 C 4.67755300 -1.00209400 -0.34051500
 H 0.27910500 -1.83240900 1.06868600
 C 4.68963700 -1.56351900 0.94700500
 C 3.54718300 -0.47604800 -0.97683000
 H -2.06433300 0.94510300 -3.09434700
 C 3.46578700 -1.61717300 1.61111300
 H 3.38908100 -2.07222000 2.59381100
 H 5.83012800 0.43363400 -2.47087100
 C -1.49149800 0.53699700 -2.24952300
 C -3.67790900 -0.11410400 -1.21960900
 C 2.32001800 -0.50111600 -0.25076600
 C 2.30256900 -1.11536100 1.02179100
 O 1.15465300 -0.01315900 -0.75544300
 H 1.09792200 -1.85486000 2.63934200
 H 7.97640400 -1.31219100 2.06346000
 C 0.98063100 -1.28842000 1.70671300
 H 7.25744900 -0.51902800 0.65592100
 H 5.42400300 -1.91890500 3.66222000
 C 7.03384200 -0.94655300 1.63904100
 H 3.34744500 1.98952300 -3.42853600

H -4.03440600 0.86878000 -1.52549100
 C 3.35370100 1.59088200 -2.40582900
 H 0.42965600 2.13083600 -2.80455700
 H 2.38781900 1.79033900 -1.94299300
 H -1.55582800 -0.85609900 2.03814100
 H 6.66488500 -0.13747300 2.28023600
 N -1.02896300 1.67485300 -1.39354300
 H 4.11909700 2.13415800 -1.83892200
 N 0.33488100 0.02749100 1.99866900
 Cu 0.05351100 1.14563600 0.31315800
 C -0.28604800 2.67964900 -2.18281100
 H -1.87190100 2.11666600 -1.02420300
 H -0.94869900 3.22837800 -2.86540000
 C -0.99169600 -0.12825100 2.63590400
 H -0.91545000 -0.52992000 3.65410000
 H 0.94769600 0.53235500 2.64376400
 C 0.48754200 3.64337700 -1.30543300
 N 0.88431300 3.18240500 -0.10400500
 C -1.71184900 1.19524300 2.62118900
 N -1.40720500 1.98801100 1.57426700
 H 0.47929900 5.26596900 -2.72448500
 C 0.82636700 4.92128300 -1.75504700
 H -2.85069800 0.91034800 4.42449600
 C -2.63848200 1.57342600 3.59179200
 C 1.65001600 3.97212200 0.66685300
 C -2.01073100 3.18552900 1.47683400
 H -1.71295800 3.80739100 0.63816200
 H 1.95120200 3.55892800 1.62582400
 C 1.62270700 5.73356900 -0.95044500
 C 2.04928700 5.24921800 0.28622400
 C -3.27608600 2.80649900 3.47288900
 C -2.95425400 3.63172500 2.39454500
 H 1.90478300 6.72794600 -1.28330900
 H 2.67364300 5.84498600 0.94343500
 H -4.00350100 3.12284800 4.21419600
 H -3.41567800 4.60532800 2.26962900
 C -6.01150800 -0.59319400 -0.31307200
 C -6.73079900 -0.22842700 -1.63386500
 H -6.23907600 0.60185800 -2.15281500
 H -6.75091000 -1.08406000 -2.31756300
 H -7.76647200 0.07174200 -1.43531300
 C -6.81395800 -1.71231600 0.37744600
 H -6.36284500 -2.01133100 1.33071600
 H -7.82966700 -1.36102700 0.58898100
 H -6.90200500 -2.60310200 -0.25399100
 C -6.00950400 0.64009200 0.62178200
 H -5.48531400 1.49169300 0.17295600
 H -7.03607600 0.95964900 0.83648500
 H -5.52075500 0.40848500 1.57597900

(9) Zn: E(UB+HF-LYP) = -3784.54467471

H 4.03808300 0.20875700 -4.54443400
 H 3.34282600 -2.24284000 -4.53166200
 H 5.16266000 -0.03011800 -3.19896600
 C 4.12015200 0.18830500 -3.45074000
 H 4.50426400 -2.57239500 -3.24695300
 H 3.89189500 1.19332600 -3.07476100
 C 3.47602100 -2.25648800 -3.44341100
 H 1.71886500 -0.56549600 -4.44853500
 C 3.14699000 -0.85924600 -2.85547200
 H 2.80715600 -3.01955600 -3.03005900
 C 1.73343800 -0.51294000 -3.35325000

H 1.44152200 0.49672300 -3.05753000
 H 5.29219600 -1.63791900 -1.60581900
 H -2.52918500 -4.86652000 -1.34780500
 H -2.07564500 1.00634700 -3.06600300
 H 0.98861800 -1.21859100 -2.97426800
 H -0.66209200 0.11899100 -2.49315800
 H -0.95477300 -4.14052400 -0.96968500
 C 3.32180000 -0.88601000 -1.31294700
 C 4.56525400 -1.34946100 -0.85451700
 C -1.84000700 -4.60759500 -0.53567700
 C -1.57576500 0.61392400 -2.16987600
 H -4.20101200 0.85330900 -2.03090700
 H -1.53309500 -5.54037400 -0.04746200
 C -3.88530500 -0.03364300 -1.48809100
 C -2.51000200 -0.32764500 -1.45910900
 H 0.25301600 2.29920900 -2.76488900
 O -0.74036200 -1.84316800 -0.77898200
 C -4.82923900 -0.85596700 -0.88179700
 H -1.21007700 3.27722800 -2.85528300
 C -2.05269300 -1.49237500 -0.81032400
 H -0.09252700 -1.09166400 -0.85513100
 H -4.44431500 -4.76867200 0.31784100
 C -4.33549500 -2.01347300 -0.24931000
 C -2.98754200 -2.37366000 -0.19636500
 C -0.50190300 2.81215200 -2.15678400
 C 4.94679200 -1.47025400 0.48618600
 C 2.38027300 -0.47139700 -0.32923500
 O 1.15929500 0.04093200 -0.63909800
 H -5.05511500 -2.67478900 0.21606000
 C -2.53481200 -3.68111000 0.49343800
 N -1.15141700 1.78284600 -1.31779500
 C -3.72416000 -4.46517000 1.08592500
 H -0.08769000 5.47054500 -2.74294900
 H -3.34982700 -5.37892200 1.55933800
 H -2.00413400 2.19228800 -0.93028600
 C 3.98942800 -1.09466500 1.42629600
 C 2.73629800 -0.61489500 1.03626200
 C 0.18860300 3.87152000 -1.32986900
 H -0.65463100 -2.88274800 1.30330800
 C 0.34382300 5.17942600 -1.79046700
 H -4.25886500 -3.89484900 1.85491300
 C -1.56543600 -3.36673200 1.66012700
 H -1.28224100 -4.29580100 2.16861800
 Zn 0.25985000 1.44577500 0.33658800
 H 4.19772100 -1.17991900 2.48859900
 H -2.86992400 0.80345000 0.76624200
 H 0.78597000 -0.73746600 1.96780600
 N 0.69809500 3.47219600 -0.14796100
 H -2.04688000 -2.71525000 2.40085500
 C 1.05918100 6.09217500 -1.01921700
 C 1.75274200 -0.24086100 2.10726900
 H 1.19362300 7.11387000 -1.36114400
 C -2.51007500 0.94497100 1.77843400
 H 2.13532900 -0.53860500 3.09219200
 N -1.20167700 1.23530300 1.92024300
 N 1.49776200 1.23875600 2.10238700
 C 1.38701700 4.35835700 0.59314100
 H 2.40931900 1.69327700 2.06063300
 C 1.59633700 5.67335100 0.19873200
 H -4.41364700 0.55085800 2.68208400
 C -3.37193800 0.79465900 2.85883000
 H 1.78354200 3.99119300 1.53408700

H 2.16117700 6.34884800 0.83184700
 C -0.70751200 1.37091500 3.16808600
 C 0.76554300 1.70416900 3.28662700
 C -2.86102600 0.94131700 4.14695500
 H 1.16655800 1.27034400 4.21347500
 H 0.88294900 2.79302200 3.36625500
 C -1.50642900 1.22696700 4.30075200
 H -3.50041600 0.82262400 5.01651400
 H -1.06565400 1.33116200 5.28746500
 C -6.34249100 -0.57314300 -0.90830500
 C -6.67925400 0.72315800 -1.66938700
 H -7.76174300 0.88865800 -1.65779800
 H -6.20875300 1.60192600 -1.21146700
 H -6.36708000 0.67312400 -2.71877300
 C -6.87096300 -0.43143300 0.53911200
 H -7.95414400 -0.26269000 0.53768200
 H -6.67712400 -1.32883400 1.13598200
 H -6.40229200 0.42245100 1.04559200
 C -7.07697300 -1.74346900 -1.60553800
 H -6.72845900 -1.86502900 -2.63704200
 H -6.91972300 -2.69407600 -1.08575500
 H -8.15649500 -1.55408300 -1.63123400
 C 6.34402600 -1.99859900 0.85755300
 C 7.42652100 -1.07175300 0.25502900
 H 8.42802100 -1.44316200 0.50254700
 H 7.35542400 -1.01521600 -0.83643500
 H 7.33611700 -0.05283300 0.64947500
 C 6.55542700 -2.05352200 2.38247900
 H 6.47056400 -1.06202400 2.84313400
 H 5.83767300 -2.72277600 2.87090300
 H 7.55913400 -2.43257500 2.60310100
 C 6.52524200 -3.42862000 0.29536700
 H 6.43010500 -3.45384400 -0.79528900
 H 7.51885500 -3.81576200 0.55066400
 H 5.77673800 -4.11215100 0.711676

APPENDIX B

Supplementary Information for Chapter 4

Contents:

1. Syntheses.
2. ESI–MS exact mass spectrometry.
3. X–ray structural determinations.
4. Molecular mechanics calculations.
5. Infrared spectroscopy.
6. UV–visible spectroscopy.
7. Electrochemistry.

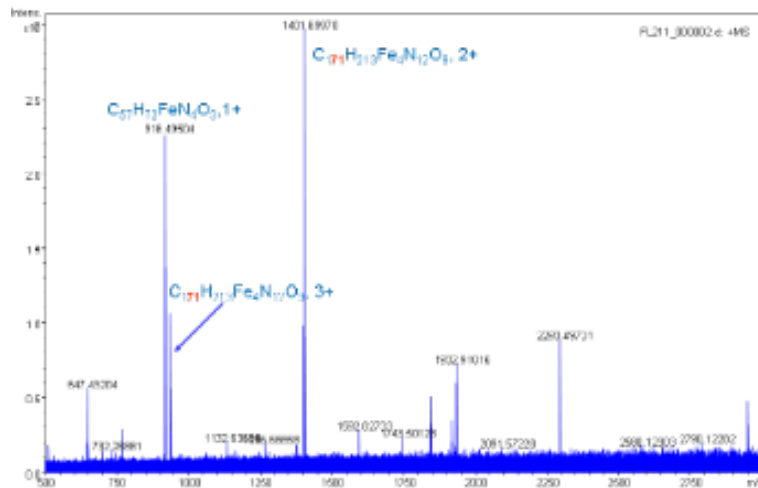
1. Syntheses.

The ligand $\mathbf{H}_3\mathbf{L}^1$ (*N,N,N'*-tris-(3,5-di-*tert*-butyl-2-hydroxybenzyl)-[1,10]-phenanthroline-5,6-diamine), $[\mathbf{Fe}^{\text{III}}\mathbf{L}^2]\cdot\mathbf{1}/2\mathbf{MeCN}$ (module), and $[\mathbf{Fe}^{\text{II}}(\mathbf{phen})_3]^{2+}(\mathbf{PF}_6)_2$ were synthesized according to procedures previously reported [see ref. 10 and Chakravarty et al, *Inorg. Chem.* **2007**, *46*, 11122]. The basic modular synthetic approach was followed for the synthesis of the tetrametallic iron cluster complex which was conducted under an argon atmosphere using Schlenk techniques.

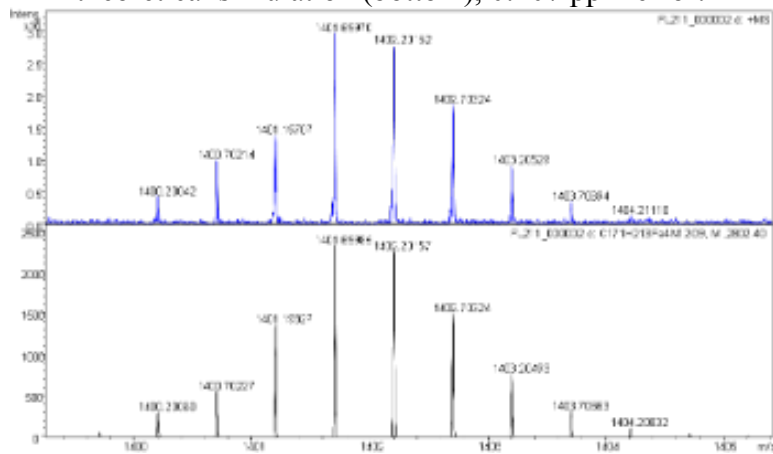
$[\mathbf{Fe}^{\text{II}}(\mathbf{Fe}^{\text{III}}\mathbf{L}^2)_3](\mathbf{PF}_6)_2$ (**1**). The module $[\mathbf{Fe}^{\text{III}}\mathbf{L}^2]\cdot\mathbf{1}/2\mathbf{MeCN}$ (1.37 g : 1.5 mmol) and KPF_6 (0.18 g : 1.0 mmol) were dissolved in anhydrous methanol under an argon atmosphere. To the resulting solution was added anhydrous FeCl_2 (0.06 g : 0.5 mmol) and the mixture was stirred at ambient temperature for 1 h. The suspension was stored at 4 °C for 3 d after which time a dark brown microcrystalline precipitate was isolated by filtration, washed with cold H_2O and cold *n*-hexane, and vacuum dried. Yield: 0.96 g, 62%. UV–visible data (DCM, 5.0×10^{-6} M): 279 (249 690), 336 (95 900), 486 (50 260), 525 (51 750). MS data (ESI⁺ in MeOH): $m/z = 1401.69970$ ($[\mathbf{Fe}^{\text{II}}(\mathbf{Fe}^{\text{III}}\mathbf{L}^1)_3]^{+2/+2}$), 2948.36578 ($[[\mathbf{Fe}^{\text{II}}(\mathbf{Fe}^{\text{III}}\mathbf{L}^1)_3]^{+2} + \mathbf{PF}_6]^{+}$), and 916.49504 ($[(\mathbf{Fe}^{\text{III}}\mathbf{L}^1)_3 + \text{H}^+]$).

2. ESI-MS exact mass spectrometry.

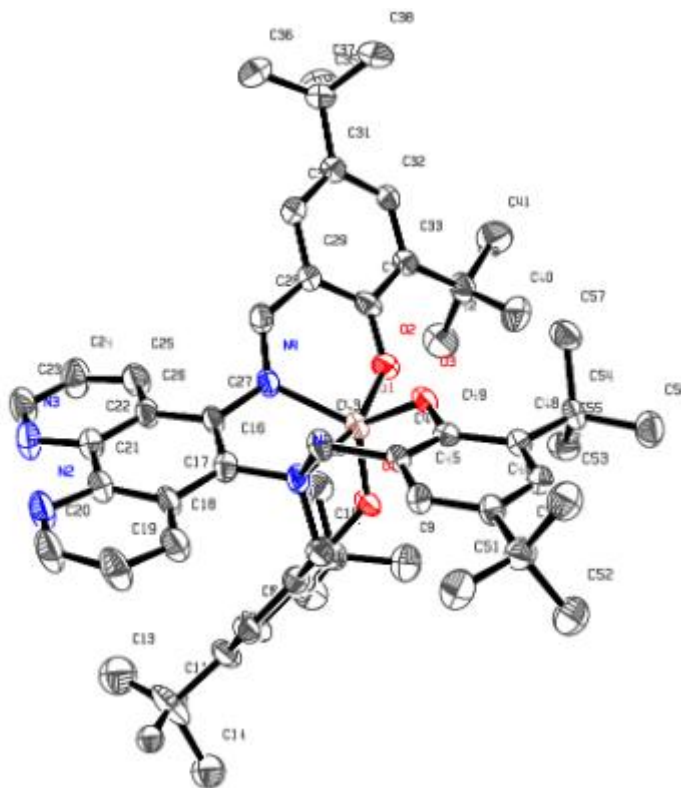
The $C_{171}H_{213}Fe_4N_{12}O_9$ full spectrum:



$C_{171}H_{213}Fe_4N_{12}O_9$, 2^+ charge state, measured (top) and theoretical simulation (bottom), 0.107 ppm error:



3. X-ray structural determinations.



Bond lengths [\AA] and angles [$^\circ$] for $[\text{Ga}^{\text{III}}\text{L}^2]$

Ga(1)-O(3)	1.828(3)	C(11)-C(12')	1.451(17)
Ga(1)-O(1)	1.828(3)	C(11)-C(14')	1.451(17)
Ga(1)-O(2)	1.899(3)	C(11)-C(12)	1.470(13)
Ga(1)-N(4)	1.975(4)	C(11)-C(13)	1.486(18)
Ga(1)-N(1)	2.266(4)	C(11)-C(12'')	1.61(3)
O(1)-C(1)	1.368(5)	C(11)-C(13')	1.67(2)
C(1)-C(6)	1.387(6)	C(11)-C(14)	1.685(15)
C(1)-C(2)	1.417(6)	C(15)-N(1)	1.502(6)
C(2)-C(3)	1.399(6)	N(1)-C(16)	1.460(5)
C(2)-C(7)	1.526(6)	N(1)-C(43)	1.497(5)
C(3)-C(4)	1.386(7)	C(16)-C(27)	1.356(6)
C(4)-C(5)	1.375(7)	C(16)-C(17)	1.450(6)
C(4)-C(11)	1.546(7)	C(17)-C(18)	1.399(6)
C(5)-C(6)	1.389(6)	C(17)-C(21)	1.423(6)
C(6)-C(15)	1.509(6)	C(18)-C(19)	1.359(6)
C(7)-C(8)	1.521(7)	C(19)-C(20)	1.393(7)
C(7)-C(9)	1.531(6)	C(20)-N(2)	1.306(6)
C(7)-C(10)	1.553(7)	N(2)-C(21)	1.355(6)
C(11)-C(13'')	1.395(19)	C(21)-C(22)	1.458(7)

C(22)-N(3)	1.354(6)	C(4)-C(3)-C(2)	124.2(4)
C(22)-C(26)	1.402(6)	C(5)-C(4)-C(3)	117.0(4)
N(3)-C(23)	1.311(6)	C(5)-C(4)-C(11)	121.6(5)
C(23)-C(24)	1.387(7)	C(3)-C(4)-C(11)	121.3(4)
C(24)-C(25)	1.356(6)	C(4)-C(5)-C(6)	121.6(4)
C(25)-C(26)	1.398(6)	C(1)-C(6)-C(5)	120.7(4)
C(26)-C(27)	1.448(6)	C(1)-C(6)-C(15)	118.8(4)
C(27)-N(4)	1.410(5)	C(5)-C(6)-C(15)	120.4(4)
N(4)-C(28)	1.313(6)	C(8)-C(7)-C(2)	109.8(4)
C(28)-C(29)	1.413(6)	C(8)-C(7)-C(9)	110.3(4)
C(29)-C(30)	1.406(6)	C(2)-C(7)-C(9)	109.9(4)
C(29)-C(34)	1.429(6)	C(8)-C(7)-C(10)	107.5(4)
C(30)-C(31)	1.369(6)	C(2)-C(7)-C(10)	112.2(4)
C(31)-C(32)	1.400(6)	C(9)-C(7)-C(10)	107.0(4)
C(31)-C(35)	1.534(7)	C(13")-C(11)-C(12')	126.0(12)
C(32)-C(33)	1.380(6)	C(13")-C(11)-C(14')	44.8(9)
C(33)-C(34)	1.423(6)	C(12')-C(11)-C(14')	95.8(11)
C(33)-C(39)	1.525(6)	C(13")-C(11)-C(12)	128.0(10)
C(34)-O(2)	1.338(5)	C(12')-C(11)-C(12)	31.2(7)
C(35)-C(38)	1.510(7)	C(14')-C(11)-C(12)	119.6(10)
C(35)-C(36)	1.524(7)	C(13")-C(11)-C(13)	32.2(9)
C(35)-C(37)	1.553(8)	C(12')-C(11)-C(13)	135.6(11)
C(39)-C(41)	1.527(6)	C(14')-C(11)-C(13)	77.0(10)
C(39)-C(40)	1.534(7)	C(12)-C(11)-C(13)	117.1(10)
C(39)-C(42)	1.535(7)	C(13")-C(11)-C(4)	116.0(9)
C(43)-C(44)	1.521(6)	C(12')-C(11)-C(4)	114.1(8)
C(44)-C(49)	1.387(6)	C(14')-C(11)-C(4)	114.6(8)
C(44)-C(45)	1.388(6)	C(12)-C(11)-C(4)	114.4(6)
C(45)-C(46)	1.385(6)	C(13)-C(11)-C(4)	108.5(8)
C(46)-C(47)	1.411(6)	C(13")-C(11)-C(12")	110.0(16)
C(46)-C(50)	1.527(6)	C(12')-C(11)-C(12")	66.4(13)
C(47)-C(48)	1.386(6)	C(14')-C(11)-C(12")	132.9(14)
C(48)-C(49)	1.413(6)	C(12)-C(11)-C(12")	35.6(12)
C(48)-C(54)	1.540(6)	C(13)-C(11)-C(12")	86.4(15)
C(49)-O(3)	1.376(5)	C(4)-C(11)-C(12")	112.5(12)
C(50)-C(51)	1.517(6)	C(13")-C(11)-C(13')	70.0(11)
C(50)-C(53)	1.528(7)	C(12')-C(11)-C(13')	115.5(11)
C(50)-C(52)	1.532(6)	C(14')-C(11)-C(13')	113.3(11)
C(54)-C(55)	1.528(6)	C(12)-C(11)-C(13')	86.4(10)
C(54)-C(56)	1.533(6)	C(13)-C(11)-C(13')	38.9(9)
C(54)-C(57)	1.551(6)	C(4)-C(11)-C(13')	103.9(8)
C(58)-C(59)	1.413(10)	C(12')-C(11)-C(13')	51.3(13)
C(59)-N(5)	1.133(9)	C(13")-C(11)-C(14)	85.1(11)
C(60)-C(61)	1.500(13)	C(12')-C(11)-C(14)	64.3(9)
C(61)-N(6)	1.187(12)	C(14')-C(11)-C(14)	40.3(8)
		C(12)-C(11)-C(14)	94.9(8)
O(3)-Ga(1)-O(1)	117.41(14)	C(13)-C(11)-C(14)	117.1(10)
O(3)-Ga(1)-O(2)	93.15(13)	C(4)-C(11)-C(14)	104.0(7)
O(1)-Ga(1)-O(2)	99.15(13)	C(12")-C(11)-C(14)	127.1(14)
O(3)-Ga(1)-N(4)	123.97(15)	C(13')-C(11)-C(14)	148.7(9)
O(1)-Ga(1)-N(4)	117.51(15)	N(1)-C(15)-C(6)	109.8(4)
O(2)-Ga(1)-N(4)	88.57(14)	C(16)-N(1)-C(43)	111.2(3)
O(3)-Ga(1)-N(1)	91.37(13)	C(16)-N(1)-C(15)	114.3(3)
O(1)-Ga(1)-N(1)	91.78(13)	C(43)-N(1)-C(15)	113.1(3)
O(2)-Ga(1)-N(1)	164.61(13)	C(16)-N(1)-Ga(1)	107.4(3)
N(4)-Ga(1)-N(1)	76.73(14)	C(43)-N(1)-Ga(1)	105.6(3)
C(1)-O(1)-Ga(1)	124.4(3)	C(15)-N(1)-Ga(1)	104.5(3)
O(1)-C(1)-C(6)	119.8(4)	C(27)-C(16)-C(17)	120.6(4)
O(1)-C(1)-C(2)	120.8(4)	C(27)-C(16)-N(1)	115.3(4)
C(6)-C(1)-C(2)	119.5(4)	C(17)-C(16)-N(1)	124.0(4)
C(3)-C(2)-C(1)	116.8(4)	C(18)-C(17)-C(21)	116.7(4)
C(3)-C(2)-C(7)	121.8(4)	C(18)-C(17)-C(16)	124.7(4)
C(1)-C(2)-C(7)	121.3(4)	C(21)-C(17)-C(16)	118.3(4)

C(19)-C(18)-C(17)	119.9(5)	C(36)-C(35)-C(31)	113.4(4)
C(18)-C(19)-C(20)	118.8(5)	C(38)-C(35)-C(37)	107.9(5)
N(2)-C(20)-C(19)	124.3(5)	C(36)-C(35)-C(37)	107.1(5)
C(20)-N(2)-C(21)	117.5(4)	C(31)-C(35)-C(37)	108.9(5)
N(2)-C(21)-C(17)	122.7(5)	C(33)-C(39)-C(41)	113.3(4)
N(2)-C(21)-C(22)	117.1(4)	C(33)-C(39)-C(40)	111.0(4)
C(17)-C(21)-C(22)	120.1(4)	C(41)-C(39)-C(40)	105.6(4)
N(3)-C(22)-C(26)	122.8(5)	C(33)-C(39)-C(42)	109.7(4)
N(3)-C(22)-C(21)	118.3(4)	C(41)-C(39)-C(42)	107.8(4)
C(26)-C(22)-C(21)	119.0(4)	C(40)-C(39)-C(42)	109.3(4)
C(23)-N(3)-C(22)	117.3(4)	N(1)-C(43)-C(44)	111.7(4)
N(3)-C(23)-C(24)	124.4(5)	C(49)-C(44)-C(45)	121.2(4)
C(25)-C(24)-C(23)	118.1(5)	C(49)-C(44)-C(43)	119.2(4)
C(24)-C(25)-C(26)	120.3(5)	C(45)-C(44)-C(43)	119.6(4)
C(25)-C(26)-C(22)	116.9(4)	C(46)-C(45)-C(44)	121.5(4)
C(25)-C(26)-C(27)	123.6(4)	C(45)-C(46)-C(47)	115.8(4)
C(22)-C(26)-C(27)	119.3(4)	C(45)-C(46)-C(50)	123.3(4)
C(16)-C(27)-N(4)	117.7(4)	C(47)-C(46)-C(50)	120.9(4)
C(16)-C(27)-C(26)	121.0(4)	C(48)-C(47)-C(46)	124.7(4)
N(4)-C(27)-C(26)	121.2(4)	C(47)-C(48)-C(49)	117.0(4)
C(28)-N(4)-C(27)	119.7(4)	C(47)-C(48)-C(54)	120.2(4)
C(28)-N(4)-Ga(1)	121.6(3)	C(49)-C(48)-C(54)	122.8(4)
C(27)-N(4)-Ga(1)	116.3(3)	O(3)-C(49)-C(44)	120.1(4)
N(4)-C(28)-C(29)	125.9(4)	O(3)-C(49)-C(48)	120.3(4)
C(30)-C(29)-C(28)	117.5(4)	C(44)-C(49)-C(48)	119.5(4)
C(30)-C(29)-C(34)	120.4(4)	C(49)-O(3)-Ga(1)	127.1(3)
C(28)-C(29)-C(34)	122.0(4)	C(51)-C(50)-C(46)	112.6(4)
C(31)-C(30)-C(29)	122.1(4)	C(51)-C(50)-C(53)	108.4(4)
C(30)-C(31)-C(32)	116.0(4)	C(46)-C(50)-C(53)	108.9(4)
C(30)-C(31)-C(35)	124.8(4)	C(51)-C(50)-C(52)	107.3(4)
C(32)-C(31)-C(35)	119.3(4)	C(46)-C(50)-C(52)	110.4(4)
C(33)-C(32)-C(31)	125.9(4)	C(53)-C(50)-C(52)	109.1(4)
C(32)-C(33)-C(34)	117.3(4)	C(55)-C(54)-C(56)	107.6(4)
C(32)-C(33)-C(39)	121.6(4)	C(55)-C(54)-C(48)	110.5(4)
C(34)-C(33)-C(39)	121.1(4)	C(56)-C(54)-C(48)	112.9(4)
O(2)-C(34)-C(33)	120.9(4)	C(55)-C(54)-C(57)	109.6(4)
O(2)-C(34)-C(29)	121.1(4)	C(56)-C(54)-C(57)	107.4(4)
C(33)-C(34)-C(29)	118.0(4)	C(48)-C(54)-C(57)	108.7(4)
C(34)-O(2)-Ga(1)	127.2(3)	N(5)-C(59)-C(58)	176.7(10)
C(38)-C(35)-C(36)	109.2(5)	N(6)-C(61)-C(60)	173.5(12)
C(38)-C(35)-C(31)	110.2(4)		

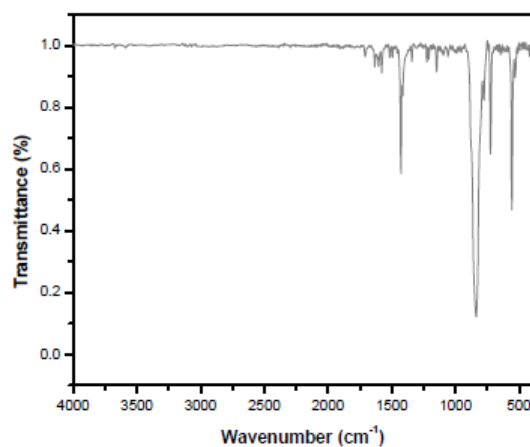
4. Molecular mechanics calculations.

Full citation for reference 17: M. J. Frisch, G.W. Trucks, H. B. Schlegel, G. E. Scuseria, M. A. Robb, J. R. Cheeseman, J. A. Montgomery, T. Vreven, K. N. Kudin, J. C. Burant, J.M. Millam, S. S. Iyengar, J. Tomasi, V. Barone, B. Mennucci, M. Cossi, G. Scalmani, N. Rega, G. A. Petersson, H. Nakatsuji, M. Hada, M. Ehara, K. Toyota, R. Fukuda, J. Hasegawa, M. Ishida, T. Nakajima, Y. Honda, O. Kitao, H. Nakai, M. Klene, X. Li, J. E. Knox, H. P. Hratchian, J. B. Cross, V. Bakken, C. Adamo, J. Jaramillo, R.

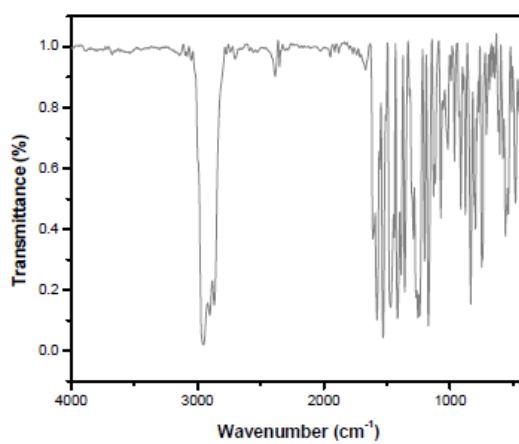
Gomperts, R. E. Stratmann, O. Yazyev, A. J. Austin, R. Cammi, C. Pomelli, J. W. Ochterski, P. Y. Ayala, K. Morokuma, G. A. Voth, P. Salvador, J. J. Dannenberg, V. G. Zakrzewski, S. Dapprich, A. D. Daniels, M. C. Strain, O. Farkas, D. K. Malick, A. D. Rabuck, K. Raghavachari, J. B. Foresman, J. V. Ortiz, Q. Cui, A. G. Baboul, S. Clifford, J. Cioslowski, B. B. Stefanov, G. Liu, A. Liashenko, P. Piskorz, I. Komaromi, R. L. Martin, D. J. Fox, T. Keith, M. A. Al-Laham, C. Y. Peng, A. Nanayakkara, M. Challacombe, P. M. W. Gill, B. Johnson, W. Chen, M. W. Wong, C. Gonzalez and J. A. Pople, 03, *GAUSSIAN*, Gaussian Inc., C. T. Wallingford, 2003.

5. Infrared spectroscopy.

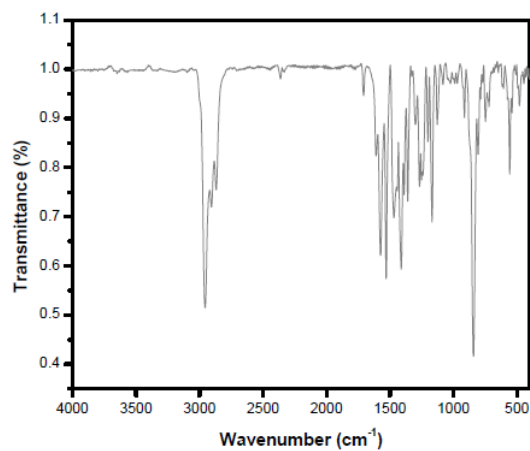
IR spectrum for $[\text{Fe}^{\text{II}}(\text{phen})_3](\text{PF}_6)_2$



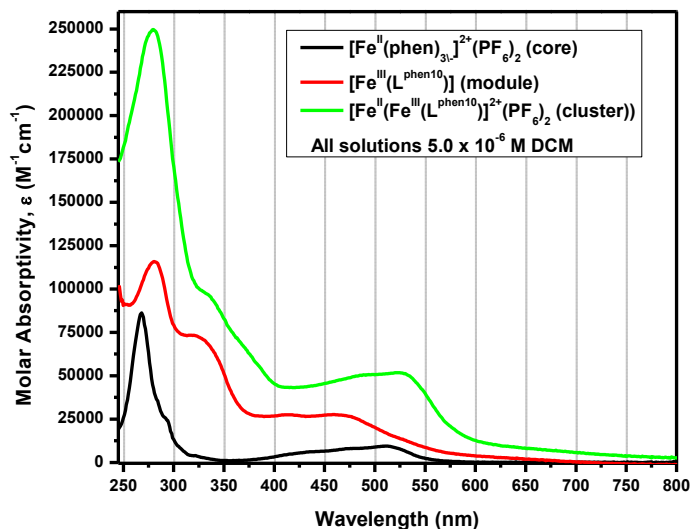
IR spectrum for $[\text{Fe}^{\text{III}}\text{L}^2]$



IR spectrum for $[\text{Fe}^{\text{II}}(\text{Fe}^{\text{III}}\text{L}^2)_3](\text{PF}_6)_2$



6. UV–visible spectroscopy.



	λ (nm) / ϵ (Lmol ⁻¹ cm ⁻¹) ^a
H ₃ L ¹	252 (22 800), 280 (30 700), 319 (7800)
[Fe ^{II} (Fe ^{III} (L ²) ₃)](PF ₆) ₂	279 (249 690), 336 (95 900), 486 (50 260), 525 (51 750)
[Fe ^{III} (L ²)]	281 (115 880), 333 (68 870), 411 (27 520), 463 (27 500)
[Fe ^{II} (phen) ₃](PF ₆) ₂	268 (86 220), 292 (25 490), 476 (8010), 511 (9390)

7. Electrochemistry.

	Process (vs Fc ⁺ /Fc)	
Fe(phen) ₃](PF ₆) ₂	N/A	0.77V (ΔE 0.08V)
[Fe(L ²)]	-1.37V (ΔE 0.25V)	0.64V (ΔE 0.06V)
[Fe ^{II} (Fe ^{III} (L ²)](PF ₆) ₂	-1.24V (ΔE 0.33V)	0.64V (ΔE 0.13V)

APPENDIX C

Supplementary Information for Chapter 5

MS Data for **(1)** (ESI⁺ in MeOH):

$m/z = 386$ (100%) for
 $[(L^{Py})Ru^{II}(bpy)_2]^{+2}/+2$

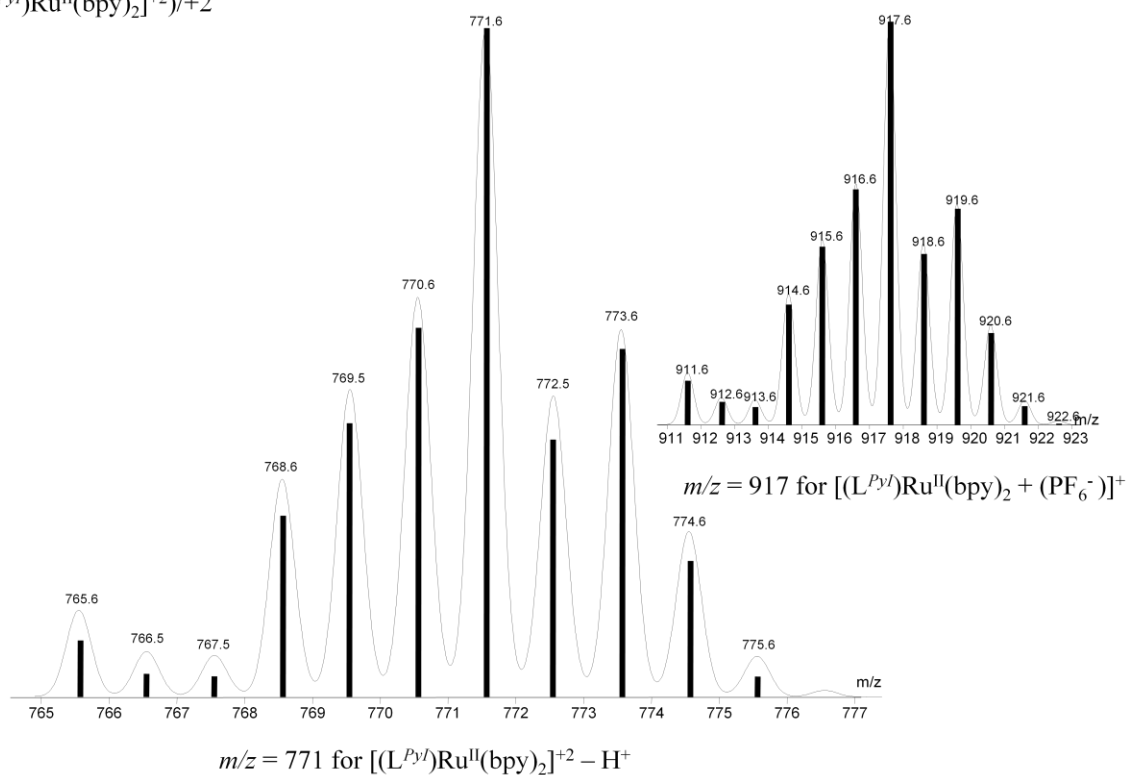


Figure B.5.1. ESI⁺ pertinent peak clusters with experimental (bars) and simulated (continuum) isotopic distributions for **1**

MS Data for **(2)** (ESI⁺ in MeOH):
 $m/z = 387$ (100%) for
 $[(L^{PyA})Ru^{II}(bpy)_2]^{+2}/+2$

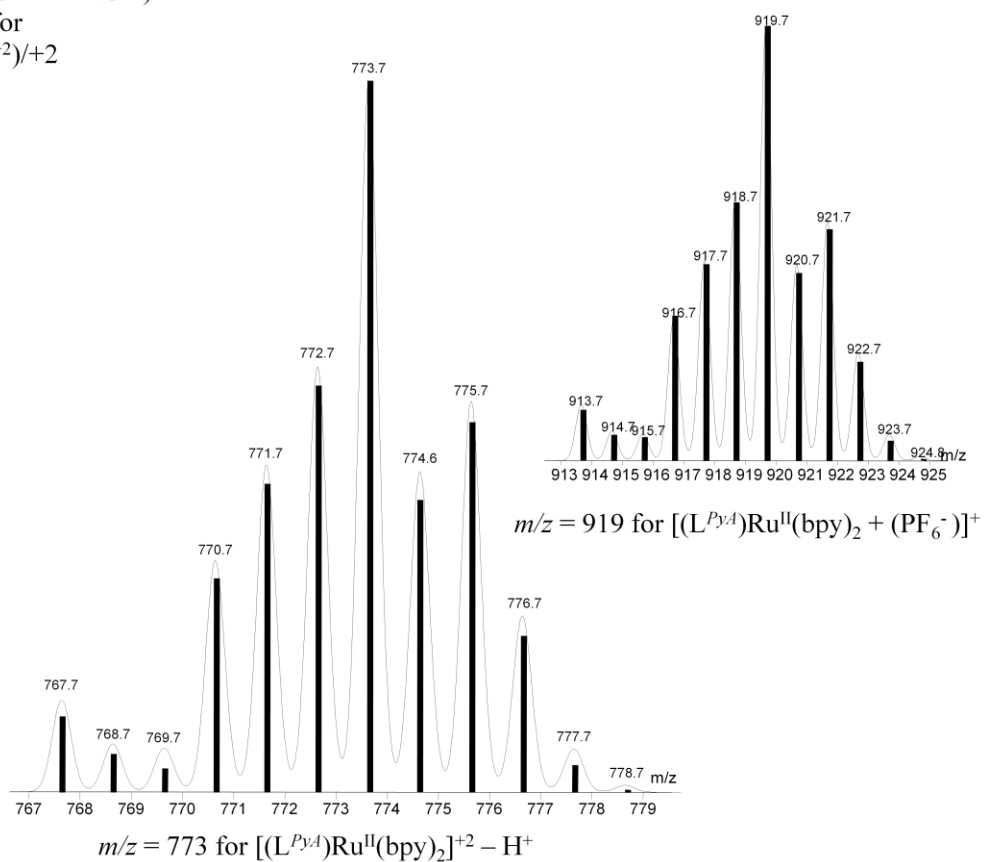


Figure B.5.2. ESI⁺ pertinent peak clusters with experimental (bars) and simulated (continuum) isotopic distributions for **2**

MS Data for **(3)** (ESI⁺ in MeOH):
 $m/z = 898$ for $[(L^{PhBu})Ru^{II}(bpy)_2]^+$

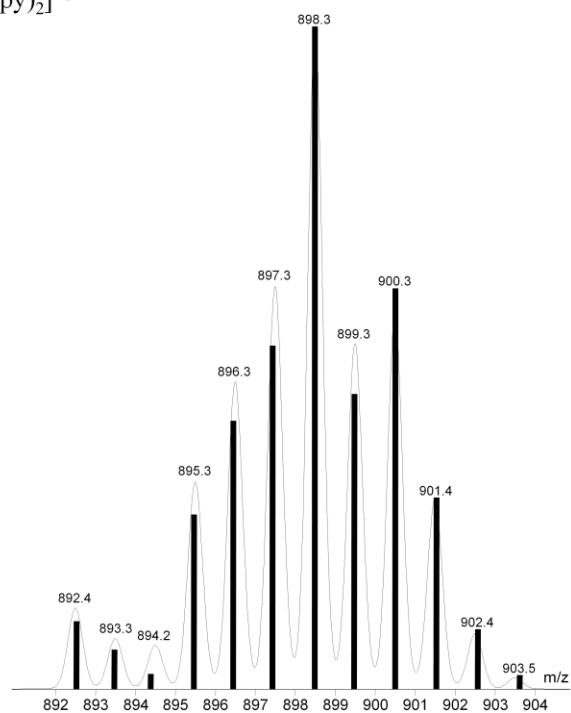


Figure B.5.3. ESI⁺ peak cluster with experimental (bars) and simulated (continuum) isotopic distributions for **3**

MS Data for **(4)** (ESI⁺ in MeOH):
 $m/z = 856$ for $[(L^{PhCl})Ru^{II}(bpy)_2]^+$

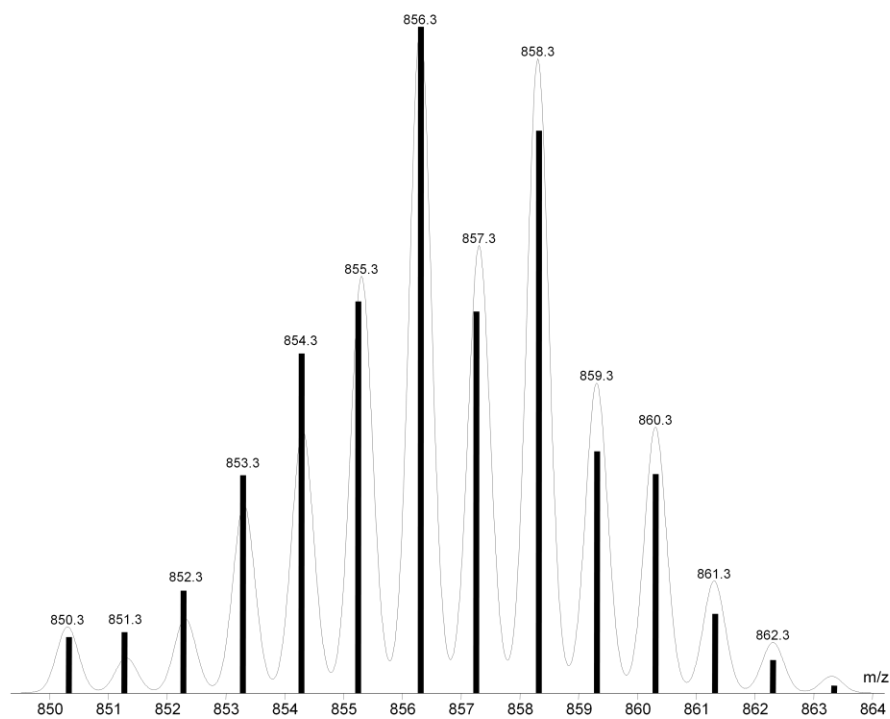


Figure B.5.4. ESI⁺ peak cluster with experimental (bars) and simulated (continuum) isotopic distributions for **4**

Photodissociation Reaction Follow in Acetonitrile and Mass in Acetonitrile at Cone 5 Voltage

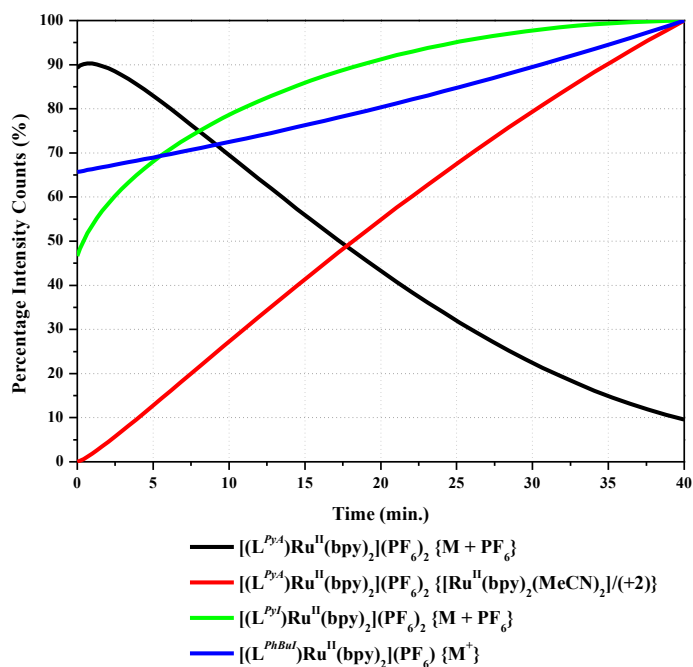


Figure B.5.5. ESI⁺ results of photosubstitution experiment in acetonitrile at cone 5 V

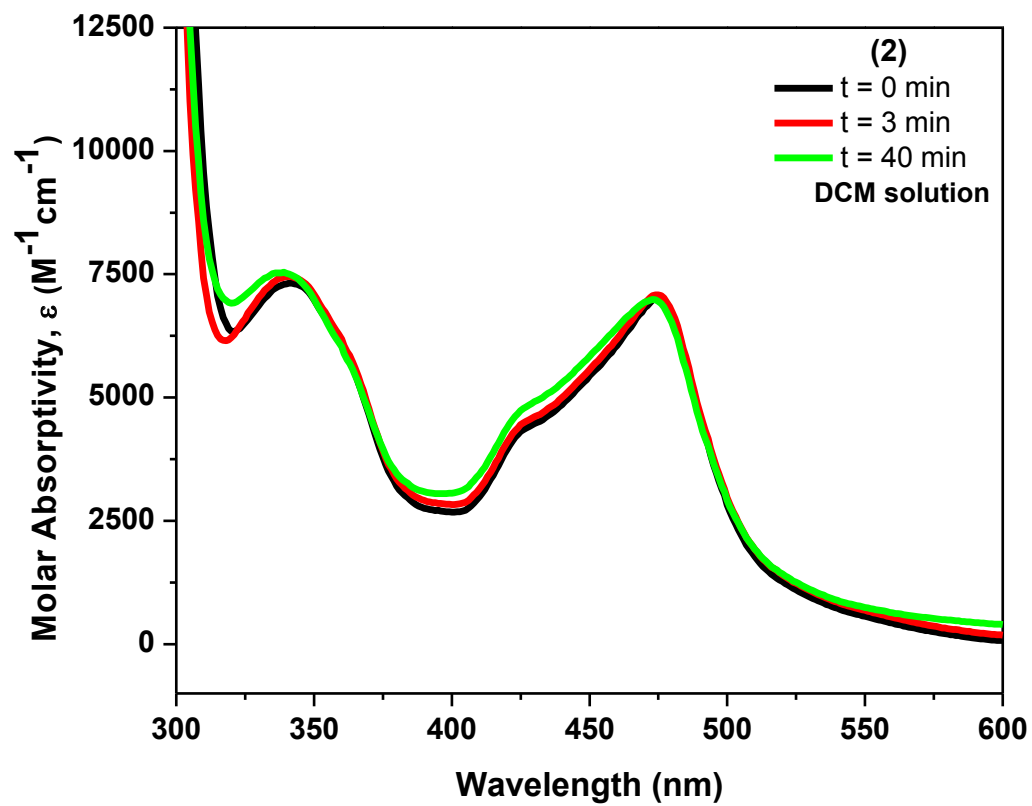


Figure B.5.6. UV-visible spectra recorded for photostability of 2 in DCM

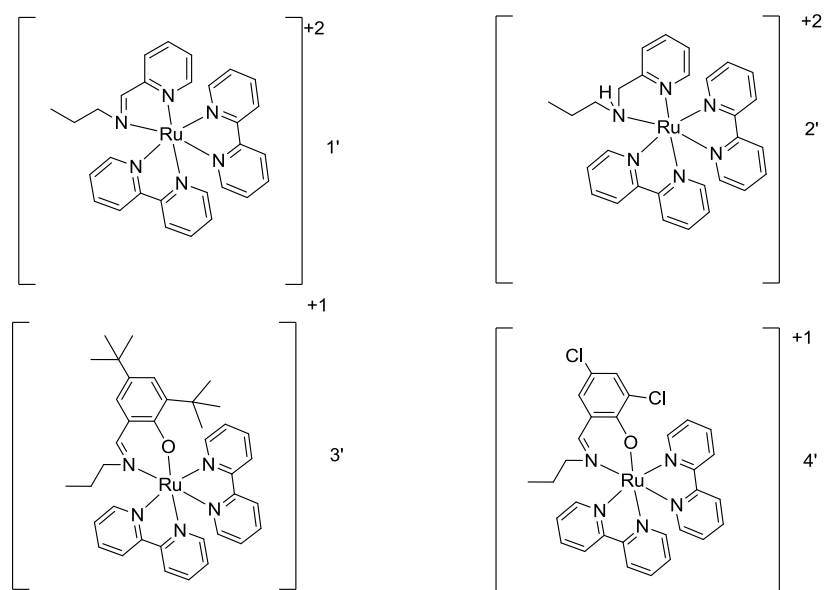


Figure B.5.7. Representative models 1', 2', 3', and 4' comprised of shortened propyl chains

Table B.5.1. Orbital Compositions and Energies

Ru(Bpy) ₂ PyImine (1')						
rb3lyp/lanl2dz (MeCN)						
	Orbital	Energy (eV)	% Ru	%L	% Bpy	
	132	LUMO+2	-2.7	6.1	0.7	93.2
	131	LUMO+1	-2.8	6.2	21.8	72.0
	130	LUMO	-2.9	2.8	69.9	27.3
	129	HOMO	-6.2	82.5	6.1	11.4
	128	HOMO-1	-6.3	75.6	3.9	20.5
	127	HOMO-2	-6.4	74.2	14.0	11.8
	126	HOMO-3	-7.6	0.3	0.8	98.9

Ru(Bpy) ₂ PyAmine (2')						
rb3lyp/lanl2dz (MeCN)						
	Orbital	Energy (eV)	% Ru	%L	% Bpy	
	133	LUMO+2	-2.0	1.2	22.3	76.5
	132	LUMO+1	-2.7	6.7	0.4	92.9
	131	LUMO	-2.8	2.5	0.5	97.0
	130	HOMO	-6.0	81.4	5.2	13.4
	129	HOMO-1	-6.2	80.3	5.8	13.9
	128	HOMO-2	-6.2	80.7	1.8	17.5
	127	HOMO-3	-7.5	0.3	0.0	99.7

Ru(Bpy) ₂ Cl Imine (4')					
rb3lyp/lanl2dz (MeCN)					
	Orbital	Energy (eV)	% Ru	%L	% Bpy
	LUMO+2	-2.0	2.8	92.4	4.8
	LUMO+1	-2.5	6.3	16.0	77.7
	LUMO	-2.5	4.1	0.9	95.0
	HOMO	-5.4	48.8	43.1	8.1
	HOMO-1	-5.6	78.7	7.4	13.9

	HOMO-2	-5.9	74.2	10.3	15.5
	HOMO-3	-6.5	31.1	61.4	7.5

Ru(Bpy) ₂ POH tbutyl Imine (3')					
rb3lyp/lanl2dz (MeCN)					
				Population	
	Orbital	Energy (eV)	% Ru	%L	% Bpy
	LUMO+2	-1.7	1.6	1.2	97.2
	LUMO+1	-2.4	7.5	0.8	91.7
	LUMO	-2.5	3.9	0.2	95.9
	HOMO	-4.9	31.2	63.4	5.4
	HOMO-1	-5.4	76.3	10.6	13.1
	HOMO-2	-5.7	69.2	15.4	15.4
	HOMO-3	-6.0	46.3	44.8	8.9

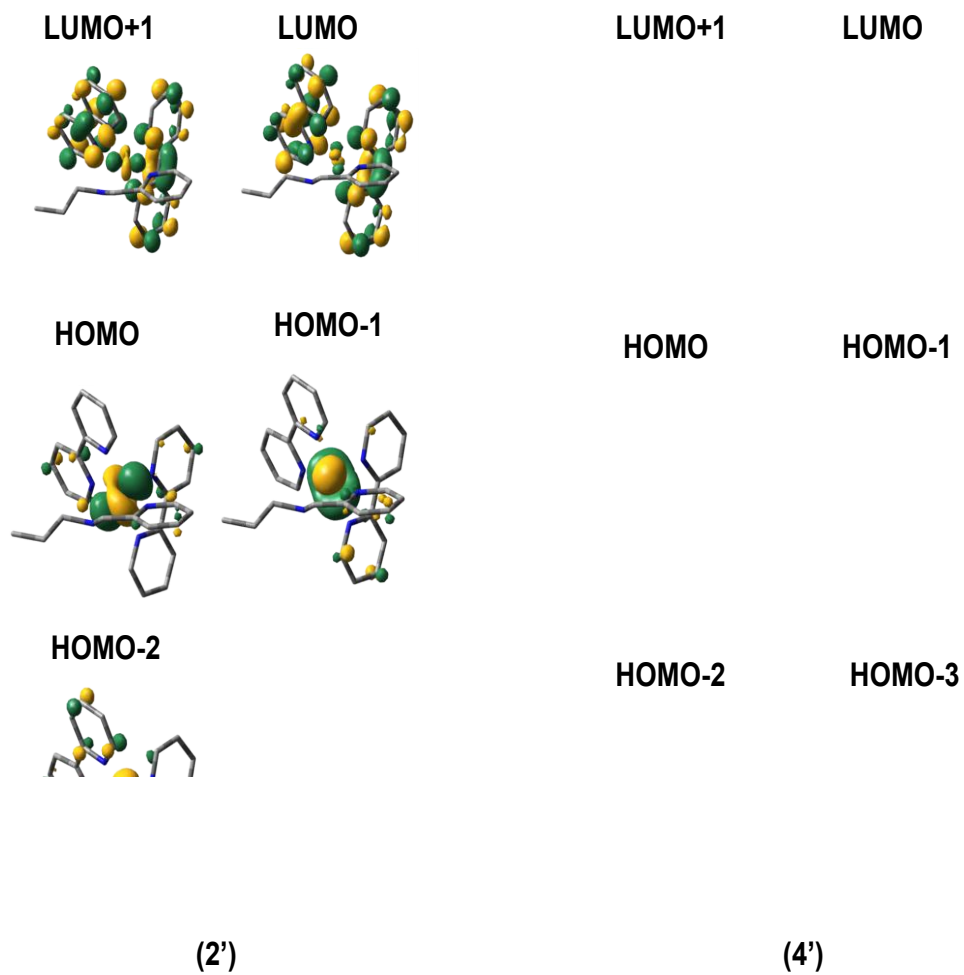
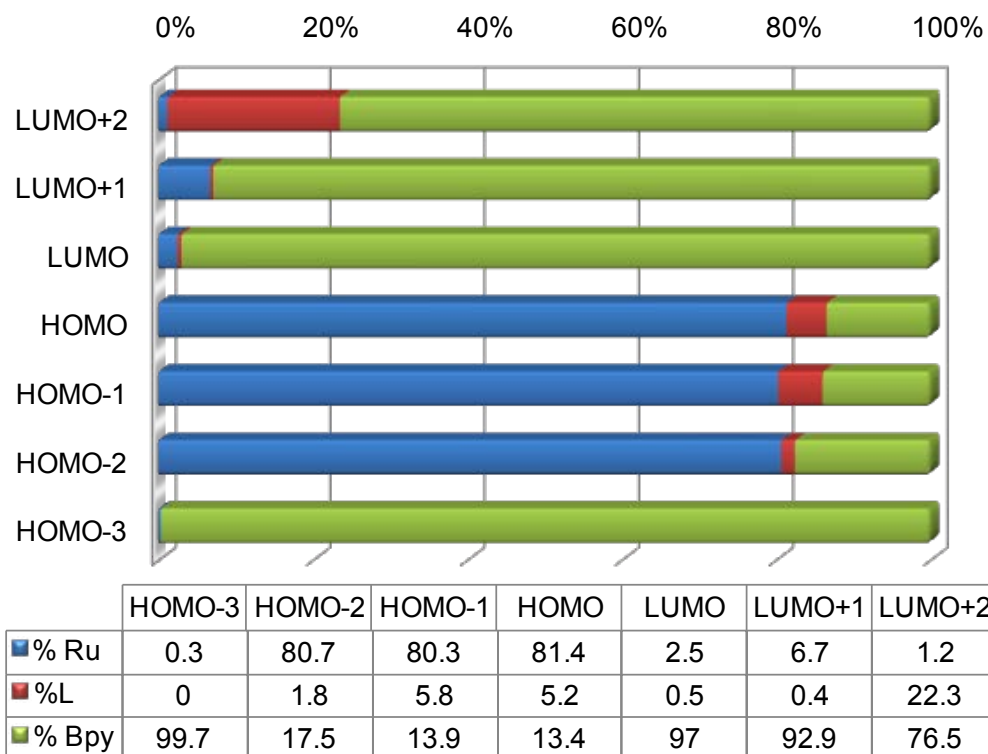


Figure B.5.8. Relative Molecular Orbital Energies for 2' and 4'

(2')



(4')

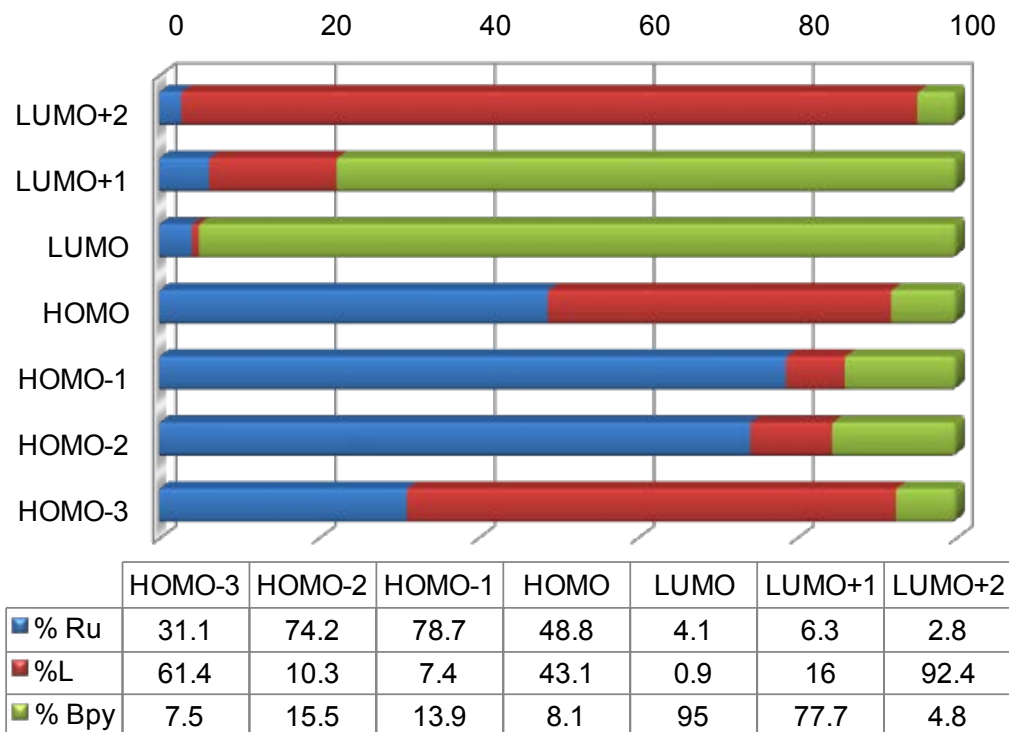


Figure B.5.9. Percent compositions of representative MOs for 2' and 4'

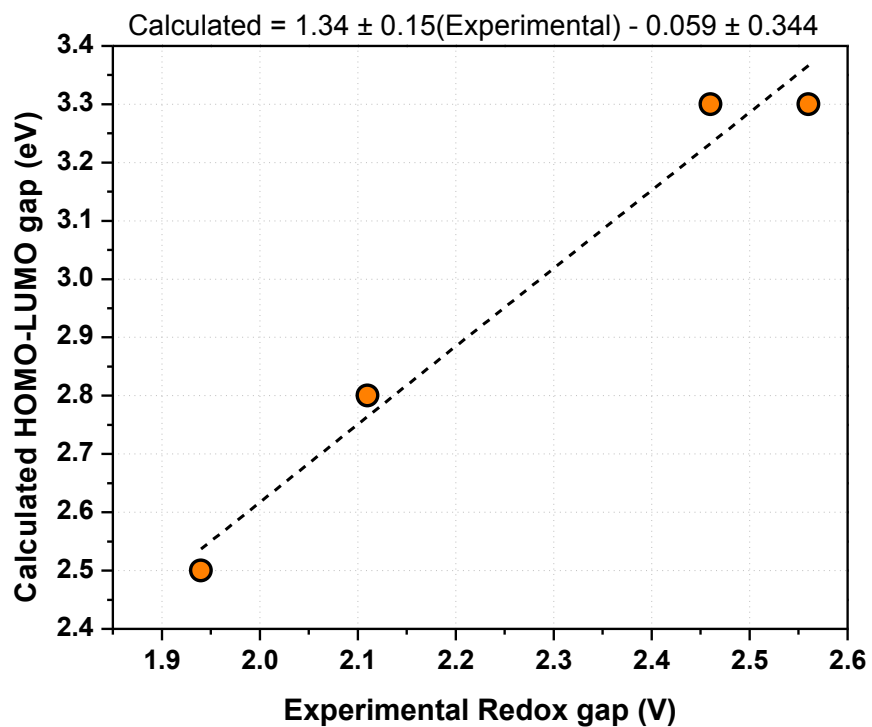


Figure B.5.10. Correlation between the differences between the half-wave potentials for oxidation and reduction and the differences between the DFT-calculated HOMO–LUMO energies

Table B.5.2. Cartesian Coordinates and Energies of the Optimized Structures

	(1') E:-1543.468381 a.u.			(2') E:-1544.651099 a.u.			
C	-2.05530900	1.67421500	1.64910500	C	-2.48355500	1.11105900	1.61105500
C	1.15699200	4.07166300	-1.28158600	C	0.59029800	4.32466400	-0.74231300
C	-0.50760900	2.92210400	0.22605500	C	-1.16957200	2.81088200	0.31545000
H	2.66855700	4.83670200	-2.63420400	H	2.15475400	5.45735400	-1.72813300
N	-0.92679200	1.77114300	0.68459400	N	-1.11478200	1.55507500	1.14777400
C	0.59327100	2.90802400	-0.73198600	C	0.14912700	3.04143800	-0.38609000
C	2.21694300	3.95270000	-2.19647200	C	1.80160400	4.47223900	-1.44048400
N	1.05136200	1.64899300	-1.06760100	N	0.88385900	1.92354100	-0.68941000
C	2.68124400	2.66691600	-2.53402500	C	2.54851000	3.32104100	-1.75331700
H	3.49717500	2.52975400	-3.23494400	H	3.48934900	3.38534700	-2.28859900
C	2.07811100	1.54060200	-1.95146000	C	2.06411900	2.06865700	-1.35717900
H	2.41348100	0.54002600	-2.19344100	H	2.61410200	1.16353500	-1.57809800
Ru	0.06026500	0.09120100	-0.06962900	Ru	0.09860000	0.10144400	0.01798400
C	-2.25471600	-1.73719000	0.19553600	C	-2.01821400	-1.96496100	-0.06693000
C	-0.86775400	-1.89743800	2.10059000	C	-0.57936400	-2.34673400	1.76658300
C	-3.12237600	-2.71075700	0.72293100	C	-2.79361700	-3.08474900	0.28563700
C	-2.46204800	-1.06767500	-1.10407100	C	-2.29742800	-1.10766600	-1.23513800
C	-1.69811200	-2.86856700	2.67464500	C	-1.31505600	-3.47079100	2.16279600
H	0.02177300	-1.55198100	2.61036600	H	0.29186500	-2.02763600	2.32289900
C	-2.84519200	-3.28417400	1.97330400	C	-2.44366800	-3.84649500	1.41067800
H	-4.00197700	-3.02020800	0.17192400	C	-3.65919700	-3.36275300	-0.30332100
C	-3.55968200	-1.31355200	-1.94868600	H	-3.35386800	-1.33053200	-2.13766700
H	-1.44550100	-3.28374200	3.64380700	H	-1.00583800	-4.03130100	3.03793300
H	-3.50804700	-4.03572800	2.38909200	H	-3.03592300	-4.71082200	1.69230600
C	-1.60727000	0.52313200	-2.62931400	C	-1.58720300	0.76594200	-2.48775400
C	-3.67245900	-0.61739800	-3.16221300	C	-3.52355700	-0.47453600	-3.23635000
H	-4.31801900	-2.03436400	-1.66896100	H	-4.03311100	-2.16116800	-1.99187300
C	-2.67885100	0.31760900	-3.50768800	C	-2.61901500	0.58910800	-3.41697300
H	-0.82182900	1.22996700	-2.86177800	H	-0.86466300	1.56341500	-2.60222500
H	-4.51509500	-0.80037800	-3.82070900	H	-4.33541200	-0.63769500	-3.93724800
H	-2.72628000	0.87817000	-4.43445100	H	-2.70433300	1.26889200	-4.25724600
N	-1.49281600	-0.15260500	-1.45340100	N	-1.42688600	-0.05229100	-1.40951800
N	-1.13339700	-1.33860500	0.88908800	N	-0.91857100	-1.60039800	0.67991200
C	2.39030600	-1.74624800	-0.05916700	C	2.61106400	-1.41605100	-0.36749300
C	0.98597800	-2.22480000	-1.89694200	C	1.20169100	-1.66856400	-2.24475700
C	3.25748800	-2.79164400	-0.42625600	C	3.57509600	-2.25458000	-0.95779700
C	2.60596500	-0.87103400	1.10982600	C	2.77155900	-0.78941200	0.95793300
C	1.81610100	-3.27414100	-2.31094900	C	2.12584900	-2.50741700	-2.87872600
H	0.09038600	-1.97292000	-2.44902500	H	0.26466700	-1.41554200	-2.72046200
C	2.97148900	-3.56465100	-1.56192000	C	3.33516700	-2.80767000	-2.22415100
H	4.14222200	-3.00382600	0.16131900	H	4.50081400	-2.47665100	-0.44168600
C	3.72211300	-0.96032600	1.96154600	C	3.92207700	-0.94776300	1.75317900
H	1.55672800	-3.84440200	-3.19582600	H	1.89671100	-2.91117100	-3.85852100
H	3.63357700	-4.37279700	-1.85450400	H	4.07215000	-3.45517000	-2.68735600
C	1.75203200	0.93566400	2.37047500	C	1.78490400	0.56673800	2.61148600
C	3.84327400	-0.07501600	3.04344700	C	3.99574200	-0.32572500	3.00763100
H	4.48911400	-1.70449000	1.78609800	C	4.75244000	-1.54752300	1.40199000
C	2.84047700	0.89025600	3.25051000	C	2.90299300	0.44486800	3.44513900
H	0.96383300	1.66589600	2.49679200	H	0.93544700	1.14854000	2.94157000
H	4.70008100	-0.13537500	3.70624700	H	4.87903500	-0.44115500	3.62678000
H	2.89442200	1.59568900	4.07202100	H	2.90837400	0.94221600	4.40843300
N	1.26003300	-1.47187200	-0.79682000	N	1.42987300	-1.12848100	-1.01524100
N	1.62762100	0.07519200	1.32299000	N	1.70460500	-0.02623800	1.38833000
H	-1.69408200	1.07384800	2.49422100	H	-2.34053000	0.18002100	2.16841500
H	-2.83437100	1.07698800	1.15699300	H	-3.07945300	0.88615500	0.72051100
C	-2.65829600	2.99180500	2.16367500	C	-3.21902600	2.13171200	2.50267100
H	-3.05958500	3.58024900	1.32667600	H	-3.44408100	3.04507900	1.93678600
H	-1.88157600	3.59901200	2.64988500	H	-2.56820000	2.42109200	3.34166600
C	-3.79077300	2.70755400	3.17314700	C	-4.53364700	1.53845300	3.05240700
H	-4.22336200	3.64542400	3.54126700	H	-5.05526700	2.26916500	3.68221500
H	-4.59707200	2.12323300	2.71026100	H	-5.21093200	1.25339000	2.23616800
H	-3.41738800	2.14510600	4.03893800	H	-4.34015600	0.64494800	3.66075100
H	0.76987000	5.04354200	-0.99366500	H	-0.00848900	5.19002200	-0.47758500
H	-0.93875800	3.87222500	0.52497300	H	-1.96949300	2.67799100	-0.42266200
				H	-1.42815600	3.68411100	0.92271300
				H	-0.57960100	1.77639100	1.99249000

(3') E: -1916.415343 a.u.
 C 1.04286900 -2.95798900 0.99216300
 C -3.51702800 -1.55141900 0.34482800
 C -1.13701300 -1.98927800 0.55566400
 N 0.16501000 -1.81410000 0.58562100
 C -2.18998400 -1.05962100 0.17794600
 C -4.64439100 -0.79432300 0.02312200
 C -4.40566700 0.50777000 -0.49607300
 H -5.26426400 1.11346800 -0.75224400
 C -3.13085200 1.05914100 -0.69863400
 Ru 1.10853500 -0.01454400 0.05931500
 C 3.64651200 -1.28033400 -0.74897600
 C 3.77122100 -0.55641700 1.49697700
 C 4.98147300 -1.72282200 -0.69869600
 C 2.78799800 -1.38459000 -1.94380400
 C 5.10126600 -0.97973600 1.60188100
 H 3.26141200 -0.09645500 2.33396600
 C 5.72011100 -1.57499400 0.48477400
 H 5.44124700 -2.17328400 -1.57047200
 C 3.17326400 -1.99207100 -3.15365600
 H 5.63368300 -0.84380100 2.53696100
 H 6.75021900 -1.91235600 0.53443600
 C 0.65733800 -0.87277500 -2.83977600
 C 2.26755800 -2.03533100 -4.22509600
 H 4.15972100 -2.42739200 -3.26104500
 C 0.98850400 -1.46533400 -4.06482600
 H -0.30488200 -0.41088300 -2.65766100
 H 2.55217200 -2.50209000 -5.16254600
 H 0.26100900 -1.47776200 -4.86918300
 N 1.53431500 -0.83180100 -1.79984900
 N 3.04670900 -0.69858000 0.35126500
 C 1.74493600 2.79072900 0.73714300
 C 2.42020000 2.31936200 -1.47562500
 C 2.17006200 4.12630100 0.60060900
 C 1.15715100 2.23551600 1.97115200
 C 2.86065900 3.63490800 -1.66787600
 H 2.49293400 1.58456000 -2.26696100
 C 2.73200300 4.55658800 -0.61071100
 H 2.06564500 4.82335200 1.42330800
 C 0.95693500 2.98027900 3.14923600
 H 3.28879700 3.92374600 -2.62150500
 H 3.06098000 5.58415800 -0.72700200
 C 0.28844700 0.30140600 3.01288100
 C 0.40764800 2.35918300 4.28058900
 H 1.22459600 4.02939300 3.18763300
 C 0.06956800 0.99332700 4.20993200
 H 0.03515100 -0.74594300 2.91396800
 H 0.24820700 2.92439400 5.19309000
 H -0.35791200 0.47197100 5.05946500
 N 1.87164000 1.89913300 -0.30404800
 N 0.81936600 0.90014700 1.90986800
 H 1.68016500 -2.59708000 1.80964500
 H 1.71007200 -3.16422000 0.14513300
 C 0.37799100 -4.27673500 1.42899800
 H -0.22869300 -4.69295100 0.61233700
 H -0.29502500 -4.10269000 2.28079300
 C 1.45233600 -5.30842700 1.83578900
 H 0.98613700 -6.25143500 2.14656900
 H 2.12928600 -5.52722500 0.99888200
 H 2.05869000 -4.93967500 2.67410300
 H -3.63328200 -2.55907700 0.74086300
 H -1.52051200 -2.96247200 0.86049500
 C -1.97267300 0.26151800 -0.35264400
 O -0.74254500 0.75334400 -0.55250200
 C -6.06566300 -1.37333500 0.22694100
 C -2.96928100 2.48810500 -1.27776800
 C -4.33280500 3.17027000 -1.57138500
 H -4.94206600 3.28534500 -0.66501700
 H -4.14736300 4.17429700 -1.97475100

H -4.92051300 2.61728200 -2.31619600
 C -2.20968100 3.39168000 -0.26152600
 H -1.22771600 2.97187600 -0.03230500
 H -2.07645200 4.39910400 -0.68103500
 H -2.78022400 3.48623800 0.67320100
 C -2.18265000 2.43398800 -2.62163200
 H -1.19436800 1.99221000 -2.47329300
 H -2.72868500 1.83699700 -3.36551200
 H -2.05947800 3.44902800 -3.02520800
 C -7.17762500 -0.37118600 -0.17438000
 H -7.13442600 0.54762900 0.42524900
 H -7.11387400 -0.09351100 -1.23471500
 H -8.16059400 -0.83097100 -0.00922300
 C -6.23671400 -2.65598500 -0.64042500
 H -5.49773200 -3.42285700 -0.37678300
 H -7.23668800 -3.08685600 -0.49273600
 H -6.11791600 -2.42335600 -1.70710900
 C -6.27180300 -1.74519900 1.72563300
 H -7.27308700 -2.17105600 1.87831700
 H -5.53639400 -2.48596200 2.06324100
 H -6.17577700 -0.85711100 2.36449800

(4') E: -1630.883151 a.u.
 C 0.65798800 -2.70536200 1.36590700
 C -3.92946200 -1.59265300 0.36528500
 C -1.54035000 -1.91441800 0.73345700
 N -0.25184400 -1.67215900 0.77048200
 C -2.60963800 -1.08884600 0.18465800
 C -5.02352500 -0.89868900 -0.13138600
 C -4.86987800 0.31398800 -0.83261300
 H -5.72778100 0.85289000 -1.21946900
 C -3.57992100 0.80042700 -1.01327800
 Ru 0.64585600 0.07803900 0.01811200
 C 3.26247400 -1.18422000 -0.47084800
 C 3.24369400 -0.11573300 1.63737500
 C 4.60717100 -1.55627900 -0.28963400
 C 2.47360800 -1.50208300 -1.67649000
 C 4.58020500 -0.46149200 1.86942300
 H 2.67514900 0.44837400 2.36558900
 C 5.27637800 -1.19636800 0.88984900
 H 5.12824700 -2.11516100 -1.05784800
 C 2.94434200 -2.26829900 -2.75892700
 H 5.05785200 -0.15931000 2.79495000
 H 6.31336700 -1.47836900 1.03963300
 C 0.38672300 -1.20155100 -2.75283000
 C 2.10423900 -2.50015800 -3.85943700
 H 3.94633100 -2.68035100 -2.74699600
 C 0.80480500 -1.95523800 -3.85704600
 H -0.59663300 -0.75087100 -2.70071500
 H 2.45518500 -3.09053400 -4.69958800
 H 0.12725400 -2.10855600 -4.68979000
 N 1.19810800 -0.98113900 -1.68323100
 N 2.58691400 -0.46621700 0.49626500
 C 1.05500500 2.98982000 0.25045300
 C 1.93358400 2.21202700 -1.79872500
 C 1.38066700 4.31579600 -0.09308000
 C 0.43328300 2.60071000 1.53134700
 C 2.28462500 3.51021100 -2.19035500
 H 2.12499000 1.36390000 -2.44309200
 C 1.99956200 4.58266900 -1.32361700
 H 1.15727200 5.13015200 0.58552100
 C 0.10349400 3.51252400 2.55185800
 H 2.76348700 3.67000100 -3.15008200
 H 2.25342400 5.60118200 -1.59893600
 C -0.32248700 0.79855400 2.85842000
 C -0.45312900 3.04321000 3.75104900
 H 0.27848000 4.57311800 2.41766700
 C -0.66527300 1.65972500 3.90787100
 H -0.47668100 -0.26973700 2.93559800
 H -0.71205100 3.73794100 4.54333600



H	-1.08979300	1.25205600	4.81870000
N	1.32905200	1.95030800	-0.60890800
N	0.21113800	1.24992500	1.68948200
H	1.25891000	-2.19346400	2.12713600
H	1.35161700	-3.00975200	0.57190300
C	0.03113800	-3.96772600	1.98560300
H	-0.54024400	-4.52634100	1.23100300
H	-0.66610700	-3.69577700	2.79083300
C	1.13546700	-4.88266300	2.55838200
H	0.69818900	-5.78654500	2.99951800
H	1.83660500	-5.19575300	1.77316100
H	1.70988400	-4.36917600	3.34095100
H	-4.07052400	-2.52883000	0.89816500
H	-1.89898600	-2.84768300	1.16391800
C	-2.39768500	0.14944800	-0.52634900
O	-1.21007100	0.68243000	-0.75650500
Cl	-3.37503800	2.36861100	-1.92289800
Cl	-6.71030100	-1.56070300	0.11804500

APPENDIX D

Supplementary Information for Chapter 6

Contents:

1. Synthesis of $[\text{Mn}(\text{HL})_2]$.

2. X-ray Structure Determination.

Table D.6.1. Crystal Data for $[\text{Co}(\text{L}'^{1-})(\text{L}'^{2-})]$

Figure D.6.1. ORTEP diagram of $[\text{Co}(\text{L}'^{1-})(\text{L}'^{2-})]$

Table D.6.2. Structural Data for $[\text{Co}(\text{L}'^{1-})(\text{L}'^{2-})]$

Table D.6.3. Crystal Data for $[\text{Mn}(\text{HL})_2]$

Figure D.6.2. ORTEP diagram of $[\text{Mn}(\text{HL})_2]$

Table D.6.4. Structural Data for $[\text{Mn}(\text{HL})_2]$

Figure D.6.3. EPR spectrum of $[\text{Co}(\text{L}'^{1-})(\text{L}'^{2-})]$

3. Computational Details.

Figure D.6.4. Comparison of spin densities for doublets

Table D.6.5. Structural Comparison

Table D.6.6. Cartesian coordinates for computed structures

Table D.6.7. Frequencies for computed structures

Table D.6.8. Energetics for computed structures

Table D.6.9. Assignments for low-energy TD-DFT transitions

Figure D.6.5. TD-DFT spectrum with transitions

Scheme D.6.1. Details of ligand nomenclature

4. References.

1. Synthesis of $[\text{Mn}(\text{HL})_2]$.

A 25 mL acetonitrile solution of the ligand H_4L (0.517 g, 1 mmol) was treated with $\text{MnCl}_2 \cdot 4\text{H}_2\text{O}$ (0.198 g, 1 mmol) and triethylamine (0.2 mL). At room temperature in the presence of air the resulting solution was stirred for 2 h. A dark brown microcrystalline solid was isolated from the solution and washed with acetonitrile. A

dichloromethane/acetonitrile (1:1) solvent mixture yielded X-ray quality crystals after slow solvent evaporation. Yield: 41%. Elemental anal. calcd for $[C_{68}H_{90}MnN_4O_4]$: C, 75.45, H, 8.38, N, 5.18 %. Found: C, 75.26, H, 8.40, N, 5.12 %. IR data (KBr, cm^{-1}): 2956, 2906, 2868, 1580, 1532, 1466, 1442, 1362, 1309, 1244, 1145, 993, 739, 600. UV-visible data (DCM, 1.0×10^{-5} M): 279 (27,150); 349 sh (19,360); 433 (13,040); 584 (8,310); 856 (8,740). MS data (ESI⁺ in CH_2Cl_2): $m/z = 1082.61$ (100%) for $[M + H]^+$ and 1104.61 (100%) for $[M + Na]^+$.

2. X-ray Structure Determination and Molecular Structure.

Diffraction data were measured on a Bruker *X8 APEX-II* kappa geometry diffractometer with Mo radiation and a graphite monochromator. Frames were collected at 100 K with the detector at 40 mm and 0.3 degrees between each frame and were recorded for 10 s. *APEX-II*² and *SHELX*³ software were used in the collection and refinement of the models. Crystals of $[^{LS}Co^{III}(L^{1-})(L^{2-})] \cdot 2CH_3CN$ were dark flat rods. The 206545 counted reflections were averaged to 20497 independent data ($R_{int} = 0.16$). **Table D.6.1** shows the collected crystal data. Hydrogen atoms were placed at calculated positions. The asymmetric consists of one cobalt complex and two molecules of acetonitrile. The ORTEP diagram is presented in **Figure D.6.1**, and selected bond lengths and angles are listed in **Table D.6.2**. All of the dark rods of crystalline $[Mn(HL)_2]$ were grown together without integrity. **Table D.6.3** shows the collected crystal data. The selected sample was solved with inclusion of a 35% twin domain rotated 180 degrees about the (001) reciprocal axis. Measured were 79526 spots, resulting in 34280 data points after averaging ($R_{int} = 0.105$). Hydrogen atoms were added in calculated positions. A disordered *t*-butyl group (C58-C60) was modeled at 2 partial occupancy sites and held

isotropic. The ORTEP diagram is presented in **Figure D.6.2**, and selected bond lengths and angles are listed in **Table D.6.4**.

Table D.6.1. Crystal Data for $[\text{LSCo}^{\text{III}}(\text{L}^{\prime 1-})(\text{L}^{\prime 2-})]\cdot 2\text{CH}_3\text{CN}^a$

Formula	$\text{C}_{72}\text{H}_{92}\text{CoN}_6\text{O}_4$
M	1164.45
Space group	$\text{P}(2_1)/c$
$a / \text{\AA}$	14.4521(7)
$b / \text{\AA}$	37.2455(2)
$c / \text{\AA}$	12.8352(6)
$\alpha / ^\circ$	
$\beta / ^\circ$	104.197(2)
$\gamma / ^\circ$	
$V / \text{\AA}^3$	6697.9(5)
Z	4
T / K	100(2)
$\lambda / \text{\AA}$	0.71073
$D_{\text{calc}} / \text{g cm}^{-3}$	1.155
μ / mm^{-1}	0.307
$R(F) (\%)$	6.16
$Rw(F) (\%)$	11.58

$$^a R(F) = \sum \|F_o\| - \|F_c\| / \sum \|F_o\| \text{ for } I > 2s(I); Rw(F) = [\sum w(F_o^2 - F_c^2)^2 / \sum w(F_o^2)^2]^{1/2} \text{ for } I > 2s(I).$$

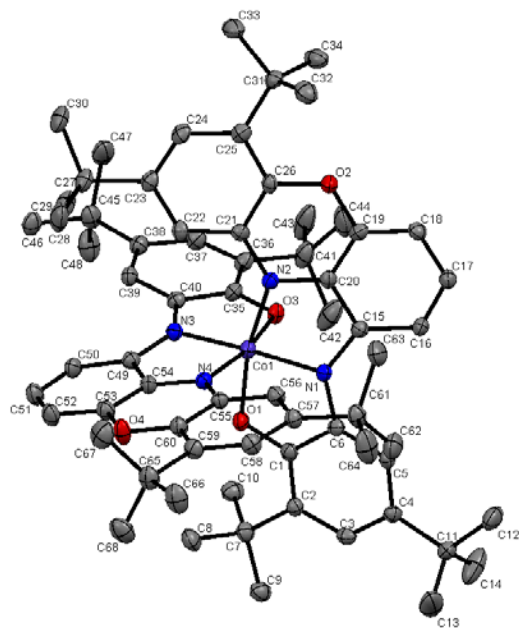


Figure D.6.1. Perspective view ORTEP diagram of $[\text{L}^{\text{S}}\text{Co}^{\text{III}}(\text{L}'^{\text{1-}})(\text{L}'^{\text{2-}})]$ showing 50% probability of the thermal ellipsoids. Solvents and hydrogen atoms are excluded for clarity.

Table D.6.2. Selected bond distances (Å) and angles (°) for $[\text{LS}\text{Co}^{\text{III}}(\text{L}^{\text{1-}})(\text{L}^{\text{2-}})]$.

$[\text{LS}\text{Co}^{\text{III}}(\text{L}^{\text{1-}})(\text{L}^{\text{2-}})] \cdot 2\text{CH}_3\text{CN}$			
Co1-N1	1.876(2)		
Co1-N3	1.887(2)		
Co1-O1	1.892(2)		
Co1-O3	1.899(2)		
Co1-N2	1.953(2)		
Co1-N4	1.956(2)		
C1-C2	1.416(3)	C35-C36	1.422(3)
C2-C3	1.389(3)	C36-C37	1.377(3)
C3-C4	1.411(3)	C37-C38	1.413(3)
C4-C5	1.380(3)	C38-C39	1.375(3)
C5-C6	1.410(3)	C39-C40	1.410(3)
C1-C6	1.413(3)	C35-C40	1.421(3)
N1-C6	1.382(3)	N3-C40	1.377(3)
O1-C1	1.334(3)	O3-C35	1.318(3)
N1-C15	1.353(3)	N3-C49	1.345(3)
C15-C16	1.422(3)	C49-C50	1.426(3)
C16-C17	1.359(3)	C50-C51	1.368(3)
C17-C18	1.413(3)	C51-C52	1.414(3)
C18-C19	1.366(3)	C52-C53	1.349(3)
C19-C20	1.405(3)	C53-C54	1.427(3)
C15-C20	1.430(3)	C49-C54	1.440(3)
N2-C20	1.353(3)	N4-C54	1.336(3)
N2-C21	1.399(3)	N4-C55	1.400(3)
C21-C26	1.406(3)	C55-C60	1.413(3)
C26-O2	1.392(3)	C60-O4	1.384(3)
C19-O2	1.379(3)	C53-O4	1.370(3)
C21-C22	1.399(3)	C55-C56	1.387(3)
C22-C23	1.389(3)	C56-C57	1.389(3)
C23-C24	1.390(3)	C57-C58	1.390(3)
C24-C25	1.402(3)	C58-C59	1.398(3)
C25-C26	1.394(3)	C59-C60	1.388(3)
N1-Co1-N3	167.93(8)		
N1-Co1-O1	84.80(7)		
N3-Co1-O1	86.55(7)		
N1-Co1-O3	86.92(7)		
N3-Co1-O3	84.88(7)		
O1-Co1-O3	91.35(7)		
N1-Co1-N2	83.83(8)		
N3-Co1-N2	104.83(8)		
O1-Co1-N2	168.60(7)		
O3-Co1-N2	88.97(7)		
N1-Co1-N4	104.64(8)		
N3-Co1-N4	83.64(8)		
O1-Co1-N4	89.33(7)		
O3-Co1-N4	168.43(7)		
N2-Co1-N4	92.64(8)		
C1-O1-Co1	112.16(1)		
C15-N1-Co1	114.23(2)		
C6-N1-Co1	113.78(2)		
C20-N2-Co1	108.98(2)		
C21-N2-Co1	133.53(2)		
C35-O3-Co1	111.70(1)		
C49-N3-Co1	114.37(2)		
C40-N3-Co1	113.34(1)		
C54-N4-Co1	109.60(2)		
C55-N4-Co1	132.92(2)		

Table D.6.3. Crystal Data for $[\text{Mn}(\text{HL})_2]^a$

Formula	$\text{C}_{68}\text{H}_{90}\text{MnN}_4\text{O}^4$
M	1082.38
Space group	P(-1)
$a / \text{Å}$	10.1391(6)
$b / \text{Å}$	12.6264(7)
$c / \text{Å}$	25.3609(1)
$\alpha / ^\circ$	86.646(3)
$\beta / ^\circ$	81.244(4)
$\gamma / ^\circ$	74.572(4)
$V / \text{Å}^3$	3092.7(3)
Z	2
T / K	100(2)
$\lambda / \text{Å}$	0.71073
$D_{\text{calc}} / \text{g cm}^{-3}$	1.162
μ / mm^{-1}	0.263
$R(F) (\%)$	7.94
$Rw(F) (\%)$	13.39

$$^a R(F) = \sum \|F_o\| - |F_c| / \sum |F_o| \text{ for } I > 2\sigma(I); Rw(F) = [\sum w(F_o^2 - F_c^2)^2 / \sum w(F_o^2)^2]^{1/2} \text{ for } I > 2\sigma(I).$$

Figure D.6.2. Perspective view ORTEP diagram of $[\text{Mn}(\text{HL})_2]$ showing 50% probability of the thermal ellipsoids. Hydrogen atoms are excluded for clarity. Each L is only tridentate in the Mn complex with one phenol arm rotated away.

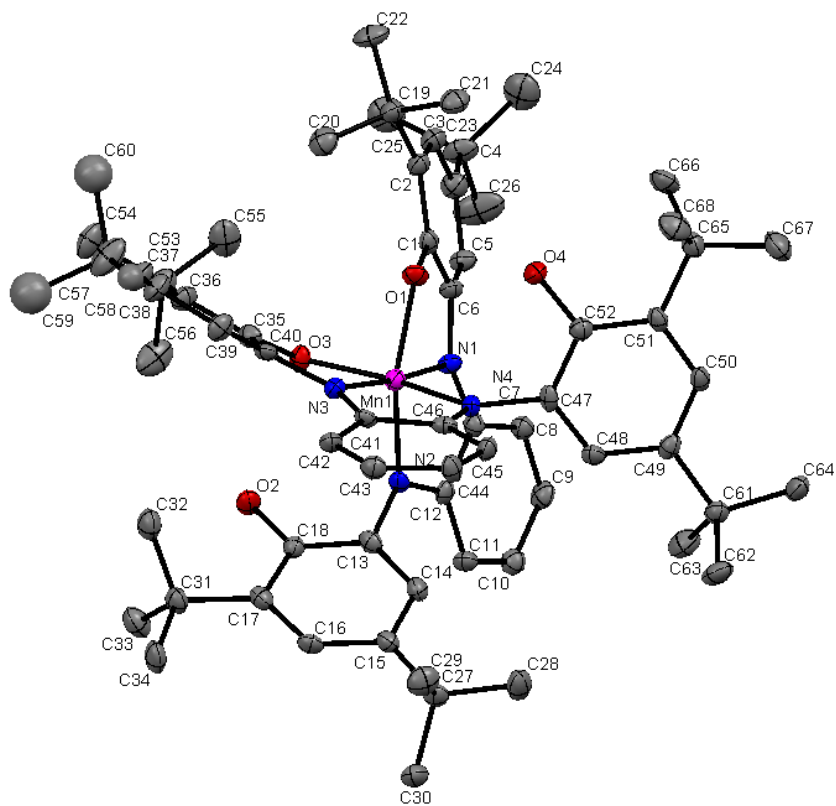
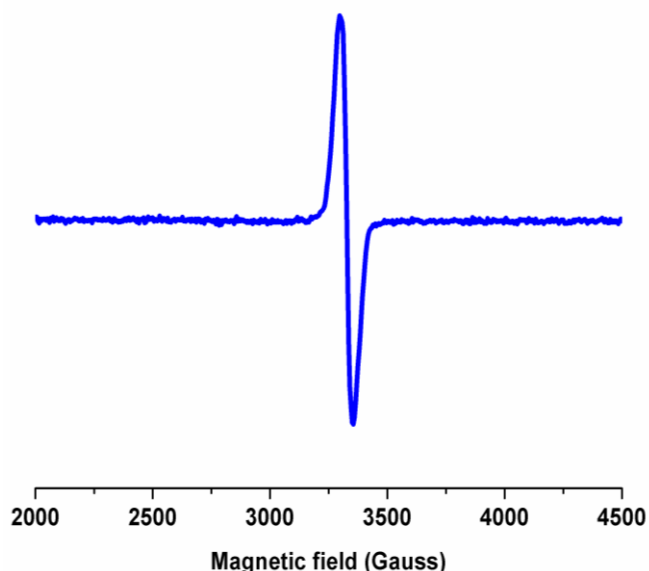


Table D.6.4. Selected bond distances (Å) and angles (°) for [Mn(HL)₂].

Mn1-N3	1.898(3)		
Mn1-N1	1.908(3)		
Mn1-O1	1.931(3)		
Mn1-O3	1.933(3)		
Mn1-N4	1.950(3)		
Mn1-N2	1.956(3)		
O1-C1	1.349(4)	O3-C35	1.345(4)
C1-C6	1.413(5)	C35-C40	1.400(5)
C1-C2	1.421(5)	C35-C36	1.413(5)
C2-C3	1.375(6)	C36-C37	1.393(5)
C3-C4	1.414(6)	C37-C38	1.396(5)
C4-C5	1.383(5)	C38-C39	1.387(5)
C5-C6	1.405(5)	C39-C40	1.393(5)
C6-N1	1.396(5)	C40-N3	1.402(5)
N1-C7	1.367(5)	N3-C41	1.351(5)
C7-C8	1.401(5)	C41-C42	1.422(5)
C7-C12	1.436(5)	C41-C46	1.431(5)
C8-C9	1.362(5)	C42-C43	1.365(5)
C9-C10	1.417(5)	C43-C44	1.412(5)
C10-C11	1.365(5)	C44-C45	1.359(5)
C11-C12	1.414(5)	C45-C46	1.421(5)
C12-N2	1.353(5)	C46-N4	1.348(5)
N2-C13	1.426(5)	N4-C47	1.419(5)
C13-C18	1.394(5)	C47-C48	1.385(5)
C13-C14	1.399(5)	C47-C52	1.409(5)
C14-C15	1.384(5)	C48-C49	1.388(5)
C15-C16	1.400(5)	C49-C50	1.394(5)
C16-C17	1.394(5)	C50-C51	1.395(5)
C17-C18	1.408(5)	C51-C52	1.394(5)
C18-O2	1.368(4)	C52-O4	1.375(5)
N3-Mn1-N1	174.59(1)		
N3-Mn1-O1	94.55(1)		
N1-Mn1-O1	82.19(1)		
N3-Mn1-O3	82.11(1)		
N1-Mn1-O3	93.63(1)		
O1-Mn1-O3	91.73(1)		
N3-Mn1-N4	80.45(1)		
N1-Mn1-N4	103.84(1)		
O1-Mn1-N4	90.78(1)		
O3-Mn1-N4	162.53(1)		
N3-Mn1-N2	103.13(1)		
N1-Mn1-N2	80.43(1)		
O1-Mn1-N2	161.99(1)		
O3-Mn1-N2	94.04(1)		
N4-Mn1-N2	88.82(1)		
C1-O1-Mn1	110.7(2)		
C7-N1-Mn1	117.7(2)		
C6-N1-Mn1	112.7(2)		
C12-N2-Mn1	114.9(2)		
C13-N2-Mn1	120.5(2)		
C35-O3-Mn1	111.3(2)		
C41-N3-Mn1	117.9(2)		
C40-N3-Mn1	112.9(2)		
C46-N4-Mn1	114.4(2)		
C47-N4-Mn1	126.0(2)		

Figure D.6.3. EPR spectrum of $[\text{LSCo}^{\text{III}}(\text{L}'^{1-})(\text{L}'^{2-})]$.

Frequency: 9.272000 GHz
Power: 0.21 mW
Modulation Frequency: 100.00 kHz
Modulation Amplitude: 2.00 G

3. Computational Details.

Electronic structure calculations were carried out using density functional theory (DFT)⁴ as implemented in the development version of Gaussian.⁵ Geometry optimizations were performed at the B3LYP/6-31G(d,p)⁶⁻⁹ level of theory employing the IEF-PCM¹⁰⁻¹² variant for the continuum solvation model (dichloromethane) with no symmetry constraints. The experimental ligands were substituted with ^tBu groups; we replaced these with H for computational efficiency. All optimized structures were confirmed to have stable wavefunctions,^{13,14} and to be local minima by analyzing the harmonic frequencies.¹⁵ Cartesian coordinates and frequencies for all species can be found in **Tables D.6.4** and **D.6.5**, respectively. TD-DFT^{16,17} was employed to estimate vertical electronic excitation energies and intensities, and the results were visualized and fit with Gaussians using GaussView.¹⁸

We initially explored multiple metal oxidation / spin state combinations with the ligand, including: $\text{LSCo}^{\text{II}} / \text{L}'^{1-} / \text{L}'^{1-}$, $\text{HSCo}^{\text{II}} / \text{L}'^{1-} / \text{L}'^{1-}$, and $\text{LSCo}^{\text{III}} / \text{L}'^{2-} / \text{L}'^{1-}$, as well as naïve calculations where we only defined the total charge and spin and ran a stable=opt calculation to ensure a reliable wavefunction. All of these calculations converged to one of three states: the localized doublet presented in **Fig. 6.2**, a doublet with spin density delocalized across both ligands (see **Figure D.6.4** for comparison of spin densities), and a quartet with three ligand based radicals. The two doublets are nearly isoenergetic (**Table**

D.6.8), and we chose to present and analyze the localized one because it did not require invoking fractional oxidation states. Given their energetic and structural similarity, we view the delocalized structure as being an average of the two localized $[\text{L}^{\text{S}}\text{Co}^{\text{III}}(\text{L}'^{1-})(\text{L}'^{2-})] / [\text{L}^{\text{S}}\text{Co}^{\text{III}}(\text{L}'^{2-})(\text{L}'^{1-})]$ structures. Structural comparison to the X-ray data does not allow us to discern which is more correct. The quartet is higher in energy by $\Delta G(\text{sol}) = 4.1 \text{ kcal mol}^{-1}$.

Figure D.6.4. Comparison of spin density isoplots (0.002 au) for the localized (left) and delocalized (right) doublets.

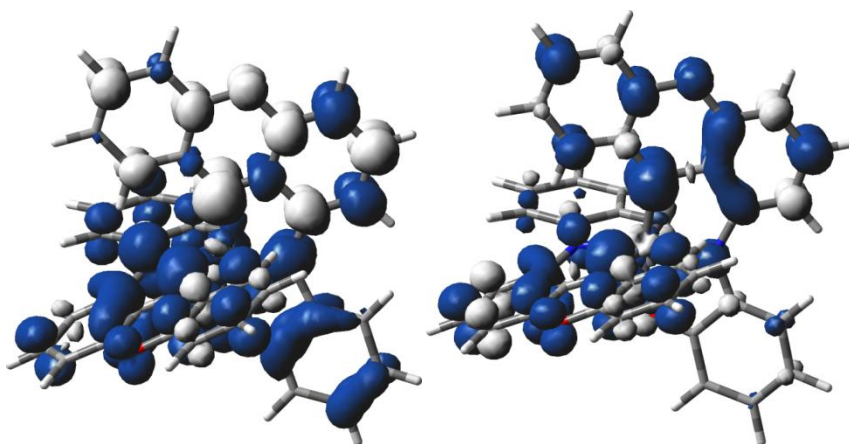
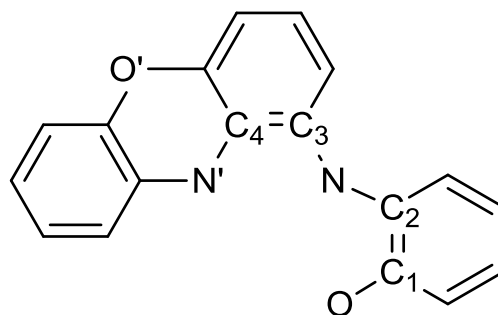


Table D.6.5. Structural comparison of the Co–L and some intraligand bond lengths (Å).



	Co–O	Co–N	Co–N'	O–C1	C1–C2	C2–N	N–C3	C3–C4	C4–N'
X-ray	1.89	1.88	1.95	1.33	1.41	1.38	1.35	1.43	1.35
	1.90	1.89	1.96	1.32	1.42	1.38	1.35	1.44	1.34
Localized $S = 1/2$	1.889	1.895	1.983	1.331	1.428	1.390	1.353	1.441	1.363
	1.906	1.912	1.985	1.303	1.445	1.367	1.347	1.451	1.343
Delocalized $S = 1/2$	1.898	1.899	1.981	1.319	1.434	1.381	1.346	1.448	1.349
	1.898	1.899	1.981	1.319	1.434	1.381	1.346	1.448	1.349
$S = 3/2$	1.897	1.904	1.986	1.316	1.440	1.372	1.365	1.435	1.374
	1.897	1.904	1.986	1.316	1.440	1.372	1.365	1.435	1.374

Table D.6.6. Cartesian coordinates (Å) for all computed species.**Localized Doublet ($S = 1/2$)**

Co	-0.009107	-0.013938	0.683590
N	-0.939072	-1.108724	-0.685673
C	-0.525821	-2.381770	-0.576844
C	-1.926665	-0.832176	-1.625114
C	-1.127928	-3.458066	-1.296630
C	0.593483	-2.671670	0.299108
C	-2.532097	-1.887842	-2.350817
C	-2.352563	0.479250	-1.903484
C	-0.710468	-4.754279	-1.118640
O	-2.164159	-3.195034	-2.147945
C	0.982939	-4.026034	0.491069
N	1.116883	-1.552295	0.835084
C	-3.528565	-1.653379	-3.289824
C	-3.347168	0.717618	-2.844117
H	-1.894596	1.296585	-1.367902
C	0.336591	-5.025997	-0.202592
H	-1.203000	-5.553077	-1.660763
H	1.751992	-4.276883	1.206418
C	2.181830	-1.362267	1.671122
C	-3.939750	-0.344778	-3.536382
H	-3.962668	-2.498334	-3.812766
H	-3.660474	1.737274	-3.041289
H	0.628295	-6.058332	-0.041268
C	2.123151	-0.063757	2.301208
C	3.272387	-2.227048	1.936242
H	-4.716454	-0.156086	-4.269835
C	3.131439	0.292907	3.230411
O	1.134961	0.735319	2.011296
C	4.251241	-1.835678	2.828367
H	3.371177	-3.165645	1.407584
C	4.169006	-0.582354	3.483584
H	3.071160	1.261955	3.713989
H	5.097607	-2.486956	3.018643
H	4.947044	-0.300002	4.186578
N	0.916115	1.125441	-0.649385
C	0.495371	2.411836	-0.487787
C	1.944356	0.909089	-1.559368
C	1.108154	3.514884	-1.130907
C	-0.632163	2.642545	0.378541
C	2.563679	2.004225	-2.213689
C	2.403556	-0.377649	-1.893317
C	0.677548	4.806484	-0.911652
O	2.176153	3.302906	-1.968916
C	-1.045194	3.980633	0.615512
N	-1.150423	1.488896	0.859282
C	3.592001	1.824079	-3.130080
C	3.433470	-0.562492	-2.811625
H	1.941624	-1.232536	-1.421888
C	-0.395003	5.023293	-0.019972

H	1.180731	5.629957	-1.405153
H	-1.840298	4.189048	1.316634
C	-2.213587	1.260844	1.725772
C	4.034747	0.535575	-3.431770
H	4.030306	2.700928	-3.594844
H	3.764769	-1.569627	-3.043476
H	-0.711561	6.042791	0.177054
C	-2.116806	-0.025399	2.338526
C	-3.320985	2.082764	1.995735
H	4.838798	0.394998	-4.146436
C	-3.097121	-0.422216	3.260959
O	-1.088822	-0.806885	2.015448
C	-4.295213	1.660894	2.901523
H	-3.444232	3.025928	1.478621
C	-4.175336	0.419149	3.537469
H	-3.003974	-1.393545	3.737136
H	-5.150564	2.298197	3.103011
H	-4.934470	0.098728	4.245587

Delocalized Doublet ($S = 1/2$)

Co	-0.000022	-0.000045	-0.686674
N	0.920845	-1.122405	0.660971
C	0.498221	-2.395938	0.519778
C	1.911995	-0.878796	1.605463
C	1.090017	-3.492194	1.209993
C	-0.622898	-2.646671	-0.361444
C	2.510345	-1.958147	2.302180
C	2.352848	0.419133	1.919069
C	0.662007	-4.781152	1.000626
O	2.132780	-3.259447	2.067777
C	-1.026912	-3.992600	-0.587303
N	-1.142607	-1.507115	-0.853492
C	3.509914	-1.755467	3.245039
C	3.353152	0.625904	2.863216
H	1.902067	1.257251	1.409355
C	-0.389939	-5.016714	0.080550
H	1.149709	-5.598301	1.519273
H	-1.804008	-4.214350	-1.304294
C	-2.210742	-1.287200	-1.701474
C	3.936599	-0.457861	3.526758
H	3.936854	-2.618407	3.744448
H	3.676094	1.637902	3.083992
H	-0.694544	-6.041462	-0.105966
C	-2.116807	-0.000537	-2.327462
C	-3.316726	-2.120697	-1.963842
H	4.716720	-0.296836	4.263235
C	-3.101848	0.378616	-3.261153
O	-1.100498	0.782056	-2.020615
C	-4.289797	-1.708822	-2.865752
H	-3.435231	-3.058146	-1.435731

C	-4.172215	-0.468182	-3.519298	H	1.849236	-1.447360	-1.368588
H	-3.012862	1.343845	-3.749201	C	0.178964	5.055544	-0.139488
H	-5.148081	-2.344513	-3.057424	H	1.840578	5.454719	-1.487903
H	-4.937071	-0.160758	-4.226670	H	-1.382866	4.403988	1.173310
N	-0.920882	1.122515	0.660867	C	-2.067684	1.543868	1.634088
C	-0.498226	2.395972	0.519566	C	4.162033	0.060129	-3.356934
C	-1.911987	0.878981	1.605428	H	4.400042	2.208732	-3.547225
C	-1.089937	3.492313	1.209778	H	3.657241	-1.999521	-2.951209
C	0.622874	2.646636	-0.361749	H	-0.037433	6.105411	0.029133
C	-2.510244	1.958386	2.302134	C	-2.138114	0.254506	2.272460
C	-2.352856	-0.418931	1.919089	C	-3.088617	2.490376	1.867082
C	-0.661895	4.781226	1.000288	H	4.961405	-0.179176	-4.050133
O	-2.132623	3.259641	2.067649	C	-3.183570	-0.013985	3.179737
C	1.026897	3.992550	-0.587728	O	-1.213212	-0.635675	1.984607
N	1.142535	1.507056	-0.853731	C	-4.118819	2.188858	2.748099
C	-3.509764	1.755789	3.245064	H	-3.097349	3.432787	1.335492
C	-3.353098	-0.625617	2.863308	C	-4.158027	0.945966	3.411251
H	-1.902139	-1.257067	1.409351	H	-3.211644	-0.982147	3.669162
C	0.389994	5.016705	0.080102	H	-4.906039	2.916308	2.918541
H	-1.149524	5.598431	1.518914	H	-4.969028	0.732017	4.101032
H	1.803934	4.214242	-1.304801	N	-1.065027	-1.013042	-0.663452
C	2.210651	1.287045	-1.701641	C	-0.781378	-2.350825	-0.532010
C	-3.936460	0.458208	3.526846	C	-2.083839	-0.679460	-1.537348
H	-3.936643	2.618758	3.744473	C	-1.527035	-3.360933	-1.171594
H	-3.676072	-1.637588	3.084152	C	0.327978	-2.722857	0.298129
H	0.694593	6.041437	-0.106502	C	-2.834416	-1.692445	-2.193310
C	2.116724	0.000269	-2.327469	C	-2.410422	0.658042	-1.844130
C	3.316622	2.120551	-1.964152	C	-1.236971	-4.705883	-0.989897
H	-4.716538	0.297232	4.263379	O	-2.581036	-3.024987	-1.978188
C	3.101781	-0.378976	-3.261146	C	0.598387	-4.092781	0.497269
O	1.100460	-0.782268	-2.020564	N	0.966261	-1.634554	0.820272
C	4.289666	1.708568	-2.865996	C	-3.858888	-1.390072	-3.083385
H	3.435125	3.058065	-1.436158	C	-3.429287	0.961708	-2.736870
C	4.172095	0.467811	-3.519392	H	-1.848969	1.448007	-1.368279
H	3.012814	-1.344269	-3.749066	C	-0.179128	-5.055474	-0.141584
H	5.147953	2.344225	-3.057758	H	-1.840655	-5.454029	-1.490314
H	4.936960	0.160328	-4.226726	H	1.382614	-4.404536	1.171611

Quartet (S = 3/2)

Co	0.000005	-0.000151	0.671606	H	2.067558	-1.544640	1.633598
N	1.065097	1.013351	-0.662897	C	-4.161665	-0.058552	-3.357426
C	0.781360	2.351082	-0.530939	H	-4.399766	-2.207072	-3.548581
C	2.084001	0.680186	-1.536816	H	-3.656790	2.000902	-2.950834
C	1.527023	3.361468	-1.170044	H	0.037187	-6.105423	0.026635
C	-0.328077	2.722726	0.299246	C	2.137994	-0.255566	2.272492
C	2.834584	1.693480	-2.192307	C	3.088423	-2.491280	1.866256
C	2.410691	-0.657186	-1.844090	H	-4.960958	0.181067	-4.050608
C	1.236884	4.706351	-0.987831	C	3.183402	0.012509	3.179925
O	2.581097	3.025911	-1.976684	O	1.213128	0.634803	1.984940
C	-0.598565	4.092533	0.498915	C	4.118604	-2.190185	2.747470
N	-0.966342	1.634157	0.820934	H	3.097135	-3.433476	1.334281
C	3.859164	1.391520	-3.082403	C	4.157824	-0.947583	3.411115
C	3.429652	-0.960429	-2.736849	H	3.211492	0.980468	3.669752
				H	4.905770	-2.917753	2.917661
				H	4.968786	-0.733934	4.101036

Table D.6.7. Frequencies (cm^{-1}) for all computed species.

Localized Doublet (S = 1/2)			Delocalized Doublet (S = 1/2)		
21.9415	32.1255	33.3324	1371.0968	1388.8078	1394.8544
35.7518	42.8661	68.0375	1414.9068	1417.8466	1443.6176
72.5741	85.8094	88.3403	1449.5601	1474.2012	1480.0472
99.4860	107.2406	127.2777	1484.9078	1491.1471	1493.1602
128.3380	164.5339	167.3005	1503.3024	1506.8146	1511.5824
175.3325	187.9608	204.2717	1523.4748	1530.4066	1570.6235
210.7399	249.4725	253.9578	1579.4133	1580.3652	1605.0876
260.1378	266.7987	272.6147	1615.1187	1619.1975	1620.9086
281.9180	290.8967	297.8713	1626.9902	1631.8823	1635.5091
307.3494	311.2094	315.7507	1659.5179	1663.1760	3179.2799
345.0385	365.8336	372.7901	3192.7848	3194.4223	3196.6795
380.1262	408.5356	416.9194	3197.8970	3203.0252	3203.6732
426.2645	439.3576	442.3763	3207.7057	3209.1610	3209.7852
465.4477	469.7643	471.9410	3215.0608	3217.2871	3219.0222
474.7177	487.8961	504.6775	3222.5632	3224.8898	3228.0418
522.9738	526.7863	537.1704	3228.6253	3241.1446	3260.4438
548.1098	553.4276	557.2964	3269.6271	3270.2695	3282.5691
559.0504	560.7493	563.6729			
576.6455	583.7661	590.5883			
596.6402	607.9248	615.2811			
619.0610	636.9663	644.9460			
648.8211	655.7131	692.9280			
696.8004	702.1556	708.8977			
716.5908	727.5680	734.4343			
741.5570	748.9488	758.3434			
760.4559	766.8025	767.7271			
770.8192	777.5914	781.3606			
832.3555	840.4107	844.7774			
851.4315	853.3810	854.9226			
859.9251	862.0155	872.5975			
879.6666	880.7914	884.7953			
901.2404	903.8995	915.2248			
916.3108	921.9414	933.6592			
947.5446	949.9740	956.2544			
961.3184	973.4080	976.2982			
987.1920	987.6168	1039.7041			
1051.3035	1057.8327	1059.9198			
1067.1203	1073.5047	1086.6254			
1094.1130	1123.0122	1136.4886			
1141.3515	1143.2437	1153.9449			
1170.1594	1177.3887	1178.3126			
1184.0881	1195.4104	1222.1959			
1227.5394	1233.9716	1235.4131			
1251.6810	1266.1810	1267.0054			
1285.3406	1294.7243	1298.2656			
1301.5219	1310.7810	1312.2134			
1321.5835	1338.9443	1339.5063			
1345.7840	1352.5801	1361.9619			
			20.7411	30.3839	33.4512
			36.2940	42.9771	61.5090
			69.0938	86.5847	86.9497
			97.9664	105.4015	126.1192
			129.3268	142.4557	166.3150
			176.7288	181.2778	198.9474
			209.1850	249.7339	252.6055
			255.6043	260.9533	271.3782
			278.7007	285.2004	290.9805
			306.0580	309.9539	313.0275
			322.8558	347.0735	371.3338
			374.1131	380.2513	415.2807
			422.9506	441.2844	442.6754
			445.1678	467.8590	471.9827
			476.9585	491.0547	500.1967
			516.1025	523.6517	531.8202
			544.8021	549.1338	556.8070
			559.6464	561.7057	562.4285
			570.7216	582.5584	586.9643
			588.3006	604.6518	608.5235
			615.1673	626.0103	646.5518
			647.2631	651.9433	692.0209
			698.9555	704.9170	707.4001
			724.9942	730.7132	732.5935
			735.8695	744.3351	754.6812
			762.4020	765.5761	768.0054
			774.1313	775.8006	779.2896
			831.1166	839.1826	848.6094
			850.9912	851.6132	855.2219
			858.7723	863.2712	868.7833

872.2705	882.2807	883.0278	566.7487	584.5813	591.1603
902.4129	904.3952	915.0029	595.1190	596.5473	612.0833
916.4686	928.4864	936.5080	614.7213	629.5400	645.7217
938.6974	942.9824	952.0627	651.2541	653.0434	692.6140
965.1526	969.8600	972.0536	696.2456	702.7986	704.0511
976.7316	978.8778	984.1164	715.1502	716.7390	731.9977
1046.2582	1048.7678	1058.5992	734.7472	743.0844	753.9555
1059.3726	1073.3960	1080.2385	762.1038	763.9959	768.4805
1092.8962	1093.6391	1139.3433	773.2648	774.3898	776.1789
1141.5693	1144.4951	1148.0624	809.7314	839.8486	846.4280
1171.1325	1176.2797	1177.8880	847.8136	853.0207	856.0737
1180.0727	1192.9248	1204.0373	857.9526	864.9400	868.8613
1229.3092	1233.0975	1239.0202	874.4216	876.2094	883.6929
1244.2147	1267.1120	1269.1694	892.3263	901.6146	908.3808
1278.9910	1294.9075	1297.1707	917.1284	925.9081	931.2916
1301.4684	1310.8105	1314.3731	937.5034	941.9175	947.0638
1320.8674	1329.2751	1337.2623	961.4502	965.9080	968.2872
1352.8673	1354.3702	1359.2960	974.1373	978.9935	983.4468
1364.3818	1395.4099	1402.0542	1043.8297	1047.5935	1057.4088
1413.1993	1417.1564	1435.3689	1058.7345	1075.1632	1077.7272
1440.8323	1451.1120	1479.0423	1098.4172	1099.6424	1140.8683
1484.3343	1491.2607	1496.5866	1143.4124	1145.9974	1149.3117
1500.5379	1500.9877	1510.2370	1174.4959	1177.3380	1178.3453
1524.9361	1530.7806	1571.0391	1194.2423	1200.6249	1206.8566
1574.2736	1587.4487	1595.6682	1231.7981	1233.4567	1239.8974
1617.6907	1619.9406	1622.5662	1241.8600	1265.6509	1268.5236
1625.5466	1632.8898	1634.3981	1292.7603	1295.7589	1297.8671
1661.3592	1663.6296	3183.7153	1299.3607	1315.5248	1318.0644
3187.3820	3199.3826	3199.5627	1335.6809	1338.6739	1343.1330
3201.9165	3202.0401	3203.6246	1350.3725	1354.0372	1357.6399
3205.4319	3207.1659	3210.6270	1360.8551	1364.3495	1372.6526
3211.0455	3213.2042	3221.2072	1383.7326	1409.4899	1423.8381
3223.2123	3224.9996	3227.2099	1455.2941	1464.7328	1475.8597
3230.1074	3233.3200	3261.0200	1487.6200	1489.5413	1494.7313
3263.8672	3276.5948	3277.9634	1497.3641	1508.0303	1509.9672
			1520.3880	1521.1709	1581.9798
			1587.2770	1591.8385	1593.0925
			1601.7562	1605.8376	1616.4720
			1617.7361	1624.2847	1627.7304
			1650.1424	1652.8613	3185.6899
			3189.6850	3198.7720	3199.7116
			3201.0870	3202.6944	3203.1445
			3206.2887	3208.6805	3209.9779
			3212.2001	3212.6675	3221.0831
			3223.0534	3225.2464	3227.6309
			3233.4253	3236.5460	3263.4167
			3265.2951	3273.6940	3275.7478

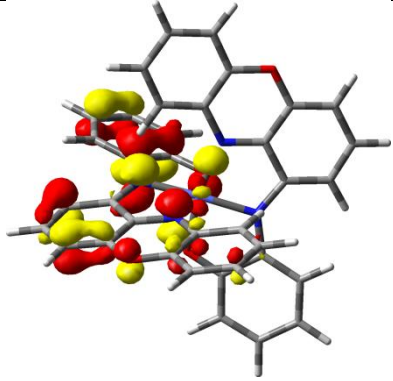
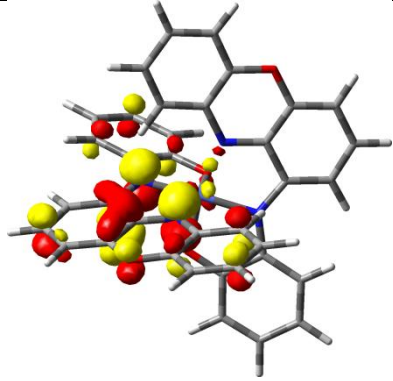
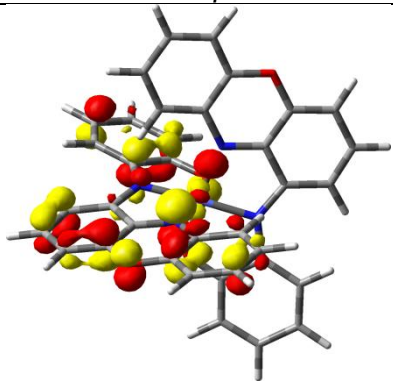
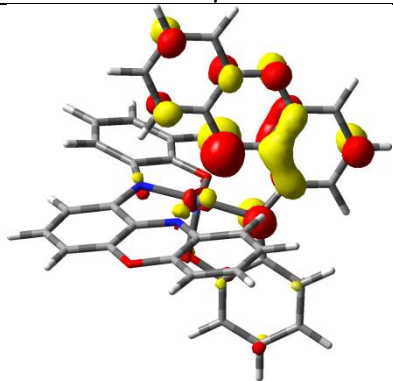
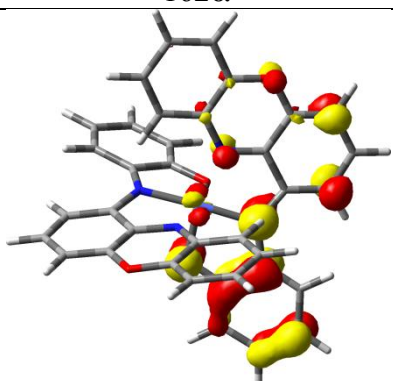
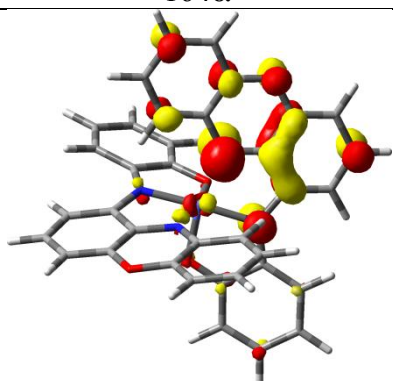
Quartet (S = 3/2)

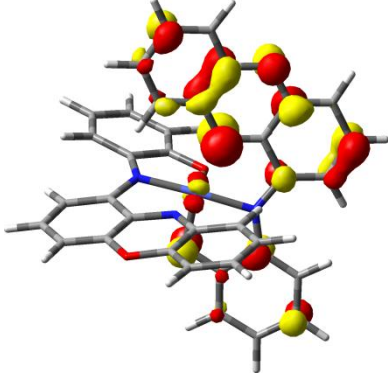
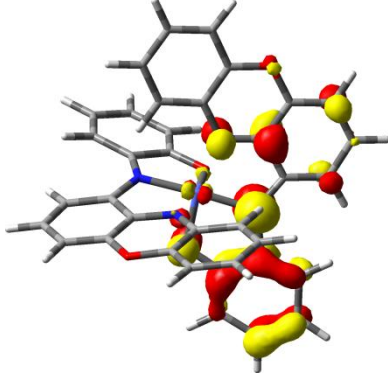
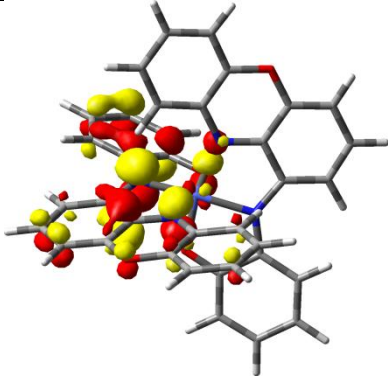
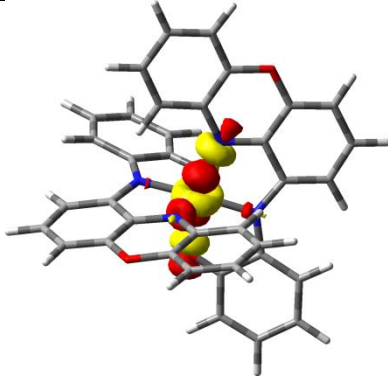
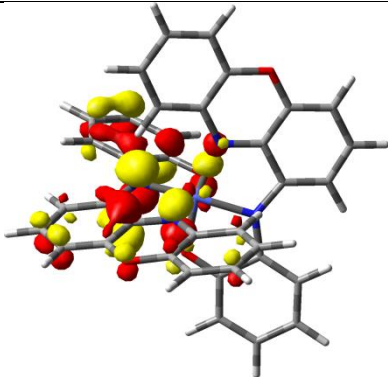
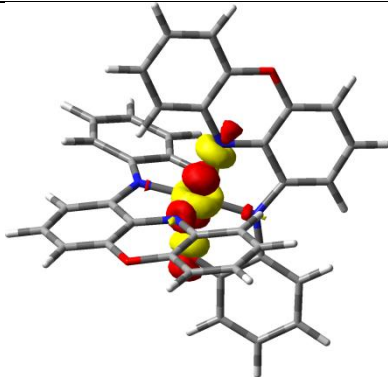
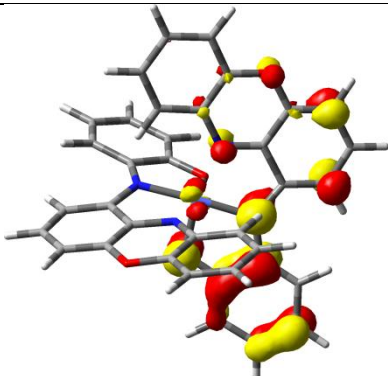
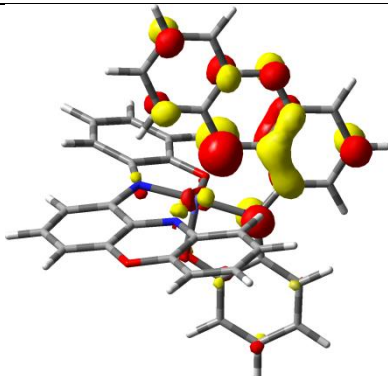
21.6153	26.8565	29.8768			
34.0367	40.6911	64.2541			
69.8314	83.3259	86.2304			
100.2086	106.4783	109.5397			
124.0972	148.6333	167.1694			
171.8242	184.2819	186.0685			
209.4871	226.6318	248.9917			
255.8656	262.6823	268.5883			
271.7134	279.6099	289.8084			
302.5550	308.1899	311.0798			
333.1941	354.0080	368.0104			
373.5545	379.5324	414.4603			
424.4121	431.5840	440.0321			
453.1206	468.5618	470.5736			
477.2635	478.0968	491.1733			
498.1928	526.2067	528.5109			
541.7928	547.8944	555.3083			
556.2302	561.1220	563.5181			

Table D.6.8. Energetics (E_h) for all computed species.

	G(sol)
Localized Doublet	-3287.313856
Delocalized Doublet	-3287.315995
Quartet	-3287.309514

Table D.6.9. Assignments for low-energy TD-DFT transitions. Contributions > 10% are shown. The low energy band at ~1000 nm arises from these three transitions (see **Figure D.6.4** which are predominantly LLCT in character, with some LMCT mixing. LLCT of both the *intra* and *interligand* type are observed.

Excited State	λ / nm	Osc. Str.	% cont.	Occ. MO	Unocc. MO
6	1220	0.09	67	 162 β	 164 β
			33	 162 α	 164 α
7	978	0.13	40	 161 α	 164 α

			38	 <p>161β</p>	 <p>163β</p>
			13	 <p>163α</p>	 <p>165α</p>
8	913	0.06	36	 <p>163α</p>	 <p>165α</p>
			13	 <p>161α</p>	 <p>164α</p>

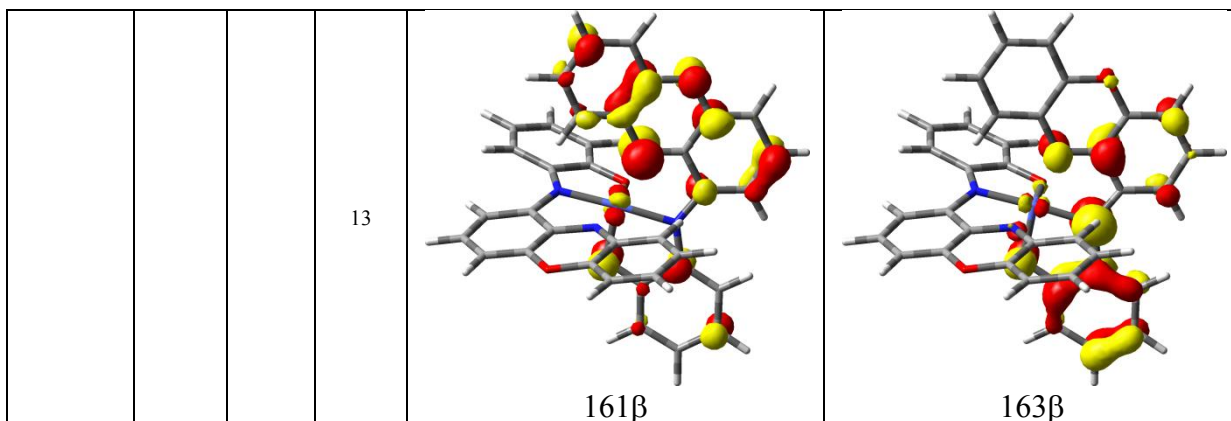
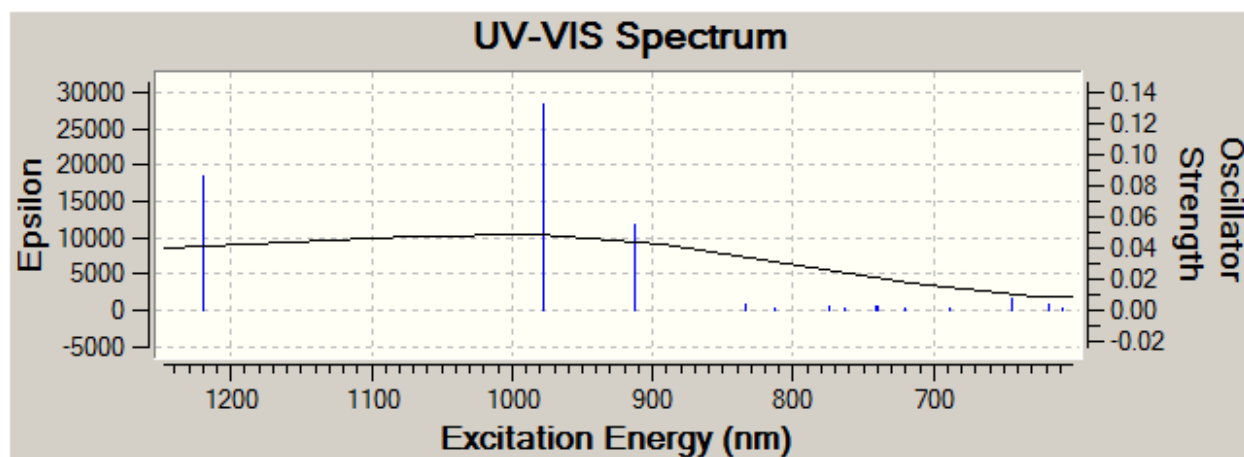
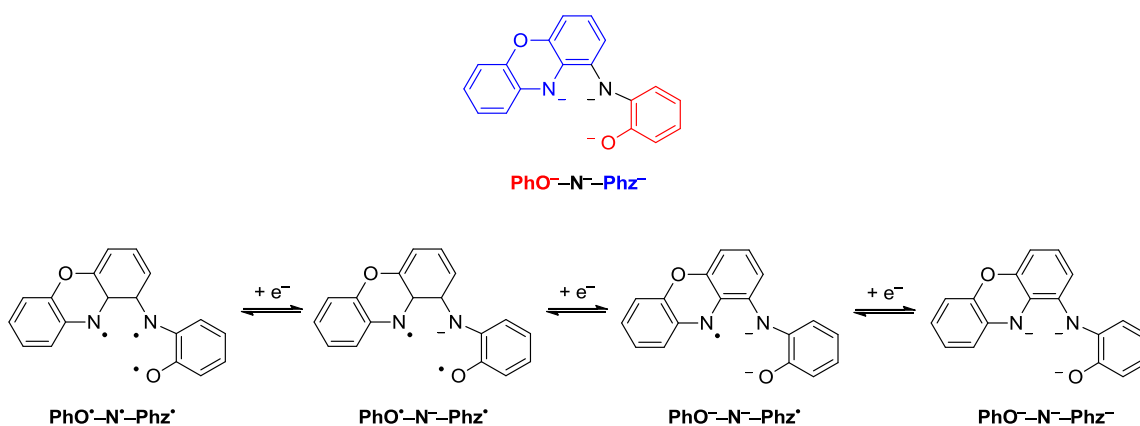


Figure D.6.5. TD-DFT spectrum with transitions shown for the energy window near 1000 nm. These transitions are outlined in **Table D.6.7**.



Scheme D.6.1. Details of ligand nomenclature.



Defining a ligand shorthand for this new ligand is complicated by the fact that the bridging amide can conjugate with both ligands. In the past, there has been reference to iminocatecholate/iminosemiquinonate or diiminocatecholate/diiminosemiquinonate redox behavior where it was easy to group this nitrogen with the phenolate or phenoxazinylate arms of the ligand, respectively. We prefer to discuss the ligand as three fragments (Scheme 1, top): (i) the phenolate (PhO⁻, red), (ii) the bridging amide (N⁻, black), and (iii) the phenoxazinylate (Phz⁻, blue). While this description is inherently too localized a description, it emphasizes correctly whether the phenoxazinyl or phenol arm is the major contributor to a given redox process.

4. References.

- 1 Gagne, R. R.; Koval, C. A.; Lisensky, G. C. "Ferrocene as an Internal Standard for Electrochemical Measurements." *Inorg. Chem.* **1980**, *19*, 2854.
- 2 Bruker AXS inc.: Madison, WI, USA, **2009**.
- 3 Sheldrick, G. "A Short History of SHELX." *Acta Crystallographica Section A* **2008**, *64*, 112.
- 4 Parr, R. G.; Yang, W. *Density-Functional Theory of Atoms and Molecules*; Oxford University Press: New York, **1989**.
- 5 Frisch, M. J.; Trucks, G. W.; Schlegel, H. B.; Scuseria, G. E.; Robb, M. A.; Cheeseman, J. R.; Scalmani, G.; Barone, V.; Mennucci, B.; Nakatsuji, G. A. P. H.; Caricato, M.; Li, X.; Hratchian, H. P.; Izmaylov, A. F.; Bloino, J.; Zheng, G.; Sonnenberg, J. L.; Hada, M.; Ehara, M.; Toyota, K.; Fukuda, R.; Hasegawa, J.; Ishida, M.; Nakajima, T.; Honda, Y.; Kitao, O.; Nakai, H.; Vreven, T.; J. A. Montgomery, J.; Peralta, J. E.; Ogliaro, F.; Bearpark, M.; Heyd, J. J.; Brothers, E.; Kudin, K. N.; Staroverov, V. N.; Keith, T.; Kobayashi, R.; Normand, J.; Raghavachari, K.; Rendell, A.; Burant, J. C.; Iyengar, S. S.; Tomasi, J.; Cossi, M.; Rega, N.; Millam, J. M.; Klene, M.; Knox, J. E.; Cross, J. B.; Bakken, V.; Adamo, C.; Jaramillo, J.; Gomperts, R.; Stratmann, R. E.; Yazyev, O.; Austin, A. J.; Cammi, R.; Pomelli, C.; Ochterski, J. W.; Martin, R. L.; Morokuma, K.; Zakrzewski, V. G.; Voth, G. A.; Salvador, P.; Dannenberg, J. J.; Dapprich, S.; Parandekar, P. V.; Mayhall, N. J.; Daniels, A. D.; Farkas, O.; Foresman, J. B.; Ortiz, J. V.; Cioslowski, J.; Fox, D. J. *Gaussian Development Version, Revision H.09+* Wallingford CT, **2010**.

- 6 Vosko, S. H.; Wilk, L.; Nusair, M. "Accurate Spin-Dependent Electron Liquid Correlation Energies for Local Spin Density Calculations: A Critical Analysis." *Can. J. Phys.* **1980**, *58*, 1200.
- 7 Lee, C.; Yang, W.; Parr, R. G. "Development of the Colle-Salvetti Correlation-Energy Formula into a Functional of the Electron Density." *Phys. Rev. B* **1988**, *37*, 785.
- 8 Becke, A. D. "Density-Functional Thermochemistry. III. The Role of Exact Exchange." *J. Chem. Phys.* **1993**, *98*, 5648.
- 9 Stephens, P. J.; Devlin, F. J.; Chabalowski, C. F.; Frisch, M. J. "Ab Initio Calculation of Vibrational Absorption and Circular Dichroism Spectra Using Density Functional Force Fields." *J. Phys. Chem.* **1994**, *98*, 11623.
- 10 Miertuš, S.; Scrocco, E.; Tomasi, J. "Electrostatic Interaction of a Solute with a Continuum. A Direct Utilization of ab Initio Molecular Potentials for the Prevision of Solvent Effects." *Chem. Phys.* **1981**, *55*, 117.
- 11 Tomasi, J.; Mennucci, B.; Cammi, R. "Quantum Mechanical Continuum Solvation Models." *Chem. Rev.* **2005**, *105*, 2999.
- 12 Scalmani, G.; Frisch, M. J.; Mennucci, B.; Tomasi, J.; Cammi, R.; Barone, V. "Geometries and Properties of Excited States in the Gas Phase and in Solution: Theory and Application of a Time-Dependent Density Functional Theory Polarizable Continuum Model." *J. Chem. Phys.* **2006**, *124*, 094107/1.
- 13 Schlegel, H. B.; McDouall, J. J. *Computational Advances in Organic Chemistry*; Ögretir, C., Csizmadia, I. G., Eds.; Kluwer Academic: Amsterdam, The Netherlands, **1991**.

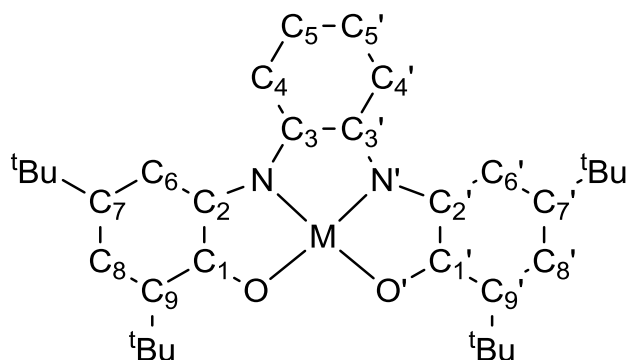
- 14 Bauernschmitt, R.; Ahlrichs, R. "Stability Analysis for Solutions of the Closed Shell Kohn-Sham Equation." *J. Chem. Phys.* **1996**, *104*, 9047.
- 15 Schlegel, H. B. "Optimization of Equilibrium Geometries and Transition Structures." *J. Comput. Chem.* **1982**, *3*, 214.
- 16 Runge, E.; Gross, E. K. U. "Density-Functional Theory for Time-Dependent Systems." *Phys. Rev. Lett.* **1984**, *52*, 997.
- 17 Stratmann, R. E.; Scuseria, G. E.; Frisch, M. J. "An Efficient Implementation of Time-Dependent Density-Functional Theory for the Calculation of Excitation Energies of Large Molecules." *J. Chem. Phys.* **1998**, *109*, 8218.
- 18 Dennington, R.; Keith, T.; Millam, J.; Semichem Inc.: Shawnee Mission, KS, **2009**.

APPENDIX E

Supplementary Information for Chapter 7

Table E.7.1. Selected bond distances (Å) and angles (°) for **1** and **2**.

[Ga(L)(Cl)(CH ₃ OH)]		[Fe(L)(Cl)]·0.5CH ₃ CN·0.5CH ₂ Cl ₂	
Ga1-O2	1.877(3)	Fe1-O2	1.942(11)
Ga1-O1	1.880(3)	Fe1-O1	1.948(11)
Ga1-N1	2.024(3)	Fe1-N1	2.022(13)
Ga1-N2	2.025(3)	Fe1-N2	2.044(13)
Ga1-Cl1	2.224(12)	Fe1-Cl1	2.220(5)
Ga1-O3	2.329(6)	O1-C1	1.299(19)
O3-C35	1.392(12)	N1-C6	1.342(2)
O1-C1	1.323(5)	N1-C7	1.395(2)
C1-C2	1.415(5)	N2-C13	1.343(2)
C1-C6	1.439(6)	N2-C12	1.394(19)
C2-C3	1.395(6)	O2-C18	1.300(18)
C3-C4	1.415(6)	C1-C2	1.435(2)
C4-C5	1.374(6)	C1-C6	1.453(2)
C5-C6	1.412(6)	C2-C3	1.374(2)
C6-N1	1.374(5)	C3-C4	1.427(3)
N1-C7	1.321(5)	C4-C5	1.366(2)
C7-C8	1.433(6)	C5-C6	1.415(2)
C7-C12	1.486(5)	C7-C8	1.401(2)
C8-C9	1.359(6)	C7-C12	1.424(2)
C9-C10	1.432(6)	C8-C9	1.386(2)
C10-C11	1.348(6)	C9-C10	1.392(3)
C11-C12	1.432(6)	C10-C11	1.389(2)
C12-N2	1.315(5)	C11-C12	1.401(2)
N2-C13	1.383(5)	C13-C14	1.424(2)
C13-C14	1.411(5)	C13-C18	1.453(2)
C13-C18	1.437(6)	C14-C15	1.371(2)
C14-C15	1.367(6)	C15-C16	1.436(2)
C15-C16	1.407(6)	C16-C17	1.371(2)
C16-C17	1.390(6)	C17-C18	1.428(2)
C17-C18	1.420(5)		
C18-O2	1.326(5)		
O2-Ga1-O1	105.00(13)	O2-Fe1-O1	101.45(5)
O2-Ga1-N1	155.50(14)	O2-Fe1-N1	143.32(5)
O1-Ga1-N1	83.64(14)	O1-Fe1-N1	79.19(5)
O2-Ga1-N2	83.91(13)	O2-Fe1-N2	78.93(5)
O1-Ga1-N2	154.40(14)	O1-Fe1-N2	135.51(5)
N1-Ga1-N2	79.48(14)	N1-Fe1-N2	75.93(5)
O2-Ga1-Cl1	101.98(10)	O2-Fe1-Cl1	108.40(4)
O1-Ga1-Cl1	102.16(11)	O1-Fe1-Cl1	110.23(4)
N1-Ga1-Cl1	98.39(10)	N1-Fe1-Cl1	105.52(4)
N2-Ga1-Cl1	99.25(10)	N2-Fe1-Cl1	111.68(4)
O2-Ga1-O3	80.95(18)		
O1-Ga1-O3	78.32(19)		
N1-Ga1-O3	78.42(18)		
N2-Ga1-O3	79.53(18)		
Cl1-Ga1-O3	176.73(16)		
C35-O3-Ga1	123.7(6)	C1-O1-Fe1	116.88(10)
C1-O1-Ga1	112.6(3)	C6-N1-C7	128.21(13)
C7-N1-Ga1	114.5(3)	C6-N1-Fe1	115.66(10)
C6-N1-Ga1	110.3(3)	C7-N1-Fe1	114.77(10)
C12-N2-Ga1	115.0(3)	C13-N2-C12	130.04(13)
C13-N2-Ga1	109.9(3)	C13-N2-Fe1	115.22(10)
C18-O2-Ga1	112.3(3)	C12-N2-Fe1	114.60(10)
		C18-O2-Fe1	117.37(10)

Table E.7.2. Phenolate arm C–C bond lengths (Å).

Å	C2–C6	C6–C7	C7–C8	C8–C9	C9–C1
X-ray Ga ^{III}	1.41	1.37	1.41	1.39	1.42
X-ray Fe ^{III}	1.42	1.37	1.43	1.37	1.43
Avg _{Ga/Fe}	1.41	1.38	1.42	1.38	1.43
Calc Ga ^{III} -L ^{2-,Q}	1.42	1.38	1.42	1.38	1.42
Calc Ga ^{III} -L ^{2-,**}	1.42	1.38	1.43	1.38	1.42
Calc ^{HS} Fe ^{III} -L ^{2-,**}	1.42	1.38	1.43	1.38	1.42
^a Cu ^{II}	1.41	1.37	1.42	1.38	1.43
^a Zn ^{II}	1.41	1.37	1.42	1.38	1.43
^b Ti ^{IV}	1.42	1.39	1.41	1.38	1.42
^c Zr ^{IV}	1.40	1.37	1.41	1.39	1.42

^a reference 5; ^b reference 7; ^c reference 6 (references within **Chapter 7**)

Table E.7.3. Table of orbital excitations that contribute to the major absorption spectrum features.

	S ²	λ / nm	f	Description
Ga (1)	-	326	0.323	95% HOMO → LUMO
	-	423	0.081	>99% HOMO-1 → LUMO
	-	576	0.076	>99% HOMO-2 → LUMO
	-	673	0.084	93% HOMO-3 → LUMO
	-	969	0.335	96% HOMO → LUMO+1
Fe (2)	5.4	422	0.072	93% βHOMO-2 → βLUMO+3
	5.4	497	0.088	62% αHOMO-3 → αLUMO, 10% βHOMO → βLUMO+4, 10% αHOMO-4 → αLUMO+1, 10% αHOMO-2 → αLUMO+1
	4.9	683	0.059	67% βHOMO-1 → βLUMO+2, 24% βHOMO-1 → βLUMO+1
	5.2	880	0.055	44% αHOMO → αLUMO, 30% αHOMO-3 → αLUMO, 18% βHOMO-1 → βLUMO

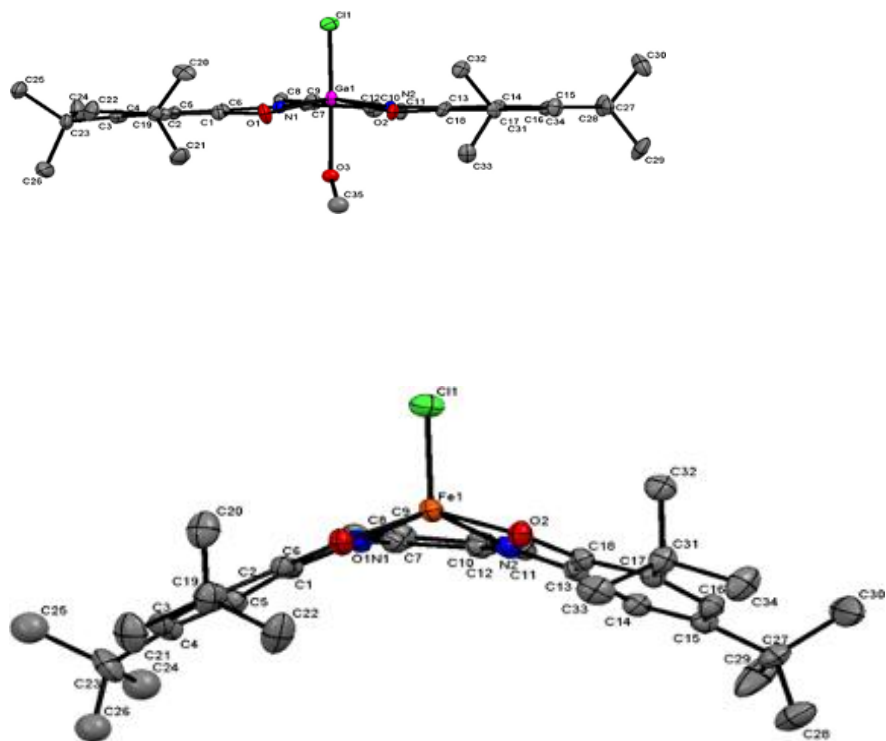



Figure E.7.1. In-plane view of the neutral molecule **1** (top) and **2** (bottom).

APPENDIX F**Permission/License Agreements for Copyrighted Material**

This dissertation entails multidisciplinary and complimentary research efforts aiming to develop responsive Langmuir–Blodgett films containing transition metal ions. My contributions to this work entailed the synthetic, spectroscopic, and electrochemical characterizations along with the development of the original drafts of the published manuscripts. Some common portions appear in Dr. Rama Shanmugam’s thesis focused on the film studies. These dissertations have not been copyright protected as stated in the following pages. All previously published materials have been reprinted with permission from the American Chemical Society or WILEY-VCH Verlag GmbH & Co. KGaA, Weinheim.

Title: SYNTHESIS, REDOX PROPERTIES, AND LANGMUIR MONOLAYER FORMATION OF SELECTED 3d- AND 4d- METALLOAMPHIPHILES

ID: 11258

Author(s): Sree Ramadevi Shanmugam 

Publishing Settings & Copyright

Traditional Publishing


Delayed Release to ProQuest: 2 years

No search engine access - I do not want search engines to discover my work.

Do not allow third party sales.

Do not file for copyright - I am requesting that ProQuest/UMI not file for copyright on my behalf.

PDF and Supplementary file(s)

 (11.4 MB)

[View ETD](#)

-- No supplemental files provided --

Degree/Department Information

Year degree awarded: 2012

Degree Awarded: Doctor of Philosophy

Year Manuscript Completed: 2011

Department: Chemistry

Advisor/Supervisor/Committee Chair: Claudio N Verani

Committee Members: Charles H Winter, Colin F Poole, Gavin Lawes

Subject Categories

Chemistry [0485] - primary

Keywords

-- none provided --

Abstract

Transition metals containing amphiphilic compounds integrate various geometric, electronic, magnetic, and electrochemical properties together with the film forming properties. These compounds thereby find potential towards the fabrication of responsive films. This dissertation confers the synthesis and analysis of film forming properties of various redox-active metalloamphiphiles. Two new azido and thiocyanato bridged copper-based amphiphiles were synthesized and characterized by IR, UV-visible, and EPR spectroscopies, mass spectrometry, cyclic voltammetry, and elemental analysis. The redox studies show that both these complexes exhibit redox reversibility with only the azido bridged complex showing good redox cycling of about 50 times with minimal decomposition of less than 30 mV. The UV-visible studies using coordinating solvent suggest that monomer/dimer equilibria might happen at the air/water interface. The LB studies show that the monolayer stability is maintained up to a pressure of ca. 49 mN/m when collapse occurs. The IRRAS spectra suggest high order of the deposited film.

The synthesis and characterization a series of single-tailed copper(II)-containing surfactants of the type $[\text{Cu}(\text{LPY18})\text{X}_2]$ with varying coligands (X) was also studied. The complexes $[\text{Cu}(\text{LPY18})(\text{OAc})_2]$, $[\text{Cu}(\text{LPY18})(\text{OBz})_2]$, $[\text{Cu}(\text{LPY18})(\text{acac})\text{Br}]$, $[\text{Cu}(\text{LPY18})(\text{dbm})\text{Br}]$, $[\text{Cu}(\text{LPY18})(\text{Ox})]$, and $[\text{Cu}(\text{LPY18})(1,10\text{-phen})\text{Cl}]\text{PF}_6$ were synthesized, isolated, and characterized. The redox characteristics change depending on the nature of the coligands without compromising the amphiphilic behavior of the complexes. The monodentate coligands (acetate and benzoate) containing complexes exhibit a quasi-reversible $\text{Cu}(\text{II})/\text{Cu}(\text{I})$ couple with a potential of about -900 mV whereas the bidentate coligands such as acetylacetonate, dibenzoyl methanate, and oxalate offered irreversible multiple processes. The phenanthroline containing complex exhibited the best reversibility together with excellent cyclability. The Langmuir monolayer isotherm indicates that the films of these complexes are stable up to a pressure of about 45 mN/m. BAM studies showed intricate variations in film topology. The IRRAS studies on selected complexes indicate the presence of well-packed condensed

monolayer on the surface of the substrate.

Three octahedral amphiphilic metal complexes of bivalent iron, cobalt, and ruthenium were also synthesized and characterized. The iron containing complex do not show good redox behavior however, the cobalt complex shows a quasi-reversible ligand based process at $E_{1/2} = -1379$ mV and the ruthenium complex shows two ligand related processes at $E_{1/2} = -1609$ and -2050 mV and $\text{Ru}(\text{II})/\text{Ru}(\text{III})$ couple at 600 mV. All the complexes reveal excellent film formation properties. The IRRAS studies display the presence the CH stretching bands at around 2850-2925 cm^{-1} .

We also report on the synthesis and characterization of various copper and nickel containing complexes containing phenolate based ligands with varying substituents. The redox studies on the nickel complexes reveal quasi-reversible ligand based process and the copper complexes show good reversibility of the copper(II)-based process. However, these amphiphilic complexes showed a compromising behavior at the air/water interface with a maximum collapse pressure of 28 mN/m.

We have also presented the Langmuir-Blodgett film formation studies on various bimetallic and tetrametallic copper complexes and the effect of changes in the subphase on the film formation.

A new family of pyridyl- and phenolato-containing amphiphiles such as $[(\text{LPY18I})\text{Ru}(\text{bpy})_2](\text{PF}_6)_2$, $[(\text{LPY18A})\text{Ru}(\text{bpy})_2](\text{PF}_6)_2$, $[(\text{LPhBuI})\text{Ru}(\text{bpy})_2](\text{PF}_6)$, and $[(\text{LPhClI})\text{Ru}(\text{bpy})_2](\text{PF}_6)$ were also described. The capability of these species as precursors for photo-responsive Langmuir-Blodgett films was evaluated. These complexes are surface active and are strong candidates for the formation of monolayer films, as characterized by compression isotherms and Brewster angle microscopy. Relative solubility in water for the ruthenium pyridyl complexes requires the presence of an aqueous NaCl subphase for proper film formation.

We have also reported on the tetrametallic complex $[\text{Fe}^{\text{II}}(\text{Fe}^{\text{III}}\text{L}_2)_3](\text{PF}_6)_2$ of discoid topology. To the best of our knowledge, this is the first species in which the presence of tert-butyl groups concurrently imposes redox activity and surfactancy. This result points that a modular approach can be used to develop redox-active homo and heterometallic film precursors of discoid topology.

Language

en (English)

[Wayne State University Graduate School](#)

© 2012 ProQuest LLC. All rights reserved. [Terms and Conditions](#)





RightsLink®



ACS Publications
High quality. High impact.

Title: A Modular Approach to Redox-Active Multimetallic Hydrophobes of Discoid Topology

Author: Frank D. Lesh et al.

Publication: Inorganic Chemistry

Publisher: American Chemical Society

Date: Aug 1, 2010

Copyright © 2010, American Chemical Society

User ID
<input type="text"/>
Password
<input type="text"/>
<input type="checkbox"/> Enable Auto Login
LOGIN
Forgot Password/User ID?
If you're a copyright.com user, you can login to Rightslink using your copyright.com credentials.
Already a Rightslink user or want to learn more?

PERMISSION/LICENSE IS GRANTED FOR YOUR ORDER AT NO CHARGE

This type of permission/license, instead of the standard Terms & Conditions, is sent to you because no fee is being charged for your order. Please note the following:

- Permission is granted for your request in both print and electronic formats.
- If figures and/or tables were requested, they may be adapted or used in part.
- Please print this page for your records and send a copy of it to your publisher/graduate school.
- Appropriate credit for the requested material should be given as follows: "Reprinted (adapted) with permission from (COMPLETE REFERENCE CITATION). Copyright (YEAR) American Chemical Society." Insert appropriate information in place of the capitalized words.
- One-time permission is granted only for the use specified in your request. No additional uses are granted (such as derivative works or other editions). For any other uses, please submit a new request.



RightsLink®

[Home](#)
[Create Account](#)
[Help](#)


ACS Publications
High quality. High impact.

Title: Investigation of the Electronic, Photosubstitution, Redox, and Surface Properties of New Ruthenium(II)-Containing Amphiphiles

Author: Frank D. Lesh et al.

Publication: Inorganic Chemistry

Publisher: American Chemical Society

Date: Feb 1, 2011

Copyright © 2011, American Chemical Society

User ID
<input type="text"/>
Password
<input type="text"/>
<input type="checkbox"/> Enable Auto Login
LOGIN
Forgot Password/User ID?
If you're a copyright.com user, you can login to Rightslink using your copyright.com credentials.
Already a Rightslink user or want to learn more?

PERMISSION/LICENSE IS GRANTED FOR YOUR ORDER AT NO CHARGE

This type of permission/license, instead of the standard Terms & Conditions, is sent to you because no fee is being charged for your order. Please note the following:

- Permission is granted for your request in both print and electronic formats.
- If figures and/or tables were requested, they may be adapted or used in part.
- Please print this page for your records and send a copy of it to your publisher/graduate school.
- Appropriate credit for the requested material should be given as follows: "Reprinted (adapted) with permission from (COMPLETE REFERENCE CITATION). Copyright (YEAR) American Chemical Society." Insert appropriate information in place of the capitalized words.
- One-time permission is granted only for the use specified in your request. No additional uses are granted (such as derivative works or other editions). For any other uses, please submit a new request.

**JOHN WILEY AND SONS LICENSE
TERMS AND CONDITIONS**

Dec 09, 2011

This is a License Agreement between Frank D Lesh ("You") and John Wiley and Sons ("John Wiley and Sons") provided by Copyright Clearance Center ("CCC"). The license consists of your order details, the terms and conditions provided by John Wiley and Sons, and the payment terms and conditions.

All payments must be made in full to CCC. For payment instructions, please see information listed at the bottom of this form.

License Number	2804910378862
License date	Dec 09, 2011
Licensed content publisher	John Wiley and Sons
Licensed content publication	European Journal of Inorganic Chemistry
Licensed content title	On the Effect of Coordination and Protonation Preferences in the Amphiphilic Behavior of Metallosurfactants with Asymmetric Headgroups (Eur. J. Inorg. Chem. 3/2009)
Licensed content author	Frank D. Lesh, Sarmad Sahiel Hindo, Mary Jane Heeg, Marco M. Allard, Prateek Jain, Bo Peng, Lew Hryhorczuk, Cláudio N. Verani
Licensed content date	Jan 1, 2009
Start page	323
End page	323
Type of use	Dissertation/Thesis
Requestor type	Author of this Wiley article
Format	Print and electronic
Portion	Full article
Will you be translating?	No
Order reference number	
Total	0.00 USD

[Terms and Conditions](#)

TERMS AND CONDITIONS

This copyrighted material is owned by or exclusively licensed to John Wiley & Sons, Inc. or one of its group companies (each a "Wiley Company") or a society for whom a Wiley Company has exclusive publishing rights in relation to a particular journal (collectively WILEY). By clicking "accept" in connection with completing this licensing transaction, you agree that the following terms and conditions apply to this transaction (along with the billing and payment terms and conditions established by the Copyright Clearance Center Inc., ("CCC's Billing and Payment terms and conditions"), at the time that you opened your Rightslink account (these are available at any time at <http://myaccount.copyright.com>)

Terms and Conditions

1. The materials you have requested permission to reproduce (the "Materials") are protected by copyright.
2. You are hereby granted a personal, non-exclusive, non-sublicensable, non-transferable, worldwide, limited license to reproduce the Materials for the purpose specified in the licensing process. This license is for a one-time use only with a maximum distribution equal to the number that you identified in the licensing process. Any form of republication granted by this licence must be completed within two years of the date of the grant of this licence (although copies prepared before may be distributed thereafter). The Materials shall not be used in any other manner or for any other purpose. Permission is granted subject to an appropriate acknowledgement given to the author, title of the material/book/journal and the publisher. You shall also duplicate the copyright notice that appears in the Wiley publication in your use of the Material. Permission is

also granted on the understanding that nowhere in the text is a previously published source acknowledged for all or part of this Material. Any third party material is expressly excluded from this permission.

3. With respect to the Materials, all rights are reserved. Except as expressly granted by the terms of the license, no part of the Materials may be copied, modified, adapted (except for minor reformatting required by the new Publication), translated, reproduced, transferred or distributed, in any form or by any means, and no derivative works may be made based on the Materials without the prior permission of the respective copyright owner. You may not alter, remove or suppress in any manner any copyright, trademark or other notices displayed by the Materials. You may not license, rent, sell, loan, lease, pledge, offer as security, transfer or assign the Materials, or any of the rights granted to you hereunder to any other person.

4. The Materials and all of the intellectual property rights therein shall at all times remain the exclusive property of John Wiley & Sons Inc or one of its related companies (WILEY) or their respective licensors, and your interest therein is only that of having possession of and the right to reproduce the Materials pursuant to Section 2 herein during the continuance of this Agreement. You agree that you own no right, title or interest in or to the Materials or any of the intellectual property rights therein. You shall have no rights hereunder other than the license as provided for above in Section 2. No right, license or interest to any trademark, trade name, service mark or other branding ("Marks") of WILEY or its licensors is granted hereunder, and you agree that you shall not assert any such right, license or interest with respect thereto.

5. NEITHER WILEY NOR ITS LICENSORS MAKES ANY WARRANTY OR REPRESENTATION OF ANY KIND TO YOU OR ANY THIRD PARTY, EXPRESS, IMPLIED OR STATUTORY, WITH RESPECT TO THE MATERIALS OR THE ACCURACY OF ANY INFORMATION CONTAINED IN THE MATERIALS, INCLUDING, WITHOUT LIMITATION, ANY IMPLIED WARRANTY OF MERCHANTABILITY, ACCURACY, SATISFACTORY QUALITY, FITNESS FOR A PARTICULAR PURPOSE, USABILITY, INTEGRATION OR NON-INFRINGEMENT AND ALL SUCH WARRANTIES ARE HEREBY EXCLUDED BY WILEY AND ITS LICENSORS AND WAIVED BY YOU.

6. WILEY shall have the right to terminate this Agreement immediately upon breach of this Agreement by you.

7. You shall indemnify, defend and hold harmless WILEY, its Licensors and their respective directors, officers, agents and employees, from and against any actual or threatened claims, demands, causes of action or proceedings arising from any breach of this Agreement by you.

8. IN NO EVENT SHALL WILEY OR ITS LICENSORS BE LIABLE TO YOU OR ANY OTHER PARTY OR ANY OTHER PERSON OR ENTITY FOR ANY SPECIAL, CONSEQUENTIAL, INCIDENTAL, INDIRECT, EXEMPLARY OR PUNITIVE DAMAGES, HOWEVER CAUSED, ARISING OUT OF OR IN CONNECTION WITH THE DOWNLOADING, PROVISIONING, VIEWING OR USE OF THE MATERIALS REGARDLESS OF THE FORM OF ACTION, WHETHER FOR BREACH OF CONTRACT, BREACH OF WARRANTY, TORT, NEGLIGENCE, INFRINGEMENT OR OTHERWISE (INCLUDING, WITHOUT LIMITATION, DAMAGES BASED ON LOSS OF PROFITS, DATA, FILES, USE, BUSINESS OPPORTUNITY OR CLAIMS OF THIRD PARTIES), AND WHETHER OR NOT THE PARTY HAS BEEN ADVISED OF THE POSSIBILITY OF SUCH DAMAGES. THIS LIMITATION SHALL APPLY NOTWITHSTANDING ANY FAILURE OF ESSENTIAL PURPOSE OF ANY LIMITED REMEDY PROVIDED HEREIN.

9. Should any provision of this Agreement be held by a court of competent jurisdiction to be illegal, invalid, or unenforceable, that provision shall be deemed amended to achieve as nearly as possible the same economic effect as the original provision, and the legality, validity and enforceability of the remaining provisions of this Agreement shall not be affected or impaired thereby.

10. The failure of either party to enforce any term or condition of this Agreement shall not constitute a waiver of either party's right to enforce each and every term and condition of this Agreement. No breach under this agreement shall be deemed waived or excused by either party unless such waiver or consent is in writing signed by the party granting such waiver or consent. The waiver by or consent of a party to a breach of any provision of this Agreement shall not operate or be construed as a waiver of or consent to any other or subsequent breach by such other party.

11. This Agreement may not be assigned (including by operation of law or otherwise) by you without WILEY's prior written consent.

12. Any fee required for this permission shall be non-refundable after thirty (30) days from receipt.

13. These terms and conditions together with CCC's Billing and Payment terms and conditions (which are incorporated herein) form the entire agreement between you and WILEY concerning this licensing transaction and (in the absence of fraud) supersedes all prior agreements and representations of the parties, oral or written. This Agreement may not be amended except in writing signed by both parties. This Agreement shall be binding upon and inure to the benefit of the parties' successors, legal representatives, and authorized assigns.

14. In the event of any conflict between your obligations established by these terms and conditions and those established by CCC's Billing and Payment terms and conditions, these terms and conditions shall prevail.

15. WILEY expressly reserves all rights not specifically granted in the combination of (i) the license details provided by you and accepted in the course of this licensing transaction, (ii) these terms and conditions and (iii) CCC's Billing and Payment terms and conditions.

16. This Agreement will be void if the Type of Use, Format, Circulation, or Requestor Type was misrepresented during the licensing process.

17. This Agreement shall be governed by and construed in accordance with the laws of the State of New York, USA, without regards to such state's conflict of law rules. Any legal action, suit or proceeding arising out of or relating to these Terms and Conditions or the breach thereof shall be instituted in a court of competent jurisdiction in New York County in the State of New York in the United States of America and each party hereby consents and submits to the personal jurisdiction of such

court, waives any objection to venue in such court and consents to service of process by registered or certified mail, return receipt requested, at the last known address of such party.

Wiley Open Access Terms and Conditions

All research articles published in Wiley Open Access journals are fully open access: immediately freely available to read, download and share. Articles are published under the terms of the [Creative Commons Attribution Non Commercial License](#), which permits use, distribution and reproduction in any medium, provided the original work is properly cited and is not used for commercial purposes. The license is subject to the Wiley Open Access terms and conditions:

Wiley Open Access articles are protected by copyright and are posted to repositories and websites in accordance with the terms of the [Creative Commons Attribution Non Commercial License](#). At the time of deposit, Wiley Open Access articles include all changes made during peer review, copyediting, and publishing. Repositories and websites that host the article are responsible for incorporating any publisher-supplied amendments or retractions issued subsequently.

Wiley Open Access articles are also available without charge on Wiley's publishing platform, **Wiley Online Library** or any successor sites.

Use by non-commercial users

For non-commercial and non-promotional purposes individual users may access, download, copy, display and redistribute to colleagues Wiley Open Access articles, as well as adapt, translate, text- and data-mine the content subject to the following conditions:

- The authors' moral rights are not compromised. These rights include the right of "paternity" (also known as "attribution" - the right for the author to be identified as such) and "integrity" (the right for the author not to have the work altered in such a way that the author's reputation or integrity may be impugned).
- Where content in the article is identified as belonging to a third party, it is the obligation of the user to ensure that any reuse complies with the copyright policies of the owner of that content.
- If article content is copied, downloaded or otherwise reused for non-commercial research and education purposes, a link to the appropriate bibliographic citation (authors, journal, article title, volume, issue, page numbers, DOI and the link to the definitive published version on Wiley Online Library) should be maintained. Copyright notices and disclaimers must not be deleted.
- Any translations, for which a prior translation agreement with Wiley has not been agreed, must prominently display the statement: "This is an unofficial translation of an article that appeared in a Wiley publication. The publisher has not endorsed this translation."

Use by commercial "for-profit" organisations

Use of Wiley Open Access articles for commercial, promotional, or marketing purposes requires further explicit permission from Wiley and will be subject to a fee. Commercial purposes include:

- Copying or downloading of articles, or linking to such articles for further redistribution, sale or licensing;
- Copying, downloading or posting by a site or service that incorporates advertising with such content;
- The inclusion or incorporation of article content in other works or services (other than normal quotations with an appropriate citation) that is then available for sale or licensing, for a fee (for example, a compilation produced for marketing purposes, inclusion in a sales pack)

- Use of article content (other than normal quotations with appropriate citation) by for-profit organisations for promotional purposes
- Linking to article content in e-mails redistributed for promotional, marketing or educational purposes;
- Use for the purposes of monetary reward by means of sale, resale, licence, loan, transfer or other form of commercial exploitation such as marketing products
- Print reprints of Wiley Open Access articles can be purchased from: corporatesales@wiley.com

Other Terms and Conditions:

BY CLICKING ON THE "I AGREE..." BOX, YOU ACKNOWLEDGE THAT YOU HAVE READ AND FULLY UNDERSTAND EACH OF THE SECTIONS OF AND PROVISIONS SET FORTH IN THIS AGREEMENT AND THAT YOU ARE IN AGREEMENT WITH AND ARE WILLING TO ACCEPT ALL OF YOUR OBLIGATIONS AS SET FORTH IN THIS AGREEMENT.

v1.7

If you would like to pay for this license now, please remit this license along with your payment made payable to "COPYRIGHT CLEARANCE CENTER" otherwise you will be invoiced within 48 hours of the license date. Payment should be in the form of a check or money order referencing your account number and this invoice number RLNK500681161.

Once you receive your invoice for this order, you may pay your invoice by credit card. Please follow instructions provided at that time.

**Make Payment To:
Copyright Clearance Center
Dept 001
P.O. Box 843006
Boston, MA 02284-3006**

For suggestions or comments regarding this order, contact RightsLink Customer Support: customercare@copyright.com or +1-877-622-5543 (toll free in the US) or +1-978-646-2777.

Gratis licenses (referencing \$0 in the Total field) are free. Please retain this printable license for your reference. No payment is required.

**JOHN WILEY AND SONS LICENSE
TERMS AND CONDITIONS**

Dec 09, 2011

This is a License Agreement between Frank D Lesh ("You") and John Wiley and Sons ("John Wiley and Sons") provided by Copyright Clearance Center ("CCC"). The license consists of your order details, the terms and conditions provided by John Wiley and Sons, and the payment terms and conditions.

All payments must be made in full to CCC. For payment instructions, please see information listed at the bottom of this form.

License Number	2804910896786
License date	Dec 09, 2011
Licensed content publisher	John Wiley and Sons
Licensed content publication	European Journal of Inorganic Chemistry
Licensed content title	On the Effect of Coordination and Protonation Preferences in the Amphiphilic Behavior of Metallosurfactants with Asymmetric Headgroups (Eur. J. Inorg. Chem. 3/2009)
Licensed content author	Frank D. Lesh,Sarmad Sahiel Hindo,Mary Jane Heeg,Marco M. Allard,Prateek Jain,Bo Peng,Lew Hryhorczuk,Cláudio N. Verani
Licensed content date	Jan 1, 2009
Start page	323
End page	323
Type of use	Dissertation/Thesis
Requestor type	Author of this Wiley article
Format	Print and electronic
Portion	Figure/table
Number of figures/tables	13
Number of extracts	
Original Wiley figure/table number(s)	Scheme 1 and 2, Figure 1-7, Tables 1-3, Figure S1
Will you be translating?	No
Order reference number	
Total	0.00 USD
Terms and Conditions	

TERMS AND CONDITIONS

This copyrighted material is owned by or exclusively licensed to John Wiley & Sons, Inc. or one of its group companies (each a "Wiley Company") or a society for whom a Wiley Company has exclusive publishing rights in relation to a particular journal (collectively WILEY). By clicking "accept" in connection with completing this licensing transaction, you agree that the following terms and conditions apply to this transaction (along with the billing and payment terms and conditions established by the Copyright Clearance Center Inc., ("CCC's Billing and Payment terms and conditions"), at the time that you opened your Rightslink account (these are available at any time at <http://myaccount.copyright.com>)

Terms and Conditions

1. The materials you have requested permission to reproduce (the "Materials") are protected by copyright.
2. You are hereby granted a personal, non-exclusive, non-sublicensable, non-transferable, worldwide, limited license to

reproduce the Materials for the purpose specified in the licensing process. This license is for a one-time use only with a maximum distribution equal to the number that you identified in the licensing process. Any form of republication granted by this licence must be completed within two years of the date of the grant of this licence (although copies prepared before may be distributed thereafter). The Materials shall not be used in any other manner or for any other purpose. Permission is granted subject to an appropriate acknowledgement given to the author, title of the material/book/journal and the publisher. You shall also duplicate the copyright notice that appears in the Wiley publication in your use of the Material. Permission is also granted on the understanding that nowhere in the text is a previously published source acknowledged for all or part of this Material. Any third party material is expressly excluded from this permission.

3. With respect to the Materials, all rights are reserved. Except as expressly granted by the terms of the license, no part of the Materials may be copied, modified, adapted (except for minor reformatting required by the new Publication), translated, reproduced, transferred or distributed, in any form or by any means, and no derivative works may be made based on the Materials without the prior permission of the respective copyright owner. You may not alter, remove or suppress in any manner any copyright, trademark or other notices displayed by the Materials. You may not license, rent, sell, loan, lease, pledge, offer as security, transfer or assign the Materials, or any of the rights granted to you hereunder to any other person.

4. The Materials and all of the intellectual property rights therein shall at all times remain the exclusive property of John Wiley & Sons Inc or one of its related companies (WILEY) or their respective licensors, and your interest therein is only that of having possession of and the right to reproduce the Materials pursuant to Section 2 herein during the continuance of this Agreement. You agree that you own no right, title or interest in or to the Materials or any of the intellectual property rights therein. You shall have no rights hereunder other than the license as provided for above in Section 2. No right, license or interest to any trademark, trade name, service mark or other branding ("Marks") of WILEY or its licensors is granted hereunder, and you agree that you shall not assert any such right, license or interest with respect thereto.

5. NEITHER WILEY NOR ITS LICENSORS MAKES ANY WARRANTY OR REPRESENTATION OF ANY KIND TO YOU OR ANY THIRD PARTY, EXPRESS, IMPLIED OR STATUTORY, WITH RESPECT TO THE MATERIALS OR THE ACCURACY OF ANY INFORMATION CONTAINED IN THE MATERIALS, INCLUDING, WITHOUT LIMITATION, ANY IMPLIED WARRANTY OF MERCHANTABILITY, ACCURACY, SATISFACTORY QUALITY, FITNESS FOR A PARTICULAR PURPOSE, USABILITY, INTEGRATION OR NON-INFRINGEMENT AND ALL SUCH WARRANTIES ARE HEREBY EXCLUDED BY WILEY AND ITS LICENSORS AND WAIVED BY YOU.

6. WILEY shall have the right to terminate this Agreement immediately upon breach of this Agreement by you.

7. You shall indemnify, defend and hold harmless WILEY, its Licensors and their respective directors, officers, agents and employees, from and against any actual or threatened claims, demands, causes of action or proceedings arising from any breach of this Agreement by you.

8. IN NO EVENT SHALL WILEY OR ITS LICENSORS BE LIABLE TO YOU OR ANY OTHER PARTY OR ANY OTHER PERSON OR ENTITY FOR ANY SPECIAL, CONSEQUENTIAL, INCIDENTAL, INDIRECT, EXEMPLARY OR PUNITIVE DAMAGES, HOWEVER CAUSED, ARISING OUT OF OR IN CONNECTION WITH THE DOWNLOADING, PROVISIONING, VIEWING OR USE OF THE MATERIALS REGARDLESS OF THE FORM OF ACTION, WHETHER FOR BREACH OF CONTRACT, BREACH OF WARRANTY, TORT, NEGLIGENCE, INFRINGEMENT OR OTHERWISE (INCLUDING, WITHOUT LIMITATION, DAMAGES BASED ON LOSS OF PROFITS, DATA, FILES, USE, BUSINESS OPPORTUNITY OR CLAIMS OF THIRD PARTIES), AND WHETHER OR NOT THE PARTY HAS BEEN ADVISED OF THE POSSIBILITY OF SUCH DAMAGES. THIS LIMITATION SHALL APPLY NOTWITHSTANDING ANY FAILURE OF ESSENTIAL PURPOSE OF ANY LIMITED REMEDY PROVIDED HEREIN.

9. Should any provision of this Agreement be held by a court of competent jurisdiction to be illegal, invalid, or unenforceable, that provision shall be deemed amended to achieve as nearly as possible the same economic effect as the original provision, and the legality, validity and enforceability of the remaining provisions of this Agreement shall not be affected or impaired thereby.

10. The failure of either party to enforce any term or condition of this Agreement shall not constitute a waiver of either party's right to enforce each and every term and condition of this Agreement. No breach under this agreement shall be deemed waived or excused by either party unless such waiver or consent is in writing signed by the party granting such waiver or consent. The waiver by or consent of a party to a breach of any provision of this Agreement shall not operate or be construed as a waiver of or consent to any other or subsequent breach by such other party.

11. This Agreement may not be assigned (including by operation of law or otherwise) by you without WILEY's prior written consent.

12. Any fee required for this permission shall be non-refundable after thirty (30) days from receipt.

13. These terms and conditions together with CCC's Billing and Payment terms and conditions (which are incorporated herein) form the entire agreement between you and WILEY concerning this licensing transaction and (in the absence of fraud) supersedes all prior agreements and representations of the parties, oral or written. This Agreement may not be amended except in writing signed by both parties. This Agreement shall be binding upon and inure to the benefit of the parties' successors, legal representatives, and authorized assigns.

14. In the event of any conflict between your obligations established by these terms and conditions and those established by CCC's Billing and Payment terms and conditions, these terms and conditions shall prevail.

15. WILEY expressly reserves all rights not specifically granted in the combination of (i) the license details provided by you and accepted in the course of this licensing transaction, (ii) these terms and conditions and (iii) CCC's Billing and Payment terms and conditions.

16. This Agreement will be void if the Type of Use, Format, Circulation, or Requestor Type was misrepresented during the

licensing process.

17. This Agreement shall be governed by and construed in accordance with the laws of the State of New York, USA, without regards to such state's conflict of law rules. Any legal action, suit or proceeding arising out of or relating to these Terms and Conditions or the breach thereof shall be instituted in a court of competent jurisdiction in New York County in the State of New York in the United States of America and each party hereby consents and submits to the personal jurisdiction of such court, waives any objection to venue in such court and consents to service of process by registered or certified mail, return receipt requested, at the last known address of such party.

Wiley Open Access Terms and Conditions

All research articles published in Wiley Open Access journals are fully open access: immediately freely available to read, download and share. Articles are published under the terms of the [Creative Commons Attribution Non Commercial License](#), which permits use, distribution and reproduction in any medium, provided the original work is properly cited and is not used for commercial purposes. The license is subject to the Wiley Open Access terms and conditions:

Wiley Open Access articles are protected by copyright and are posted to repositories and websites in accordance with the terms of the [Creative Commons Attribution Non Commercial License](#). At the time of deposit, Wiley Open Access articles include all changes made during peer review, copyediting, and publishing. Repositories and websites that host the article are responsible for incorporating any publisher-supplied amendments or retractions issued subsequently.

Wiley Open Access articles are also available without charge on Wiley's publishing platform, **Wiley Online Library** or any successor sites.

Use by non-commercial users

For non-commercial and non-promotional purposes individual users may access, download, copy, display and redistribute to colleagues Wiley Open Access articles, as well as adapt, translate, text- and data-mine the content subject to the following conditions:

- The authors' moral rights are not compromised. These rights include the right of "paternity" (also known as "attribution" - the right for the author to be identified as such) and "integrity" (the right for the author not to have the work altered in such a way that the author's reputation or integrity may be impugned).
- Where content in the article is identified as belonging to a third party, it is the obligation of the user to ensure that any reuse complies with the copyright policies of the owner of that content.
- If article content is copied, downloaded or otherwise reused for non-commercial research and education purposes, a link to the appropriate bibliographic citation (authors, journal, article title, volume, issue, page numbers, DOI and the link to the definitive published version on Wiley Online Library) should be maintained. Copyright notices and disclaimers must not be deleted.
- Any translations, for which a prior translation agreement with Wiley has not been agreed, must prominently display the statement: "This is an unofficial translation of an article that appeared in a Wiley publication. The publisher has not endorsed this translation."

Use by commercial "for-profit" organisations

Use of Wiley Open Access articles for commercial, promotional, or marketing purposes requires further explicit permission from Wiley and will be subject to a fee. Commercial purposes include:

- Copying or downloading of articles, or linking to such articles for further redistribution, sale or licensing;
- Copying, downloading or posting by a site or service that incorporates advertising with such content;
- The inclusion or incorporation of article content in other works or services (other than normal

quotations with an appropriate citation) that is then available for sale or licensing, for a fee (for example, a compilation produced for marketing purposes, inclusion in a sales pack)

- Use of article content (other than normal quotations with appropriate citation) by for-profit organisations for promotional purposes
- Linking to article content in e-mails redistributed for promotional, marketing or educational purposes;
- Use for the purposes of monetary reward by means of sale, resale, licence, loan, transfer or other form of commercial exploitation such as marketing products
- Print reprints of Wiley Open Access articles can be purchased from: corporatesales@wiley.com

Other Terms and Conditions:

BY CLICKING ON THE "I AGREE..." BOX, YOU ACKNOWLEDGE THAT YOU HAVE READ AND FULLY UNDERSTAND EACH OF THE SECTIONS OF AND PROVISIONS SET FORTH IN THIS AGREEMENT AND THAT YOU ARE IN AGREEMENT WITH AND ARE WILLING TO ACCEPT ALL OF YOUR OBLIGATIONS AS SET FORTH IN THIS AGREEMENT.

v1.7

If you would like to pay for this license now, please remit this license along with your payment made payable to "COPYRIGHT CLEARANCE CENTER" otherwise you will be invoiced within 48 hours of the license date. Payment should be in the form of a check or money order referencing your account number and this invoice number RLNK500681166.

Once you receive your invoice for this order, you may pay your invoice by credit card. Please follow instructions provided at that time.

**Make Payment To:
Copyright Clearance Center
Dept 001
P.O. Box 843006
Boston, MA 02284-3006**

For suggestions or comments regarding this order, contact RightsLink Customer Support: customercare@copyright.com or +1-877-622-5543 (toll free in the US) or +1-978-646-2777.

Gratis licenses (referencing \$0 in the Total field) are free. Please retain this printable license for your reference. No payment is required.

**JOHN WILEY AND SONS LICENSE
TERMS AND CONDITIONS**

Dec 27, 2011

This is a License Agreement between Frank D Lesh ("You") and John Wiley and Sons ("John Wiley and Sons") provided by Copyright Clearance Center ("CCC"). The license consists of your order details, the terms and conditions provided by John Wiley and Sons, and the payment terms and conditions.

All payments must be made in full to CCC. For payment instructions, please see information listed at the bottom of this form.

License Number	2817190476339
License date	Dec 27, 2011
Licensed content publisher	John Wiley and Sons
Licensed content publication	European Journal of Inorganic Chemistry
Licensed content title	Unexpected Formation of a Cobalt(III) Phenoxazinylate Electron Reservoir
Licensed content author	Frank D. Lesh, Richard L. Lord, Mary Jane Heeg, H. Bernhard Schlegel, Cláudio N. Verani
Licensed content date	Dec 20, 2011
Start page	n/a
End page	n/a
Type of use	Dissertation/Thesis
Requestor type	Author of this Wiley article
Format	Print and electronic
Portion	Full article
Will you be translating?	No
Order reference number	
Total	0.00 USD

[Terms and Conditions](#)

TERMS AND CONDITIONS

This copyrighted material is owned by or exclusively licensed to John Wiley & Sons, Inc. or one of its group companies (each a "Wiley Company") or a society for whom a Wiley Company has exclusive publishing rights in relation to a particular journal (collectively WILEY). By clicking "accept" in connection with completing this licensing transaction, you agree that the following terms and conditions apply to this transaction (along with the billing and payment terms and conditions established by the Copyright Clearance Center Inc., ("CCC's Billing and Payment terms and conditions"), at the time that you opened your Rightslink account (these are available at any time at <http://myaccount.copyright.com>)

Terms and Conditions

1. The materials you have requested permission to reproduce (the "Materials") are protected by copyright.
2. You are hereby granted a personal, non-exclusive, non-sublicensable, non-transferable, worldwide, limited license to reproduce the Materials for the purpose specified in the licensing process. This license is for a one-time use only with a maximum distribution equal to the number that you identified in the licensing process. Any form of republication granted by this licence must be completed within two years of the date of the grant of this licence (although copies prepared before may be distributed thereafter). The Materials shall not be used in any other manner or for any other purpose. Permission is granted subject to an appropriate acknowledgement given to the author, title of the material/book/journal and the publisher. You shall also duplicate the copyright notice that appears in the Wiley publication in your use of the Material. Permission is also granted on the understanding that nowhere in the text is a previously published source acknowledged for all or part of this Material. Any third party material is expressly excluded from this permission.

3. With respect to the Materials, all rights are reserved. Except as expressly granted by the terms of the license, no part of the Materials may be copied, modified, adapted (except for minor reformatting required by the new Publication), translated, reproduced, transferred or distributed, in any form or by any means, and no derivative works may be made based on the Materials without the prior permission of the respective copyright owner. You may not alter, remove or suppress in any manner any copyright, trademark or other notices displayed by the Materials. You may not license, rent, sell, loan, lease, pledge, offer as security, transfer or assign the Materials, or any of the rights granted to you hereunder to any other person.

4. The Materials and all of the intellectual property rights therein shall at all times remain the exclusive property of John Wiley & Sons Inc or one of its related companies (WILEY) or their respective licensors, and your interest therein is only that of having possession of and the right to reproduce the Materials pursuant to Section 2 herein during the continuance of this Agreement. You agree that you own no right, title or interest in or to the Materials or any of the intellectual property rights therein. You shall have no rights hereunder other than the license as provided for above in Section 2. No right, license or interest to any trademark, trade name, service mark or other branding ("Marks") of WILEY or its licensors is granted hereunder, and you agree that you shall not assert any such right, license or interest with respect thereto.

5. NEITHER WILEY NOR ITS LICENSORS MAKES ANY WARRANTY OR REPRESENTATION OF ANY KIND TO YOU OR ANY THIRD PARTY, EXPRESS, IMPLIED OR STATUTORY, WITH RESPECT TO THE MATERIALS OR THE ACCURACY OF ANY INFORMATION CONTAINED IN THE MATERIALS, INCLUDING, WITHOUT LIMITATION, ANY IMPLIED WARRANTY OF MERCHANTABILITY, ACCURACY, SATISFACTORY QUALITY, FITNESS FOR A PARTICULAR PURPOSE, USABILITY, INTEGRATION OR NON-INFRINGEMENT AND ALL SUCH WARRANTIES ARE HEREBY EXCLUDED BY WILEY AND ITS LICENSORS AND WAIVED BY YOU.

6. WILEY shall have the right to terminate this Agreement immediately upon breach of this Agreement by you.

7. You shall indemnify, defend and hold harmless WILEY, its Licensors and their respective directors, officers, agents and employees, from and against any actual or threatened claims, demands, causes of action or proceedings arising from any breach of this Agreement by you.

8. IN NO EVENT SHALL WILEY OR ITS LICENSORS BE LIABLE TO YOU OR ANY OTHER PARTY OR ANY OTHER PERSON OR ENTITY FOR ANY SPECIAL, CONSEQUENTIAL, INCIDENTAL, INDIRECT, EXEMPLARY OR PUNITIVE DAMAGES, HOWEVER CAUSED, ARISING OUT OF OR IN CONNECTION WITH THE DOWNLOADING, PROVISIONING, VIEWING OR USE OF THE MATERIALS REGARDLESS OF THE FORM OF ACTION, WHETHER FOR BREACH OF CONTRACT, BREACH OF WARRANTY, TORT, NEGLIGENCE, INFRINGEMENT OR OTHERWISE (INCLUDING, WITHOUT LIMITATION, DAMAGES BASED ON LOSS OF PROFITS, DATA, FILES, USE, BUSINESS OPPORTUNITY OR CLAIMS OF THIRD PARTIES), AND WHETHER OR NOT THE PARTY HAS BEEN ADVISED OF THE POSSIBILITY OF SUCH DAMAGES. THIS LIMITATION SHALL APPLY NOTWITHSTANDING ANY FAILURE OF ESSENTIAL PURPOSE OF ANY LIMITED REMEDY PROVIDED HEREIN.

9. Should any provision of this Agreement be held by a court of competent jurisdiction to be illegal, invalid, or unenforceable, that provision shall be deemed amended to achieve as nearly as possible the same economic effect as the original provision, and the legality, validity and enforceability of the remaining provisions of this Agreement shall not be affected or impaired thereby.

10. The failure of either party to enforce any term or condition of this Agreement shall not constitute a waiver of either party's right to enforce each and every term and condition of this Agreement. No breach under this agreement shall be deemed waived or excused by either party unless such waiver or consent is in writing signed by the party granting such waiver or consent. The waiver by or consent of a party to a breach of any provision of this Agreement shall not operate or be construed as a waiver of or consent to any other or subsequent breach by such other party.

11. This Agreement may not be assigned (including by operation of law or otherwise) by you without WILEY's prior written consent.

12. Any fee required for this permission shall be non-refundable after thirty (30) days from receipt.

13. These terms and conditions together with CCC's Billing and Payment terms and conditions (which are incorporated herein) form the entire agreement between you and WILEY concerning this licensing transaction and (in the absence of fraud) supersedes all prior agreements and representations of the parties, oral or written. This Agreement may not be amended except in writing signed by both parties. This Agreement shall be binding upon and inure to the benefit of the parties' successors, legal representatives, and authorized assigns.

14. In the event of any conflict between your obligations established by these terms and conditions and those established by CCC's Billing and Payment terms and conditions, these terms and conditions shall prevail.

15. WILEY expressly reserves all rights not specifically granted in the combination of (i) the license details provided by you and accepted in the course of this licensing transaction, (ii) these terms and conditions and (iii) CCC's Billing and Payment terms and conditions.

16. This Agreement will be void if the Type of Use, Format, Circulation, or Requestor Type was misrepresented during the licensing process.

17. This Agreement shall be governed by and construed in accordance with the laws of the State of New York, USA, without regards to such state's conflict of law rules. Any legal action, suit or proceeding arising out of or relating to these Terms and Conditions or the breach thereof shall be instituted in a court of competent jurisdiction in New York County in the State of New York in the United States of America and each party hereby consents and submits to the personal jurisdiction of such court, waives any objection to venue in such court and consents to service of process by registered or certified mail, return receipt requested, at the last known address of such party.

Wiley Open Access Terms and Conditions

All research articles published in Wiley Open Access journals are fully open access: immediately freely available to read, download and share. Articles are published under the terms of the [Creative Commons Attribution Non Commercial License](#), which permits use, distribution and reproduction in any medium, provided the original work is properly cited and is not used for commercial purposes. The license is subject to the Wiley Open Access terms and conditions:

Wiley Open Access articles are protected by copyright and are posted to repositories and websites in accordance with the terms of the [Creative Commons Attribution Non Commercial License](#). At the time of deposit, Wiley Open Access articles include all changes made during peer review, copyediting, and publishing. Repositories and websites that host the article are responsible for incorporating any publisher-supplied amendments or retractions issued subsequently.

Wiley Open Access articles are also available without charge on Wiley's publishing platform, **Wiley Online Library** or any successor sites.

Use by non-commercial users

For non-commercial and non-promotional purposes individual users may access, download, copy, display and redistribute to colleagues Wiley Open Access articles, as well as adapt, translate, text- and data-mine the content subject to the following conditions:

- The authors' moral rights are not compromised. These rights include the right of "paternity" (also known as "attribution" - the right for the author to be identified as such) and "integrity" (the right for the author not to have the work altered in such a way that the author's reputation or integrity may be impugned).
- Where content in the article is identified as belonging to a third party, it is the obligation of the user to ensure that any reuse complies with the copyright policies of the owner of that content.
- If article content is copied, downloaded or otherwise reused for non-commercial research and education purposes, a link to the appropriate bibliographic citation (authors, journal, article title, volume, issue, page numbers, DOI and the link to the definitive published version on Wiley Online Library) should be maintained. Copyright notices and disclaimers must not be deleted.
- Any translations, for which a prior translation agreement with Wiley has not been agreed, must prominently display the statement: "This is an unofficial translation of an article that appeared in a Wiley publication. The publisher has not endorsed this translation."

Use by commercial "for-profit" organisations

Use of Wiley Open Access articles for commercial, promotional, or marketing purposes requires further explicit permission from Wiley and will be subject to a fee. Commercial purposes include:

- Copying or downloading of articles, or linking to such articles for further redistribution, sale or licensing;
- Copying, downloading or posting by a site or service that incorporates advertising with such content;
- The inclusion or incorporation of article content in other works or services (other than normal quotations with an appropriate citation) that is then available for sale or licensing, for a fee (for example, a compilation produced for marketing purposes, inclusion in a sales pack)
- Use of article content (other than normal quotations with appropriate citation) by for-profit

organisations for promotional purposes

- Linking to article content in e-mails redistributed for promotional, marketing or educational purposes;
- Use for the purposes of monetary reward by means of sale, resale, licence, loan, transfer or other form of commercial exploitation such as marketing products
- Print reprints of Wiley Open Access articles can be purchased from: corporatesales@wiley.com

Other Terms and Conditions:

BY CLICKING ON THE "I AGREE..." BOX, YOU ACKNOWLEDGE THAT YOU HAVE READ AND FULLY UNDERSTAND EACH OF THE SECTIONS OF AND PROVISIONS SET FORTH IN THIS AGREEMENT AND THAT YOU ARE IN AGREEMENT WITH AND ARE WILLING TO ACCEPT ALL OF YOUR OBLIGATIONS AS SET FORTH IN THIS AGREEMENT.

v1.7

If you would like to pay for this license now, please remit this license along with your payment made payable to "COPYRIGHT CLEARANCE CENTER" otherwise you will be invoiced within 48 hours of the license date. Payment should be in the form of a check or money order referencing your account number and this invoice number RLNK500689733.

Once you receive your invoice for this order, you may pay your invoice by credit card. Please follow instructions provided at that time.

**Make Payment To:
Copyright Clearance Center
Dept 001
P.O. Box 843006
Boston, MA 02284-3006**

For suggestions or comments regarding this order, contact RightsLink Customer Support: customercare@copyright.com or +1-877-622-5543 (toll free in the US) or +1-978-646-2777.

Gratis licenses (referencing \$0 in the Total field) are free. Please retain this printable license for your reference. No payment is required.

**JOHN WILEY AND SONS LICENSE
TERMS AND CONDITIONS**

Jan 04, 2012

This is a License Agreement between Frank D Lesh ("You") and John Wiley and Sons ("John Wiley and Sons") provided by Copyright Clearance Center ("CCC"). The license consists of your order details, the terms and conditions provided by John Wiley and Sons, and the payment terms and conditions.

All payments must be made in full to CCC. For payment instructions, please see information listed at the bottom of this form.

License Number	2817191061695
License date	Dec 27, 2011
Licensed content publisher	John Wiley and Sons
Licensed content publication	European Journal of Inorganic Chemistry
Licensed content title	Unexpected Formation of a Cobalt(III) Phenoxazinylate Electron Reservoir
Licensed content author	Frank D. Lesh,Richard L. Lord,Mary Jane Heeg,H. Bernhard Schlegel,Cláudio N. Verani
Licensed content date	Dec 20, 2011
Start page	n/a
End page	n/a
Type of use	Dissertation/Thesis
Requestor type	Author of this Wiley article
Format	Print and electronic
Portion	Figure/table
Number of figures/tables	6
Number of extracts	
Original Wiley figure/table number(s)	Scheme 1, Figures 1-4, and TOC artwork
Will you be translating?	No
Order reference number	
Total	0.00 USD

[Terms and Conditions](#)

TERMS AND CONDITIONS

This copyrighted material is owned by or exclusively licensed to John Wiley & Sons, Inc. or one of its group companies (each a "Wiley Company") or a society for whom a Wiley Company has exclusive publishing rights in relation to a particular journal (collectively WILEY"). By clicking "accept" in connection with completing this licensing transaction, you agree that the following terms and conditions apply to this transaction (along with the billing and payment terms and conditions established by the Copyright Clearance Center Inc., ("CCC's Billing and Payment terms and conditions"), at the time that you opened your Rightslink account (these are available at any time at <http://myaccount.copyright.com>)

Terms and Conditions

1. The materials you have requested permission to reproduce (the "Materials") are protected by copyright.
2. You are hereby granted a personal, non-exclusive, non-sublicensable, non-transferable, worldwide, limited license to reproduce the Materials for the purpose specified in the licensing process. This license is for a one-time use only with a maximum distribution equal to the number that you identified in the licensing process. Any form of republication granted by

this licence must be completed within two years of the date of the grant of this licence (although copies prepared before may be distributed thereafter). The Materials shall not be used in any other manner or for any other purpose. Permission is granted subject to an appropriate acknowledgement given to the author, title of the material/book/journal and the publisher. You shall also duplicate the copyright notice that appears in the Wiley publication in your use of the Material. Permission is also granted on the understanding that nowhere in the text is a previously published source acknowledged for all or part of this Material. Any third party material is expressly excluded from this permission.

3. With respect to the Materials, all rights are reserved. Except as expressly granted by the terms of the license, no part of the Materials may be copied, modified, adapted (except for minor reformatting required by the new Publication), translated, reproduced, transferred or distributed, in any form or by any means, and no derivative works may be made based on the Materials without the prior permission of the respective copyright owner. You may not alter, remove or suppress in any manner any copyright, trademark or other notices displayed by the Materials. You may not license, rent, sell, loan, lease, pledge, offer as security, transfer or assign the Materials, or any of the rights granted to you hereunder to any other person.

4. The Materials and all of the intellectual property rights therein shall at all times remain the exclusive property of John Wiley & Sons Inc or one of its related companies (WILEY) or their respective licensors, and your interest therein is only that of having possession of and the right to reproduce the Materials pursuant to Section 2 herein during the continuance of this Agreement. You agree that you own no right, title or interest in or to the Materials or any of the intellectual property rights therein. You shall have no rights hereunder other than the license as provided for above in Section 2. No right, license or interest in any trademark, trade name, service mark or other branding ("Marks") of WILEY or its licensors is granted hereunder, and you agree that you shall not assert any such right, license or interest with respect thereto.

5. NEITHER WILEY NOR ITS LICENSORS MAKES ANY WARRANTY OR REPRESENTATION OF ANY KIND TO YOU OR ANY THIRD PARTY, EXPRESS, IMPLIED OR STATUTORY, WITH RESPECT TO THE MATERIALS OR THE ACCURACY OF ANY INFORMATION CONTAINED IN THE MATERIALS, INCLUDING, WITHOUT LIMITATION, ANY IMPLIED WARRANTY OF MERCHANTABILITY, ACCURACY, SATISFACTORY QUALITY, FITNESS FOR A PARTICULAR PURPOSE, USABILITY, INTEGRATION OR NON-INFRINGEMENT AND ALL SUCH WARRANTIES ARE HEREBY EXCLUDED BY WILEY AND ITS LICENSORS AND WAIVED BY YOU.

6. WILEY shall have the right to terminate this Agreement immediately upon breach of this Agreement by you.

7. You shall indemnify, defend and hold harmless WILEY, its Licensors and their respective directors, officers, agents and employees, from and against any actual or threatened claims, demands, causes of action or proceedings arising from any breach of this Agreement by you.

8. IN NO EVENT SHALL WILEY OR ITS LICENSORS BE LIABLE TO YOU OR ANY OTHER PARTY OR ANY OTHER PERSON OR ENTITY FOR ANY SPECIAL, CONSEQUENTIAL, INCIDENTAL, INDIRECT, EXEMPLARY OR PUNITIVE DAMAGES, HOWEVER CAUSED, ARISING OUT OF OR IN CONNECTION WITH THE DOWNLOADING, PROVISIONING, VIEWING OR USE OF THE MATERIALS REGARDLESS OF THE FORM OF ACTION, WHETHER FOR BREACH OF CONTRACT, BREACH OF WARRANTY, TORT, NEGLIGENCE, INFRINGEMENT OR OTHERWISE (INCLUDING, WITHOUT LIMITATION, DAMAGES BASED ON LOSS OF PROFITS, DATA, FILES, USE, BUSINESS OPPORTUNITY OR CLAIMS OF THIRD PARTIES), AND WHETHER OR NOT THE PARTY HAS BEEN ADVISED OF THE POSSIBILITY OF SUCH DAMAGES. THIS LIMITATION SHALL APPLY NOTWITHSTANDING ANY FAILURE OF ESSENTIAL PURPOSE OF ANY LIMITED REMEDY PROVIDED HEREIN.

9. Should any provision of this Agreement be held by a court of competent jurisdiction to be illegal, invalid, or unenforceable, that provision shall be deemed amended to achieve as nearly as possible the same economic effect as the original provision, and the legality, validity and enforceability of the remaining provisions of this Agreement shall not be affected or impaired thereby.

10. The failure of either party to enforce any term or condition of this Agreement shall not constitute a waiver of either party's right to enforce each and every term and condition of this Agreement. No breach under this agreement shall be deemed waived or excused by either party unless such waiver or consent is in writing signed by the party granting such waiver or consent. The waiver by or consent of a party to a breach of any provision of this Agreement shall not operate or be construed as a waiver of or consent to any other or subsequent breach by such other party.

11. This Agreement may not be assigned (including by operation of law or otherwise) by you without WILEY's prior written consent.

12. Any fee required for this permission shall be non-refundable after thirty (30) days from receipt.

13. These terms and conditions together with CCC's Billing and Payment terms and conditions (which are incorporated herein) form the entire agreement between you and WILEY concerning this licensing transaction and (in the absence of fraud) supersedes all prior agreements and representations of the parties, oral or written. This Agreement may not be amended except in writing signed by both parties. This Agreement shall be binding upon and inure to the benefit of the parties' successors, legal representatives, and authorized assigns.

14. In the event of any conflict between your obligations established by these terms and conditions and those established by CCC's Billing and Payment terms and conditions, these terms and conditions shall prevail.

15. WILEY expressly reserves all rights not specifically granted in the combination of (i) the license details provided by you and accepted in the course of this licensing transaction, (ii) these terms and conditions and (iii) CCC's Billing and Payment terms and conditions.

16. This Agreement will be void if the Type of Use, Format, Circulation, or Requestor Type was misrepresented during the licensing process.

17. This Agreement shall be governed by and construed in accordance with the laws of the State of New York, USA, without regards to such state's conflict of law rules. Any legal action, suit or proceeding arising out of or relating to these Terms and Conditions or the breach thereof shall be instituted in a court of competent jurisdiction in New York County in the State of New York in the United States of America and each party hereby consents and submits to the personal jurisdiction of such court, waives any objection to venue in such court and consents to service of process by registered or certified mail, return receipt requested, at the last known address of such party.

Wiley Open Access Terms and Conditions

All research articles published in Wiley Open Access journals are fully open access: immediately freely available to read, download and share. Articles are published under the terms of the [Creative Commons Attribution Non Commercial License](#), which permits use, distribution and reproduction in any medium, provided the original work is properly cited and is not used for commercial purposes. The license is subject to the Wiley Open Access terms and conditions:

Wiley Open Access articles are protected by copyright and are posted to repositories and websites in accordance with the terms of the [Creative Commons Attribution Non Commercial License](#). At the time of deposit, Wiley Open Access articles include all changes made during peer review, copyediting, and publishing. Repositories and websites that host the article are responsible for incorporating any publisher-supplied amendments or retractions issued subsequently.

Wiley Open Access articles are also available without charge on Wiley's publishing platform, **Wiley Online Library** or any successor sites.

Use by non-commercial users

For non-commercial and non-promotional purposes individual users may access, download, copy, display and redistribute to colleagues Wiley Open Access articles, as well as adapt, translate, text- and data-mine the content subject to the following conditions:

- The authors' moral rights are not compromised. These rights include the right of "paternity" (also known as "attribution" - the right for the author to be identified as such) and "integrity" (the right for the author not to have the work altered in such a way that the author's reputation or integrity may be impugned).
- Where content in the article is identified as belonging to a third party, it is the obligation of the user to ensure that any reuse complies with the copyright policies of the owner of that content.
- If article content is copied, downloaded or otherwise reused for non-commercial research and education purposes, a link to the appropriate bibliographic citation (authors, journal, article title, volume, issue, page numbers, DOI and the link to the definitive published version on Wiley Online Library) should be maintained. Copyright notices and disclaimers must not be deleted.
- Any translations, for which a prior translation agreement with Wiley has not been agreed, must prominently display the statement: "This is an unofficial translation of an article that appeared in a Wiley publication. The publisher has not endorsed this translation."

Use by commercial "for-profit" organisations

Use of Wiley Open Access articles for commercial, promotional, or marketing purposes requires further explicit permission from Wiley and will be subject to a fee. Commercial purposes include:

- Copying or downloading of articles, or linking to such articles for further redistribution, sale or licensing;
- Copying, downloading or posting by a site or service that incorporates advertising with such content;
- The inclusion or incorporation of article content in other works or services (other than normal quotations with an appropriate citation) that is then available for sale or licensing, for a fee (for

example, a compilation produced for marketing purposes, inclusion in a sales pack)

- Use of article content (other than normal quotations with appropriate citation) by for-profit organisations for promotional purposes
- Linking to article content in e-mails redistributed for promotional, marketing or educational purposes;
- Use for the purposes of monetary reward by means of sale, resale, licence, loan, transfer or other form of commercial exploitation such as marketing products
- Print reprints of Wiley Open Access articles can be purchased from: corporatesales@wiley.com

Other Terms and Conditions:

BY CLICKING ON THE "I AGREE..." BOX, YOU ACKNOWLEDGE THAT YOU HAVE READ AND FULLY UNDERSTAND EACH OF THE SECTIONS OF AND PROVISIONS SET FORTH IN THIS AGREEMENT AND THAT YOU ARE IN AGREEMENT WITH AND ARE WILLING TO ACCEPT ALL OF YOUR OBLIGATIONS AS SET FORTH IN THIS AGREEMENT.

v1.7

If you would like to pay for this license now, please remit this license along with your payment made payable to "COPYRIGHT CLEARANCE CENTER" otherwise you will be invoiced within 48 hours of the license date. Payment should be in the form of a check or money order referencing your account number and this invoice number RLNK500689734.

Once you receive your invoice for this order, you may pay your invoice by credit card. Please follow instructions provided at that time.

Make Payment To:
Copyright Clearance Center
Dept 001
P.O. Box 843006
Boston, MA 02284-3006

For suggestions or comments regarding this order, contact RightsLink Customer Support:
customercare@copyright.com or +1-877-622-5543 (toll free in the US) or +1-978-646-2777.

Gratis licenses (referencing \$0 in the Total field) are free. Please retain this printable license for your reference. No payment is required.



ABSTRACT**SYNTHESIS, SPECTROSCOPIC, AND ELECTROCHEMICAL PROPERTIES
OF *3d* METAL AND RUTHENIUM COMPLEXES WITH PHENOLATE AND
CATECHOLATE LIGANDS**

by

FRANK DONALD LESH**May 2012****Advisor:** Dr. Cláudio N. Verani**Major:** Chemistry (Inorganic)**Degree:** Doctor of Philosophy

The integration of amphiphilic properties into transition metal coordination systems is a pertinent step toward the development of candidate metallosurfactant precursors for the formation of responsive monolayer films. This concept is intended to preserve the solution-observed redox, spectroscopic, and magnetic responses onto solid surfaces for potential application. Selected metal ions and various ligand designs are investigated to address the effect of coordination and protonation preferences on amphiphilic behavior, the aspects of new modular approaches for Langmuir film precursors of differentiated topologies to extend amphiphilicity and redox behavior, and the introduction of photosensitizing properties into electroactive metallosurfactant precursors. In an attempt to enhance the redox response of our current phenolato-based ligand scaffolds, rich multielectronic ligand-centered redox reactivity is established with the amino-catecholate functionality and will be incorporated into prospective ligand schemes. A concerted effort merges the comprehensive synthetic, electrochemical,

spectroscopic, and photophysical evidence, film formation methods, and computational techniques.

AUTOBIOGRAPHICAL STATEMENT

FRANK DONALD LESH

EDUCATION

Ph.D. Inorganic Chemistry, Wayne State University, Detroit, MI–February 2012

Dissertation: “Synthesis, Spectroscopic, and Electrochemical Properties of 3d Metal and Ruthenium Complexes with Phenolate and Catecholate Ligands”

Advisor: Cláudio N. Verani

B.Sc. Chemistry, Lawrence Technological University, Southfield, MI–May 2005

Distinction: Cum Laude

High School Diploma, Lee M. Thurston High School, Redford, MI–June 2001

Distinction: Highest Honors

PUBLICATIONS

1. Lesh, F. D.; Lord, R. L.; Heeg, M. J.; Schlegel, H. B.; Verani, C. N. “Unexpected Formation of a Cobalt(III) Phenoxazinylate Electron Reservoir.” *Eur. J. Inorg. Chem.* **2012**, 3, 463–466. *Special Issue: Cooperative & Redox Non-Innocent Ligands in Directing Organometallic Reactivity (Cluster Issue)*.
2. Lesh, F. D.; Allard, M. M.; Shanmugam, R.; Hryhorczuk, L. M.; Endicott, J. F.; Schlegel, H. B.; Verani, C. N. “Investigation of the Electronic, Photosubstitution, Redox, and Surface Properties of New Ruthenium(II)-Containing Amphiphiles.” *Inorg. Chem.* **2011**, 50, 969–977. *Ranked among the “top accessed” articles in March 2011 for Inorg. Chem.*
3. Lesh, F. D.; Shanmugam, R.; Allard, M. M.; Lanznaster, M.; Heeg, M. J.; Rodgers, M. T.; Shearer, J. M.; Verani, C. N. “A Modular Approach to Redox-Active Multimetallic Hydrophobes of Discoid Topology.” *Inorg. Chem.* **2010**, 49, 7226–7228.
4. Lesh, F. D.; Hindo, S. S.; Heeg, M. J.; Allard, M. M.; Jain, P.; P., Bo; Hryhorczuk, L.; Verani, C. N. “On the Effect of Coordination and Protonation Preferences in the Amphiphilic Behavior of Metallosurfactants with Asymmetric Headgroups.” *Eur. J. Inorg. Chem.* **2009**, 3, 345–356. *Received cover art for the issue.*
5. Lesh, F. D.; Lord, R. L.; Heeg, M. J.; Schlegel, H. B.; Verani, C. N. “The Rich Electron Transfer Behavior of Iron(III) and Gallium(III) Complexes with a Redox-Active Bis(phenolate) Phenylenediamine Ligand.” *In preparation for Inorg. Chem.*

AWARDS, HONORS, AND SCHOLARSHIPS

- Graduate research assistantship support provided by NSF and DOE, May 2008 – present
- Institute for Manufacturing Research (IMR) Fellowship, August 2007 – May 2008
- Honor Citation for Teaching Service in Chemistry Award, August 2007
- Lawrence Technological University Trustee Grant
- Lawrence Technological University Dean’s List
- Michigan Merit Award Scholarship and State of Michigan Competitive Scholarship